SERDP

FINAL REPORT

Development of Coupled Physicochemical and Biological Systems for In Situ Remediation of Mixed Perfluorinated Chemical and Chlorinated Solvent Groundwater Plumes

Kurt Pennell
Natalie Cápiro
John Fortner
Brown University

John Fortner
Washington University in St. Louis

December 2023

SERDP Project ER-2714

DISTRIBUTION STATEMENT A
This document has been cleared for public release.

This report was prepared under contract to the Department of Defense Strategic Environmental Research and Development Program (SERDP). The publication of this report does not indicate endorsement by the Department of Defense, nor should the contents be construed as reflecting the official policy or position of the Department of Defense. Reference herein to any specific commercial product, process, or service by trade name, trademark, manufacturer, or otherwise, does not necessarily constitute or imply its endorsement, recommendation, or favoring by the Department of Defense.

REPORT DOCUMENTATION PAGE

Form Approved
OMB No. 0704-0188

The public reporting burden for this collection of information is estimated to average 1 hour per response, including the time for reviewing instructions, searching existing data sources, gathering and maintaining the data needed, and completing and reviewing the collection of information. Send comments regarding this burden estimate or any other aspect of this collection of information, including suggestions for reducing the burden, to Department of Defense, Washington Headquarters Services, Directorate for Information Operations and Reports (0704-0188), 1215 Jefferson Davis Highway, Suite 1204, Arlington, VA 22202-4302. Respondents should be aware that notwithstanding any other provision of law, no person shall be subject to any penalty for failing to comply with a collection of information if it does not display a currently valid OMB control number.
PLEASE DO NOT RETURN YOUR FORM TO THE ABOVE ADDRESS.

1. REPORT DATE *(DD-MM-YYYY)*	**2. REPORT TYPE**	**3. DATES COVERED** *(From - To)*
12/01/2023	SERDP Final Report	09/28/2018 - 09/21/2023

4. TITLE AND SUBTITLE

Development of Coupled Physicochemical and Biological Systems for In Situ Remediation of Mixed Perfluorinated Chemical and Chlorinated Solvent Groundwater Plumes

5a. CONTRACT NUMBER
18-C-0002

5b. GRANT NUMBER

5c. PROGRAM ELEMENT NUMBER

6. AUTHOR(S)
Pennell, Kurt, D., Capiro, Natalie, L., Fortner, John, D.

5d. PROJECT NUMBER
ER-2714

5e. TASK NUMBER

5f. WORK UNIT NUMBER

7. PERFORMING ORGANIZATION NAME(S) AND ADDRESS(ES)
Brown University
1 Prospect Street
Providence, RI 02910-9100

8. PERFORMING ORGANIZATION REPORT NUMBER
ER-2714

9. SPONSORING/MONITORING AGENCY NAME(S) AND ADDRESS(ES)
Office of the Deputy Assistant Secretary of Defense (Energy Resilience & Optimization)
3500 Defense Pentagon, RM 5C646
Washington, DC 20301-3500

10. SPONSOR/MONITOR'S ACRONYM(S)
SERDP

11. SPONSOR/MONITOR'S REPORT NUMBER(S)
ER-2714

12. DISTRIBUTION/AVAILABILITY STATEMENT
DISTRIBUTION STATEMENT A. Approved for public release: distribution unlimited.

13. SUPPLEMENTARY NOTES

14. ABSTRACT
Aqueous film foaming foams (AFFF) were widely used at Department of Defense (DoD) installations for fire fighter training exercises and fire response. Due to their stability at high temperature and amphiphilic properties, these foams contain per- and polyfluoroalkyl substances (PFAS), including perfluorooctanoic acid (PFOA) and perfluorooctane sulfonate (PFOS). Additionally, chlorinated solvents, such as tetrachloroethene (PCE) and trichloroethene (TCE), were commonly used for aircraft engine cleaning, paint removal, and degreasing metal parts. Thus, contaminated groundwater plumes at DoD sites often contain mixtures of chlorinated solvents and PFAS, both of which have stringent drinking water standards. Although bioremediation is commonly used to treat PCE and TCE, most PFAS are extremely recalcitrant to conventional thermal, chemical or biological treatments. The goals of this project were to develop coupled in situ remediation approaches that could be used to effectively treat groundwater plumes containing mixtures of PFAS and chlorinated ethenes, and to understand the potential synergies and limitations of these combined remedies.

15. SUBJECT TERMS
Aqueous film forming foam (AFFF), PFAS, per and polyfluoroalkyl substances, nanomaterials, bioremediation, adsorption, permeable adsorptive barrier, ion exchange resin, in situ remediation, powdered activated carbon, polydadmac, polymer, graphene, chlorinated solvents, reductive dechlorination, tetrachloroethene, trichloroethene

16. SECURITY CLASSIFICATION OF:			**17. LIMITATION OF ABSTRACT**	**18. NUMBER OF PAGES**	**19a. NAME OF RESPONSIBLE PERSON**
a. REPORT	**b. ABSTRACT**	**c. THIS PAGE**			Pennell, Kurt, D.
UNCLASS	UNCLASS	UNCLASS	UNCLASS	214	**19b. TELEPHONE NUMBER** *(Include area code)* 781-502-8545

Table of Contents

Table of Contents i
List of Tables vi
List of Figures viii
List of Acronyms xvi
Keywords xviii
Acknowledgements xix
Abstract 1
Graphical Abstract 2
Executive Summary 3
Introduction 3
Objectives 4
Technical Approach 5
Results and Discussion 6
Development of Highly Sorptive Nanomaterials for PFAS Sequestration 6
Development of Reactive Nanomaterials for PFAS Transformation 8
Impacts of PFAS on Organohalide Respiration 9
Permeable Adsorptive Barriers for PFAS Sequestration 11
Coupled Treatment Systems for Groundwater Containing Chlorinated Solvents and PFAS 12
Implications for Future Research and Benefits 13
1. Objectives 14
1.1 Introduction 14
1.2 Research Goals 16
1.3 Research Approach 17
2. Background 20
2.1 PFAS Contamination 20
2.2 PFAS Health Effects 21
2.3 PFAS Drinking Water Regulations 21
2.4 PFAS Accumulation at the Air-Water Interface 22
2.5 Potential Impacts of Co-contaminants on Bioremediation of Chlorinated Ethenes 23
2.6 Mathematical Modeling of PFAS Fate and Transport 24
2.7 Bioremediation of chlorinated ethenes and potential impact of co-contaminants 25

2.8 In situ remediation of comingled per- and polyfluoroalkyl substances (PFAS) and chlorinated ethenes groundwater 25
2.9 Biotransformation of PFAS Precursors 25
2.10 PFAS removal techologies 26
2.11 Abiotic degradataion of PFAS 28
3. Materials and Methods 29
3.1 Preparation of Multifunctional Nanoscale Sorbents for PFAS Treatment 29
3.1.1 Preparation of Organic (Surface) Functionalized IONPs 29
3.1.2 Batch Adsorption Isotherms 29
3.1.3 Quartz Crystal Microbalance with Dissipation (QCM−D) 30
3.1.4 IONP Column Studies 31
3.1.5 Photocatalytic Oxidation Processes for PFOA Degradation 31
3.1.5.1 Preparation of TiO2/MOF Composite Materials 31
3.1.5.2 Surface Functionalization of Composite Materials 32
3.1.5.3 Material Characterization 33
3.1.5.4 Photocatalytic PFOA Degradation Tests 33
3.1.6 Electrochemical Oxidation Processes for PFOS Treatment 33
3.1.6.1 Preparation and Characterization of CNTs Coated Electrode 33
3.1.6.2 Experimental Procedure and Analytical Methods 34
3.2 Biotransformation Experiments 36
3.2.1 Chemicals and Materials 36
3.2.2 Batch reactor and microcosm experiments 37
3.2.2.1 Reactor and microcosm preparation 37
3.2.2.2 Sampling batch reactors and microcosms 42
3.2.2.3 Rate and statistical analysis for MRD in batch reactors 42
3.3 Permeable Adsorptive Barrier Experiments 44
3.3.1 Stabilized Powdered Activated Carbon (S-PAC) Batch and Column Studies 44
3.3.1.1 Materials 44
3.3.1.2 S-PAC batch adsorption tests 44
3.3.1.3 S-PAC column studies 44
3.3.1.4 Analytical methods 46
3.3.2 Stabilized Ion Exchange Resin (S-IXR) Batch and Column Studies 46
3.3.2.1 Materials 46
3.3.2.2 Batch adsorption studies with IXR 47
3.3.2.3 Column experiments with S-IXR 48

3.3.2.4 Analytical Methods used for S-IXR experiments 49
3.4 Coupled Adsorptive and Bioactive Column Experiments 50
3.4.1 Column Setup 50
3.4.1.1 Configuration, preparation and operation of columns 50
3.4.1.2 Column sampling 53
3.5 Aquifer Cell Experiments 54
3.5.1 Aquifer cell desing 54
3.5.2 Aquifer Cell Operation 54
3.6 PFAS Analyticdal Methods 55
3.6.1 Targeted PFAS Analysis 55
3.6.2 Non-targeted PFAS Analysis 56
4. Results and Discussion 57
4.1 Ultra–High Capacity Multifunctional Nanoscale Sorbents for PFOA and PFOS Treatment 57
4.1.1 Role of Surface Coating of Nanocrystals on PFAS Sorption Behavior 57
4.1.2 Real Time Analysis of PFAS Sorption via QCM-D 60
4.1.3 Competitive Sorption of PFAS: Multi-Sorbate System 64
4.1.4 Critical Role of Functional Groups of PFAS on Sorption Behavior 65
4.1.5 Effect of Water Chemistry on PFAS Sorption Behavior 66
4.1.6 Sequestration of PFOA and PFOS in Column Studies 68
4.2 Enhanced Photocatalytic Oxidation of PFOA with Functionalized Metal Organic Framework (MOF) Composite Materials 70
4.2.1 PFOA Degradation by TiO2/MOF Composites 70
4.2.2 Enhancing MOF Composite Photocatalytic Activity 71
4.2.3 Proposed Reaction Mechanisms 72
4.3 Development of Novel Electrochemical Oxidation Reaction for PFOS Transformation 74
4.3.1 Morphological Features and Characterization of CNTs−NF Electrodes 74
4.3.2 Enhanced PFOS Degradation with Carbon-based NF Cathodes 77
4.3.3 Mechanistic Investigation Based on Surface of CNTs-bound Sulfate Radicals 79
4.3.4 Mechanistic investigation of Adsorption Capacity of CNTs-NF Electrodes 81
4.3.5 Stability Tests for Repeated PFOS Oxidation and Defluorination 84
4.4 Biotic Batch Reactors and Microcosoms 86
4.4.1 Impacts of PFAAs on MRD in the Absence of Soil 86
4.4.2 Modeling MDR in Batch Reactors 88
4.4.3 Modeling MDR in Microcosms 91

4.4.4 Total and Strain-specific Growth of Dhc in Batch reactors and Microcosms 93
4.5 Batch Reactors and Microcososms 97
4.5.1 Single and Coupled Column Experiments for Mixed Chlorinated Ethenes and PFAA Treatment 97
4.5.1.1 Set 1: Single IONP column experiment 97
4.5.1.2 Set 2: Single S-PAC column experiment 99
4.5.1.3 Set 3: Coupled bioactive and IONP columns experiment 100
4.5.1.4 Set 4: Coupled bioactive and S-PAC columns experiment 101
4.2.5 Enhanced sequestration of PFAAs in coupled bioactive and adsorptive columns 103
4.6 Evaluation of S-PAC as a Permeable Adsorptive Barrier 106
4.6.1 S-PAC Batch Adsorption Results 106
4.6.2 S-PAC Column Results 106
4.6.3 S-PAC Aquifer Cell Results 113
4.7 Evaluation of S-IXR as a Permeable Adsorptive Barrier 116
4.7.1 S-IXR batch adsorption results for individual PFAS 116
4.7.2 S-IXR batch adsorption results for mixtures of PFAS 119
4.7.3 Delivery and Retention of S-IXR 124
4.7.4 Sequestration of PFOA or PFOS by S-IXR Treated Sand 125
4.7.5 Sequestration of a PFAS Mixture by S-IXR Treated Sand 129
5. Conclusions and Implications 132
5.1 Development of sorptive and reactivce materials 132
5.2 Impacts of PFAS on organohalide respiration 133
5.3 Injectable particulate amendments for permeable adsorptive barriers 134
5.4 Coupled treatment systems for groundwater containing chlorinated ethenes and PFAS . 134
6. Literature Cited 136
Appendix A: Supporting Information 153
A.1 Biological Analytical Methods 153
A.2 Chemical Analytical Methods 156
A.3 Mathematical Modeling of Biodegradation 168
A.3.1 Model Fitting 171
A.4 Sorption of TCE and PCE 179
A.5 PFOS Degradation Products 181
Appendix B: List of Scientific/Technical Publications 183
B.1 Peer-Reviewed Papers 183
B.2 Presentations/Posters: 184

B.3 Patents and Patent Applications: 185
Appendix C: Other Supporting Materials 186
C.1 Per- and Polyfluoroalkyl Substances (PFAS) Analyte List 186
C.2 Standard Operating Procedures for PFAS Sample Collection Preparation, and Analysis 187

List of Tables

Table 2.1 Summary of adsorption capacities for PFAS (considering PFOA and PFOS) for various adsorbents for comparison. 27

Table 3.1 Physical and chemical properties of Robins, Loring, and Hudson soils. 36

Table 3.2 Batch reactor experiments, identified by the target initial total PFAA concentration.. 37

Table 3.3 Microcosm experiments, identified by the average final PFAA concentration. 38

Table 3.4 Initial gene abundances for inoculum bottles used in batch reactor and microcosm experiments. All values shown as gene copies/mL. Average and standard deviations for three samples of each inoculum with each sample measured in triplicate. Batch reactor experiments inoculated with 3 mL each from bottles 1 and 2 and microcosm experiments inoculated with 6mL from bottle 3 or bottle 4. 39

Table 3.5 Composition of PFAA Mixture in Batch Reactor Experiments 41

Table 3.6 Properties of PFAS used in S-IXR experiments. 47

Table 3.7 Overview of column experiments and operating conditions. 51

Table 3.8 Targeted concentrations of PCE, TCE, and 10 PFAAs in the influent solution introduced into columns and corresponding composition of PFAA mixture (% total PFAAs by mass) measured in the column experiments compared to previous microcosm study (Hnatko et al., 2023)..... 52

Table 4.1 Organic loading on the iron oxide nanoparticles (IONPs). 59

Table 4.2 Sorption isotherm constants and regression data for Langmuir and Freundlich adsorption isotherm models. 60

Table 4.3 Ionic composition of synthetic groundwater. 67

Table 4.4 Mean of triplicate measurements of initial and final *GeoSZ* abundances in gene copies/mL in batch reactors. Initial abundances were calculated using the measured abundance in inoculum and mass of inoculum added. 88

Table 4.5 Mean of triplicate measurements of initial and final *GeoSZ* abundances in gene copies/mL in microcosms. Initial abundances were calculated using the measured abundance in inoculum and mass of inoculum added. 88

Table 4.6 Retained mass of PFAAs and PCE/TCE in adsorptive columns in all four sets of column experiments (PFAAs in µg, PCE/TCE in mg) 104

Table 4.7 Adsorption capacity of PFAAs and PCE/TCE in adsorptive columns in all four sets of column experiments (retained mass per gram adsorptive material, in unit mg/g Fe or C)..... 105

Table 4.8 Linear adsorption coefficient (K_D) values obtained for individual PFAS and mixture of the six PFAS in completely mixed batch reactors in the low concentration range (1 to 100 µg/L). 117

Table 4.9 Freundlich adsorption parameters (K_F and n) obtained for individual PFAS in completely mixed batch reactors in the high concentration range (10 to 500 mg/L). 117

Table A.1 qPCR target gene, chemistry, calibration curve parameters, and standard linear range for each analytical run..... 154

Table A.2 PFAS concentrations (mg/L) in batch reactors. For each entry, the average value of 5 batch reactor measurements is shown. The standard deviation is provided in parenthesis and the proportion of total PFAAs by mass for each PFAA is shown as a percentage. PFBA= perfluorobutrycic acid, PFPeA=perfluoropentanoic acid, PFBS=perfluorobutane sulfonic acid, PFHxA=perfluorohexanoic acid, PFHpA= perfluoroheptanoic acid, PFHxS=perfluorohexane sulfonic acid, PFOA=perfluorooctanoic acid, PFNA=perfluorononanoic acid, PFOS= perfluorooctane sulfonic acid, and PFDA=perfluorodecanoic acid..... 157

Table A.3 Initial and final PFAS concentrations (mg/L) in microcosms. For each entry, the average value of 5 microcosm measurements is shown. The standard deviation is provided in parenthesis and the proportion of total PFAAs by mass for each PFAA is shown as a percentage. PFBA=perfluorobutrycic acid, PFPeA=perfluoropentanoic acid, PFBS=perfluorobutane sulfonic acid, PFHxA=perfluorohexanoic acid, PFHpA= perfluoroheptanoic acid, PFHxS=perfluorohexane sulfonic acid, PFOA=perfluorooctanoic acid, PFNA=perfluorononanoic acid, PFOS= perfluorooctane sulfonic acid, and PFDA=perfluorodecanoic acid. 161

Table A.4 Diffusional mass loss parameters (see **equations 4.1** and **A.7**). Here, PCE and TCE mass loss parameters were fit to abiotic batch reactor data; parameters for *cis*-DCE, vinyl chloride, and ethene were estimated using literature data and correlations, as described in **Appendix A.3**. 173

Table A.5 Summary of Monod kinetic parameters (see **equations A.1** and **A2**) fitted to chlorinated ethene and qPCR biomass data from three biotic control batch reactor experiments (**Figure A.6**) by minimizing the objective function **A.19** (Phase 1 optimization). Parameter optimization ranges were derived from literature ranges and are presented in column 3. 175

Table A.6 Average maximum substrate utilization rates for each set of batch reactors in units of mmol/day/cell. **Bold** entries are significantly lower than the average for the 0 mg/L reactor set ($p<0.05$). *Italicized* entries are higher than the average for the 0 mg/L reactor set. Calculated p-values are included comparing the average maximum substrate utilization rate for each set of reactors with PFAAs to those of the positive control (0 mg/L PFAA) reactors..... 178

Table A.7 Intermediate by-products derived from PFOS degradation, characterized by their mass-to-charge ratio (m/z) 181

List of Figures

Figure 1.1 Schematic diagram of two treatment train approaches for comingled a PFOS-PFOA-PCE-TCE groundwater plume: (1) Sorption followed by anaerobic reductive dechlorination, and (2) Catalyzed reduction reaction. 16

Figure 1.2 Project flow diagram illustrating synergistic integrated project tasks. 17

Figure 3.1 Schematic diagram of the experimental system used for the S-PAC column studies. 45

Figure 3.2 Schematic diagrams of column experimental configuration (a) single adsorptive column and (b) coupled bioactive and adsorptive columns. 52

Figure 3.3 Schematic diagram of the aquifer cell showing the overall dimensions, location of injection and sampling ports, and size and location of lower-permeability lenses. 55

Figure 4.1 TEM images of monodisperse iron oxide nanoparticles (IONPs) and histograms of the size distribution of NCs. Average diameter of NPs was measured using Image-Pro 6.0 with over a thousand counted. Scale bar is 50 nm. 57

Figure 4.2 (a) Hydrodynamic diameters and (b) zeta potential of organic functionalized IONPs with polyethyleneimine (PEI), cetyltrimethylammonium bromide (CTAB), and oleic acid (OA) at pH 7.0 ± 0.2. 58

Figure 4.3 (a) PFOA and (b) PFOS sorption isotherm on iron oxide nanoparticles (IONPs) with different organic (surface) coating; positively charged PEI (25k and 10k of MW) and CTAB, and negatively charged OA, respectively. All experiments were performed at pH 7. 58

Figure 4.4 Real time frequency responses of QCM-D for PFAS sorption on organic functionalized iron oxide nanoparticles (IONPs) coated Q-sensor. 61

Figure 4.5 Frequency shift and slope with respect to the different concentration of IONCs with various surface coating; (a, b) CTAB, (c, d) PEI25k, and (e, f) PEI10k, respectively. 61

Figure 4.6 Time dependent normalized sorption density of PEI coated IONPs (Fe_3O_4@PEI25k) for 0.6 mmol/L of (a) PFOA and (b) PFOS. 62

Figure 4.7 Real time deposition rates ($-f_{3_slope}$) of (a) PFOA and (b) PFOS on IONPs with respect to the different surface coating (PEI25k, PEI10k, and CTAB). 62

Figure 4.8 Frequency shift of quartz crystal sensor (overtone = 3) with 0.6 mmol/L of (a) PFOA and (b) PFOS solutions at pH 7. 63

Figure 4.9 (a) PFOA and (b) PFOS sorption isotherm on iron oxide nanocrystals (IONCs) obtained from mass of IONCs deposited on Q-sensor and mole of PFAS attached to IONCs via QCM-D. Note that no correction factor is applied here to consider water sorption. 63

Figure 4.10 (a) PFOA and (b) PFOS sorption isotherm on IONPs obtained via batch (circle dot and solid line) and QCM-D (reverse triangle dot and dotted line) methods. Data for batch sorption is replotted from Figure 1 for direct comparison. QCM-D results are obtained by multiplying QCM-D correction factor with sorption density. 63

Figure 4.11 Single- and multi-sorption isotherms on PEI coated IONCs for (a) PFOA and (b) PFOS; single-sorbate systems (black line) and multi-sorbate systems (PFOA and PFOS (blue line)). Multi-sorption tests were performed with the same initial concentration of both PFOA and

PFOS from 0.02 to 0.1 mmol/L at pH 7. (c-d) Time dependent frequency and dissipation shift (overtone n = 3) of the IONPs coated Q-sensor with introducing both PFOA and PFOS sequentially, and vice versa, by QCM-D analysis. 64

Figure 4.12 Thickness of the attached layer of PFOA and PFOS on the IONC coated Q-sensor obtained as calculated by the Voigt model via frequency shift (*f*) and dissipation (*D*) during PFAS sorption. 65

Figure 4.13 (a) PFOA and (b) PFOS sorption isotherm on PEI-coated IONPs (Fe_3O_4@PEI25k) as a function of pH (4.0 (blue), 7.0 (black), and 10.0 (red)). Sorption isotherm for (c) PFOA and (d) PFOS with different water chemistry of ultrapure water (UPW, black), NaCl (red), $CaCl_2$ (blue), $MgCl_2$ (green), and synthetic groundwater (SGW, purple), respectively. Total ionic strength for all solutions was adjusted to be identical with SGW. 66

Figure 4.14 Zeta potential of PEI coated IONCs with different molecular weight (25k and 10k) as a function of solution pH. 67

Figure 4.15 Aggregation profile of Fe_3O_4@PEI25k NCs in the presence of (a) 1000 mmol/L of NaCl and (b) 1000 mmol/L of $CaCl_2$ concentrations at pH 7. 68

Figure 4.16 Normalized sorption density for (a) PFOA and (b) PFOS on Fe_3O_4@PEI25k NCs as a function of humic acid (HA) concentrations via QCM-D method. 68

Figure 4.17 Effluent breakthrough curves for (a) PFOA and (b) PFOS in columns packed with IONCs (2.9 mg) treated 40-50 mesh Ottawa Sand (80 g)..... 69

Figure 4.18 SEM images of TiO_2/ZIF−8 composite materials with varied concentration of TiO_2 NPs. 70

Figure 4.19 Concentration-time profiles for PFOA degradation using ZIF−8 synthesized with different ratios of precursor ratios of (a) 1:6.7 and (b) 1:1. All experiments were performed at pH 3 under UVC irradiation. Initial concentration of PFOA is 10 mg/L. 71

Figure 4.20 Concentration profiles of related byproducts, which is in accordance with observed rate constants for PFOA degradation 71

Figure 4.21 (a) XRD analysis for various materials including ZIF−8, TiO_2/ZIF−8, functionalized TiO_2/ZIF−8 via methanol and solvothermal methods. (b) Concentration−time profiles for PFOA degradation using TiO_2/ZIF−8, functionalized TiO_2/ZIF−8 via methanol-based and solvothermal-based methods. Initial concentration of PFOA is 10 mg/L and 200 mg/L of each materials were applied. 72

Figure 4.22 (a) PFOA degradation in the presence of various scavengers including methanol and TBA compared to no scavenger (1:1, methanol-based modified ZIF-8 and TiO_2). (b) PFOA removal with different concentrations of hydrogen peroxide (H_2O_2, 3 and 10 g/L), peroxymonosulfate (PMS, 1.2 and 12 mM), and peroxydisulfate (PDS, 1.2 and 12 mM) under UVC irradiation (254 nm) for 24 h. Initial PFOA concentration is 10 mg/L for all. 73

Figure 4.23 Concentration profiles of PFOA, PFHpA, PFHxA, PFPeA, and PFBA using 200 mg/L of functionalized TiO_2/ZIF−8 composite materials under UVC irradiation. Initial concentration of PFOA is 10 mg/L and all experiments conducted at pH 3 under UVC irradiation..... 73

Figure 4.24 Scheme of CVD process of CNTs-NF electrode. 74

Figure 4.25 FE-SEM images of CNTs-NF with (a) low resolution, (b) high resolution, HR-TEM images of (c) CNTs-NF, and (d) SAED patterns, respectively. 75

Figure 4.26 FE-SEM images of (a-b) pristine Ni, (c-d) G-Ni, (e-f) NG-NF, and (g-h) CNTs-Ni. 76

Figure 4.27 XPS spectra of (a) Pristine NF, (b) G-NF, (c) NG-NF, and (d) CNTs-NF, respectively. 77

Figure 4.28 Comparative results of PFOS removal efficiency through the use of different electrode types under different conditions ($[PFOS]_0$ = 20 mg/L, $[Na_2SO_4]_0$ = 100 mM, [Applied current density] = 50 mA/cm^2, $[pH]_i$ = 6). 78

Figure 4.29 PFOS removal efficiency in different types of electrolyte ($[PFOS]_0$ = 20 mg/L, [KOH, NaOH, NaCl, Na_2SO_4]$_0$ = 100 mM, [Applied current] = 50 mA/cm^2, $[pH]_i$ = 6). 78

Figure 4.30 EPR spectra observed (a) in the absence of PDS, and (b) observed in the presence of PDS with a cathode in a divided cell ($[PDS]_0$ = 10 mM, $[Na_2SO_4]_0$ = 100 mM, [Applied current density] = 50 mA/cm^2, $[pH]_i$ = 6). 79

Figure 4.31 Influences of hydrophilic and hydrophobic scavengers on surface-bound radicals on the CNTs-NF electrode ($[PFOS]_0$ = 20 mg/L, $[Na_2SO_4]_0$ = 100 mM, $[Scavengers]_0$ = 200 mM, [Applied current density] = 50 mA/cm^2, $[pH]_I$ = 6). 80

Figure 4.32 The intermediate analysis of PFOS oxidation in BDD anode and CNTs-NF cathode using K-mean cluster algorithm. 81

Figure 4.33 A comparison of the electrochemically active surface area using pristine NF, G-NF, NG-NF, and CNTs-NF electrodes. 82

Figure 4.34 The equilibrium adsorption capacity of PFOS at 1.2 V using various types of electrodes ($[PFOS]_0$ = 10 mg/L, $[Na_2SO_4]_0$ = 100 mM, [Applied potential] = 1.2V, $[pH]_i$ = 6). . 83

Figure 4.35 pH effects on (a) PFOS rate constants and (b) zeta potential on CNTs-NF ((a)$[PFOS]_0$ = 20 mg/L, $[Na_2SO_4]_0$ = 100 mM, [Applied current density] = 50 mA/cm^2, $[pH]_i$ = 6 and (b) $[PFOS]_0$=20 mg/L, $[Na_2SO_4]_0$=100 mM, $[pH]_i$ = 3, 5, 7, 9, and 11). 84

Figure 4.36 Repeated PFOS degradation along with defluorination by BDD/CNTs-NF electrode system over 10 cycles ($[PFOS]_0$ = 20 mg/L, $[Na_2SO_4]_0$ = 100 mM, [Applied current density] = 50 mA/cm^2, $[pH]_i$ = 6). 85

Figure 4.37 Stability analysis of the CNTs-NF electrode using the chronoamperometric technique (0.1M Na_2SO_4 solution with an applied voltage of 5V over a 100-hour electrolysis duration). .. 85

Figure 4.38 Transformation of chlorinated ethenes in batch reactor experiments. Symbols represent average **a)** PCE **b)** TCE **c)** cis-DCE and **d)** VC concentrations in triplicate batch reactors. Vertical error bars represent one standard deviation. 86

Figure 4.39 Average aqueous ethene concentrations over time in **a)** triplicate batch reactor and **b)** triplicate microcosm experiments. Vertical error bars represent one standard deviation between triplicate batch reactors. Note that the aqueous volume decreased over time due to sampling, and thus, the ratio of dissolved to gaseous ethene is not constant over time. 87

Figure 4.40 Average **a)** PCE **b)** TCE **c)** *cis*-DCE and **d)** VC concentrations in duplicate abiotic batch reactors. Vertical error bars represent one standard deviation between duplicate batch reactors. 89

Figure 4.41 Average maximum substrate utilization rates (k_{max}) for **a)** PCE degradation, **b)** TCE degradation, **c)** cis-DCE degradation, and **d)** vinyl chloride degradation. Each bar represents the value fit to each set of triplicate batch reactors in units of mmol/day/cell and error bars represent the standard deviation. Values within dashed rectangles are significantly lower than the average for the 0 mg/L reactor set ($p<0.05$). 90

Figure 4.42 Estimated maximum substrate utilization rates for batch reactor experiments conducted with varying concentrations of total PFAAs. Plotted curves show fit of log-logistic dose-response model for inhibition of MRD by PFAA. Points represent the mean of three k_{max} estimates and each error bar indicates the corresponding 95% confidence interval. 91

Figure 4.43 Average **a)** PCE **b)** TCE **c)** cis-DCE and **d)** VC concentrations in triplicate microcosms. Vertical error bars represent one standard deviation..... 92

Figure 4.44 *Dhc* 16S rRNA and RDase gene abundance in batch reactor experiments containing concentrations of **a)** 0 mg/L, **b)** 12 mg/L, **c)** 27 mg/L, **d)** 50 mg/L, **e)** 62, and **f)** 101 mg/L PFAAs. Each bar represents the average of 3 replicates with one standard deviation represented with error bars. The time 0 abundances are based on the composition of the inoculum used in each batch reactor set. 94

Figure 4.45 *Dhc* 16S rRNA and RDase gene abundance in microcosm experiments containing final concentrations of **a)** 0 mg/L, **b)** 9 mg/L, **c)** 19 mg/L, **d)** 39 mg/L, and **e)** 91 mg/L PFAAs. Each bar represents the average of 3 replicates with one standard deviation represented with error bars. The time 0 abundances are based on the composition of the inoculum used in each microcosm set. 94

Figure 4.46 Proportion of RDase genes in a) batch reactor and b) microcosm experiments at the end of dechlorination. End of dechlorination in batch reactors varied from day 32 to 101 depending on PFAA concentration. In microcosms, end of dechlorination occurred at day 28 at all PFAA concentrations. 96

Figure 4.47 Proportion of RDase genes vs PFAA concentration at the end of experiment with linear regression fit to all data in **a)** batch reactor (day 32 to 101) and **b)** microcosm (day 28) experiments and with linear regression fit to all data except highest PFAA concentration data in **c)** batch reactor (day 32 to 101) and **d)** microcosm (day 28) experiments. 97

Figure 4.48 Concentrations of PCE/TCE and cis-DCE in the effluent during an injection of influent solution containing a mixture of PFAAs and PCE/TCE for 42.1 PVs in set 1 experiment (single IONP column). 98

Figure 4.49 Breakthrough of 10 PFAAs, during an injection of influent solution containing a mixture of PFAAs and PCE/TCE for 42.1 PVs in set 1 experiment (single IONP column). 98

Figure 4.50 Concentrations of PCE and TCE in the effluent during an injection of influent solution containing a mixture of PFAAs and PCE/TCE for 87.5 PVs in set 2 experiment (single S-PAC column). 99

Figure 4.51 Breakthrough curves of 10 PFAAs, during an injection of influent solution containing a mixture of PFAAs and PCE/TCE for 87.5 PVs in set 2 experiment (single S-PAC column).. 100

Figure 4.52 Average concentrations of PCE and TCE dechlorinated transformation products (cis-DCE, VC, and ethene) in the effluent of (a) the upgradient bioactive columns (n = 2) and (b) the downgradient adsorptive (IONP) columns (n = 2) during a 42.1/65.5-PV injection of influent solution containing a mixture of PFAAs and PCE/TCE in set 3 experiment (coupled bioactive and IONP columns). 100

Figure 4.53 Breakthrough curves of 10 PFAAs in the IONP columns (n = 2), during a 42.1/65.5-PV injection of influent solution containing a mixture of PFAAs and PCE/TCE in set 3 experiment (coupled bioactive and IONP columns). 101

Figure 4.54 Average concentrations of PCE and TCE dechlorinated transformation products (cis-DCE, VC, and ethene) in the effluent of (a) the upgradient bioactive columns (n = 2) and (b) the downgradient adsorptive (S-PAC) columns (n = 2) during a 38.0/59.0-PV injection of influent solution containing a mixture of PFAAs and PCE/TCE in set 4 experiment (coupled bioactive and S-PAC columns). 102

Figure 4.55 Breakthrough curves of 10 PFAAs in the S-PAC columns (n = 2), during a 38.0/59.0-PV injection of influent solution containing a mixture of PFAAs and PCE/TCE in set 4 experiment (coupled bioactive and S-PAC columns). 103

Figure 4.56 Adsorption of PFOA (A) and PFOS (B) on 100-mesh PAC and corresponding fits to the Freundlich adsorption model. Error bars represent standard deviation of mean for three replicates. 106

Figure 4.57 Representative bromide tracer breakthrough curve (BTC) obtained for a water-saturated column containing untreated 40-50 mesh Ottawa sand. The pore volume was approximately 20 mL, and the 10 mM NaBr solution was introduced at a flow rate of 0.12 mL/min, yielding a residence time of approximately 2.75 h. Experimental data were fit to a one-dimensional form of the advective-dispersive transport equation using the CXTFIT program. 107

Figure 4.58 Photographs showing the injection of S-PAC and retention PAC (dark color) in a water-saturated column packed with 40-50 mesh Ottawa sand. Approximately 3.5 PV of S-PAC were injected followed by 3.5 PV of background solution (10 mM NaCl) at a flow rate was 0.12 mL/min. 108

Figure 4.59 Distribution of retained carbon after the injection of 3.5 pore volumes of S-PAC into a column packed with water-saturated 40-50 mesh Ottawa sand followed by 3.5 pore volumes of background electrolyte solution (10 mM NaCl) at a flow rate of 0.12 mL/min. 108

Figure 4.60 Particle size distribution of stabilized PAC obtained by dynamic light scattering using a Zetasizer Nano ZS Analyzer operated in back-scattering mode at an angle of 173º. 109

Figure 4.61 Images of 40-50 mesh Ottawa sand (A) before and (B) after treatment with S-PAC obtained using a Zeiss Leo 1530 VP SEM-EDS. 109

Figure 4.62 Effluent breakthrough curves obtained for pulse injections of aqueous solutions containing either (A) PFOA (100 µg/L) or (B) PFOS (100 µg/L) in water-saturated columns containing untreated 40-50 mesh Ottawa sand at a flow rate of 0.12 mL/min (pore-water velocity of 1 m/day). 111

Figure 4.63 Effluent breakthrough curves obtained for the injection of either (A) PFOA or (B) PFOS (100 µg/L then 20 mg/L) in water-saturated columns containing S-PAC treated 40-50 mesh Ottawa sand. Shaded areas show the amount of PFOA or PFOS retained in the columns. The pore

volume of each column was approximately 20 mL and the flow rate was 0.12 mL/min, yielding a residence time of 2.75 h. 112

Figure 4.64 Photograph showing retained PAC (dark color) following the injection of 80 mL of S-PAC into side-ports 8 and 9 of the aquifer cell at a flow rate of 0.08 mL/min. 113

Figure 4.65 Fluorescein tracer test (0.5 PV pulse injection) conducted in the aquifer cell prior to injection of S-PAC at a flow rate of 2.4 mL/min. Images collected at intervals of 0.26 PV. 114

Figure 4.66 Aquifer cell side-port and effluent samples for PFOA in (A) upper untreated control region and (B) lower S-PAC treated region, and for PFOS in (C) upper untreated control region and (D) lower S-PAC treated region. A 260 mL pulse of solution containing 50 µg/L PFOS, 50 µg/L PFOA, and 10 mM NaBr (tracer) was injected through ports 2 and 4 immediately up-gradient from the control and S-PAC treated regions of the aquifer cell, respectively. 114

Figure 4.67 Aquifer cell side-port and effluent samples for PFOA in (A) upper untreated control region and (B) lower S-PAC treated region, and for PFOS in (C) upper untreated control region and (D) lower S-PAC treated region. A 260 mL pulse of solution containing 50 µg/L PFOS, 50 µg/L PFOA, and 10 mM NaBr (tracer) was injected through ports 2 and 4 immediately up-gradient from the control and S-PAC treated regions of the aquifer cell, respectively. 115

Figure 4.68 Sorption of PFOS, PFOA, PFNA, PFHxS, PFHpA, or PFBS on Amberlite® IRA910 in single-solute experiments over a concentration range of (A) 1 to 100 µg/L and (B) 10 to 500 mg/L with corresponding fits (dashed lines) to (A) linear and (B) Freundlich adsorption model. 118

Figure 4.69 Sorption of mixtures of PFOS, PFOA, PFNA, PFHxS, PFHpA, and PFBS on Amberlite® IRA910 over a concentration range of (A) 1 to 100 µg/L and (B) 2 to 100 mg/L. 120

Figure 4.70 Sorption of mixtures of PFOS, PFOA, PFNA, PFHxS, PFHpA, and PFBS on Amberlite® IRA910 over a concentration range of 1 to 100 µg/L in single solute or multiple solute batch experiments. 121

Figure 4.71 Sorption of mixtures of PFOS, PFOA, PFNA, PFHxS, PFHpA, and PFBS on Amberlite® IRA910 over a concentration range of 1 to 100 mg/L in single solute or multiple solute batch experiments. 122

Figure 4.72 Comparison of PFBS, PFHpA, PFHxS, PFOA, PFNA and PFOS adsorption on 10 mg Amberlite® IRA910 in single and multi-solute batch experiments at an initial concentration of 100 mg/L each. 123

Figure 4.73 Particle size distribution of S-IXR obtained by dynamic light scattering using a Zetasizer Nano ZS Analyzer operated in back-scattering mode at an angle of 173°. 124

Figure 4.74 Distribution of retained carbon after the injection of 3.5 pore volumes of S-IXR into a column packed with water-saturated 40-50 mesh Ottawa sand followed by 3.5 pore volumes of background electrolyte solution (10 mM NaCl) at a flow rate of 0.12 mL/min prior to (A) PFOA injection and (B) PFOS injection, where 67.1 mg of IRA910 was retained in (A) and 61.3 mg of IRA910 was retained in (B). 125

Figure 4.75 Images of 40-50 mesh Ottawa sand (a) before and (b) after treatment with S-IXR obtained using a Zeiss Leo 1530 VP Scanning Electron Microscope (SEM). 126

Figure 4.76 Images of 40-50 mesh Ottawa sand (A) before and (B) after treatment with S-IXR obtained using a Zeiss Leo 1530 VP Scanning Electron Microscope (SEM) coupled with an Oxford Instruments 7426 Energy Dispersive Spectrometer (EDS)..... 127

Figure 4.77 Effluent breakthrough curves for (a) PFOA and (b) PFOS in a water-saturated column containing S-IXR treated 40-50 mesh Ottawa sand. Shaded areas show the amount of retained PFOS or PFOA for injected concentrations of 100 µg/L and 100 mg/L. 128

Figure 4.78 Effluent breakthrough curves obtained for pulse injections of aqueous solutions containing either (a) PFOA (100 µg/L) or (b) PFOS (100 µg/L) in water-saturated columns containing untreated 40-50 mesh Ottawa sand. The flow rate was 0.12 mL/min (pore-water velocity of 0.88 m/day), yielding a residence time of approximately 2.77 h. The pore volume of each column was approximately 20 mL. 129

Figure 4.79 Effluent breakthrough curves obtained for a mixture of PFBS, PFHpA, PFHxS, PFOA, PFOS, and PFNA (60 ug/L and 60 mg/L) applied to a water-saturated column containing S-IXR treated 40-50 mesh Ottawa sand..... 130

Figure 4.80 Effluent breakthrough curves obtained for pulse injections of aqueous solutions containing a 600 µg/L mixture of PFHpA, PFBS, PFOA, PFHxS, PFNA and PFOS (100 µg/L each) in a water-saturated column containing untreated 40-50 mesh Ottawa sand. The flow rate was 0.12 mL/min (pore-water velocity of 1.03 m/day), yielding a residence time of approximately 2.57 h. The pore volume of the column was 18.52 mL. 131

Figure A.1 Total PFAA concentration in batch reactors over time. Batch reactor sets are grouped by color and labeled based on the average total PFAA concentration. For each PFAA concentration set, the average PFAA concentrations are plotted for bioaugmented batch reactors (B) and abiotic, sterilized batch reactors (A). One standard deviation is represented with error bars. 165

Figure A.2 Total PFAA concentration in microcosms over time. Microcosm sets are grouped by color and labeled based on the average total PFAA concentration at the end of the experiments. For each final PFAA concentration set, the average PFAA concentrations are plotted for bioaugmented microcosms (B), non-bioaugmented microcosms (N), and microcosms inhibited by the addition of sodium azide (I). One standard deviation is represented with error bars. 166

Figure A.3 Average pH in bioaugmented **a)** batch reactor and **b)** microcosm experiments over time. The average of three measurements are plotted and one standard deviation is represented by vertical error bars. 167

Figure A.4 Example fit of model with original mass loss formulation (curves) to abiotic batch reactor experiment data (points). 172

Figure A.5 Example fits of model with improved mass loss formulation (curves) to abiotic batch reactor data (points). 172

Figure A.6 Model fits to batch reactors with 0 mg/L PFAAs (parameters from **Table A.1**). Curves represent model values, points represent measurements, and error bars around qPCR measurements represent one standard deviation as estimated by **equation A.22**. As noted in **Appendix A.1**, *GeoSZ qPCR* measurements were not used to fit *GeoSZ* biomass values and were omitted from this figure. 176

Figure A.7 Example model fits to batch reactors with varying concentrations of PFAAs. Curves represent model values, points represent measurements, and error bars around qPCR measurements represent one standard deviation as estimated by **equation A.22**. As noted in **Appendix A.1**, *GeoSZ qPCR* measurements were not used to fit *GeoSZ* biomass values and were omitted from this figure. 177

Figure A.8 TCE sorption isotherms and equilibrium measurements 180

Figure A.9 PCE sorption isotherms and equilibrium measurements 180

List of Acronyms

AFB	Air Force Base
AFFF	Aqueous film forming foam
AWIA	Air-water interfacial area
BTC	Breakthrough curve
CMC	Critical micelle concentration
DoD	Department of Defense
DGBE	Diethylene glycol butyl ether
DOC	Dissolved organic carbon
ERSON	Environmental Restoration Statements of Need
FOSA	Perfluoro-1-octanesulfonamide
FTS	Fluorotelomer sulfonic acid
GAC	Granular activated carbon
GC-MS	Gas chromatography mass spectrometer
GO	Graphene oxide
HDPE	High-density polyethylene
HFPO-DA	Hexafluoropropylene oxide dimer acid
HOCs	Hydrophobic organic compounds
IFT	Interfacial tension
IONP	Iron oxide nanoparticles
ITRC	Interstate Technology and Regulatory Council
LC-MS/MS	Liquid chromatography tandem mass spectrometer
LOD	Limit of detection
LOQ	Limit of quantitation
MDEP	Maine Department of Environmental Protection
MOF	Metal organic framework
MRD	Microbial reductive dechloration
MRI	Major research instrumentation
MS^2	Tandem mass spectrometry
NAPL	Nonaqueous phase liquids
NPDWR	National Primary Drinking Water Regulation
NSF	National Science Foundation
OC	Organic carbon
PCE	Perchloroethylene
PEI	Polyethylenimine
PFAAs	Perfluroalkyl acids
PFAS	Poly- and perfluoroalkyl substances
PFASAs	Perfluoroalkane sulfonamides
PFBA	Perfluorobutanoic acid
PFBS	Perfluorobutanesulfonic acid
PFCAs	perfluoroalkyl carboxylates
PFDA	Perfluorodecanoic acid
PFDoA	Perfluorododecanoic acid
PFDoS	Perfluorododecane sulfonic acid
PFDS	Perfluorodecane sulfonic acid

PFHpA	Perfluoroheptanoic acid
PFHxA	Perfluorohexanoic acid
PFHxS	Perfluorohexanesulfonic acid
PFNA	Perfluorononanoic acid
PFNS	Perfluorononane sulfonic acid
PFOA	Perfluorooctanoic acid
PFOS	Perfluorooctane sulfonic acid
PFPeA	Perfluoropentanoic acid
PFPeS	Perfluoropentane sulfonic acid
PFSAs	perfluoroalkyl sulfonates
PFTeDA	Perfluorotetradecanoic acid
PFTrDA	Perfluorotridecanoic acid
PFUnA	Perfluoroundecanoic acid
PV	Pore Volume
S-IXR	Stabilized ion exchange resin
S-PAC	Stabilized powdered activated carbon
SERDP	Strategic Environmental Research and Development Program
TCE	Trichloroethylene
TDS	Total dissolved solids
TQ	Triple quadrupole
UPLC	Ultra-performance liquid chromatography
USEPA	U.S. Environmental Protection Agency

Keywords

Aqueous film forming foam (AFFF), PFAS, per and polyfluoroalkyl substances, nanomaterials, bioremediation, adsorption, permeable adsorptive barrier, ion exchange resin, in situ remediation, powdered activated carbon, polydadmac, polymer, graphene, chlorinated solvents, reductive dechlorination, tetrachloroethene, PCE, trichloroethene, TCE

Acknowledgements

In addition to co-PI's Dr. Kurt D. Pennell, Dr. Natalie L. Cápiro, and Dr. John D. Fortner, the following individuals contributed to the research presented in this report:

Auburn University: Dr. Sheng Dong (Graduate student, Ph.D. 2023), Dr. PengFei Yan (Graduate student, Ph.D. 2022)

Brown University: Dr. Linda Abriola (Professor), Chloe Gray (Undergraduate student), Dr. Shuchi Liao (Graudate student, Ph.D. 2021), Dr. Chen Liu (Graduate student, Ph.D. 2021), Dr. Katherine E. Manz (Post-doctoral fellow, Research Assistant Professor), Dorothea Pinchbeck (Undergraduate student), Zachary S. Saleeba (Graduate student, Laboratory manager) and Dr. Matthew J. Woodock (Research engineer).

Jacobs Engineering Group: James W. Hatton (Senior Engineer)

Tufts University: Dr. Masoud Arshadi (Post-doctoral fellow), Dr. Jack Elsey (graduate student, Ph.D., 2023), Dr. Jason P. Hnatko (Graduate student, Ph.D. 2020)

University of Minnesota: William A. Arnold (Professor), Matt F. Simcik (Associate Professor)

Yale University: Junseok Lee (Graduate student), Seung Soo Lee (Post-doctoral fellow), Changwoo Kim (Graduate student and Post-doctoral fellow)

Woodard & Curran: Dr. J. Daniel Bryant (Director of Practices).

The authors thank Mr. Naji Akladiss, formerly of the Maine Department of Environmental Protection (MDEP), for providing access to collect soil and groundwater samples from former Loring AFB, Dr. J. Daniel Bryant, Direct of Practices at Woodard & Curran for providing soil and groundwater samples, and Dr. Joseph Wong and Dr. Micala Mitchek of ADA Carbon Solutions for providing activated carbons. Sheng Dong and Peng-Fei Yan acknowledge the financial support from the China Scholarship Council and Auburn University Graduate School and Office of International Programs. The high-resolution mass spectrometer used to identify reaction byproducts was partially funded by National Science Foundation (NSF) Major Research Instrumentation (MRI) award CBET-1919870. The initial work with activated carbon was partially supported by the Strategic Environmental Research and Development Program (SERDP) provided funding for this research under Contract W912HQ-14-C-0042 "Development of a Novel Approach for in situ Remediation of PFC Contaminated Groundwater (Project ER-2425)". The development of analytical methods and experimental procedures was partially supported by SERDP under contract W912HQ-18-C-0014, "Development and Laboratory Validation of Mathematical Modeling Tools for Prediction of PFAS Transformation, Transport, and Retention in AFFF Source Areas (Project ER18-1149)"

Abstract

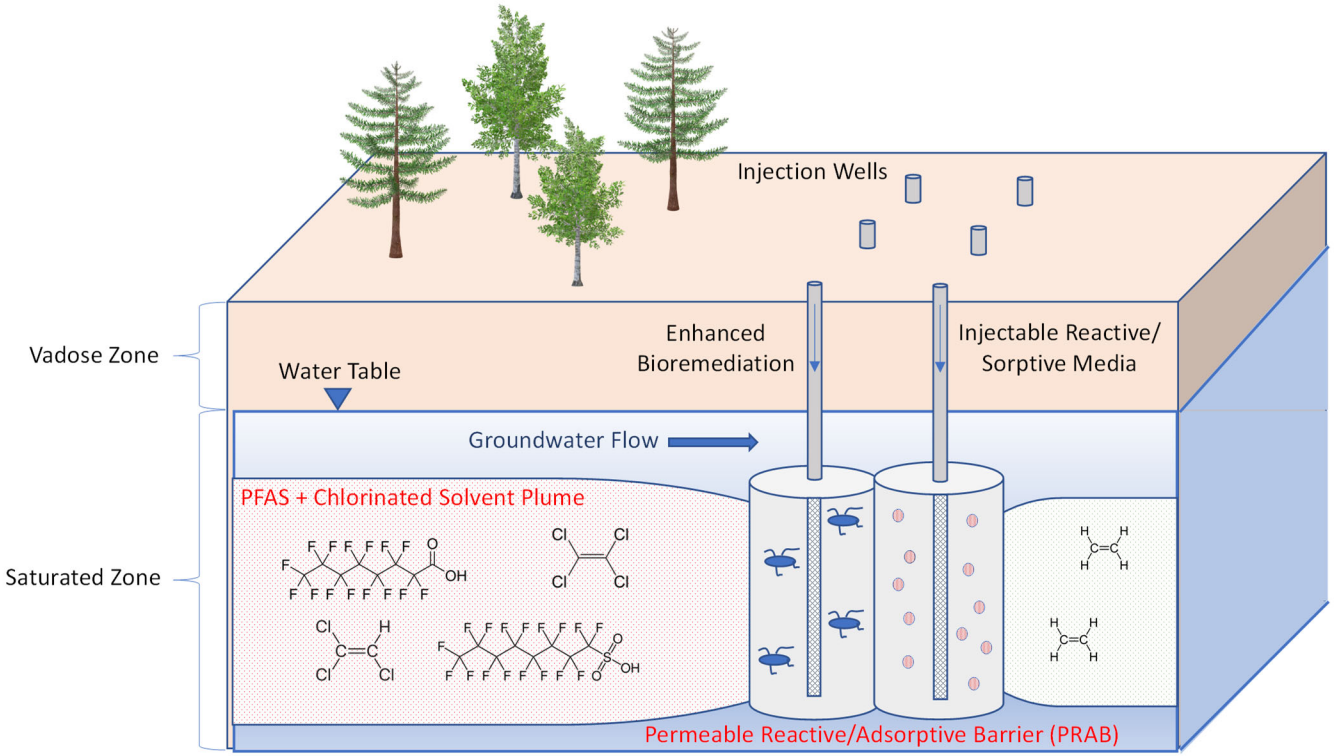
Introduction. Aqueous film foaming foams (AFFF) were widely used at Department of Defense (DoD) installations for fire fighter training exercises and fire response. Due to their stability at high temperature and amphiphilic properties, these foams contain per- and polyfluoroalkyl substances (PFAS), including perfluorooctanoic acid (PFOA) and perfluorooctane sulfonate (PFOS). Additionally, chlorinated solvents, such as tetrachloroethene (PCE) and trichloroethene (TCE), were commonly used for aircraft engine cleaning, paint removal, and degreasing metal parts. Thus, contaminated groundwater plumes at DoD sites often contain mixtures of chlorinated solvents and PFAS, both of which have stringent drinking water standards. Although bioremediation is commonly used to treat PCE and TCE, most PFAS are extremely recalcitrant to conventional thermal, chemical or biological treatments. The goals of this project were to develop coupled in situ remediation approaches that could be used to effectively treat groundwater plumes containing mixtures of PFAS and chlorinated ethenes, and to understand the potential synergies and limitations of these combined remedies.

Technical Approach. The research program was structured around three integrated tasks that were designed to (1) Develop and test highly reactive materials capable of degrading and/or sequestering PFAS and chlorinated ethenes, (2) Develop biological systems to treat chlorinated ethenes and PFAS reaction byproducts following sorptive and reactive treatment, and (3) Evaluate the performance of the combined physicochemical and biological systems developed in Tasks 1 and 2 using groundwater containing mixtures of PFAS and chlorinated ethenes.

Results: Microcosm studies, conducted with a mixture of 10 PFAS at concentrations of up to 120 mg/L, indicated that the time required for microbial reductive dechlorination (MRD) of PCE and TCE was not impaired in the presence of PFAS. In addition, growth of *Dehalococcoides mccartyi* (*Dhc*) strains responsible for ethene formation were not impacted by PFAS, but at the highest PFAS concentration tested, *Dhc* shifted from cells harboring the *vcrA* gene to cells harboring the *bvcA* gene. We synthesized iron oxide nanocapsules (IONCs) coated with polyethylenimine (PEI), which exhibited large adsorption capacities for both PFOA and PFOS. Composite materials were also synthesized from metal organic frameworks (MOFs) with titanium dioxide (TiO_2) nanoparticles to degrade PFOA under UV irradiation, and an electrochemical-based (cathodic) process was demonstrated for rapid PFOS degradation. Finally, injectable stabilized ion excahnge resin (S-IXR) and powdered activated carbon (S-PAC) were developed for permeable adsorptive barriers (PABs) that could be implemented individually or combined in series to treat groundwater plumes containing mixtures of chlorinated ethenes and PFAS.

Benefits: The findings of this project were distributed to remediation professionals, site managers and academic researchers via publications, web-based media, seminars, and active participation of the research team in organizations such as the Interstate Technology and Regulatory Council (ITRC). In addition, five doctoral students, a post-doctoral fellow, and two undergraduate research students were supported on this project.

Graphical Abstract



Executive Summary

Introduction

Aqueous film foaming foams (AFFF) were widely used at Department of Defense (DoD) installations for fire fighter training exercises and fire response. Due to their stability at high temperature and amphiphilic properties, these foams contain per- and polyfluoroalkyl substances (PFAS), including perfluorooctanoic acid (PFOA) and perfluorooctane sulfonate (PFOS). Additionally, chlorinated solvents, such as tetrachloroethene (PCE) and trichloroethene (TCE), were commonly used for aircraft engine cleaning, paint removal, and degreasing metal parts. Thus, contaminated groundwater plumes at DoD sites often contain mixtures of chlorinated solvents and PFAS, both of which have stringent drinking water standards. The U.S. Environmental Protection Agency (USEPA) has established a maximum contaminant level (MCL) in drinking water of 5 parts per billion (ppb, µg/L) for PCE and TCE. In 2016, the USEPA established a health advisory level (HAL) of 70 parts per trillion (ppt, ng/L) for total (combined) PFOA and PFOS. In March 2023, the USEPA proposed national drinking water regulation (NPDWR) of 4.0 ppt for PFOA and PFOS.

Although *in situ* bioremediation is commonly used to treat groundwater plumes containing dissolved phase chlorinated ethenes (e.g., PCE and TCE), many PFAS, including PFOA and PFOS, are extremely recalcitrant and can persist in the environment for long periods of time. Unlike other persistent organic pollutants such as polychlorinated biphenyls (PCBs), PFAS are have relatively high aqueous solubilities and are mobile in the environment, negatively impacting surface and groundwater throughout the United States. Despite concerted efforts to develop *in situ* treatment technologies that could degrade, the strength of the covalent carbon-fluorine bond, which has a dissociation energy of 130 kcal/mol, has severely limited the utility of conventional treatment technologies. Although chemical oxidation has been effective for PFOA under laboratory-simulated groundwater conditions, this approach has shown minimal success for PFOS, and there is concern over the potential formation of shorter chain length byproducts. Biodegradation of PFAS precursors has been documented in the literature, and recently, the transformation of PFOA and PFOS by *Acidimicrobium sp.* Strain A6 was reported, but the reported reaction rates are relatively slow. As a consequence, PFAS-impacted groundwater plumes are typically managed using conventional "pump and treat" remediation approaches that rely on extraction and above-ground treatment with granular activated carbon (GAC) or ion exchange resin (IXR).

In response to SERDP Statement of Need (SON) ERSON-17-01, which focused on approaches that would improve our ability to treat mixed contaminants of concern (COCs) in groundwater, this project was designed to address the treatment of groundwater plumes containing mixtures of chlorinated ethenes and PFAS, which are of particular interest to the DoD. Specifically, the

proposed research program focused on the development and evaluation of *in situ* technologies that could be combined in series to sequentially treat groundwater plumes containing chlorinated ethenes co-mingled with recalcitrant PFAS, such as PFOS and PFOA.

Objectives

The goal of this project is to develop coupled *in situ* remediation technologies to treat groundwater plumes containing mixtures of PFAS and chlorinated ethenes. Due to their prevalence at DoD sites and persistence in the environment, the research program focused on aqueous solutions containing PFOA and PFOS, which were used in aqueous film forming foams (AFFF); and two chlorinated ethenes; PCE and TCE. In order to assess performance for a range of carbon chain lengths, four additional PFAS were evaluated, perfluorohexanoic acid (PFHxA, $C_6HF_{11}O_2$), perfluorobutanoic acid (PFBA, $C_4HF_7O_2$), perfluorohexane sulfonate (PFHS, $C_6HF_{13}O_3S$), and perfluorobutane sulfonate (PFBS, $C_4HF_9O_3S$), as well as mixtures of six and ten PFAS. While microbial reductive dechlorination of PCE and TCE has been widely used chemical oxidation of PFOA has been recently demonstrated, PFOS is extremely recalcitrant to conventional thermal, chemical or biological treatments. In addition, a PFAS mixture was recently shown to inhibit microbial reductive dechlorination of TCE and subsequent byproduct formation. Therefore, we propose to develop two types of *in situ* permeable barrier systems, using sequential or "treatment train" remediation approaches, to effectively treat groundwater containing mixtures of PFAS and chlorinated solvents (**Figure ES 1**). The first system consisted of an upgradient microbial reductive dichlorination zone to treat PCE and TCE, followed in series by a *sorptive barrier* to remove and sequester PFAS and any other byproducts. The second system consists of a *reactive barrier* to degrade PFAS and chlorinated ethenes, coupled with a downgradient *sorptive barrier* to capture residual reaction byproducts. Materials used in the

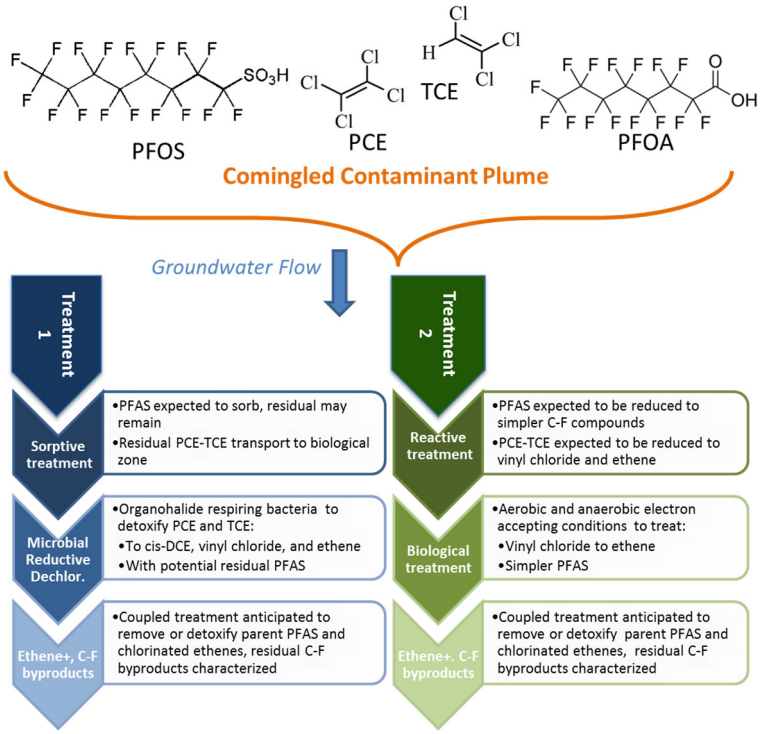


Figure ES 1. Schematic diagram of two treatment train approaches for comingled a PFOS-PFOA-PCE-TCE groundwater plume: 1. Sorption followed by anaerobic reductive dechlorination and 2. Catalyzed reduction reaction.

permeable barriers can be delivered as an aqueous suspension, emplaced as a trench, or as a "funnel and gate" system.

Technical Approach

The technical approach was structured around three integrated tasks:

Task 1: Develop highly reactive materials capable of degrading and/or sequestering PFAS, including PFOA and PFOS, in the presence of chlorinated ethenes.

Task 2: Develop biological systems to treat chlorinated ethenes and PFAS reaction byproducts down-gradient from sorptive and reactive barrier wall systems, respectively.

Task 3: Evaluate the performance of two coupled physicochemical and biological reactive barrier systems using groundwater containing mixtures of PFAS and chlorinated ethenes.

In Task 1A, three types of sorptive materials were evaluated for *in situ* treatment applications; (a) stabilized powdered activated carbon (S-PAC), (b) stabilized ion exchange resin (S-IXR), and (c) nanoscale iron oxide core structures. For the latter system, single crystal, paramagnetic iron oxide (Fe_3O_4 as magnetite) nanoparticles (IONPs) were selected due to their ability to respond to an external magnetic field, which allows for low-energy magnetic placement and recovery. In Task 1B, highly reactive nanomaterials were synthesized by conjugating or encapsulating engineered magnetic and/or metal nanocrystals (mixed/doped Co, Ni, Mn, Fe – based materials) with highly water stable graphene oxides (produced from the exfoliation of graphite).

The goal of Task 2 was to identify and characterize synergistic and inhibitory relationships between the sorptive and reactive materials developed in Task 1 and biological processes capable of transforming chlorinated ethenes and/or PFOA and PFOS reaction byproducts. Experimental studies were conducted to assess the ability of a reductive dechlorinating microbial consortium to detoxify PCE, TCE and *cis*-dichloroethene (cis-DCE) in the presence of residual PFAS and to develop biological systems that can effectively treat effluent streams composed of PFAS and chlorinated ethene byproducts formed during catalyzed reduction reactions.

The goals of Task 3 were to (a) couple the physicochemical and biological systems developed in Tasks 1 and 2 as sequential treatment train systems, and (b) test the ability of these systems to treat mixtures of PFAS and chlorinated ethenes under conditions that are representative of a dynamic aquifer formation, (c) assess synergistic benefits of the treatment train approaches, including reaction kinetic parameters, treatment capacities, and reactive material longevities. Column experiments were conducted to individual and coupled remediation methods developed in Tasks 1 and 2, which were followed by larger-scale aquifer cell experiments to investigate the effects of subsurface heterogeneity and multi-dimensional flow.

Results and Discussion

Development of Highly Sorptive Nanomaterials for PFAS Sequestration

Sorption data obtained for PFOA and PFOS on IONPs coated with either polyethyleneimine (PEI, 25K Da and 10K Da), cetyltrimethylammonium bromide (CTAB) or oleic acid (OA) were fit to the Langmuir adsorption isotherm model;

$$C_s = \frac{C_{s,max} b C_w}{1 + b C_w} \quad \textbf{(ES.1)}$$

where C_s is the solid-phase concentration, $C_{s,max}$ is the maximum solid-phase concentration, b is the Langmuir adsorption parameter that represents the ratio of the adsorption and desorption rates, and C_w is the aqueous phase concentration. Regardless of the surface coating and water chemistry, all of the sorption data showed that PFOS exhibited a larger maximum adsorption capacity (Q_{max}) than PFOA, whereas the Langmuir adsorption constant (b) was greater for PFOA than PFOS, which indicates a more rapid increase to the maximum adsorption capacity (**Figure ES 2**). For example, on PEI (25K Da) coated IONPs, the fitted Langmuir parameters for PFOS and PFOA were $C_{s,max}$ = 88.8 mmol/g and 18.3 mmol/g, and b = 4.2 L/mmol and 657 L/mmol, respectively. This finding was attributed to the carboxyl functional group of PFOA, which has a lower pKa value compared to sulfonic group of PFOS which resulted in a higher affinity, while sulfonic group of PFOS has a resonance structure that resulted in larger $C_{s,max}$ value. Here, the functional (head)

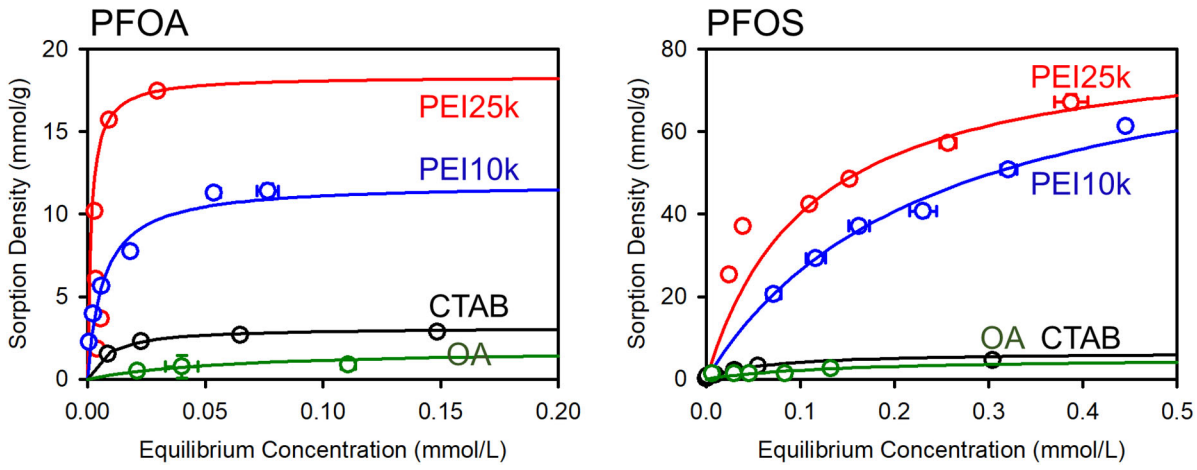


Figure ES 2. Sorption of PFOA and PFOS on polyethyleneimine (PEI)-coated iron oxide nanoparticles (IONPs) as a function of PEI molecular weight (25K Da versus 10K Da), and compared to cetyltrimethylammonium bromide (CTAB) and Oleic acid (OA) coated IONPs.

groups of PFAS not only affects the sorption constant, but also sorption capacity through the orientation of adsorbed PFAS on IONP surfaces. We verified the different orientation of PFAS using quartz crystal microbalance (QCM-D) experiments by calculating the thickness of adsorbed layer. We hypothesize that PFOS is attached vertically on the surface of IONPs because of sulfonic group having resonance structure, while PFOA can be adsorbed horizontally, resulting in

difference of layer thickness as 5 Å, which is corresponded with the C-8 carbon chain length of PFOS.

Batch adsorption tests were also conducted with S-PAC (ground Darco® <100 mesh) and PFOA or PFOS (**Figure ES 3)**. Using a non-linear least squares regression procedure, the adsorption data were fit to the Freundlich adsorption model;

$$C_s = K_F C_w^n \quad \textbf{(ES.2)}$$

where K_F is the Freundlich distribution coefficient and n is the Freundlich exponent. For PFOA and PFOS, the fitted values of K_F were 135 and 629 L/g^{-n} and n were 0.54 and 0.30, respectively.

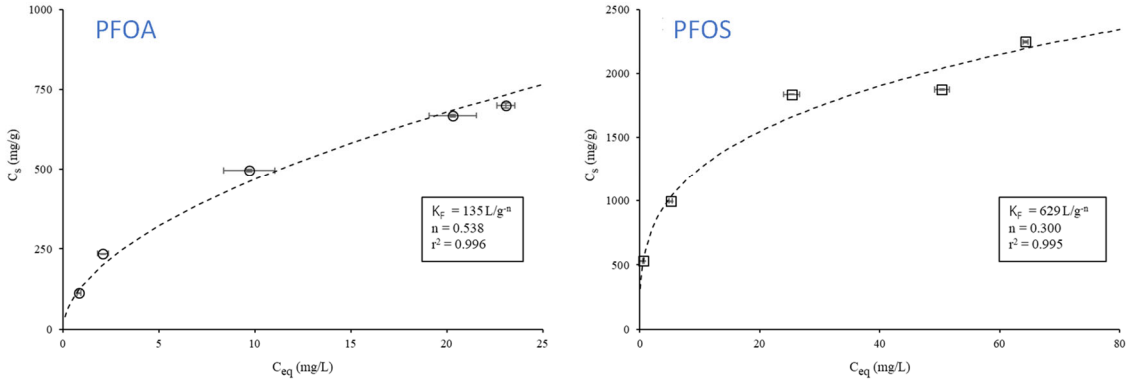


Figure ES 3. Adsorption of PFOA (A) and PFOS (B) on 100-mesh PAC and corresponding fits to the Freundlich Langmuir adsorption model.

Single-solute batch adsorption experiments were conducted for S-IXR (ground Amberlite® IRA910 beads) and each of six PFAS (PFOS, PFOA, PFNA, PFHxS, PFHpA, or PFBS). In the low concentration range (1 to 100 µg/L), all six PFAS exhibited linear adsorption. However, over the higher concentration range (10 to 500 mg/L), the PFAS adsorption isotherms were non-linear and were therefore fit to the Freundlich model (**Figure ES 4**). When comparing among the six PFAS tested, adsorption was greater for longer C-F chain length sulphonates or carboxylates (i.e., PFOS>PFHxS>PFBS and PFNA>PFOA>PFHpA). For PFAS of equal C-F chain length, sulphonates exhibited stronger adsorption than carboxylates (e.g., PFOS > PFNA). These adsorption trends are consistent with previous studies, which reported adsorption capacities ranging from 900 to 1,750 mg/g for PFOS and PFOA on ion exchange resins under similar conditions, and are approximately three times greater than adsorption capacities reported for granular activated carbon and are similar to those obtained for S-PAC (**Figure ES 3**).

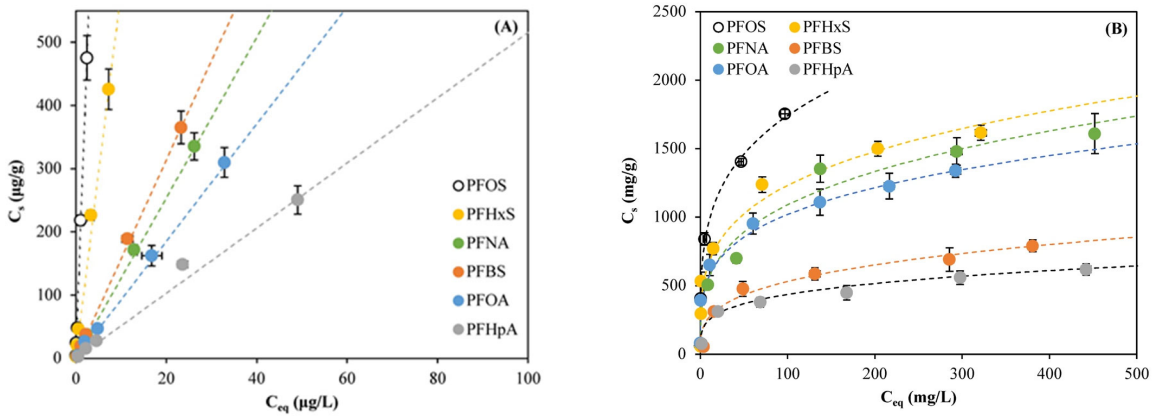


Figure ES 4. Adsorption data for PFOS, PFOA, PFNA, PFHxS, PFHpA, or PFBS (single solute) on S-IXR over concentration ranges of (A) 1 to 100 µg/L and (B) 10 to 500 mg/L.

Development of Reactive Nanomaterials for PFAS Transformation

Ultraviolet (UV) based photoactive nanocomposite materials, including graphene oxide (GO)–TiO2 composites, were synthesized to degrade PFAS. To enhance the photocatalytic performance, nitrogen doping using GO as substrate for both titanium dioxide (TiO_2) and metal-organic frameworks loaded with TiO_2. For nitrogen doped GO (N-GO), the well-mixed GO solution was freeze-dried to minimize re-stacking of the GO sheets, and then the dried sample was heated under a NH_3 atmosphere to dope the nitrogen on the GO. The N-GO samples were probe-sonicated in deionized (DI) water to resuspend the materials for subsequent reaction/degradation experiments. PFOA degradation was observed with 10 mg/L of N-GO under UV light (254 nm), with rates comparable or better than commercial materials such as anatase at an initial PFOA concentration

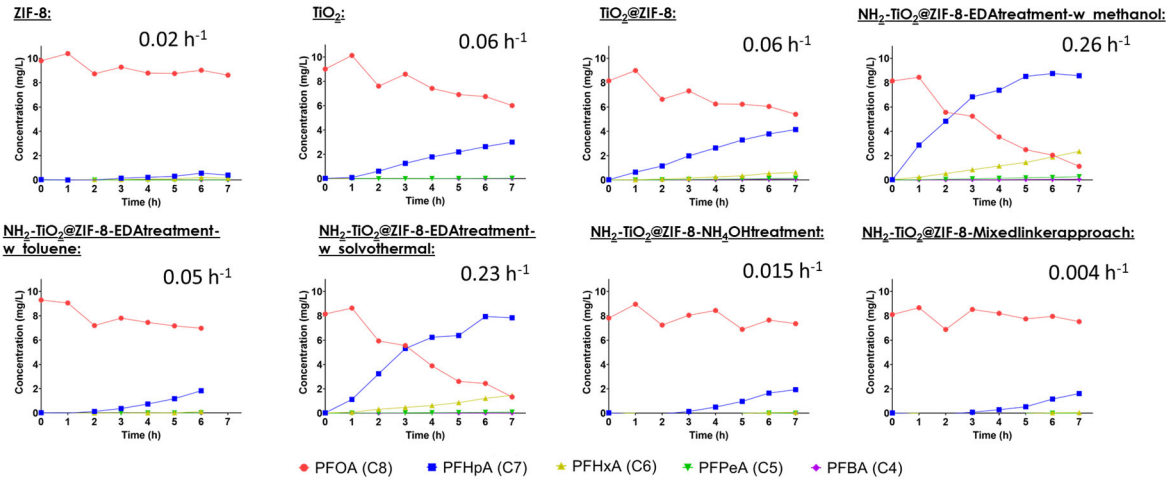


Figure ES5. Photocatalytic degradation of perfluorooctanoic acid (PFOA) with functionalized MOF composites under UV (wavelength = 254 nm) irradiation at pH 3.

of 50 mg/L (**Figure ES 5**). Reaction byproducts with lower carbon chains included PFHpA (C7), PFHxA (C6), PFPeA (C5), and PFBA (C4), and corresponded to an increase in measured fluoride ions.

A carbon nanotube (CNT) electrode interface was developed to achieve PFOS transformation using Nickel foam electrode surface, which was able to generate sulfate radicals based on electron paramagnetic resonance (EPR) analysis (Figure ES 6). EPR spectroscopy is commonly used to identify reactive species by measuring the absorption of specific adducts signals from the corresponding electromagnetic radiation. Here, DMPO was used as the radical trapping agent after adding peroxodisulfate (PDS) at CNTs-NF electrode. The CNTs-NF cathode exhibited a strong DMPO-SO_4 signal, indicating generation of sulfate radical which is highly effective for PFOS degradation. Further, the enhanced PFOS transformation with CNTs-NF electrode(s) was attributed to PFOS adsorption on the electrode surface where sulfate radical generation occurs.

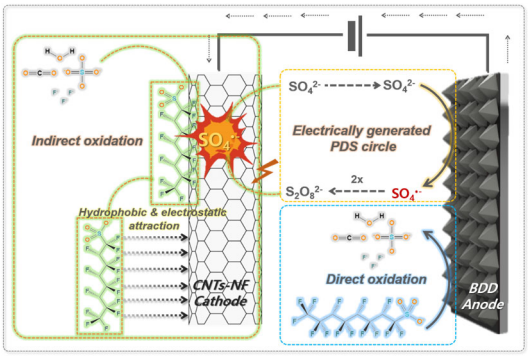


Figure ES 6. Schematic diagram of PFOS electrochemical oxidation process facilitated by a novel CNTs-NF electrode.

Impacts of PFAS on Organohalide Respiration

In batch reactors, the time to transform PCE and TCE to daughter products was the same or faster at all PFAA concentrations tested (up to 101 mg/L) when compared to reactors without PFAAs. The biodegradation time, i.e., time until TCE was not detected (TCE<0.18 mg/L), averaged 6.0 days in reactors without PFAS (**Figure ES 7**). In reactors with PFAAs, average biodegradation time was 5.3 days, demonstrating that PFAAs did not impede biodegradation of PCE and TCE to *cis*-DCE. MRD of *cis*-DCE to vinyl chloride (VC) and VC to ethene, however, required additional time in reactors with PFAS when compared to control reactors. In batch reactors without PFAS, *cis*-DCE was no longer detected (<0.15 mg/L) after 32.0 days and VC was no longer detected (<0.10 mg/L) after 34.7 days, while reactors with 11.7 mg/L PFAS required 17% more time (37.3 days) until *cis*-DCE was not detected, and 15% more time (40.0 days) until VC was not detected. In all cases, PCE and TCE were fully transformed to ethene. The additional time required to transform *cis*-DCE to ethene in reactors with PFAAs indicates that MRD by *Dehalococcoides mccartyi* (*Dhc*) strains was impeded by PFAS in batch reactor experiments. Additionally, there was no evidence of PFAS transformation in the batch reactors.

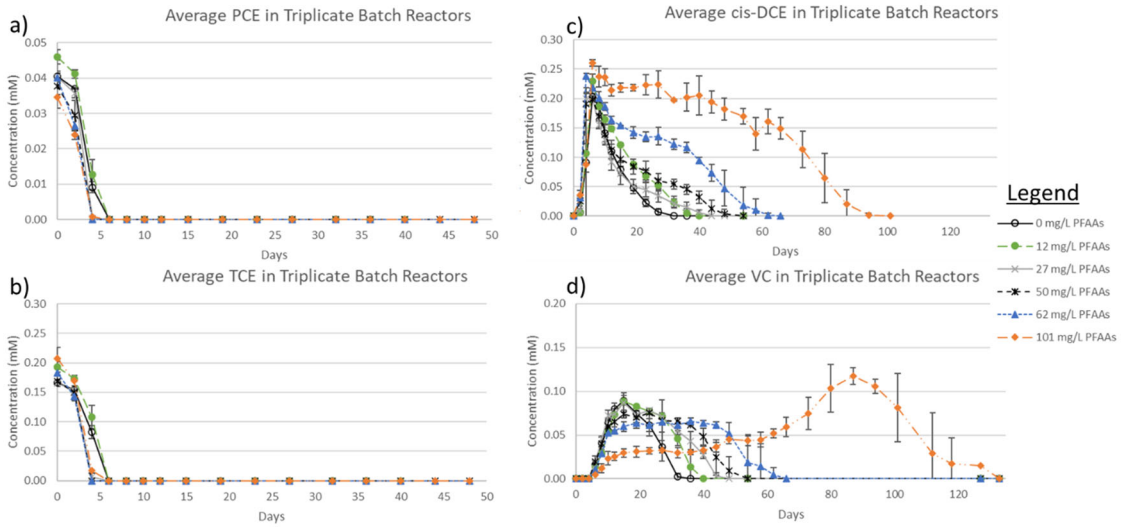


Figure ES 7. Transformation of chlorinated ethenes in batch reactor experiments. Symbols represent average a) PCE b) TCE c) cis-DCE and d) VC concentrations.

In microcosm studies, which contained soil from former Loring AFB, there was no difference in the time to dechlorinate PCE and TCE to cis-DCE at any of the PFAS concentrations tested. TCE was not detected 9 days after bioaugmentation and the time until cis-DCE was transformed after 26.3 days at PFAS concentrations up to 38.7 mg/L, and only the microcosms containing 91.3 mg/L PFAS required additional time (28 days) until cis-DCE was not detected (**Figure ES 8**). The difference between batch reactor results, in which additional time was required to transform *cis*-DCE and VC, indicates that the presence of a solid phase reduced the inhibition of *cis*-DCE and VC MRD by PFAS. In microcosms, the proportions of *vcrA* and *bvcA* genes, which are associated with enzymes capable of TCE and *cis*-DCE transformation to ethene, respectively, were strongly correlated with PFAS concentrations, but the proportion of *tceA* genes, which are associated with enzymes capable of the transformation of TCE to VC, did not correlate strongly with PFAS concentration. These correlations suggest that PFAS concentrations may preferentially impact *Dhc* strains containing the *vcrA* gene by lowering the relative proportion in the overall population, especially at high PFAS concentrations. The change in *Dhc* strain was observed in the highest concentration batch reactors (101 mg/L PFAS) and in microcosms with final PFAS concentrations of 38.7 mg/L and 91.3 mg/L. This analysis indicated a potential change in the *Dhc* strain responsible for ethene formation from cells harboring the *vcrA* gene in the absence of PFAS to cells harboring the *bvcA* gene at high PFAS concentrations.

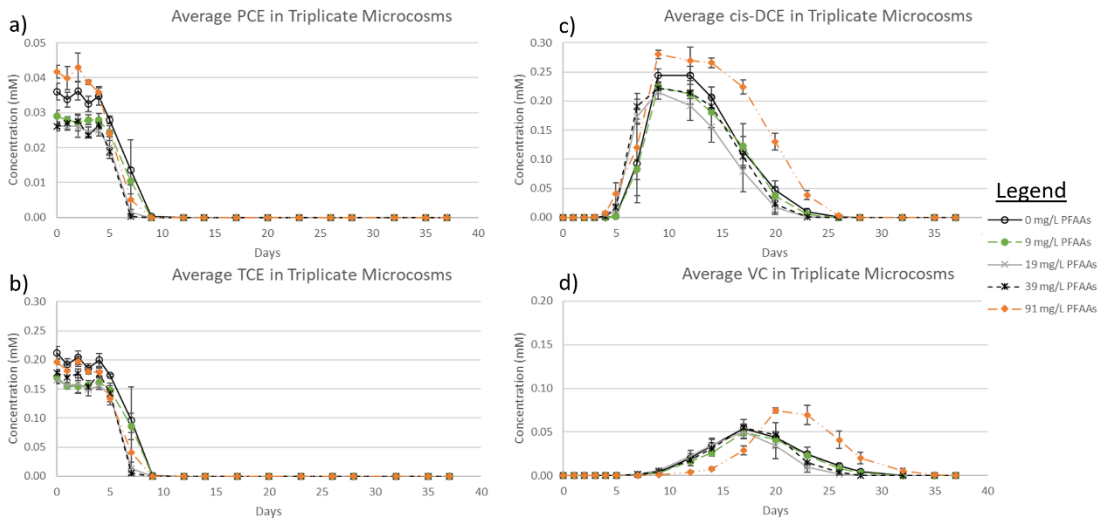


Figure ES 8 Average **a)** PCE **b)** TCE **c)** cis-DCE and **d)** VC concentrations in triplicate microcosms. Vertical error bars represent one standard deviation of mean.

Permeable Adsorptive Barriers for PFAS Sequestration

A series of column studies was conducted to evaluate the delivery and sorptive capacity of an aqueous suspension containing powdered activated carbon stabilized with a cationic polymer, polydiallyldimethylammonium chloride (polyDADMAC). In columns packed with 40-50 mesh Ottawa sand, the injection of a S-PAC suspension consisting of 1,000 mg/L PAC + 5,000 mg/L polyDADMAC created a permeable adsorptive zone. Aqueous solutions containing 100 ug/L of PFOS or PFOA followed by 20 mg/L of PFOS or PFOA were introduced into the treated columns and pore-water velocity of approximately 1 m/day. Retention of PFOA and PFOS was approximately three orders of magnitude greater than observed in the untreated control column, Based on the amount of PAC retained (~27 mg) and the batch adsorption isotherms, the capacity of the column should be ~ 8.65 mg PFOS, consistent with the observed retention of ~10.04 mg PFOS. If the injected concentration of PFOS had remained at 100 µg/L, the capacity of the S-PAC treated Ottawa sand would have been reached after ~5,020 pore volumes, demonstrating the potential utility of this permeable adsorptive barrier approach. Subsequent experiments conducted in a heterogenous aquifer cell, in which S-PAC was injected, further demonstrated the potential for this technology to be an effective *in situ* treatment option for PFAS-impacted groundwater.

A second set of column studies was conducted to evaluate the delivery and PFAS sorption capacity of an injectable ion exchange resin (Amberlite® IRA910 beads) stabilized with Pluronic® F-127. In columns packed with 40-50 mesh Ottawa sand, injection of the S-IXR suspension created a uniform sorptive zone that increased PFOA or PFOS retention by more than five orders-of-magnitude compared to untreated control columns. Multi-solute column studies revealed earlier breakthrough of shorter-chain length PFAS, which was consistent with the mixed PFAS adsorption data. For a 100 µg/L injection of PFOS, the capacity the resin would be reached after approximately 50,500 PV, which is a 10-fold increase compared to the S-PAC column study shown

in **Figure ES 9**. These findings indicate that injectable ion exchange resins could provide an even more effective remediation strategy for PFAS-impacted groundwater plumes.

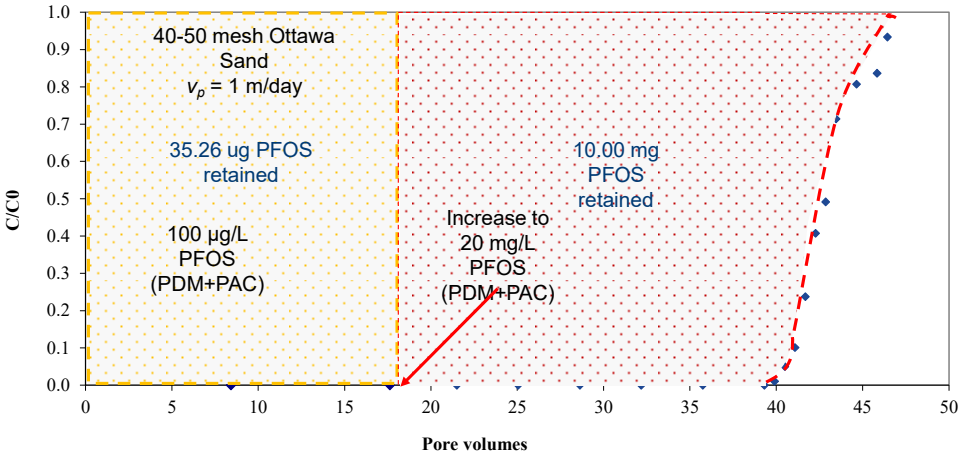


Figure ES 9. Effluent breakthrough curve for the injection of either PFOS (100 µg/L then 20 mg/L) into a water-saturated column containing S-PAC treated 40-50 mesh Ottawa sand. Shaded areas represent the amount of PFOS retained in the columns.

Coupled Treatment Systems for Groundwater Containing Chlorinated Solvents and PFAS

A series of dual column experiments were conducted to couple physicochemical and biological systems developed as part of project Tasks 1 and 2, to test the potential of a biological system to enhance the removal or transformation of a mixed contaminant plume composed of PFAS and chlorinated ethenes. A schematic diagram of the dual column system is shown in **Figure ES 10**. In both the single IONP and S-PAC column experiments, the breakthrough of TCE occurred earlier than that of PCE, indicating a higher adsorption affinity of PCE to both adsorptive materials. The breakthrough of 10 PFAAs in both columns showed similar adsorption preferences, with PFOS leading the sequence, followed by PFDA, PFNA, PFHxS, PFOA, PFHpA, PFBS, PFHxA, PFPeA, and PFBA. In the coupled column systems, upon passing through the bioactive columns, the concentrations of 10 PFAAs in the influent and effluent were comparable, highlighting the recalcitrance of PFAAs to microbial degradation. PCE and TCE were completely transformed to non-toxic ethene, and the breakthrough order of 10 PFAAs in both adsorptive columns (IONP and S-PAC) within the coupled column systems mirrored trends in the previous single adsorptive columns.

In the IONP columns, within the coupled bioactive and IONP columns system, a greater mass of total PFAAs was retained (437.3 µg) compared to the single IONP column (394.0 µg). It took longer for the IONP columns in the coupled system (~57 PVs) to reach their adsorption capacity compared to the single IONP column (~40 PVs). Similarly, the adsorption capacity of the S-PAC columns within the coupled column system hads not been exhausted since PFOS and PFDA

havedid not yet reached their applied concentrations at the conclusion of the experiment (59 PVs). However, the effluent concentrations of all 10 PFAAs in the single S-PAC column reached the applied concentrations in the influent after 59 PVs. In addition, a greater mass of total PFAAs was retained in the S-PAC columns within the coupled system (622.4 µg) compared to the single S-PAC column (601.2 µg) within the same timeframe. These results suggest that with reductive dechlorination in upgradient bioactive columns, the adsorptive columns (both IONP and S-PAC) exhibited enhanced sequestration of PFAAs.

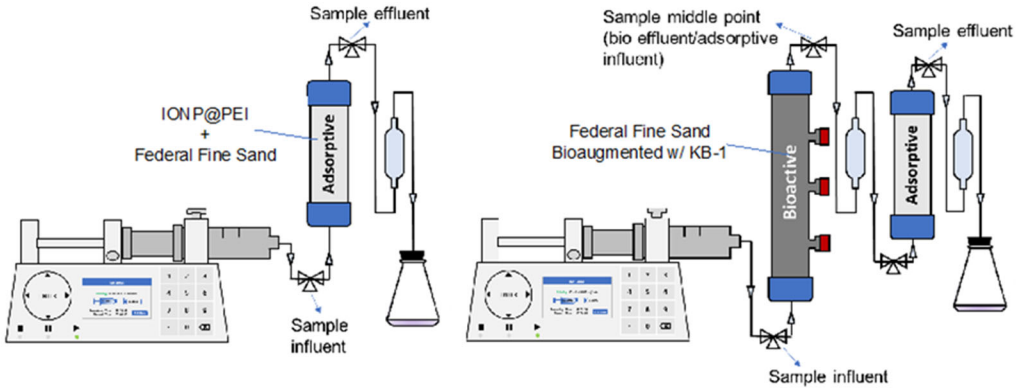


Figure ES 10. Single and dual column systems used to evaluate coupled bioactive and adsorptive treatment train for mixed plumes containing chlorinated ethenes and PFAS

Implications for Future Research and Field Implementation

The overall goal of this project was to develop coupled biological and physical-chemical systems that can be used to treat groundwater plumes containing mixtures of chlorinated ethenes and PFAS. We were able to synthesize iron oxide nanoparticles (IONPs) coated with polyethyleneimine (PEI) that exhibited large adsorption capacities for both PFOA and PFOS. Furthermore, we demonstrated rapid PFOA degradation with a novel graphene oxide (N-GO) and UV irradiation. Transformation of PFOS, which requires sulfate radicals, was achieved using an electrochemical oxidation with a carbon nanotube (CNT-NF) electrode. From bioremediation perspective, we found that the presence of PFAS is unlikely to impact MRD of chlorinated ethenes at typical field concentrations (< 10 mg/L total PFAS). We also developed injectable formulations of ion exchange resin (S-IXR) and powdered activated carbon (S-PAC) that function as permeable adsorptive barriers for treatment of chlorinated ethenes and PFAS, either separately or as mixed groundwater plumes. The coupled column system showed the advantage of complete detoxification of PCE and TCE to ethene and greater adsorption of PFAAs with the bioactive column upgradient followed by the downgradient adsorptive column. The results of this work have been distributed to the greater research community, regulators, and practitioners through webinars, conference presentations and posters, eight refereed journal publications. Two of injectable adsorptive materials developed as part of this project (S-PAC and S-IXR) will be evaluated in the field as part of two ESTCP demonstration projects.

1. Objectives

1.1 Introduction

Aqueous film foaming foams (AFFF) were widely used at Department of Defense (DoD) installations for fire fighter training exercises and fire response. Due to their stability at high temperature and amphiphilic properties, these foams contain per- and polyfluoroalkyl substances (PFAS), including perfluorooctanoic acid (PFOA) and perfluorooctane sulfonate (PFOS). Additionally, chlorinated solvents, such as tetrachloroethene (PCE) and trichloroethene (TCE), were commonly used for aircraft engine cleaning, paint removal, and degreasing metal parts. Thus, contaminated groundwater plumes at DoD sites often contain mixtures of chlorinated solvents and PFAS, both of which have stringent drinking water standards. For PCE and TCE, the U.S. Environmental Protection Agency (USEPA) established a maximum contaminant level (MCL) in drinking water of 5 parts per billion (ppb, μg/L), respectively. Although the USEPA has not established MCLs for PFAS, a health advisory level (HAL) of 70 parts per trillion (ppt, ng/L) for total (combined) PFOA and PFOS was established in 2016 [1]. In March 2023, the USEPA proposed a National Primary Drinking Water Regulation (NPDWR) of 4.0 ppt for PFOA and PFOS [2]. In addition, multiple states have established drinking water regulations with stringent threshold limits of ≤ 20 ng/L [3-5].

The persistence of per- and polyfluoroalkyl substances (PFAS) has resulted in widespread contamination of the environment, impacting both surface water and groundwater supplies [6-10]. A national survey of six PFAS conducted by the USEPA from 2013-2015 found that 1.6% of the samples collected from public water supply systems were contaminated with PFAS, with concentrations ranging from 0.01 to 7 μg/L [6]. The state of Michigan Department of Environmental Protection (DEP) recently identified 68 sites with groundwater concentrations of perfluorooctane sulfonic acid (PFOS) and perfluorooctanoic acid (PFOA) exceeding the USEPA combined HAL of 70 ng/L [11]. With the prevalence of PFAS in the environment, public concern regarding the toxicity and health effects of PFAS has also increased [12]. The association of PFAS with liver and kidney damage, developmental harm, immune system dysfunction and cancer have been widely reported [13-16]. In addition to contaminated drinking water [17, 18], exposure to PFAS via food, including crops and animal products such as terrestrial livestock and game species, has also been reported [19, 20]. These findings prompted the U.S. Environmental Protection Agency (EPA) to develop a PFAS action plan in 2019 [21]. Although the total number of PFAS-impacted sites in the US remains uncertain, a recent analysis suggests that more than 40,000 sites are contaminated with PFAS at levels that will require remedial action [22].

Over the past 10-20 years, a number of *in situ* remediation technologies have been developed and successfully deployed to treat groundwater plumes containing chlorinated solvents [23]. In marked contrast, efforts to degrade PFAS using thermal, chemical or biological processes have

largely met with failure, or are of limited practical value. The recalcitrant nature of PFAS primarily results from the strength of covalent bond (~ 450 kJ/mole) between carbon and fluorine [24]. As a result, advanced oxidation processes (AOP) typically used in water and wastewater treatment are of limited value because hydroxyl radicals (OH•) exhibit minimal reactivity with PFAS [25]. Recent studies have reported successful degradation of PFOA with heat-activated persulfate [26] and catalyzed hydrogen peroxide, which generates hydroperoxide anions and superoxide anions [27]. Unfortunately, neither of these approaches has been shown to degrade PFOS. Several other oxidative methods, including ultraviolet (UV) photolysis, photocatalysis (with TiO_2) and sonication, have been shown to degrade PFOA, and in some cases PFOS [25], but these techniques are not readily amenable to *in situ* remediation. As a consequence, PFAS-impacted groundwater plumes are typically managed using conventional "pump and treat" remediation approaches that rely on extraction and above-ground treatment with granular activated carbon (GAC) or ion exchange resin (IXR). However, the adsorption capacity of activated carbon is known to decline precipitously for short-chain length PFAS and precursors [28-30], while resins have been shown to provide more consistent removal efficiency for both long- and short-chained PFAS [28, 31]. Thus, there is a clear need to develop new technologies and approaches to treat groundwater plumes containing mixed contaminants of concern (COCs).

1.2 Research Goals

In response to SERDP Statement of Need (SON) ERSON-17-01, which focused on approaches that would improve our ability to treat mixed contaminants of concern (COCs), this project was designed to address the treatment of groundwater plumes containing mixtures of chlorinated ethenes and PFAS. Due to their prevalence at DoD sites and persistence in the environment, the research program focused on aqueous solutions containing PFOA and PFOS, which were used in aqueous film forming foams (AFFF); and two chlorinated ethenes; PCE and TCE.

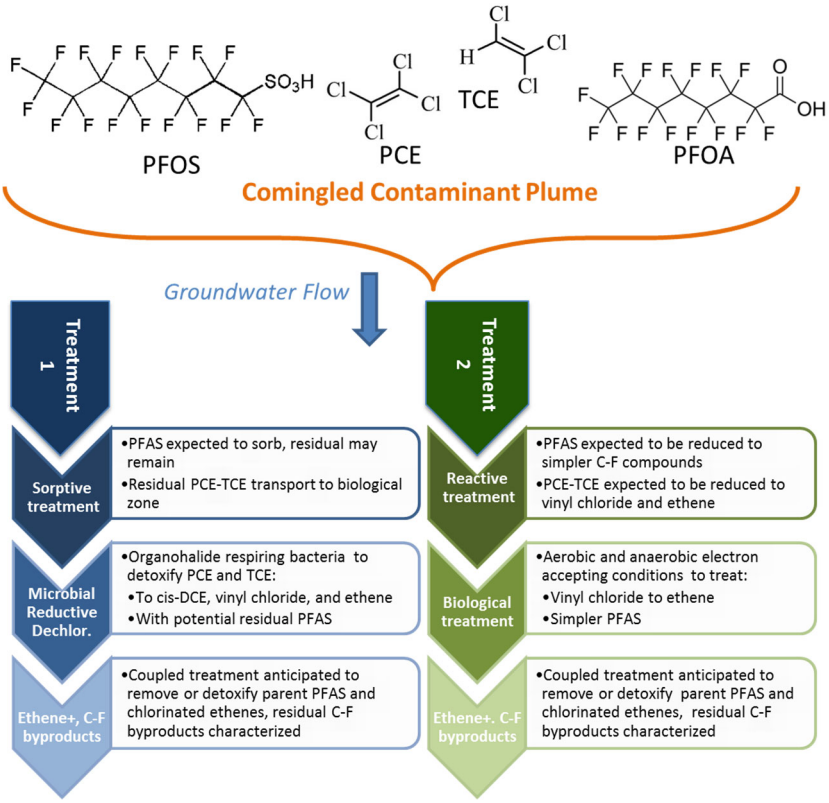


Figure 1.1 Schematic diagram of two treatment train approaches for comingled a PFOS-PFOA-PCE-TCE groundwater plume: (1) Sorption followed by anaerobic reductive dechlorination, and (2) Catalyzed reduction reaction.

In order to assess performance for a range of carbon chain lengths, four additional PFAS compounds were evaluated, perfluorohexanoic acid (PFHxA, $C_6HF_{11}O_2$), perfluorobutanoic acid (PFBA, $C_4HF_7O_2$), perfluorohexane sulfonate (PFHS, $C_6HF_{13}O_3S$), and perfluorobutane sulfonate (PFBS, $C_4HF_9O_3S$). While microbial reductive dechlorination of PCE and TCE has been widely used chemical oxidation of PFOA has been recently demonstrated, PFOS is extremely recalcitrant to conventional thermal, chemical or biological treatments. In addition, groundwater containing a mixture of PFAS was recently shown to inhibit microbial reductive dechlorination of TCE and subsequent formation of reduced byproduct (.e.g, cis-DCE, ethene) [32].

Therefore, we developed *in situ* permeable barrier systems, using sequential or "treatment train" remediation approaches, to more effectively treat groundwater containing mixtures of PFAS and chlorinated solvents (**Figure 1.1**). One of these systems consisted of microbial reductive dechlorination to treat PCE and TCE, coupled with down-gradient a *sorptive barrier* to remove and sequester PFAS. The stabilized particulate materials used in the permeable barriers can be delivered as an aqueous suspension, emplaced as a trench, or as a "funnel and gate" system.

1.3 Research Approach

The technical approach was structured around three integrated tasks:

Task 1: Develop highly reactive materials capable of degrading and/or sequestering PFAS, including PFOA and PFOS, in the presence of chlorinated ethenes.

Task 2: Develop biological systems to treat chlorinated ethenes and PFAS reaction byproducts down-gradient from sorptive and reactive barrier wall systems, respectively.

Task 3: Evaluate the performance of two coupled physicochemical and biological reactive barrier systems using groundwater containing mixtures of PFAS and chlorinated ethenes.

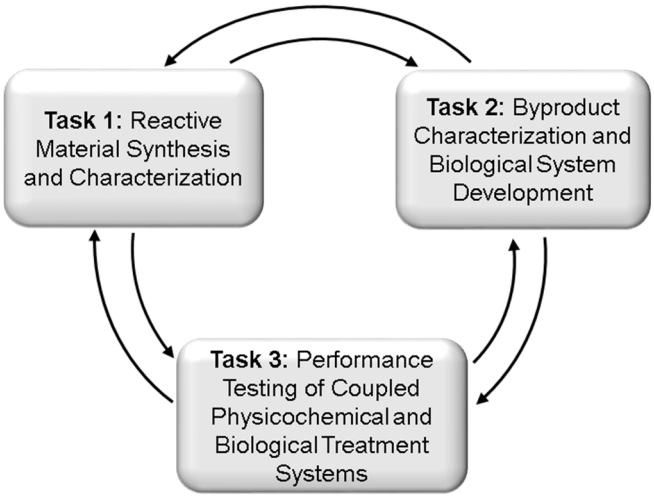


Figure 1.2 Project flow diagram illustrating synergistic integrated project tasks.

In Task 1A, three types of sorptive materials were evaluated for *in situ* treatment applications; (a) stabilized powdered activated carbon (S-PAC), (b) stabilized ion exchange resin (S-IXR), and (c) nanoscale iron oxide core structures. For the latter system, single crystal, paramagnetic iron oxide (Fe_3O_4 as magnetite) nanoparticles (IONPs) were selected due to their ability to respond to an external magnetic field, which allows for low-energy magnetic placement and recovery. In Task 1B, highly reactive nanomaterials were synthesized by conjugating or encapsulating engineered

magnetic and/or metal nanocrystals (mixed/doped Co, Ni, Mn, Fe – based materials) with highly water stable graphene oxides (produced from the exfoliation of graphite).

The goal of Task 2 was to identify and characterize synergistic and inhibitory relationships between the sorptive and reactive materials developed in Task 1 and biological processes capable of transforming chlorinated ethenes and/or PFOA and PFOS reaction byproducts. Experimental studies were conducted to assess the ability of a reductive dechlorinating microbial consortium to detoxify PCE, TCE and cis-dichloroethene (cis-DCE) in the presence of residual PFAS and to develop biological systems that can effectively treat effluent streams composed of PFAS and chlorinated ethene byproducts formed during catalyzed reduction reactions. A series of batch reactor and microcosm experiments was completed to provide insight into the conditions under which perfluoroalkyl acids (PFAAs) may inhibit microbial reductive dechlorination (MRD) in the presence and absence of soil and to assess their impact on specific *Dehalococcoides mccartyi* (*Dhc*) strains. All reactors were prepared with a mixture of ten common PFAAs co-contaminants with total concentrations ranging from 0 to 120 mg/L and subsets were bioaugmented with KB-1® (SIREM; Guelph, ON) [33, 34]. Six concentrations of PFAA mixture were tested in batch reactors and five concentrations of PFAA mixture were tested in microcosms. Reductive dehalogenase (RDase) genes were quantified to provide insight into the strain-specific responses of *Dhc*. Microcosm experiments, containing soil from a PFAS-contaminated site, were used to assess the impact of a solid phase on batch-measured MRD rates and extent. To provide additional quantitative and statistical comparisons among batch reactors, a numerical model was developed and employed to fit kinetic parameters including substrate utilization rates and yield coefficients.

The goals of Task 3 were to (a) couple the physicochemical and biological systems developed in Tasks 1 and 2 as sequential treatment train systems, and (b) test the ability of these systems to treat mixtures of PFAS and chlorinated ethenes under conditions that are representative of a dynamic groundwater formation, (c) assess synergistic benefits of the treatment train approaches, including reaction kinetic parameters, treatment capacities, and reactive material longevities. Column experiments were conducted to individual and coupled remediation methods developed in Tasks 1 and 2, which were followed by larger-scale aquifer cell experiments to investigate the effects of subsurface heterogeneity and multi-dimensional flow. Two different sorptive materials, polyethylenimine-coated iron oxide nanoparticles (PEI-IONP) and powdered activated carbon stabilized with polydiallyldimethylammonium chloride (S-PAC) were tested in column experiments to investigate the retention and breakthrough of PCE, TCE, and 10 PFAAs. These two materials were previously demonstrated to have high sorptive capacity for single PFAA (i.e., PFOA or PFOS) [35, 36]. *In situ* bioremediation (ISB) can effectively treat PCE/TCE-contaminated plume, even in the presence of PFAAs at environmentally relevant concentrations [37, 38]. In this context, a sequential ISB and sorptive remedial approach for treatment of comingled PCE/TCE and PFAAs-contaminated groundwater was investigated in coupled column systems. Two sets of coupled column systems were prepared with a bioactive column (bioaugmented with the commercially available dechlorinating consortium KB-1®) upgradient, followed by a sorptive

column packed with PEI-IONCs or S-PAC as sorbents. The coupled column experiments were conducted to evaluate the bioremediation of PCE and TCE in the presence of environmentally-relevant PFAA concentrations within saturated porous media under flowing conditions. Further, the benefit of the enhanced retention of PFAAs by eliminating the competitive sorption of PCE and TCE due to upgradient MRD was examined.

2. Background

2.1 PFAS Contamination

Per- and polyfluoroalkyl substances (PFAS) represent a broad class of compounds consisting of a fully or partially fluorinated carbon chain and several types of end or "head" groups including sulfonate, carboxylate, sulfonamide, and alcohol. Due to their unique amphiphilic properties and chemical stability, PFAS have been widely used in products such as firefighting foams, mineral extraction surfactants, floor polishes, photographic film, waterproof clothing and non-stick coatings for cookware [9, 39]. It has been estimated that the PFAS family includes approximately 5,000 to 10,000 chemicals[40], with a recent inventory identifying more than 4,700 PFAS that could have been, or may be, in the global market [41]. Of particular concern at DoD installations are aqueous film forming foams (AFFFs), which were developed in the 1960's to fire-extinguish or suppress flammable organic liquid fires. In the 1980's, the military sector comprised 75% of the total AFFF product market [9]. Although production of sulfonamide-containing AFFF by 3M ceased in the early 2000s [42], the military continued to use these stockpiled compounds for fire-fighting training until very recently and also began using fluorotelomer-based AFFFs. The commercial AFFF formulations are complex proprietary mixtures typically composed of a solvent, fluorocarbon surfactants, and hydrocarbon-based surfactants [9]. In a study of 10 AFFFs concentrates, which included nine from fire fighting sites in Ontario, Canada, a total of 103 PFAS were identified with chain lengths ranging from C3 to C15 [43]. In a study of AFFF and AFFF-impacted groundwater, 40 classes of novel PFAS were identified using nontargeted mass spectrometry analysis. Thirty-four of the 40 newly identified PFAS classes were derived from the electrochemical fluorination (ECF) process. Of the newly identified PFAS, 25% were anionic, 13% were cationic, and 55% were zwitterionic [44]. Ultra-short-chain PFSAs (i.e., C2 and C3) were also found in 3M AFFFs [45]. In a study of nine different firefighting foams in France, 122 emerging PFAS were identified with three PFAS quantified at concentrations up to 3 g/L [46]. A report in 2014 estimated that the total inventory of AFFF in the U.S. is around 10 million gallons [42], roughly 55% of which was estimated to be telomer-based concentrate and other 45% to be ECF-based concentrate. In addition to the complexities noted above, AFFFs were often used in conjunction with flammable liquids, such as fuels and chlorinated solvents. Thus, the repeated historic use of AFFF in fire-fighting training and suppression activities has resulted in groundwater contamination at hundreds of DoD sites [47], where per- and polyfluoroalkyl substance (PFAS) contamination is likely to be commingled with hydrocarbons and chlorinated solvents [48, 49]. Therefore, this project was designed to develop and test technologies that could be used to treat both PFAS and chlorinated solvents, and to understand the potential effects of PFAS on microbial reductive dichlorination of chlorinated solvents

At sites where AFFF has been released into the environment, PFAS have been detected in the areas near or downward from the the source. In a study of groundwater collected from two fire-training

sites at Naval Air Station Fallon, NV, and Tyndal Air Force Base, FL, PFAS with chain lengths of six to eight carbons were detected at total concentration of up to 7,000 µg/L 7-10 years after the sites were inactive [50]. Another study analyzed over 36,000 drinking water samples collected between 2013 and 2015 from the USEPA's UCMR 3 program, and correlated samples with detectable PFAS to the existence of industrial sites, military fire training areas, AFFF certified airports and wastewater treatment plants in the watershed using a spatial regression model [51]. The persistence of PFAS contamination over time from the release of AFFF was investigated in groundwater, soil and aquifer solids samples obtained in 2011 from a fire training site where AFFF was used between 1970 and 1990 [52]. Their results indicated that many of the precursors released, including PFHxSAm, FOSA, FHxSA, 6:2 FtS and 8:2 FtS, persisted at this site and were converted to more stable perfluoroalkyl carboxylates (PFCAs) and perfluoroalkyl sulfonates (PFSAs).

2.2 PFAS Health Effects

Although the toxicity of PFAS remains an active area of research, human exposure to PFAS has been linked to liver and kidney damage, developmental alterations, immune system dysfunction and several types of cancer [13-16]. For example, studies on a cohort living near the West Virginia DuPont Washington Works fluorotelomer plant revealed links between PFOA exposure and high cholesterol, thyroid disease, pregnancy-induced hypertension, ulcerative colitis, and kidney and testicular cancer [15, 53-55]. Adverse health effects other than carcinogenicity that have been associated with PFAS exposure include liver and kidney damage, developmental harm, immune system dysfunction, asthma, high blood pressure, peripheral arterial disease, stroke, and myocardial infarction [13, 14, 16, 56-63]. Positive associations between PFAS exposures and dyslipidemia, immunity, renal function and age at menarche were identified in a systematic review of 64 studies [64]. Reproductive health effects linked with PFAS exposure have also been reported, including impairment of sperm motility, change in endometrial regulation, infertility, decrease in infant birth weight, pregnancy-induced hypertension or preeclampsia [53, 65-71].

2.3 PFAS Drinking Water Regulations

Due to concerns over potential human health effects, production of long-chain PFAS (e.g., PFOS) was voluntarily phased out by the primary manufacturer (3M) in 2002. In 2012, six PFAS were listed in USEPA's third Unregulated Contaminant Monitoring Rule (UCMR 3)[72], which supported a nation-wide survey for water supplies serving more than 10,000 people in the United States [51]. In May 2016, the USEPA issued a drinking water health advisory of 0.07 µg/L for two persistent PFAS, perfluorooctanoic acid (PFOA) and perfluorooctanesulfonic acid (PFOS) [1, 73]. In June 2022 the HAL was updated to 0.004 nanograms per liter (ng/L) for PFOA and 0.02 ng/L for PFOS. At the same time, USEPA issued HALs for perfluorobutane sulfonic acid (PFBS) and hexafluoropropylene oxide dimer acid (HFPO-DA), commonly referred to as GenX, which are considered to be potential replacement chemicals for PFOS, and PFOA, respectively. Following this interim advisory, the USEPA announced a proposed NPDWR for six PFAS, including the

above four (with PFOA and PFOS at 4 ng/L) as well as perfluorononanoic acid (PFNA) and perfluorohexane sulfonic acid (PFHxS) in June 2023 [74].

As a result of the strict PFAS regulations in North America and Europe, PFAS manufacturers took the following actions: (1) migrating PFAS manufacturing to other countries with less regulation, such as China, India and Russia, which potentially offset the anticipated global reduction [75], and (2) developing replacement chemicals with shorter C-F chain lengths, such PFBS in replacement of PFOS or in other subcategories such as FTOH and GenX[76]. The existence of these replacement substances in the environment has been reported [77, 78]. However, studies on the toxicology and environmental effects of these emerging replacement PFAS are limited. Some of the replacement PFAS may not be less hazardous than the long-chain predecessors as expected ([79]. The different physicochemical properties of the replacement PFAS bring addition challenges to the remediation of them as some conventional treatment techniques may not be as effective for shorter chain length PFAS

2.4 PFAS Accumulation at the Air-Water Interface

Due to their amphiphilic properties, many PFAS tend to strongly accumulate at fluid-solid and fluid-fluid interfaces in natural subsurface environments. For example, PFOA and PFOS are water soluble substances that exhibit the unique property of spontaneously concentrating at the air-water interface [80]. This rapid transfer of PFOA or PFOS from bulk water to air-water interfaces can be used to remove [81] or degrade [82] these substances, and also has implications for their fate and transport in contaminated source areas. For example, the mass of PFOA concentrated at the air-water interface, rather than adsorbed to solids, was reported to be a major sink for the retention of PFOA in flow-through columns containing quartz sand, with water saturations ranging from 0.68 to 0.86 [83, 84]. Because PFAS typically contaminate surface soils through fire training, equipment maintenance, or emergency response activities [9, 85], they may remain entrained at air-water interfaces in the vadose zone [86-88], serving as a long-term source of contamination to the underlying groundwater.

The surface excess of a surfactant at the air-water interface is related to the decrease in surface tension associated with the increase in bulk water concentration, commonly referred to as the the Gibbs surface excess. The surface tension of surfactants strongly depends on the counterions of their respective salt formulations [89], and thus, dissolved cations and anions present in groundwater can impact the surface tension and, the resulting surface excess of PFOA and PFOS [90, 91]. Although experiments employing PFOA or PFOS alone or in combination are important, the results of such studies may not be applicable to conditions at sites where AFFF was released. This is due to the fact that commercial AFFF formulations consisting of complex proprietary mixtures, typically composed of fluorocarbon (e.g. PFOS) and hydrocarbon surfactants along with solvents [92]. The combination of fluorocarbon and hydrocarbon surfactants in AFFF has a synergistic effect that could increase the concentration of these surfactants at the NAPL-water interface [89]. Such relationships, along with an understanding of the air-water interfacial area,

are required to understand and accurately predict the fate and transport of PFAS in unsaturated soils and to estimate the potential mass stored in the vadose zone.

2.5 Potential Impacts of Co-contaminants on Bioremediation of Chlorinated Ethenes

Enhanced *in situ* bioremrediation (ISB) of chlorinated solvents, including the widespread groundwater contaminants PCE and TCE, is an effective remedy implemented at numerous sites [93]. Current PCE and TCE bioremediation relies on *Dhc* strains to complete biodegradation of PCE to ethene [94]. Multiple *Dhc* strains have been identified and those implicated in transformation of chlorinated ethenes harbor specific reductive dehalogenase (RDase) genes [95]. Each *Dhc* strain has the capacity to transform specific chlorinated compounds including TCE, dichloroethane (DCE), and vinyl chloride (VC), while only a limited number of strains that transform VC to ethene have been identified [96]. *Dhc* strains harboring the *tceA* gene are known to metabolically transform TCE to VC and to (co)-metabolically transform VC to ethene [96, 97]. *Dhc* strains harboring the *vcrA* gene are able to transform DCE to VC and VC to ethene metabolically and strains harboring the *bvcA* gene metabolically transform VC to ethene and may be able to transform some DCE isomers to VC [97, 98]. Metabolic transformations result in more efficient biodegradation, so understanding the conditions that favor strains capable of these transformations is critical to enhanced ISB.

Chlorinated solvents rarely occur in isolation and co-contaminants can negatively impact bioremediation [99]. The co-contaminants 1,1,1-trichloroethane, triclocarban, and chloroform have been shown to impact specific *Dhc* strains, typically having a greater impact on cells harboring the *vcrA* gene than those harboring the *tceA* gene [100-102]. One study demonstrated that PFAAs can inhibit TCE degradation by *Dhc* strain 195 (harboring the *tceA* gene) but did not examine the strain-specific impact of PFAAs on a culture containing multiple *Dhc* strains [103]. Since specific *Dhc* strains are necessary to fully transform PCE to ethene, understanding strain-specific impacts of co-contaminants is essential to successful enhanced ISB.

Additionally, the presence of a solid phase has been shown to prevent inhibition of microbial reductive dechlorination (MRD) at high PCE and TCE concentrations by potentially providing microenvironments where microbes do not experience the high concentrations present in the bulk liquid [104]. The presence of certain solids also provided protection at low pH (≤5.5), allowing MRD to proceed at a pH that inhibited MRD when solids were absent [105]. Similarly, it is hypothesized that the PFAA inhibition of MRD observed in batch reactors may not occur at the same PFAA concentrations if a solid phase is present.

PFAAs may affect the bioremediation of other compounds, including chlorinated solvents and recent studies have shown an effect of PFAS on the diversity of microbial communities, indicating that certain species may be more affected by PFAS than others [106]. A recent study reported inhibition of TCE degradation by *Dhc* strains at PFAA concentrations above 66 mg/L in a

methanogenic PCE-to-ethene dechlorinating culture [103]. Another study found that TCE dechlorination by *Dhc* strains was inhibited by AFFF manufactured by Ansul and National, but not by AFFF manufactured by 3M, for total PFAS concentrations ranging from 30 to 120 mg/L [38]. Thus, to treat chlorinated solvents in co-mingled plumes, the conditions under which *Dhc* activity is inhibited by PFAS must be better understood.

2.6 Mathematical Modeling of PFAS Fate and Transport

Prior to 2018, most PFAS partitioning and transformation experiments focused exclusively on batch systems. The only published packed-column studies were conducted to explore the potential effect of specific treatment technologies (i.e., *in situ* chemical oxidation) on PFAA mobility and decomposition [107, 108]. In these studies, experiments were conducted with a single porous medium material (loamy sand) and a fixed-composition PFAA mixture under one set of flow conditions. Thus, there were no systematic investigations of PFAS transport in natural porous media under varying flow conditions. In addition, few published studies on PFAS transport prior to 2018 incorporated a mathematical modeling component. Those that did seek to model field or laboratory observations Typically implemented simple linear (equilibrium) sorption [49, 108] and NAPL partitioning [107] expressions, with no attempt to account for nonlinearities, the competitive or synergistic influence of co-constituents, rate-limited mass transfer, or formation heterogeneity.

A number of modeling studies, based upon the solution of coupled aqueous phase flow and PFAS transport equations, have explored the field-scale migration of PFAS in the vadose zone. Guo et al. [109] proposed a 1-D model to simulate the transport of PFOS in two types of media (sand and soil) under two types of climatic conditions (semiarid and humid). They simulated a periodic release of PFOS and predicted a mass retention of >70% at the air-water interface, which resulted in low migration rates. An alternative approach was presented by Silva et al. [110, 111], who modified a commercial simulator (HYDRUS [112]) to include accumulation at the air-water interface and the influence of surface-active substances on moisture retention curves. Their work, which explored the extent of interfacial and solid phase sorption, suggested that accumulation at the air-water interface is less important in media containing solids with high sorption capacity. Later efforts by Zeng et al. [113, 114] considered both 1-D and 3-D models for the flow-transport problem in homogeneous and heterogeneous systems. Their simulations suggested that retention in the vadose zone was correlated with PFAS chain length and demonstrated the critical influence of soil heterogeneity on the migration process. The modeling study of Wallis et al. [115] also highlighted the importance of soil lithology, but their work suggested that net recharge due to precipitation and evaporation is the key process controlling the retention of PFAS in the vadose zone.

2.7 In situ remediation of comingled per- and polyfluoroalkyl substances (PFAS) and chlorinated ethenes groundwater

PFAS are currently thought to be recalcitrant to biodegradation. There are no well-studied or documented biotransformation pathways that mineralize PFAS to non-toxic endpoints, although recent studies have identified potential microbial defluorination [116, 117]. With the advantages of more cost-effective, less energy intensive, and smaller carbon footprint compared to ex-situ remediation, *in situ* treatment of PFAS is desired. However, *in situ* treatment for PFAS contaminated groundwater has not been well established. Lately, a few of studies demonstrated the promise of *in situ* immobilizing PFAS in groundwater by stationary adsorption barriers [35, 118, 119]. In these studies, only single PFAS was used for investigation, however, in the field, the treatment performance can be complicated by potential sorptive competition among different PFAS species and/or co-contaminants (e.g., PCE/TCE). For example, the presence of 8 mg/L TCE was reported to diminish the PFOS adsorption by colloidal activated carbon due to the competition for adsorptive sites, but had no effect on PFOA adsorption [120]. Therefore, research is needed to gain an improved understanding of the retention and breakthrough of various PFAAs and chlorinated ethenes during the implementation of *in-situ* adsorption barriers.

Given that concentration of chlorinated ethenes at AFFF-impacted sites could be several orders of magnitude greater than PFAAs [121], it is imperative to minimize and/or detoxificate chlorinated ethenes in groundwater plumes prior to the contaminant plume encountering an adsorption barrier. Recently, coupling biological and physicochemical remediation methods has attracted growing attention for treating groundwater plumes containing mixtures of different types of contaminants. For example, combined electrochemical oxidation with aerobic biodegradation was shown to be effective in treating mixed 1,4-dioxane and chlorinated solvent contamination [122]. In addition, a simultaneous removal of TCE and arsenic (As) from co-contaminated groundwater was achieved by adding biochar to a microbial dechlorination system [123]. Furthermore, a field study demonstrated the use of colloidal activated carbon combined with micro-sulfidated zero-valent iron to treat groundwater contaminated by TCE and PFAS [124]. These results indicate the potential promise of integrated biological and physicochemical processes in addressing co-mingled PFAAs and chlorinated ethenes groundwater plume. However, to date, there remains a scarcity of studies investigating these coupled remedial systems [124].

2.8 Biotransformation of PFAS Precursors

Several PFAS that are potential degradation precursors to PFOA and PFOS, such as perfluoro-1-octanesulfonamide (FOSA) and 8:2 fluorotelomer alcohol (8:2 FTOH), are also present in AFFFs [125, 126]. A number of studies have suggested that anomalous field observations of PFAA concentrations could be explained by the abiotic or biotic transformation of the nonfluorinated part of the molecule attached to the perfluorinated chain of such precursors [49, 127]. Previous laboratory studies have demonstrated the potential biotransformation products of PFAA precursors found in AFFF under different redox conditions. The majority of these biotransformation studies

were conducted with single compound fluorotelomer precursors under oxic conditions, utilizing bacteria from: activated sludge reactors [128, 129], aerobic surface soils [130-134], aerobic bacterial enrichments [132, 135], and soil from an AFFF site [136]. Additionally, two fluorotelomer precursors were also found to transform under methanogenic conditions utilizing anaerobic digester sludge [137] . Another study with river sediments found that a fluorotelomer precursor was not readily degraded under sulfate-reducing conditions with a terminal sulfonate group (-SO3-), while those with a terminal hydroxyl group (-OH) were transformed [138]. In each of these fluorotelomer precursor studies, perfluorinated carboxylates (including PFOA) were observed as minor products (i.e., <11% of PFAA precursor transformed) with intermediate fluorotelomer products over the two- to three-month duration of the experiment. The biotransformation of sulfonamide-containing precursors with structures similar to those found in AFFF formulations manufactured by 3M has been investigated in limited studies utilizing activated sludge [139, 140] and marine sediments [141]. In these studies, completed under aerobic conditions, PFOS accounted for the transformation of 0.6-40% of the perfluorooctane sulfonamide (FOSA)-containing precursors.

2.9 PFAS removal techologies

Physical separation process, such as adsorption and membrane processes can effectively remove PFASs regardless of carbon chain length and functional head groups. The removal of PFAS by various adsorbents, including activated carbon,[30, 35, 142, 143] carbon nanotubes,[144] anion−exchange resin,[29, 145, 146] polymer,[119, 147-150] metal, and/or metal oxide,[151-153] has been studied. We summarized sorption capacities of various adsorbents in **Table 2.1.** To improve the removal efficiency by adsorption, additional treatment processes were also applied with physical attachment, including air bubbles,[154] and heat.[155] In addition, hybrid composite materials and organic functionalization (i.e. modification) were also used to enhance adsorption performance.[156-158] However, there are still limitations on adsorption capacities and related application for different PFAS compounds based on surface and water chemistries. Based on the state of the art, there is still a critical need to develop and demonstrate materials with high affinity to PFAS compounds regardless of their structures, functional groups, and hydrophobicity.

Table 2.1 Summary of adsorption capacities for PFAS (considering PFOA and PFOS) for various adsorbents for comparison.

Adsorbate	Adsorbent	Water Matrix	pH	Adsorption Capacity		Ref.
				mg/g	mmol/g	
PFOA	PAC	DI water	3	426	1.03	[159]
	GAC	DI water	5	476	1.15	[160]
	Polyacrylonitrile fiber-derived activated carbon fibers (PACFs)	DI water	5	302	0.73	[143]
	SWCNT	DI water	6	80	0.19	[161]
	Modified titanate nanotubes	DI water	2-10	1,100	2.66	[162]
	Anion Exchange Resin (IRA910)	DI water	6	1,440	3.47	[163]
	Anion Exchange Resin (IRA400)	DI water	2-12	1,210	2.92	[164]
	Polyaniline nanotubes (PANTs)	DI water	2-9	1,100	2.66	[165]
	Quaternized Cotton	DI water	3-10	1,240	2.99	[166]
	Aminated rice husk	DI water	5	1,030	2.49	[167]
	MOF	DI water	5	500	1.2	[168]
	Magnetite NPs	DI water	7	62.5	0.15	[158]
PFOS	PAC	DI water	3	440	0.88	[159]
	GAC	DI water	5	1,160	2.32	[160]
	Polyacrylonitrile fiber-derived activated carbon fibers (PACFs)	DI water	5	760	1.52	[143]
	SWCNT	DI water	6	560	1.12	[161]
	SWCNT	DI water		710	1.42	[169]
	Polyaniline nanotubes (PANTs)	DI water	2-9	1,650	3.30	[165]
	Anion Exchange Resin (IRA67)	Actual WW	3	2,750	5.5	[170]
	Anion Exchange Resin (IRA67)	DI water	3	2,500	5.0	[171]
	Aminated polyacrylonitrile fibers (APANFs)	DI water	3	7,500	15.0	[154]
	Chitosan-based molecularly imprinted polymer (MIP)	DI water	3-10	1,460	3.53	[172]
	Crosslinked Chitosan	DI water	3	2,500	6.04	[173]
	Quaternized Cotton	DI water	3-10	1,750	3.50	[166]
	Aminated rice husk	DI water	5	1,330	2.65	[167]
	Porous aromatic framework (PAF-45)	DI water	3	5,850	11.7	[174]
	Magnetic fluorinated vermiculite	DI water	6	1,130	2.26	[153]

*PAC: Powdered activated carbon; GAC: Granular activated carbon; SWCNT: Single-walled carbon nanotubes; MOF: Metal organic framework; NPs: Nanoparticles; WW: Wastewater.

Membrane filtration, including ultrafiltration (UF), nanofiltration (NF), and reverse osmosis (RO) has been widely used in water and wastewater treatment processes. Previous research has shown that virtually complete removal of various PFASs can be accomplished by NF and RO membranes, while the removal of PFASs by NF membranes is varied depending on their physicochemical properties, such as hydrophobicity, functional groups, and carbon chain length.[175] The removal efficiency of PFAS by membranes can be also affected by other factors, including membrane properties, operating conditions, and water chemistries (pH, temperature, electrolytes, and natural organic matter (NOM)).

2.10 Abiotic degradataion of PFAS

Advanced treatment processes including photocatalysis, [176, 177] electrochemical oxidation, [178] sulfate radical−based advanced redox process, [179] thermal destruction,[180] biological treatment,[116] and other oxidative and reductive methods[181] have been proposed and evaluated to breakdown PFAS in aqueous systems. Additional processes, such as electron beam[182] and plasma,[183] have been also applied, providing high energy inputs/source and concentrated reactive radicals. Photocatalysis is the most explored process for PFAS degradation, as it generates free radicals for favorable (secondary) reactions. Further, photocatalytic techniques offer the advantages of simple operation under mild conditions, low energy requirement, high efficiency on degradation, and little to no secondary pollution. Despite the development of novel (photo)catalytic materials for PFAS degradation by a number of groups, there remains considerable research gaps regarding structure function relationships and fundamental understanding, including band gap, effective surface area, light sources, concentration of catalysts, and water chemistries among others.[184] Another promising method is based on electrochemical oxidation processes to form hydroxyl radicals from at the surface of an electrode during direct and/or indirect electrolytic process. This method has potential advantages as there is no use of additional (reactants) chemicals, and is scalable for larger volumes of water. Additionally, such processes can generate not only hydroxyl radicals, but also other oxidizing species, such as superoxide radical and hydroperoxyl radical, towards PFAS transformation.[185]

While various PFAS remediation technologies have been widely studied, such strategies are often energy intensive, “one size fits all” approaches, not allowing for flexibility (tenability) for a range of PFAS compounds and chemistries. For truly effective PFAS treatment under environmental conditions, multi−functionality is needed to achieve precise separation and transformation. In particular, there is considerable need (space) for technologies that can simultaneously concentrate (considering low environmental concentrations) and transform PFAS, which can also be rationally tuned to account for molecular structure(s) and PFAS chemistry. Toward this end, development and demonstration of organic−inorganic nanocomposites with a rational design of core and surface modification offer significant potential for PFAS remediation, both physical and chemical aspects.

3. Materials and Methods

3.1 Preparation of Multifunctional Nanoscale Sorbents for PFAS Treatment

3.1.1 Preparation of Organic (Surface) Functionalized IONPs

Iron oxide nanoparticles (IONPs) were synthesized by iron precursor decomposition at high temperature as described previously.[186] Synthesized NPs were then functionalized with different organic surfactants using probe sonication via ligand exchange and encapsulation methods.[187, 188] Branched PEI, CTAB, and OA were used as surface stabilizers. 0.4 mL of NPs in hexane solution was mixed with particular amounts of surface stabilizer in 5 mL of ultrapure water (18.2 MΩ·cm, Millipore) by applying a probe sonicator (UP50H, Hielscher) at 80% amplitude and full cycle for 10 min. The remaining hexane in solution was removed by putting the solution under the fume hood for 24 h. To remove excess surfactants the solution was filtered by ultrafiltration membrane (cellulose, 100kDa MWCO, Millipore) with stirring, followed by syringe filtration (0.22 μm PES, Millipore). The concentration of functionalized IONPs in water was measured by inductively coupled plasma mass spectroscopy (ICP-MS, Elan DRC-e, Perkin Elmer).

3.1.2 Batch Adsorption Isotherms

Engineered IONPs (10 mg/L NC) were tested for PFAS sorption in the range of 0.01 to 0.2 mmol/L of PFOA and 0.01 to 0.6 mmol/L of PFOS concentrations at different pH conditions (4.0, 7.0, and 10.0 ± 0.2). Solution pH was adjusted using HNO_3 and NaOH immediately after initiating sorption test, and further adjusted and/or confirmed again during the course of the experiment (after 4 h). At equilibrium (after 24 h), the NPs were separated using ultracentrifuge (Sorvall WX 80, Thermo Scientific) at 50,000 rpm for 2 h, and the remaining concentrations of PFAS were measured by ultra performance liquid chromatograph (UPLC−MS/MS) (Waters Corporation, Milford, MA). The detailed procedures for PFAS quantification are presented in the Supporting Information. The measured sorption density (mmol of adsorbed PFAS per mass of NPs in the sample) as a function of equilibrium concentration of PFAS (mmol/L) was fitted by both Langmuir and Freundlich sorption isotherms. The Langmuir isotherm was obtained by following equation:

$$q_e = \frac{q_{max} k C_e}{(1+kC_e)} \quad \textbf{(3.1)}$$

where q_e is sorption density at equilibrium (mmol/g), q_{max} is the maximum sorption density, k is Langmuir sorption constant (L/mmol), and C_e is equilibrium concentration of PFAS (mmol/L). And the Freundlich isotherm was determined as follow:

$$q_e = K C_e^{1/n} \quad \textbf{(3.2)}$$

where K and n are Freundlich sorption constants. Competitive sorption experiments were

conducted with the initial concentrations of both PFOA and PFOS from 0.02 to 0.1 mmol/L at pH 7. We adjusted solution pH twice, and other experimental conditions and procedures were identical to the single-sorbate sorption isotherm tests.

3.1.3 Quartz Crystal Microbalance with Dissipation (QCM−D)

We performed quartz crystal microbalance with dissipation (QCM-D, Q-sense E4, Biolin Scientific) measurements by frequency (f) and energy dissipation (D) of silica coated Q−sensor (QSX−303, Q−sense). The mass deposited on the crystal surface per unit area (Δm) was determined by measuring frequency shift of the crystal using Sauerbrey relationship as described below:

$$\Delta m = -\frac{C}{n}\Delta f_n \quad (\mathbf{3.3})$$

where C is the crystal constant (17.7 ng/(cm^2·Hz) for 5 MHz quartz crystal), n is the overtone number (1, 3, 5, 7, 9, 11, and 13), and Δf_n is frequency shift at overtone number n. Considering the stability of the instrument, we used third overtone for the analysis of data in this study. For all measurements, we maintained the flowrate of solutions at 0.1 mL/min and the temperature inside the unit at 20.0°C.

Real time frequency shifts were obtained to determine PFAS sorption isotherm on IONCs using QCM-D as following sequence. First, positively charged IONCs (PEI and CTAB coated) were introduced to quartz crystal sensor. We determined the maximum surface NC coverage by evaluating wide range of NC concentrations, as shown in Figure S4. Sensors were saturated with NCs (solution) for 20 min, and subsequently flowed with ultrapure water to stabilize and eliminate any loosely associated NCs to the Q-sensor. After stabilization, we introduced PFAS solutions, which showed additional frequency shifts regard to mass of PFAS attached to the IONCs on sensor. Sorption isotherm is determined from the deposited mass of PFAS and IONCs on the Q-sensor, which calculated from frequency shift through Sauerbrey equation.

To compensate the underestimation of sorption capacity in QCM−D measurement due to attachment of water molecules on the Q−sensor, we applied QCM−D correction factor for sorption density. We calculated the QCM−D correction factor as described below.

$$\text{QCM-D factor} = \frac{Mass\ of\ (NCs+Water)}{Mass\ of\ NCs} \quad (\mathbf{3.4})$$

The mass of sorbed water is calculated from the difference of volume between NC core size and hydrodynamic diameter by multiplying density of water.

The thickness of deposited layer was calculated by analyzing the recorded Δf and ΔD data through Voigt model.[189] The resulting thickness (δ) was obtained by equation below:

$$\delta = \sqrt{\frac{2\eta_0}{\omega\rho_0}} \quad (\mathbf{3.5})$$

where η is shear viscosity, ω is angular velocity ($\omega = 2\pi f$), and ρ is density.

3.1.4 IONP Column Studies

Column experiments were performed to quantify the adsorption of PFOA or PFOS by IONCs under dynamic flow conditions. A suspension of IONCs (20 mL at 145 mg/L) was mixed with 80 g of 40-50 mesh Ottawa sand and allowed to dry at 60°C for 48 h. The IONC-treated sand, which contained approximately 2.9 mg IONC, was then packed into a borosilicate glass column (2.5 cm i.d. × 10 cm length) in 1-cm increments, flushed with CO_2 gas for 1 h, and then saturated with degassed background electrolyte solution (10 mmol/L NaCl) at a flow rate of 1.0 mL/min. The resulting pore volume (PV) of the water-saturated columns was approximately 20.5 mL. Non-reactive tracer tests were performed after water saturation of each column by injecting 3.5 PVs of 10 mmol/L NaBr followed by 3.5 PVs of 10 mmol/L NaCl using a Chrome Tech P-010 isocratic pump (Apple Valley, MN) at a flow rate of 0.12 mL/min, which corresponds to a pore-water velocity of approximately 1 m/day. A schematic diagram of the column apparatus is shown in Figure S12.

To assess the ability of the IONC-treated sand to sequester PFOA and PFOS, aqueous solutions containing either PFOA (100 µg/L) or PFOS (100 µg/L) in 10 mmol/L NaCl were injected into the columns at a flow rate of 0.12 mL/min. After approximately 10 PV, the influent concentration of PFOA or PFOS was increased from 100 µg/L to 10 mg/L to determine to maximum adsorption capacity of the IONCs. Effluent samples were collected continuously using a Spectra/Chrom® CF-2 fraction collector (Spectrum Chemical Mfg. Corp., New Brunswick, NJ) to monitor for PFAS breakthrough. Effluent samples were filtered through 0.45 µm GE Healthcare Whatman™ GD/X Glass Micro Fiber (GMF) syringe filter (GE Healthcare, Chicago, IL) and diluted to an appropriate concentration range prior to analysis using a Waters Xevo™ TQ-S Micro triple quadrupole mass spectrometer (LC–MS/MS) as described in the Supporting Information.

3.1.5 Photocatalytic Oxidation Processes for PFOA Degradation

3.1.5.1 Preparation of TiO2/MOF Composite Materials

For encapsulation and/or incorporation of titanium dioxide (TiO_2) with zeolitic imidazolate framework (ZIF−8), *in−situ* incorporation of commercial TiO_2 nanoparticles (NPs) was applied during the synthesis procedure of ZIF−8. We mixed zinc nitrate solution (3.5 g of zinc nitrate hexahydrate (Zn) dissolved in 150 mL of methanol (Zn/MeOH solution)) with 2−methylimidazole solution (6.5 g of 2−methylimidazole (Hmim) dissolved in 150 mL of methanol (Hmim/MeOH solution)) at room temperature. And then desired amount of TiO_2 NPs were dispersed and sonicated in methanol, and the suspension was added slowly to the above synthetic reaction and kept for 24 h. Final products was washed using methanol by centrifuging, this procedure was followed by vacuum drying and storage for subsequent degradation experiments.

3.1.5.2 Surface Functionalization of Composite Materials

For *in−situ* incorporation of amine functional groups into the structure, mixed linker approach was employed.[190] Solution was prepared with 15 mmol of Hmim, 5 mmol of Bmim, and 5 mmol of sodium formate in 60 ml deionized (DI) water under magnetic stirring at 70ºC for 2 h until a clear solution formed. Then, the solution was left to cool down to room temperature. Later, 5 mmol of Zn was dissolved in 50 ml methanol and added into mixture of Hmim, Bmim, and sodium formate. Immediately after the addition of zinc nitrate hexahydrate, TiO_2 solution (dissolved in 15 ml methanol) was added into the mixture dropwise at an approximate rate of 1 ml/min. As the last step, the obtained particles were centrifuged (10,000 rpm, 17 min) and washed with DI water 3 times followed by vacuum drying and storage.

Various methods for amine functionalization were conducted with (1) methanol, (2) toluene, (3) ammonium hydroxide, and (4) solvothermal treatment applied after synthesis of composite materials. For amine functionalization with methanol method, 0.75 g of TiO_2/ZIF−8, synthesized prior to amine functionalization, was mixed with 20 ml of methanol. Then, 1 g of EDA was added to the suspension containing methanol and TiO_2/ZIF−8 particles. The obtained mixture was sonicated for 5 min, then mixed at 60 ºC for 20 h under constant stirring. Later, the solution containing amine-functionalized TiO_2/ZIF−8 particles was centrifuged (10,000 rpm, 17 min) and washed with DI water 3 times followed by vacuum drying and subsequent storage. For amine functionalization with toluene method, 0.75 g of TiO_2/ZIF−8, synthesized prior to amine functionalization, was mixed with 20 ml of toluene. Then, 1 g of EDA was added to the suspension containing toluene and TiO_2/ZIF−8 particles. The obtained mixture was sonicated for 5 min, then mixed at 107 ºC for 20 h under constant stirring. Later, the solution containing amine-functionalized TiO_2/ZIF−8 particles was centrifuged (10,000 rpm, 17 min) and washed with DI water 3 times followed by vacuum drying and subsequent storage. For amine functionalization through NH_4OH treatment, 1 g of TiO_2/ZIF−8, synthesized prior to amine functionalization, was added into 25 ml of NH_4OH (25 vol.%) solution with an additional 10 ml of DI water. The obtained suspension was sonicated for 1 h to break down the particles, then, was stirred at 1000 rpm for 24 h. Later, the solution containing amine-functionalized TiO_2/ZIF−8 particles was centrifuged (10,000 rpm, 17 min) and washed with DI water 3 times followed by vacuum drying and subsequent storage. Lastly, for solvothermal treatment method, 1 g of TiO_2/ZIF−8, synthesized prior to amine functionalization, was added into 30 vol.% EDA solution prepared in DI water (containing 2.5 ml EDA and 5.83 ml DI water). The obtained mixture was placed in a stainless steel high pressure autoclave for solvothermal reaction and kept at 144 ºC for 1 h, then, at 108 ºC for 6 h. Later, the solution containing amine functionalized TiO_2/ZIF−8 particles was centrifuged (10,000 rpm, 17 min) and washed with DI water 3 times followed by vacuum drying and subsequent storage.

3.1.5.3 Material Characterization

Characterization of the synthesized particles was conducted by various characterization techniques including X−ray diffraction (XRD), Fourier−transform infrared spectroscopy (FTIR), scanning electron microscopy (SEM), transmission electron microscopy (TEM), Ultraviolet–visible spectroscopy (UV−Vis). Crystalline structure was investigated by using Rigaku Miniflex 600 benchtop XRD instrument with a HyPix−400 MF 2D hybrid pixel array detector (HPAD) together with an available 600 W X−ray source. For the X−ray generator, Cu radiation source was utilized at 40 kV voltage and 40 mA current with a slit size of 10 mm. The diffraction data was collected between the 2θ range of 5−90°. Corresponding crystalline lateral size (La) and d-spacing values were calculated by using Scherrer Equation and Bragg's Law, respectively. FTIR analysis of each material was performed by using Bruker Vertex 80v IR spectrometer equipped with a platinum attenuated total reflection (ATR) cell. Spectral resolution of 2 cm^{-1} was used under atmospheric pressure and the spectra were collected between the wavelength of 4000−400 cm^{-1}. Data visualization was conducted with the help of OPUS software after compensating for atmospheric gasses, such as CO_2 and H_2O, and corrected by extended ATR modification. Morphology was analyzed by using Hitachi SU7000 ultra−high resolution Schottky SEM. Analyses were conducted under vacuum with an accelerating voltage of 15 kV and a working distance of 2−4 mm. TEM was utilized to investigate the resulting change in morphology and the location of TiO_2 NPs in the composite structure. UV−Vis analysis was performed by using Cary 100 (Agilent) to obtain the corresponding Tauc plots for energy band gap calculations. Data were collected between 800−200 nm.

3.1.5.4 Photocatalytic PFOA Degradation Tests

Photocatalytic experiments were conducted in a 100 mL of quartz vial, which is placed in the center of the reactor with stirring under irradiation of UV light (wavelength = 254 nm). The suspension contained 10 mg/L of initial PFOA solution and the initial solution pH was adjusted by HNO_3 and NaOH solutions. Prior to UV irradiation, the suspension was stirred in the dark for 30 min for the pre−adsorption. We collected samples at different reaction time, and measured the concentration of PFOA and byproducts using ultra performance liquid chromatograph coupled with mass spectrometer (UPLC−MS, Waters Corporation, Milford, MA) and fluoride concentration by ion chromatography (IC, 940 Professional IC Vario, Metrohm). To demonstrate the effect of different ROSs on PFOA degradation, we carried out the photocatalytic reaction in the presence of ethylenediaminetetraacetic acid (EDTA), superoxide dismutase (SOD), and tert-butanol (TBA) as ROS scavenging agents.

3.1.6 Electrochemical Oxidation Processes for PFOS Treatment

3.1.6.1 Preparation and Characterization of CNTs Coated Electrode

Referring to the procedures outlined in Scheme 1, we fabricated a large area CNT (8 × 2 cm^2) electrode using the chemical vapor deposition (CVD) process. Before initiating CNT growth, we

thoroughly cleaned the Ni foam by ultrasonication with HCl and methanol solutions, followed by drying in a vacuum oven to remove any remaining impurities. The cleaned Ni foam was then coated with platinum (Pt) as catalyst layer. The coated Pt/Ni foams were placed to CVD reactor for a straightforward thermal oxidation process. After H_2 and Ar carrier gases were initiated, with flow rates of 100 and 200 sccm respectively, the reaction chamber was thermally stabilized at a constant temperature of 700°C. At this precise temperature, the carbon precursor, acetylene (C_2H_2), was carefully introduced into the system, with a managed gas flow rate of 40 sccm. Once the chemical reaction was finished, the system quickly moved into a cooling phase.

The morphological features of carbon-based Ni foam (NF) electrodes were investigated using a high-resolution transmission electron microscope equipped with an energy dispersive X−ray spectroscope (HR−TEM, JEM−2100F, JEOL). The crystalline structures of the metal cores were analyzed through X−ray diffraction (XRD) patterns acquired from an X−ray diffractometer (Ultima III, Rigaku) with Cu Kα radiation (λ = 0.1541 nm). The defect density and crystalline structure of carbon shells were determined by Raman spectroscopy performed on a LabRam ARAMIS Raman spectrometer (Horiba Jobin-Yvon) with an argon ion laser (excitation at 514.5 nm). The oxidation states of NF film and carbon species was achieved through the use of X−ray photoelectron spectroscopy (XPS, K−alpha+, Thermo Fisher Scientific) with a Kα X−ray source (1486.7 eV). To evaluate the quantity of active sites and the electrochemically active surface area (ECSA) of carbon-based NF electrodes, we monitored their double layer capacitance (Cdl) at range of scan rates (from 10 to 400 mVs^{-1}) in a non-faradaic region, utilizing the cyclic voltammetry (CV) mode. Cdl was inferred from the linear regression plot, correlating the double layer current and the scan rate (Figure S6.).

3.1.6.2 Experimental Procedure and Analytical Methods

Electrochemical experiments were conducted utilizing 100 mL magnetically stirred, divided and undivided batch reactors, based upon a parallel−plate electrode configuration. The single compartment cell was assembled with a boron−doped diamond (BDD) serving as the anode, paired with an array of cathodes including Ni foam (NF), graphene−Ni foam (G−NF), nitrogen−doped graphene−Ni foam (NG−NF), and carbon nanotubes−Ni foam (CNTs−NF) electrodes. Each solution maintained a predetermined target concentration of 20 mg/L, predominantly compose of PFOS, and supplemented by 0.1 M Na_2SO_4 serving as the electrolyte. A direct current (DC) power supply (E3630, Keysight) was linked to a pair of electrodes, each measuring 2 cm × 6 cm of active area, with an inter−electrode distance set at 2 cm. This particular configuration allowed for the uninterrupted implementation of electrolysis at a consistent current density of 50 mA cm^{-2}. A stable pH level of 6.0 was maintained during electrochemical oxidation reactions by means of the abundant sulfate−based electrolyte, obviating the necessity for any buffering agents. At specified time intervals, 1 mL samples were meticulously extracted from the reactor and filtered through PTFE filters (Millipore). Subsequently, these samples were transferred to 2 mL glass vials containing a surplus of MeOH. The surplus of methanol (MeOH) plays a crucial role in preventing

the undesired further oxidation of organic compounds by potentially residual radicals. To investigate PFOS degradation in the separate anodic and cathodic compartments, a two-chamber electrochemical system with 50 mL per compartments was used, with a cation exchange membrane separating the cathode and anode. Quenching experiments were conducted to analyze the role of surface−bound sulfate radicals. In these procedure, two distinct groups of quenching agents were used at an excess amount of concentration (200 mM). The first group, classified as hydrophilic scavengers, comprised agents included methanol (MeOH), tert−butyl alcohol (t−BuOH), and thiosulfate. The second group, identified as hydrophobic chemicals, included DMSO, alginate, and humic acid (HA). These agents were introduced into electrochemical oxidation system to evaluate their respective impacts. The concentrations of PFOS was monitored using a Vanquish Flex UHPLC connected to a TSQ Quantis triple quadrupole mass spectrometer (UHPLC−MS, Thermo). This system was equipped with a PFAS delay column (Thermo Hypersil Gold Vanquish C18 column, 1.9 μm dia., 3 x 50 mm^2). The mobile phase for the UHPLC−MS consisted of a binary mixture of ammonium acetate (5 mM) in water and ammonium acetate (5 mM) in methanol, as referenced in McCord's method[191]. Peroxydisulfate (PDS), generated through anodic oxidation in sulfate−based electrolytes, was precisely quantified utilizing a colorimetric method. This technique effectively facilitates the spectrophotometric analysis of iodine, which results from the persulfate−induced oxidation of iodide and can be detected at a wavelength of 352 nm[192]. To examine the influence of pH fluctuations on PFOS removal during the electrolysis process, the zeta potentials of the CNT materials harvested from the electrode were analyzed regarding their pH responsiveness using a zeta potential and particle size analyzer (ELSZ−1000, Otsuka Electronics Co). To identify the reactive radical intermediates involved in the organic oxidation mechanism, electron paramagnetic resonance (EPR) spectra were obtained from anodic oxidation and CNTs−NF cathode along with PDS addition (10 mM) in divided cell, including electrochemical involvement. These procedures were undertaken in the presence of 5,5−Dimethyl−1−pyrroline N−oxide (DMPO), serving as a spin trap, employing a JEOL JES-TE 300 spectrometer. The operating parameters engaged encompassed a microwave power setting of 0.998 mW, a microwave frequency of 9.415 GHz, a center field intensity of 335 mT, a modulation width of 0.2 mT, and a modulation frequency of 100 kHz.

3.2 Biotransformation Experiments

3.2.1 Chemicals and Materials

Nonafluorobutane-1-sulfonic acid (PFBS) 97%, heptafluorobutrycic acid (PFBA) 98%, perfluoropentanoic acid (PFPeA) 97%, tridecafluorohexane-1-sulfonic acid potassium salt (PFHxS) >98%, undecafluorohexanoic acid (PFHxA) >97%, perfluoroheptanoic acid (PFHpA) 99%, heptadecafluorooctanesulfonic acid potassium salt (PFOS) >98%, perfluorooctanoic acid (PFOA) 95%, perfluorononanoic acid (PFNA) 97%, and perfluorodecanoic acid (PFDA) 98%, PCE 99% extra pure, and TCE >99.5% were purchased from Sigma Aldrich (St. Louis, MO) or VWR (Randor, PA).

Porous media used in microcosm experiments consisted of surficial soils collected at Loring Air Force Base (Aroostook County, ME) in October 2017 (**Table 3.1**). This location, approximately 30 m northeast of the Crash Fire Station, had been impacted by PFAS from AFFF with measured concentrations of 3.57 mg/kg PFOS, 0.015 mg/kg PFOA, and 0.001 mg/kg PFBS. The soil has an organic carbon content of 3.5 ± 0.17%, pH of 7.2 ± 0.2, and a cation exchange capacity (CEC) of 18.7 ± 0.0 meq/100 grams soil. This soil is composed of 53.1 ± 3.1 sand, 32.7 ± 2.3% silt, and 14.2 ± 0.8% clay based on particle size distribution.

Table 3.1 Physical and chemical properties of Robins, Loring, and Hudson soils.

	Robins AFB soil	Loring AFB soil	Hudson soil
Sand, Silt, Clay (%)	77.5 ± 1.3, 5.6 ± 1.0, 16.9 ± 0.3	53.1 ± 3.1, 32.7 ± 2.3, 14.2 ± 0.8	15.6 ± 3.1, 68.3 ± 1.7, 16.1 ± 1.4
USDA Textual Class	Sandy Loam	Loam/Sandy Loam	Silt Loam
CEC (meq/100 grams)	2.8 ± 0.5	18.7 ± 0.0	14.7 ± 1.1
Organic Carbon (%)	0.6 ± 0.1	3.5 ± 0.1	1.1 ± 0.0
Moisture Content (%)	7.0 ± 0.1	24.1 ± 1.1	13.8 ± 0.6
pH (1-part soil: 1-part deionized water)	5.1 ± 0.1	7.2 ± 0.2	6.5 ± 0.0

Federal Fine Ottawa sand (FF sand; 30-140 mesh) was purchased from U.S. Silica Company (Berkeley Spring, WV) with an organic carbon (OC) content of < 0.1 mg/g, a mean grain size of 0.32 mm, and an intrinsic permeability of 4.2×10^{-11} m^2. The FF sand was selected as a solid phase in the columns to represent a high permeability, low adsorption capacity aquifer material. Two sorbents, IONPs and S-PAC, were developed previously and demonstrated to be materials with high PFOA/PFOS adsorption capacity. Detailed description and preparation of these two sorptive materials are provided in previous studies [35, 36].

The aqueous phase in the batch reactors and microcosms (**Section 3.2**), and the background solution used in column experiments (**Section 3.3**) consisted of an anoxic growth medium [193], modified to reduce total ionic strength from 102.7 mM to 19.9 mM to prevent PFOS precipitation

(PFOS solubility is affected by salt concentration) [194]. Specifically, the concentration of 100X salts solution was reduced to 12.5% of the original concentration; the concentration of the sodium bicarbonate buffer was reduced from 30 mM to 10 mM; and the concentrations of trace element solution, Se/Wo solution, L-cysteine, and sodium sulfide were reduced by 50% each. The medium was prepared with 5 mM lactate as the fermentable electron donor substrate and carbon source. Sodium sulfide nonahydrate (Fisher Scientific; Hampton, NH) and L-cysteine (Sigma Aldrich; St. Louis, MO) were used as reductants to maintain anoxic conditions and sodium DL-lactate solution, 60% w/w (Sigma Aldrich; St. Louis, MO) was used as an electron donor. Aqueous solutions were prepared in deionized water produced by a Milli-Q® Integral Water Purification System (EMD Millipore; Burlington, MA).

3.2.2 Batch reactor and microcosm experiments

3.2.2.1 Reactor and microcosm preparation

A total of 30 batch reactor experiments (without porous media) and 35 microcosm experiments (with porous media) were completed under the conditions detailed in **Table 3.2** and **Table 3.3**. Both experiments were performed in 160 mL glass serum bottles capped with butyl rubber stoppers and aluminum crimp caps (Chemglass Life Sciences; Vineland, NJ) and prepared at room temperature in an anaerobic chamber with a 97% N2/3% H2 atmosphere (Coy Laboratory Products; Grass Lake, MI). Batch reactors were prepared with 120 mL of aqueous volume; microcosms were prepared with 100 mL of aqueous volume and 14.7–18.6 g (wet weight, 21.2 ± 2.21% moisture content) of porous media. The aqueous phase used in the batch reactors and microcosms were detailed in **Section 3.2.1.**

Table 3.2 Batch reactor experiments, identified by the target initial total PFAA concentration.

Total PFAA concentration (mg/L)	Replicate Number	Type	Initial aqueous mass (g)	Initial solid mass (g)	Inoculated (Y/N)	Sterilized (Y/N)
0	1	Positive Control	124	0.0	Y	N
0	2	Positive Control	124	0.0	Y	N
0	3	Positive Control	124	0.0	Y	N
0	A1	Abiotic Control	124	0.0	N	Y
0	A2	Abiotic Control	123	0.0	N	Y
12	1	Bioaugmented	124	0.0	Y	N
12	2	Bioaugmented	124	0.0	Y	N
12	3	Bioaugmented	125	0.0	Y	N
12	A1	Abiotic Control	125	0.0	N	Y
12	A2	Abiotic Control	122	0.0	N	Y
27	1	Bioaugmented	125	0.0	Y	N
27	2	Bioaugmented	123	0.0	Y	N

27	3	Bioaugmented	123	0.0	Y	N
27	A1	Abiotic Control	124	0.0	N	Y
27	A2	Abiotic Control	124	0.0	N	Y
50	1	Bioaugmented	122	0.0	Y	N
50	2	Bioaugmented	123	0.0	Y	N
50	3	Bioaugmented	123	0.0	Y	N
50	A1	Abiotic Control	124	0.0	N	Y
50	A2	Abiotic Control	121	0.0	N	Y
62	1	Bioaugmented	130	0.0	Y	N
62	2	Bioaugmented	126	0.0	Y	N
62	3	Bioaugmented	125	0.0	Y	N
62	A1	Abiotic Control	126	0.0	N	Y
62	A2	Abiotic Control	127	0.0	N	Y
101	1	Bioaugmented	120	0.0	Y	N
101	2	Bioaugmented	122	0.0	Y	N
101	3	Bioaugmented	123	0.0	Y	N
101	A1	Abiotic Control	123	0.0	N	Y
101	A2	Abiotic Control	123	0.0	N	Y

Table 3.3 Microcosm experiments, identified by the average final PFAA concentration.

Total PFAA concentration (mg/L)*	Replicate Number	Type	Initial aqueous mass (g)	Initial solid mass (g)	Inoculated (Y/N)	Sterilized (Y/N)
0	1	Bioaugmented	103	15.1	Y	N
0	2	Bioaugmented	104	15.4	Y	N
0	3	Bioaugmented	104	15.5	Y	N
0	N1	Native Microbes	103	15.0	N	N
0	N2	Native Microbes	103	16.3	N	N
0	N3	Native Microbes	102	14.8	N	N
0	I1	Inactive Control	103	16.9	N	Y
0	I2	Inactive Control	102	16.9	N	Y
9	1	Bioaugmented	103	16.0	Y	N
9	2	Bioaugmented	103	15.6	Y	N
9	3	Bioaugmented	102	16.2	Y	N
9	N1	Native Microbes	104	16.1	N	N

9	N2	Native Microbes	104	15.1	N	N
9	N3	Native Microbes	104	14.7	N	N
9	I1	Inactive Control	102	18.6	N	Y
9	I2	Inactive Control	104	15.5	N	Y
19	1	Bioaugmented	101	15.9	Y	N
19	2	Bioaugmented	102	15.4	Y	N
19	3	Bioaugmented	104	14.9	Y	N
19	I1	Inactive Control	103	16.7	N	Y
19	I2	Inactive Control	104	16.3	N	Y
39	1	Bioaugmented	102	15.0	Y	N
39	2	Bioaugmented	104	16.7	Y	N
39	3	Bioaugmented	103	15.4	Y	N
39	I1	Inactive Control	105	17.5	N	Y
39	I2	Inactive Control	103	15.0	N	Y
91	1	Bioaugmented	101	16.3	Y	N
91	2	Bioaugmented	102	18.1	Y	N
91	3	Bioaugmented	103	15.9	Y	N
91	I1	Inactive Control	103	17.4	N	Y
91	I2	Inactive Control	102	15.2	N	Y
0	PC1	Positive Control	120	0.0	Y	N
0	PC2	Positive Control	120	0.0	Y	N
0	PC3	Positive Control	120	0.0	Y	N
0	I1	Inactive Control	120	0.0	N	Y
0	I2	Inactive Control	120	0.0	N	Y

Batch reactors and microcosms were bioaugmented with KB-1® (SiREM; Guelph, ON), a microbial consortium capable of reductively dechlorinating PCE to ethene. The inoculum contains the dechlorinating microorganisms *Geobacter sp*. (*Geo*) and multiple strains of *Dhc*, fermenters, and other anaerobic bacteria, which act synergistically to support MRD [33]. Four bottles, containing 100 mL of KB-1 inoculum were provided by SiREM for use in these experiments. Samples from each bottle were collected and analyzed to determine initial cell and gene abundance, including initial *Dhc* 16S rRNA, and *Geobacter lovleyi* strain SZ (*GeoSZ)* 16S rRNA, *tceA* RDase, *vcrA* RDase, and *bvcA* RDase (**Table 3.4**), using a Step One Plus Real-Time polymerase chain reaction (PCR) System (Applied Biosystems; Foster City, CA). Detailed procedures of PCR analyses are provided in **Appendix A.1**.

Table 3.4 Initial gene abundances for inoculum bottles used in batch reactor and microcosm experiments. All values shown as gene copies/mL. Average and standard deviations for three samples of each inoculum with each sample measured in triplicate. Batch reactor experiments

inoculated with 3 mL each from bottles 1 and 2 and microcosm experiments inoculated with 6mL from bottle 3 or bottle 4.

Inoculum Bottle #	Average *GeoSZ 16S rRNA* abundance (±st.dev)	Average *Dhc 16S rRNA* abundance (±st.dev)	Average *tceA* abundance (±st.dev)	Average *vcrA* abundance (±st.dev)	Average *bvcA* abundance (±st.dev)
1	1.95×10^{8} ($\pm7.90\times10^{7}$)	1.47×10^{8} ($\pm9.69\times10^{7}$)	1.39×10^{7} ($\pm6.20\times10^{6}$)	3.09×10^{7} ($\pm1.23\times10^{7}$)	2.92×10^{7} ($\pm1.12\times10^{7}$)
2	3.63×10^{8} ($\pm2.34\times10^{8}$)	1.65×10^{8} ($\pm1.25\times10^{8}$)	1.66×10^{7} ($\pm9.30\times10^{6}$)	3.70×10^{7} ($\pm1.74\times10^{7}$)	3.72×10^{7} ($\pm1.62\times10^{7}$)
3	2.88×10^{10} ($\pm1.06\times10^{10}$)	9.93×10^{6} ($\pm6.07\times10^{6}$)	5.28×10^{6} ($\pm2.09\times10^{6}$)	1.59×10^{7} ($\pm8.01\times10^{6}$)	1.34×10^{7} ($\pm1.80\times10^{7}$)
4	6.35×10^{10} ($\pm2.00\times10^{10}$)	2.79×10^{7} ($\pm1.39\times10^{7}$)	1.44×10^{6} ($\pm7.11\times10^{5}$)	5.32×10^{7} ($\pm3.09\times10^{7}$)	1.60×10^{6} ($\pm7.11\times10^{5}$)

All batch reactor experiments were inoculated with 3 mL of inoculum from bottle 1 and 3 mL of inoculum from bottle 2. Microcosms containing total final PFAA concentrations of 9.52 mg/L, 19.4 mg/L, and 38.7 mg/L were inoculated with 5 mL of inoculum from bottle 4. Microcosms containing a final PFAA concentration of 86.3 mg/L were inoculated with 5 mL of inoculum from bottle 3. Two microcosms containing 0 mg/L total PFAAs were inoculated with 5 mL of inoculum from bottle 4 and one was inoculated with 5 mL of inoculum from bottle 3. In order to assess the dechlorinating capability of the microbial community in the porous media collected from the Loring Air Force Base, six microcosm experiments were prepared with the same soil and aqueous phase as other microcosms but were not bioaugmented. Three bottles were prepared without PFAAs and three were prepared with the same PFAA solution as the 9.25 mg/L total PFAA concentration microcosms.

In contrast to previous work that explored *Dhc* strain 195 MRD in the presence of an equal component mixture of 11 PFAAs [103], this study used a commercially available dechlorinating consortium and a mixture of 10 PFAAs, at concentration ratios approximating those measured in groundwater at the fire training area at the Loring Air Force Base (**Table 3.5)**. The ratios of PFAAs in the experiments had to be adjusted from those measured at the Air Force Base because of potential precipitation of PFOS at high concentrations. When PFOS was added to the PFAS mixture at concentrations above 25 mg/L (0.050 mM), its measured concentration was lower than the mass added, attributed to precipitation of PFOS from the growth medium. To prevent PFOS concentrations from exceeding 25 mg/L (0.050 mM) at the highest mixture concentrations, its proportion of the total PFAS mass was reduced from the 44.3% observed at the site to 15-20% and the proportions of other compounds were increased (**Table 3.5**).

Table 3.5 Composition of PFAA Mixture in Batch Reactor Experiments

PFAA	% total PFAAs (by mass) in Loring AFB Overburden	Average % total PFAAs (by mass) in Batch Reactors	Average % total PFAAs (by mass) in Microcosms (initial)	Average % total PFAAs (by mass) in Microcosms (Final)
PFBS	0.43%	5.67%	4.42%	4.93%
PFBA	3.74%	6.41%	10.3%	10.9%
PFPeA	13.3%	14.9%	18.2%	18.8%
PFHxS	14.5%	17.9%	14.0%	14.6%
PFHxA	10.2%	10.7%	18.8%	18.8%
PFHpA	5.20%	6.30%	6.16%	6.57%
PFOS	44.3%	22.7%	15.1%	12.3%
PFOA	7.02%	9.33%	8.57%	9.01%
PFNA	1.13%	3.45%	3.24%	3.45%
PFDA	0.17%	2.59%	1.08%	0.66%

PFAA stock solution with a total concentration of 101-122 mg/L was prepared by dissolving 10 PFAAs in pre-prepared medium. The stock solution was used for 6 sets of 5 batch reactors containing initial measured concentrations of 101 mg/L, 61.7 mg/L, 49.8 mg/L, 26.5 mg/L, 11.7 mg/L, and 0 mg/L total PFAAs (**Table A.2**, **Figure A.1**), to achieve a range that encompassed the 66 mg/L total PFAA concentration previously shown to impact *Dhc* strain 195 [103]. Reactors were amended with 15 mL of low salts medium containing PCE and TCE to achieve average initial concentrations of 6.5 (± 0.66) mg/L (0.039 [± 0.004] mM) PCE and 24 (± 2.6) mg/L (0.18 [± 0.02] mM) TCE. For the highest PFAA concentration reactors, the PCE/TCE solution was prepared in medium containing 101 mg/L PFAAs to maintain the target PFAA concentrations. Reactors were also amended with 0.6 mL of 200x Wolin vitamin[58] solution to provide nutrients, including vitamin B_{12}, necessary for dechlorinating microorganisms [195]. In each set of 5 batch reactors, 3 were bioaugmented with 6 mL of KB-1® inoculum (SIREM; Guelph, ON) containing the gene abundances shown in **Table 3.5**, while 2 received 6 mL of low salts growth medium and were sterilized via autoclave (liquid cycle at 121 °C) as abiotic controls.

Microcosms were prepared similarly with initial measured concentrations of 119.8 mg/L, 53.5 mg/L, 25.9 mg/L, 12.8 mg/L, and 0 mg/L total PFAAs (**Table A.2**, **Figure A.2**) with PFAA proportions given in **Table 3.5** Composition of PFAA Mixture in Batch Reactor Experiments. Negative control microcosms were not autoclaved; instead, 10 mg/L of sodium azide was added to establish bacterial-static conditions for native soil microbial community [196]. An additional six microcosms were prepared without bioaugmentation and without sodium azide to assess the

dechlorinating capability of the native microbial population. Three of these reactors were prepared with 12.8 mg/L PFAS and three were prepared without PFAAs. Hereafter, microcosms are referred to by the final measured PFAA concentrations because aqueous concentrations decreased as described in **Section 4.1.3** and shown on **Figure A.2**. The pH in batch reactors averaged 7.02 (± 0.28) and the pH in microcosms averaged 7.14 (± 0.092), see **Figure A.3**.

3.2.2.2 Sampling batch reactors and microcosms

All reactors were stored inverted so that only the aqueous phase was in contact with the rubber stopper, except during sampling. Every 2 to 7 days, 1.0-2.5 mL samples were collected from each reactor using a sterile 25-gauge needle and polypropylene syringe (Becton, Dickinson and Company; Franklin Lakes, NJ). During several sampling events (4 for batch reactors and 3 for microcosms), an additional 3.0 mL sample was collected for pH analysis. Prior to sampling, 1.0-3.0 mL of nitrogen gas was injected to maintain positive atmospheric pressure in the bottles. The change in aqueous volume due to sampling was considered in numerical modeling. All experiments were sampled concurrently so changes in partitioning between the gas and aqueous phase were consistent regardless of experimental setup. Abiotic and inactivated reactors were sampled concurrently with bioaugmented reactors to identify any potential effects of sampling on measured concentrations.

Sample aliquots of 1.0 mL were analyzed for chlorinated ethenes and ethene using an Agilent 7890B gas chromatography system with flame ionization detection (GC-FID) equipped with a DB-625 column (Agilent Technologies; Santa Clara, CA). Additional sample aliquots of 1.0 mL were prepared for future DNA extraction and qPCR analysis by centrifugation as described in **Appendix A.1**. After centrifugation, the aqueous phase was analyzed for volatile fatty acid (VFA) and fluoride ion using a Dionex ICS-2100 ion chromatography (IC) system with IonPac AS-18 Fast column (Thermo Scientific; Waltham, MA). The remaining 0.5 mL sample volume was analyzed for PFAA concentrations using a Waters Acquity ultra high-performance liquid chromatograph with a Waters Xevo TQ-S triple quadrupole mass spectrometer (LC/MS-MS). Samples for PFAS analysis were placed in 15 mL HDPE bottles containing 9.5 mL of 4M equivalent sodium hydroxide (20:1 dilution) and stored at 4°C prior to analysis. At the time of analysis, samples were further diluted into an 80:20 water:methanol solution as necessary to ensure that the expected concentration fell within the calibration range of the analytical instrument (10-10,000 ng/L). Detailed procedures of GC-FID, IC, and LC-MS/MS analyses are provided in **Appendix A.2.**

3.2.2.3 Rate and statistical analysis for MRD in batch reactors

A numerical model, implemented in SciPy [197], was formulated to simulate MRD in batch reactors using the following mass balance equation [198, 199]:

$$\frac{d}{dt}\left(V^a C_i^a\right) + \frac{d}{dt}\left(V^g C_i^g\right) = V^a R_i^b + R_i^s \qquad \textbf{(3.6)}$$

where i corresponds to PCE, TCE, *cis*-DCE, VC or ethene, t is time, V^a and V^g are the aqueous and gaseous phase volumes [L^3], respectively, C_i^a and C_i^g are the aqueous and gaseous phase concentrations [M/L^3], respectively, R_i^b is the overall MRD reaction rate [$M/L^3/T$], and R_i^s is the mass transfer rate [M/T] between the reactor aqueous and gaseous phases and between the reactor aqueous phase and the stopper. Typical of other MRD models [200], it was assumed that partitioning between aqueous and gaseous phases conformed to Henry's law and MRD was governed by Monod kinetics. The change in aqueous volume due to sampling was also incorporated into the numerical model. See **Appendix A.3** for model details.

Model fitting was performed with a weighted least squares maximum likelihood method (see **Appendix A.3.1**) [201]. The model was first fit simultaneously to the triplicate, bioaugmented batch reactors without PFAAs (biotic controls) to estimate Monod kinetic parameters. The model was then individually fit to each batch reactor triplicate set containing PFAAs. During the individual fitting, all Monod kinetic parameters except the maximum substrate utilization rates ($k_{max,i}$) were held constant to the biotic control best-fit values. This fitting yielded multiple $k_{max,i}$ estimates for each PFAA concentration tested, enabling statistical inference regarding the PFAA concentrations at which MRD is significantly inhibited. The $k_{max,i}$ for each compound represents the maximum rate at which each *Geobacter* or *Dhc* cell can affect reductive dechlorination of a specific species *i*, provided there is a sufficient concentration of growth substrates in solution. See **Appendix A.3.1** for additional details on the kinetic parameters used in the model. A one-sided student's t-test was used to determine if the mean $k_{max,i}$ of reactors with a certain PFAA concentration was equal to (null hypothesis) or less than (alternative hypothesis) the mean $k_{max,i}$ of reactors without PFAAs.

3.3 Permeable Adsorptive Barrier Experiments

3.3.1 Stabilized Powdered Activated Carbon (S-PAC) Batch and Column Studies

3.3.1.1 Materials

PFOA and PFOS standards (>99% purity) were purchased from Wellington Laboratories (Ontario, Canada) for use as calibration standards. Perfluoro-n-[1,2,3,4-$^{13}C_4$]-octanoic acid and sodium perfluoro-1-[1,2,3,4-$^{13}C_4$]-octanesulfonate were also purchased from Wellington Labs (>99% purity) to serve as internal standards. PFOS potassium salt (98% purity) and PFOA (96% purity) were purchased from Sigma-Aldrich (St. Louis, MO) for preparation of aqueous solutions. PolyDADMAC (40% active ingredient, molecular weight ~240,000 Da) was purchased from Accepta (Manchester, United Kingdom). DARCO® 100 mesh (< 149 μm) PAC was purchased from Sigma-Aldrich (St. Louis, MO). Ottawa sand (40-50 mesh) was selected as a solid phase for this study to represent a high permeability, low adsorption capacity aquifer material. The 40-50 mesh size fraction (300 – 420 μm) was obtained by sieving F-50 Ottawa sand (U.S. Silica, Berkeley Springs, WV) for 10 min cycles with a Model RX-29 Ro-Tap sieve shaker (W.S. Tayler, Inc., Mentor, OH). The 40-50 mesh size fraction was then used in column studies without further treatment (e.g., acid washing). Aqueous solutions were prepared with deionized (DI) water (18.2 MΩ cm^{-1}, total OC <5 μg/L) that had passed through a Milli-Q® Reference Water Purification System equipped with a LC-Pak™ Point-of-Use Polisher from a Milli-Q® System (Millipore-Sigma, Burlington, MA).

3.3.1.2 S-PAC batch adsorption tests

For batch adsorption tests, 2 or 10 mL of S-PAC (2 or 10 mg as PAC) was combined with either PFOA or PFOS in 10 mM NaCl (to minimize dispersion of fines) in 35 mL Corex glass centrifuge tubes (Kimble Chase, Vineland, NJ) to achieve concentrations ranging from 0 to 400 mg/L. Tubes were prepared in triplicate with controls at the same PFAS concentration without PAC and blanks containing only PAC and 10 mM NaCl. The contents of tubes were then mixed for 96 h on a rotary shaker. The mixing time was selected based on previous studies that have evaluated PFAS adsorption on activated carbon [29, 202-207]. After mixing, the tubes were allowed to settle for 1 h and the supernatant was transferred to a polypropylene centrifuge tube and separated at 4,000 rpm for 30 min. A 1 mL aliquot was then filtered through 0.45μm GE Healthcare Whatman™ GD/X Glass Micro Fiber (GMF) syringe filters and diluted prior to analysis.

3.3.1.3 S-PAC column studies

Based on a series of preliminary stability tests, 1,000 mg/L PAC + 5,000 mg/L polyDADMAC were combined and sonicated in a Fisherbrand™ CPX3800 ultrasonic bath at power level high for 24 h to prepare stable aqueous suspensions of S-PAC. Sonication served to reduce the size of the PAC and promote the formation of a stable suspension. Column experiments were performed to assess the delivery and retention of PAC within the column, and to quantify the sorption of PFOA or PFOS under dynamic conditions following the S-PAC treatment. The columns consisted of

borosilicate glass with dimensions of 2.5 cm (i.d.) × 10 cm (length). After packing with air-dried 40-50 mesh Ottawa sand, the columns were flushed with CO_2 gas for 1 h, and then saturated with 10 pore volumes (PV, where 1 PV ~ 30 mL) of electrolyte solution (10 mM NaCl) at a flow rate of 1.0 mL/min. Non-reactive tracer tests were performed by injecting 3.5 PV of 10 mM NaBr followed by 3.5 PV 10 mM NaCl using a Chrome Tech P-010 isocratic pump (Apple Valley, MN). Effluent samples were collected continuously, and bromide concentrations were measured using a bromide probe (Cole Parmer, Vernon Hills, IL). A schematic diagram of the column apparatus is shown in **Figure 3.1**.

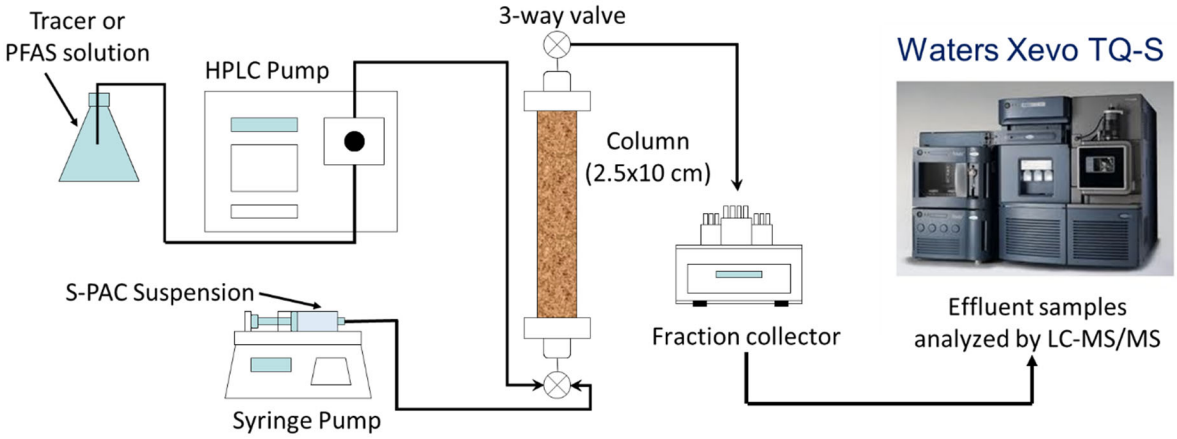


Figure 3.1 Schematic diagram of the experimental system used for the S-PAC column studies.

To assess the delivery and retention of S-PAC, a pulse (3.5 PV) of S-PAC suspension (1,000 mg/L PAC + 5,000 mg/L polyDADMAC) was introduced into a column containing water-saturated 40-50 mesh Ottawa sand at a flow rate of 0.12 mL/min using a Chemyx Nexus 3000 syringe pump (Stafford, TX), which was followed by flushing with 10 mM NaCl at the same flow rate to remove unretained PAC and polyDADMAC. Transport and retention of PAC was observed visually, and solid samples were collected at the conclusion of each experiment to measure the amount of retained PAC by carbon analysis. Baseline transport behavior of PFOA and PFOS in untreated 40-50 mesh Ottawa sand (negative control) was evaluated in a set of preliminary column studies by introducing a pulse (3.5 PV) of the PFOA or PFOS (100 µg/L) in 10 mM NaCl at a flow rate of 0.12 mL/min (pore-water velocity ~1 m/day), followed by a pulse (3.5 PV) of 10 mM NaCl. Aqueous solutions containing either PFOS (100 µg/L) or PFOA (100 µg/L) and a background electrolyte (10 mM NaCl) were then injected into separate columns that had been treated with S-PAC at a flow rate of 0.12 mL/min. After approximately 20 PV, the influent concentration of PFOA or PFOS was increased from 100 µg/L to 20 mg/L to determine to maximum retention capacity of the treated sand. Effluent samples were collected continuously to monitor for PFOA and PFOS breakthrough. At the completion of each column experiment, sand was removed in 5 sections of approximately 20 g each and analyzed for total carbon to obtain a PAC retention profile.

Changes in pressure between the column inlet and outlet were measured using a pressure transducer (Omega PX30-030GV, Norwalk, CT) connected to a digit multimeter (Keithley 2110, Beaverton, OR) and calibrated using five water column heights (0 to 1 m). All column experiments were conducted at room temperature (22 ± 1 ºC) in duplicate or triplicate to confirm reproducibility.

3.3.1.4 Analytical methods

The carbon content of dried sand collected at the conclusion of each column study was measured using a Shimadzu total organic carbon analyzer equipped with a solid sample module (TOC-SSM, Columbia, MD). Bromide concentrations in aqueous samples collected from column and aquifer cell studies were quantified using a bromide specific probe (Cole Parmer, Vernon Hills, IL) using a 5-point standard curve. The hydrodynamic diameter of stabilized PAC was measured by dynamic light scattering (DLS) using a Zetasizer Nano ZS Analyzer (Malvern Instruments Ltd., Southborough, MA) operated in back-scattering mode at an angle of 173º. To obtain scanning electron microscopy (SEM) images of Ottawa sand before and after S-PAC treatment, grains of sand were dried at 80 ℃ for 24 h and mounted on carbon adhesive tabs and attached to aluminum mounts (Electron Microscopy Sciences, Hatfield, PA). The mounted samples were sputtered with gold for 5 min and imaged on a Zeiss Leo 1530 VP SEM coupled with an Oxford Instruments 7426 Energy Dispersive Spectrometer (EDS) system.

3.3.2 Stabilized Ion Exchange Resin (S-IXR) Batch and Column Studies

3.3.2.1 Materials

Analytical PFAS standards (>99% purity) including PFOS, PFOA, PFNA, PFHxS, PFHpA and PFBS were purchased from Waters (Milford, MA) for use as calibration standards. Perfluoro-n-[1,2,3,4-$^{13}C_4$]-octanoic acid and sodium perfluoro-1-[1,2,3,4-$^{13}C_4$]-octanesulfonate were purchased from Wellington Labs (>99% purity) to serve as internal standards. PFOS potassium salt (98% purity), PFOA (96% purity), PFNA (97% purity), PFHxS potassium salt (98% purity), PFHpA (99% purity), and PFBS potassium salt (98% purity) were purchased from Sigma-Aldrich (St. Louis, MO) for preparation of aqueous solutions. Physicochemical properties of the PFAS used in this study are provided in **Table 3.6**. Ottawa sand (40-50 mesh) was selected as the solid phase to represent a relatively high permeability, low adsorption capacity aquifer material. The 40-50 mesh size fraction was obtained by sieving F-50 Ottawa sand (U.S. Silica, Berkeley Springs, WV) for 10-min cycles with a Model RX-29 Ro-Tap sieve shaker (W.S. Tayler, Inc., Mentor, OH). Aqueous solutions were prepared with deionized (DI) water (18.2 MΩ cm^{-1}, total OC <5 µg/L) that had passed through a Milli-Q® Reference Water Purification System (MilliporeSigma, Burlington, MA).

Pluronic® F-127 and Amberlite® IRA910 anionic exchange resin in the chloride form were purchased from Sigma-Aldrich. The preparation procedure for the polymer stabilized ion exchange resin suspension (S-IXR) consisted of the following three steps: (a) Amberlite® IRA910 beads were placed in stainless-steel vials and subjected for ball-mill grinding (SPEX SamplePrep,

Metuchen, NJ) for 30 min; (b) ground beads (5,000 mg/L) were transferred to a Vanaheim KB64 blender (Vanaheim, City of Industry, CA) and mixed with 1,500 mg/L Pluronic® F-127 in 10 mM NaCl at 18,000 rpm for 30 min; and (c) the mixture was then sonicated for 30 min in a Fisherbrand™ CPX3800 ultrasonic bath to obtain the final S-IXR suspension.

Table 3.6 Properties of PFAS used in S-IXR experiments.

Compound name	Acronym	Formula	MW (g/mol)	Aqueous Solubility (mg/L) [208]	Log Kow [209]	pKa [210]
Perfluorobutane sulfonic acid	PFBS	$C_4F_9SO_3H$	300.095	344	0.03	0.14
Perfluoroheptanoic acid	PFHpA	$C_6F_{13}COOH$	364.062	3.65	0.03	-2.29
Perfluorohexane sulfonic acid	PFHxS	$C_6F_{13}SO_3H$	400.11	6.2	1.24	0.14
Perfluorooctanoic acid	PFOA	$C_7F_{15}COOH$	414.07	2290	1.9	-0.2
Perfluorononanoic acid	PFNA	$C_8F_{17}COOH$	464.08	0.0625	2.57	-0.21
Perfluorooctane sulfonic acid	PFOS	$C_8F_{17}SO_3H$	500.13	0.0032	2.45	-3.27

3.3.2.2 Batch adsorption studies with IXR

For single solute batch adsorption tests, ground Amberlite® IRA910 beads (~ 10 mg) were mixed with solutions containing 10 mM NaCl as the background electrolyte and individual PFAS (PFOS, PFOA, PFNA, PFHxS, PFHpA, PFBS) at two different concentration ranges; a low concentration group (1 to 100 µg/L) to represent environmentally relevant concentrations and a high concentration group (10 to 500 mg/L) to establish maximum adsorption capacities. For the low concentration group, batch reactors were prepared with 50 mL of solution in 50 mL polypropylene centrifuge tubes (Thermo Fisher Scientific, Waltham, MA). For the high concentration group, batch reactors were prepared with 100 mL of solution in 125 mL Nalgene™ HDPE bottles (Thermo Fisher Scientific, Waltham, MA). The reactors were prepared in triplicate with negative controls at the same PFAS concentration without IRA910 beads, and blank controls containing only IRA910 beads and 10 mM NaCl. The solution pH in all reactors was adjusted to 6 with NaOH [211]. The contents of the HDPE bottles were mixed for 72 h on an orbital shaker at 150 rpm. The mixing time was selected based on previous studies that have evaluated PFAS adsorption on activated carbon [29, 30, 202-204, 206, 207]. After mixing, the bottles were allowed to settle for

1 h, and 1 mL of supernatant was transferred to a polypropylene centrifuge tube and centrifuged at 4,000 rpm for 30 min. The supernatant was then filtered through 0.45μm GE Healthcare Whatman™ GD/X Glass Micro Fiber (GMF) syringe filter (GE Healthcare, Chicago, IL) and diluted to appropriate concentration ranges prior to analysis. The amount of adsorbed mass was calculated based on the difference between initial and final aqueous concentrations, accounting for any losses in the control (blank) reactors.

The multi-solute batch adsorption tests were also conducted at two different concentration levels; a low concentration group (1 to 100 μg/L) to represent environmentally relevant concentrations and a high concentration group (2 to 100 mg/L) to establish maximum adsorption capacities and evaluate competitive adsorption effects. For the low concentration group, batch reactors were prepared in triplicate with 50 mL centrifuge tubes containing 10 mg of IRA 910 and 50 mL of aqueous solutions containing PFOS, PFOA, PFNA, PFHxS, PFHpA, and PFBS at equal concentrations of 1, 5, 10, 50 and 100 μg/L. For the high concentration group, batch reactors were prepared in triplicate with 125 mL Nalgene™ HDPE bottles containing 10 mg of IRA 910 and 100 mL of aqueous solutions containing PFOS, PFOA, PFNA, PFHxS, PFHpA, and PFBS at equal concentrations of 2, 10, 20, 50, 100 mg/L. The sampling preparation and mixing procedures were identical to those used for the single-solute batch reactor studies.

3.3.2.3 Column experiments with S-IXR

Column experiments were performed to assess the delivery and retention of the S-IXR suspension in water-saturated quartz sand, and to quantify the sequestration of PFOS or PFOA and a mixture containing equal concentrations of PFOS, PFOA, PFNA, PFHxS, PFHpA, and PFBS under dynamic conditions. Borosilicate glass columns (2.5 cm i.d. × 10 cm length) were packed with air-dried 40-50 mesh Ottawa sand, flushed with CO_2 gas for 1 h, and then saturated with degassed background electrolyte solution (10 mM NaCl) at a flow rate of 1.0 mL/min, which corresponds to a pore-water velocity (v_p) of 7.8 m/day. The pore volume (PV), which represents the volume of solution contained in each packed column, was approximately 20.0 mL. Non-reactive tracer tests were performed before and after the S-IXR treatment by injecting 3.5 PV of 10 mM NaBr followed by 3.5 PV 10 mM NaCl using a Chrome Tech P-010 isocratic pump (Apple Valley, MN).

To assess the delivery and retention capacity of resin beads, a pulse (3.5 PV) of S-IXR suspension was introduced into the water-saturated column at a flow rate of 0.12 mL/min (v_p = 0.945 m/day, residence time = 2.8 h) using a Chemyx Nexus 3000 syringe pump (Stafford, TX). This flow rate was selected to represent the upper limit or worst-case scenario with respect to the contact time between PFAS and retained resin in a sandy aquifer formation. The column was then flushed with 10 mM NaCl at the same flow rate to remove any unretained Amberlite® IRA910 and Pluronic® F-127. For individual PFAS experiments, aqueous solutions containing either PFOS (100 μg/L) or PFOA (100 μg/L) in 10 mM NaCl were injected into S-IXR treated columns at a flow rate of 0.12 mL/min. After approximately 7 PV, the influent concentration of PFOS or PFOA was increased from 100 μg/L to 100 mg/L to determine to maximum adsorption capacity of the S-IXR treated

sand. For multi-solute column experiments, an aqueous solution containing equal concentrations of PFOS, PFOA, PFNA, PFHxS, PFHpA, and PFBS (10 µg/L each, 60 µg/L total) with 10 mM NaCl were then injected into S-IXR treated columns at a flow rate of 0.12 mL/min for approximately 10 PVs. The influent concentration was increased to from 10 µg/L to 10 mg/L for each PFAS (60 mg/L total) to determine to maximum adsorption capacity of the S-IXR treated sand. Effluent samples were collected continuously using a Spectra/Chrom® CF-2 fraction collector (Spectrum Chemical Mfg. Corp., New Brunswick, NJ) to monitor for PFAS breakthrough. At the conclusion of each experiment, the sand was removed in 5 increments (ca. 20 g each) to obtain S-IXR retention profiles and SEM images.

3.3.2.4 Analytical Methods used for S-IXR experiments

Analysis of PFAS and their corresponding ^{13}C-labeled internal standards was performed following the method of McCord et al. [212]. Aqueous samples were diluted with water and methanol to the concentration range of the standards (10 ng/L to 10 µg/L) with the ratio of water:methanol (v/v) = 90:10 and spiked with internal standards (2 µg/L). Analyte separation and detection was achieved using a Waters ACQUITY ultra high-performance liquid chromatograph coupled with a Waters Xevo UPLC-MS/MS. The mass spectrometer was operated in ESI- and MRM modes. Quantification was achieved using a 7-point calibration curve and ^{13}C labeled standards were used to verify compound identity.

The carbon content of sand collected from columns treated with S-IXR was determined using a Shimadzu TOC-SSM analyzer (Columbia, MD). Aqueous bromide concentrations were quantified using a bromide specific probe (Cole Parmer, Vernon Hills, IL) with a 5-point calibration curve. The hydrodynamic diameter of S-IXR was measured by DLS using a Zetasizer Nano ZS Analyzer (Malvern Instruments Ltd., Southborough, MA) operated in back-scattering mode at an angle of 173^{o}. SEM images of untreated and S-IXR treated sand were obtained by placing sand grains on carbon adhesive tabs attached to aluminum mounts (Electron Microscopy Sciences, Hatfield, PA). The mounted samples were sputtered with gold for 5 min and imaged on a Zeiss Leo 1530 VP SEM coupled with an Oxford Instruments 7426 EDS system.

3.4 Coupled Adsorptive and Bioactive Column Experiments

3.4.1 Column Setup

3.4.1.1 Configuration, preparation and operation of columns

Four sets of column experiments were conducted (**Table 3.7**), according to the configuration illustrated in **Figure 3.2**. Set 1 and set 2 were single adsorptive columns with IONPs and S-PAC, respectively. These two sets of columns aimed to investigate the transport and retention of comingled PCE, TCE, and 10 PFAAs in water-saturated sand with respective sorbent. Set 3 and set 4 consisted of a bioactive column connected to an adsorptive column (IONPs or S-PAC). These two sets of coupled column systems aimed to investigate the synergistic performance of combined biological-sorptive treatments for the detoxification of PCE/TCE and enhanced retention of PFAAs.

Sorptive columns in sets 1-4 were prepared following the procedures reported previously [35, 36], with slightly different amounts of IONPs or S-PAC packed in the columns (**Table 3.7**). Upon the completion of packing, columns were flushed with CO_2 gas for 30 min to facilitate dissolution of entrapped gas, and then saturated with 10 pore volumes (PV) of sterile background solution in an up-flow mode at a flow rate of 1.0 mL/min. Non-reactive tracer tests were then performed by injecting 3 PVs of 20 mM sodium bromide followed by 2 PVs of the background solution, with the objective of assessing hydrodynamic dispersion and confirming the PV.

The influent solution used in the column experiments contained a mixture of PCE, TCE, and 10 PFAAs with targeted concentrations (**Table 3.8**). The concentrations of the 10 PFAAs were determined at ratios approximating those used in the microcosm study [37] to mimic the ratios detected in groundwater at contaminated site (**Table 3.8**). Neat PCE (150 μL) and TCE (120 μL) were added to a 1-L serum bottle containing 800 mL background solution to serve as a PCE/TCE saturated stock solution. A certain amount of 10 PFAAs were added to another 1-L serum bottle to make a 10x PFAAs stock solution. Both bottles were sealed with a rubber stopper and sterilized in an autoclave at 121 ºC for 30 min. The concentration of the PCE/TCE stock was measured by gas chromatography (GC) prior to column influent preparation. The influent was prepared by withdrawing appropriate volumes of the background solution, PCE/TCE and PFAAs stock into a sterile 50- or 100-mL gas-tight Chemyx stainless steel syringes (Stafford, TX) using a Chemyx Fusion 4000-X syringe pump (Stafford, TX).

Following the tracer test, set 1 and set 2 experiments were initiated by continuously injecting the column influent containing PCE, TCE, and 10 PFAAs via a Chemyx Fusion 4000-X syringe pump (Stafford, TX) in an up-flow mode at a flow rate of 0.015 mL/min (pore-water velocity ≈ 9.80 cm /day) (**Table 3.7**). IONP column and S-PAC column were operated for approximately 42.1 PVs and 87.5 PVs, respectively.

Table 3.7 Overview of column experiments and operating conditions.

	Single sorptive column experiments		**Coupled bioactive and sorptive column experiments**			
	Set 1	Set 2	Set 3		Set 4	
System Configuration[a]	IONP column (n=1)	S-PAC column (n=1)	Bioactive column (n=2)	IONP column (n=2)	Bioactive column (n=2)	S-PAC column (n=2)
Column Dimension[b]	2.5 cm x 10 cm	2.5 cm x 10 cm	2.5 cm x 15 cm	2.5 cm x 10 cm	2.5 cm x 15 cm	2.5 cm x 10 cm
Column Matrix[c]	Sand & IONPs	Sand & S-PAC	Sand & KB-1®	Sand & IONPs	Sand & KB-1®	Sand & S-PAC
Mass of sorbent[d]	5.1 mg Fe	31.4 mg C	N/A	5.1 ± 0.0 mg Fe	N/A	35.5 ± 2.7 mg C
Column Influent[e]	10 mg/L PCE, 15 mg/L TCE, and 10 PFAAs (2 mg/L in total)					
Flow rate (mL/min)	0.015	0.015	0.010	0.010	0.010	0.010
Pore volume (PV; mL)	22.0	21.5	31.1 ± 0.4	21.9 ± 0.5	31.1 ± 0.4	21.3 ± 0.2

[a] See **Figure 3.1** for detailed configuration of single adsorptive and coupled column systems. Number in the parenthesis denotes the number of columns operated in each set of experiment.

[b] Column dimension is expressed in inner diameter (ID) x length (L).

[c] IONP sorptive column was directly packed with IONP-treated sand (sand mixed with PEI-IONPs). S-PAC column was packed with sand first, followed by an injection of S-PAC suspension. Bioactive column was also packed with sand first, followed by the bioaugmentation with KB-1® inoculum (SiREM; Guelph, ON).

[d] Prior to mixing with sand, Fe content in PEI-IONPs was measured by inductively coupled plasma-optical emission spectrometry (ICP-OES). The carbon content in solid phases of S-PAC column was measured at the conclusion of column experiment using a total organic carbon analyzer equipped with a solid sample module (TOC-SSM).

[e] The concentrations of 10 PFAAs were determined at ratios approximating those used in a previous microcosm study [37] to mimic the ratios detected in groundwater at contaminated site (see **Table 3.8** Targeted concentrations of PCE, TCE, and 10 PFAAs in the influent solution introduced into columns and corresponding composition of PFAA mixture (% total PFAAs by mass) measured in the column experiments compared to previous microcosm study (Hnatko et al., 2023).).

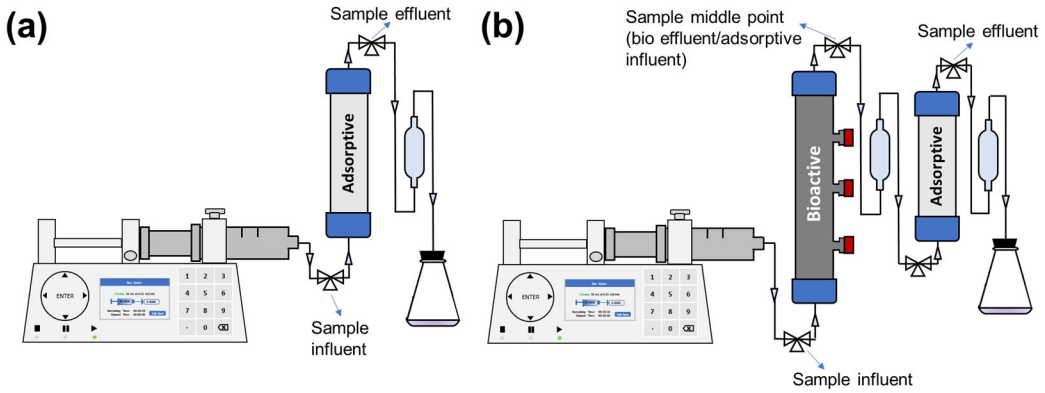


Figure 3.2 Schematic diagrams of column experimental configuration (a) single adsorptive column and (b) coupled bioactive and adsorptive columns.

Table 3.8 Targeted concentrations of PCE, TCE, and 10 PFAAs in the influent solution introduced into columns and corresponding composition of PFAA mixture (% total PFAAs by mass) measured in the column experiments compared to previous microcosm study (Hnatko et al., 2023).

Compound	Targeted concentration[a]	Targeted concentration[b]	Composition in this study	Composition in previous microcosm study
PCE	10	0.06		
TCE	15	0.11		
PFBS	110	0.37	5.5%	4.4%
PFBA	160	0.75	8.1%	10.3%
PFPeA	280	1.06	14.0%	18.2%
PFHxS	350	0.87	17.2%	14.0%
PFHxA	355	1.13	17.8%	18.8%
PFHpA	160	0.44	8.1%	6.2%
PFOS	245	0.49	12.2%	15.1%
PFOA	165	0.40	8.3%	8.6%
PFNA	75	0.16	3.8%	3.2%
PFDA	100	0.19	5.0%	1.1%

a. The units for PCE/TCE and PFAAs are mg/L and µg/L, respectively.
b. The units for PCE/TCE and PFAAs are mM and µM, respectively.

Bioactive columns in set 3 and set 4 were prepared following well-established previously documented procedures [213]. Briefly, the preparation consisted of FF sand packing, saturation, non-reactive tracer test, reduced condition establishment, and bioaugmentation with KB-1® inoculum (SiREM; Guelph, ON). Following the bioaugmentation, the column influent was delivered to the two bioactive columns in parallel at a flow rate of 0.01 mL/min (pore-water velocity ≈ 7.0 cm /day) via a Chemyx Fusion 6000-X syringe pump (Stafford, TX) in an up-flow mode. The concentrations of PFAAs, chlorinated ethenes and ethene in the effluent of two bioactive columns were monitored. Upon the establishment of stable effluent concentration of PFAAs and dechlorination performance after 60 PVs of operation (data not shown), two of IONPs sorptive columns were connected to bioactive columns in parallel (**Figure 3.2**). This connection between bioactive and sorptive columns was considered PV=0 for set 3 experiments (i.e., initiation point). Set 3 experiments were continuously operated for approximately 42.1 and 65.5 PVs for the bioactive columns and INOC columns, respectively (note the duration was same but PV was different for the bioactive column and the INOC column). Set 4 experiments were conducted after the completion of set 3 experiments, by replacing two IONPs columns with S-PAC sorptive columns. The coupled bioactive and S-PAC columns were continuously operated for approximately 38.0 and 59.0 PVs for the bioactive columns and S-PAC columns, respectively.

3.4.1.2 Column sampling

During set 1-4 experiments, influent and effluent from each column were collected periodically through 3-way Hamilton valves (Reno, NV) (shown in **Figure 3.2**; two sampling locations in sets 1-2 and three sampling locations in sets 3-4). To prevent volatilization of the analytes and minimize disruption in flow, a 1-mL polypropylene syringes (BD; Franklin Lakes, NJ) was also connected to a Hamilton valve, and used to withdraw the aqueous sample from the 10-mL customized glass sampling bulb at each sampling time point and location (**Figure 3.2**). Sample aliquots of 1.0 mL were immediately transferred into 20-mL headspace autosampler vials and capped with rubber septa. These samples were immediately analyzed for chlorinated ethenes, including PCE/TCE and their biotransformation products *cis*-1,2-dichloroethene (*cis*-DCE) and vinyl chloride (VC) as well as ethene. Additionally, 65 µL of each sample was promptly diluted with 1,235 µL of methanol, filtered through a 0.45-µm Whatman GD/X glass microfiber filter (GMF) syringe filter (GE Healthcare, Chicago, IL), and stored at -20 ºC prior to targeted PFAS analysis. Analytical method details regarding GC-FID analysis for chlorinated ethenes and ethene, and LC-MS/MS analysis for PFAS are provided in **Appendix A.2**.

3.5 Aquifer Cell Experiments

3.5.1 Aquifer cell desing

An aquifer cell (64 cm length × 40.5 cm height × 1.4 cm internal thickness) was constructed using two pieces of glass separated by a stainless-steel frame. The interface between the frame and glass was sealed with rubber O-ring embedded in the notch on the frame. Stainless-steel screws along the two end plates and bottom boundary of the frame were used to secure the glass within the frame. The flow cell was packed under water-saturated conditions with 40-50 mesh Ottawa sand as the background porous medium. A layer of F-90 Federal fine sand, approximately 5 cm thick, was packed at the bottom of the aquifer cell to serve as a lower confining layer. Soil was collected from a DoD facility located in the south-central United States within the Central Redbed Plains of the Central Lowland Physiographic Province. The soil is classified as a silty sand derived from the Hennessey group and has a distinct red color due to the presence of ferric anhydride. The field soil was oven-dried at 105 ºC, gently ground with a motar and pestle, sieved (ASTM 20-mesh, < 850 μm) and then packed within the 40-50 mesh Ottawa sand as 9 separate arc-shape lenses, approximately 2 cm height × 12 cm length to create the heterogeneous domain. Open chambers (1.27 cm × 1.27 cm) located at each end of the aquifer cell were screened over the entire height of the flow cell. The influent and effluent wells were constructed from 0.64 cm outer diameter stainless steel tubing that was inserted into the screened end chambers. A schematic diagram of the packed flow cell, which had a PV of approximately 1.45 L, is shown in **Figure 3.3.** The front-side glass panel was fitted with eighteen, 2-mm diameter holes using a water jet milling machine. Small-bore borosilicate glass tubes were glued into each hole using silicone glue (Dow Corning Corporation, Auburn, MI). The side-ports were then capped with Grace ThermoRed Septa (Columbia, MD). A constant head reservoir was used to deliver the background electrolyte solution (10 mM NaCl) at a pore-water velocity of approximately 1.52 m/day. The influent solution flowed through stainless steel screens that were placed inside the influent chamber to promote uniform flow into the aquifer cell.

3.5.2 Aquifer Cell Operation

The aquifer cell was initially saturated with an aqueous solution containing 10 mM NaCl. After the flow rate stabilized, a non-reactive tracer test was carried out by injecting a 0.5 PV pulse of aqueous solution containing 10 mM NaBr and 20 mg/L fluorescein at flow rate of 2.4 mL/min (pore-water velocity of 1.52 m/day), followed by the background solution (10 mM NaCl). Images were collected every 20 min using an EOS Rebel T2 digital camera (Canon; Melville, NY). Effluent samples were collected in 50 mL polypropylene centrifuge tubes using a fraction collector. To create a permeable adsorption region within the aquifer cell, the S-PAC suspension (1,000 mg/L PAC + 5,000 mg/L polyDADMAC) was injected through side-ports 8 and 9 of the aquifer cell (Figure 1). Approximately 80 mL of S-PAC was injected into each side port at a flow rate of 0.08 mL/min to create treatment zone with a radius of approximately 5 cm. After the S-PAC injection, the background flow was resumed at a flow rate of 2.4 mL/min. The S-PAC suspension was not injected into the upper portion of the aquifer cell (ports 6 and 7), which served as an untreated control region. Solutions containing 50 μg/L PFOS, 50 μg/L PFOA and 10 mM NaBr were then injected using a peristatic pump through side-ports 2 (upper region) and 4 (lower region) at a flow rate of 0.23 mL/min for 24 h (ca. 330 mL total injected volume). During the PFOA and PFOS injection, the background solution (10 mM NaCl) continued to flow through the aquifer cell at a flow rate of 2.4 mL/min to simulate a realistic injection scenario. Aqueous samples were collected from the effluent continuously and from down-gradient side-ports every 3 hours.

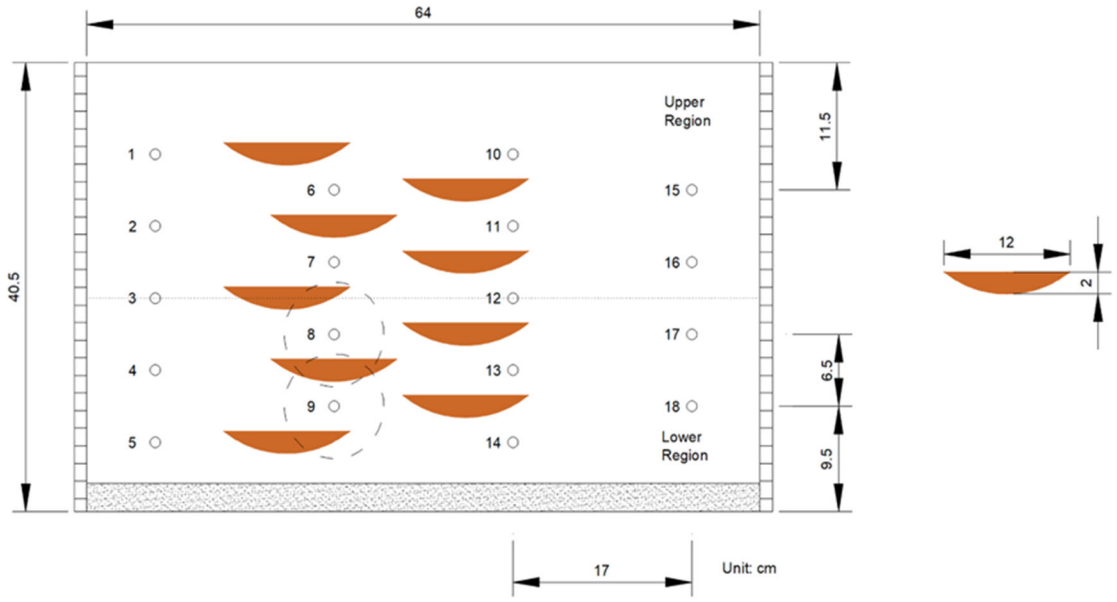


Figure 3.3 Schematic diagram of the aquifer cell showing the overall dimensions, location of injection and sampling ports, and size and location of lower-permeability lenses.

3.6 PFAS Analytical Methods

3.6.1 Targeted PFAS Analysis

The analysis was performed on an Vanquish Flex Binary Ultra Performance Liquid Chromatography (UPLC) system (Thermo Scientific) fitted with a PFC-free kit (P/N 80100-62142) coupled to a quadrupole orbitrap mass spectrometer (Orbitrap Exploris 120, Thermo Scientific) with heated electrospray ionization (H-ESI) in negative mode using Xcalibur software (V4.4.16.14). A delay column was placed between the pump and autosampler (HypersilGOLD, 1.9 µm, 175 Å, 3 x 50 mm) to separate any PFAS in the LC system and solvents from the analytes. The standard or sample (10 µL) was injected onto a C18 column (Accucore RP-MS, 2.6 µm, 2.1 x 100 mm) maintained at 40°C, with a 200 µL/min flow rate of mobile phase of solution A (2 mM ammonium acetate in water) and solution B (100% acetonitrile) beginning at 20% B for the first 1.8 min to 95% B at 13.4 min, held at 95% B for 0.5 min, back to 20% B at 14.5 min, and with re-equilibration of 3.5 min. The MS scan range was 100-1000 m/z with resolution of 60,000, standard AGC target, 70% RF lens, maximum injection time auto, with EASY-IC run-start on. The spray voltage was 2200 V, ion transfer tube temperature was 250 °C, and the vaporizer temperature was 175 °C and mild trapping was on. The sheath gas was 30 and aux gas 5 (arbitrary units). A targeted inclusion mass list with retention time windows was used for comparing the standard and sample fragmentation pattern with a 5-ppm mass tolerance.

Targeted LC-MS/MS analysis of samples was conducted using a Waters ACQUITY ultra high-performance liquid chromatograph coupled with a Waters Xevo triple quadrupole mass spectrometer (UPLC-MS/MS) (Waters Corporation, Milford, MA). PFAAs analysis was

performed following established methods [212]. Analyte separation was achieved using a Waters ACQUITY UPLC BEH C18 Column (130Å, 1.7 µm, 2.1 mm X 50 mm).

3.6.2 Non-targeted PFAS Analysis

Non-targeted PFAS analysis was also performed on the aqueous samples and soil methanol extracts. Sampling time points were selected based on targeted LC-MS/MS analysis results to include the samples collected before and after the occurrence of the biotransformation. Samples were injected in triplicate with a 10 µL injection volume on a Thermo QExactive HF-X Orbitrap MS equipped with a Vanquish ultra-high-performance liquid chromatograph (UHPLC-Orbitrap). Sample components were separated on a Thermo Hypersil Gold Vanquish C18 column (50 mm × 2.1 mm × 1.9 µm) at a constant temperature of 60 ºC with a solvent gradient consisting of two mobile phases, A (water) and B (methanol). PFAS were eluted from the column at a constant flow rate of 0.4 mL/min using a mobile phase gradient as follows: equilibration with 10% B for 1 minute, followed by a gradient ramp from 10% B to 100% B over 4 minutes and held for 2 minutes, and back to 10 % B over 1 minute and held for 2 minutes (total run time 11 minutes, data collected from 0.6 to 9 minutes). The MS was operated in full scan dd-MS^2 mode (stepped 15 and 55 NCE) with an inclusion list for 21 PFAS. Ionization was performed in negative mode (operated in both positive (ESI+) and negative (ESI-) ionization modes for AFFF microcosm samples) with an ionization window of 1.0 *m/z*, sheath gas flow rate of 40, auxiliary gas flow rate of 10, sweep gas flow rate of 2, spray voltage of 2.7 kV, 310 ºC capillary temperature, funnel RF level of 35, and 320 ºC auxiliary gas heater temperature. For the full-scan, the Orbitrap was operated with a resolution of 120,000, automatic gain control (AGC) of 3×10^6, and maximum dwell time of 100ms. For dd-MS^2, the Orbitrap was operated with a resolution of 15,000, AGC of $2x10^5$, and maximum dwell time of 400ms. MS^2 fragmentation was performed in the HCD collision cell filled with N_2 (produced by a Peak Scientific Nitrogen Generator, Genius NM32LA). The data files were saved in the .RAW file format and analyzed in Thermo Compound Discoverer (CD) 3.2 software. Spectral libraries included Thermo mzCloud, ChemSpider, and an in-house MS^2 mass spectral library containing 40 PFAS compounds. The mass lists included approximately 200 hypothesized potential transformation products, transformation products predicted by BioTransformer 3.0, and 8,142 fluorinated compounds from the EPA's ToxCast/CompTox database [215, 216].

A final candidate list containing a total of 705-14,000 features was exported to Microsoft Excel after processing the raw data. We developed an R script to facilitate the selection of features of interest based on the peak intensity comparison between samples from an individual treatment over time, and between samples from the live-spiked treatments and abiotic/positive controls at each sampling point. Confidence scores of the features detected were assigned based on the Schymanski Scale to evaluate the certainty of the structure identification [217]. Briefly, the highest confidence level 1 (confirmed structure) represents the proposed structure was confirmed via the comparison of the appropriate measurement of a reference standard. Level 2 (probable structure) was achieved when the MS^2 spectrum and fragmentation have been reported previously for a compound of interest and the spectrum-structure match is unambiguous, or when the structure of the compound could be determined unambiguously by MS^2 fragmentation analysis. Level 3 (tentative candidate) was assigned when the MS^2 spectrum and fragmentation were informative for possible structures, but the information was insufficient for one exact structure only. When the MS^2 fragmentation data was not available while a molecular formula can be assigned unambiguously based on the spectral information, level 4 (unequivocal molecular formula) was assigned.

4. Results and Discussion

4.1 Ultra–High Capacity Multifunctional Nanoscale Sorbents for PFOA and PFOS Treatment

4.1.1 Role of Surface Coating of Nanocrystals on PFAS Sorption Behavior

TEM micrographs in **Figure 4.1** show as synthesized, monodisperse IONPs, and their size distribution (20.9 ± 1.5 nm, 55.3 m^2/g of core specific surface area). IONP crystalline structure is well matched with magnetite (Fe_3O_4) (JCPDS card #190629) by XRD analysis, which is superparamagnetic in this size range, as reported previously.[218] Superparamagnetic functionality was included as part of the material platform for potential applications in low energy, precise (magnetic) separations from larger volumes and/or as a safety feature with regard to unwanted release.

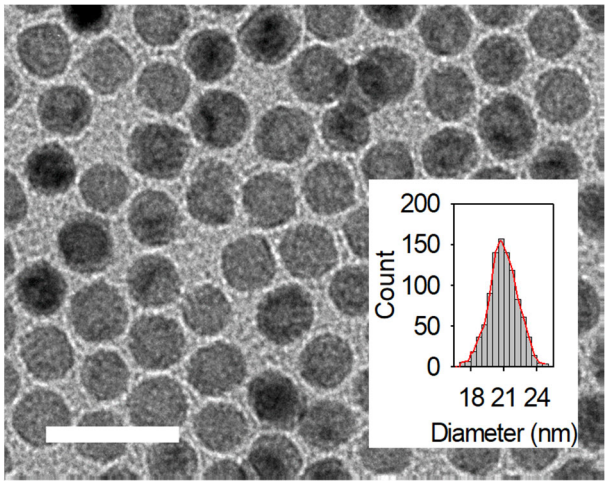


Figure 4.1 TEM images of monodisperse iron oxide nanoparticles (IONPs) and histograms of the size distribution of NCs. Average diameter of NPs was measured using Image-Pro 6.0 with over a thousand counted. Scale bar is 50 nm.

IONPs were subsequently surface functionalized with a series of organic coatings, including branched polyethyleneimine (PEI) with different molecular weights (10 kDa and 25 kDa), cetyltrimethylammonium bromide (CTAB), and oleic acid (OA), all allowing for phase transfer into water, termed here as Fe_3O_4@PEI, Fe_3O_4@CTAB, and Fe_3O_4@OA, respectively. Surface functionalized IONCs were characterized in water by dynamic light scattering (DLS) to measure hydrodynamic diameter and surface zeta potential at pH 7 ± 0.2. As tabulated in **Figure 4.2a**, the hydrodynamic diameter is 63.0 ± 2.4 nm for Fe_3O_4@PEI25k, 40.4 ± 2.8 nm for Fe_3O_4@PEI10k, 25.8 ± 3.0 nm for Fe_3O_4@CTAB, and 32.6 ± 3.6 nm for Fe_3O_4@OA. Zeta potential of Fe_3O_4@PEI25k, Fe_3O_4@PEI10k, Fe_3O_4@CTAB, and Fe_3O_4@OA is 54.3 ± 1.3, 57.4 ± 1.5, 29.1 ± 4.9, and -24.2 ± 1.8 mV, respectively (**Figure 4.2b**). Coating analysis, including grafting densities and composition are presented in **Table 4.1**.

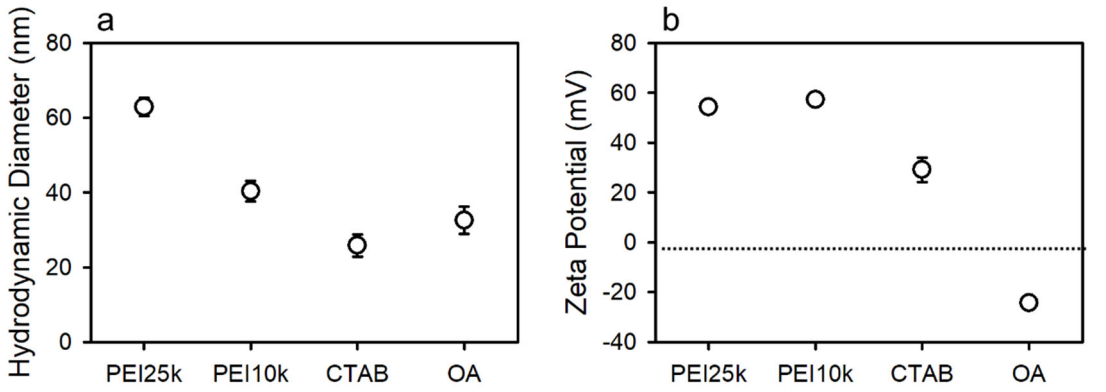


Figure 4.2 (a) Hydrodynamic diameters and (b) zeta potential of organic functionalized IONPs with polyethyleneimine (PEI), cetyltrimethylammonium bromide (CTAB), and oleic acid (OA) at pH 7.0 ± 0.2.

Batch surface coating dependent PFAS sorption tests were performed at pH 7 ± 0.2. As shown in **Figure 4.3**, positively charged Fe_3O_4@PEI nanocrystals (NCs) demonstrate significantly higher sorption density compared to negatively charged Fe_3O_4@OA NCs. The maximum sorption capacity of PFOA and PFOS was 18.3 mmol PFOA g^{-1} NC and 88.8 mmol PFOS g^{-1} NC for Fe_3O_4@PEI25k, and 11.9 mmol PFOA g^{-1} NC and 83.5 mmol PFOS g^{-1} NC for Fe_3O_4@PEI10k, respectively. Negatively charged Fe_3O_4@OA have significantly lower sorption capacities for both PFOA and PFOS (1.83 mmol PFOA g^{-1} NC and 6.58 mmol PFOS g^{-1} NC). As highlighted in **Table 4.1**, Fe_3O_4@PEI materials described in this study demonstrate some of the highest sorption capacities reported to date. This is not only due to a high number (related to PEI amine density, **Table 4.1**) of favorable amine-anion (PFAS) head group interactions per particle,[219, 220] but also a function of high particle (aqueous) stability, thus maximum surface area/site availability (**Figure 4.3**). Comparatively, Fe_3O_4@PEI25k is observed to have higher sorption capacities than Fe_3O_4@PEI10k despite having a similar number of amine groups. This is likely due to a combination of relatively higher grafting (mass) density of PEI25k and a higher amine to carbon ratio compared to PEI10k.

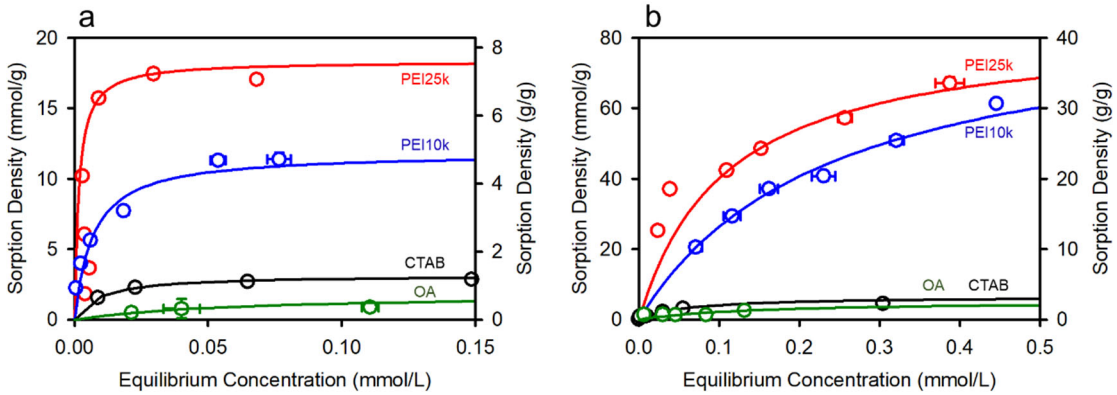


Figure 4.3 (a) PFOA and (b) PFOS sorption isotherm on iron oxide nanoparticles (IONPs) with different organic (surface) coating; positively charged PEI (25k and 10k of MW) and CTAB, and negatively charged OA, respectively. All experiments were performed at pH 7.

Table 4.1 Organic loading on the iron oxide nanoparticles (IONPs).

Nanocrystals	Molecular weight of coating material	Total organic carbon (mg/L of carbon)[α]	Number of carbon per nanocrystal	Number of amine groups per carbon[β, γ]	Number of amine groups per nanocrystal	Number of molecules per nanocrystal
Fe_3O_4@PEI25k	25,000	63 ± 1.3	690,306	0.5[β]	345,153	297
Fe_3O_4@PEI10k	10,000	57 ± 0.7	627,729	0.5	313,864	676
Fe_3O_4@CTAB	364.45	6.3 ± 0.1	685,526	0.037[γ]	25,364	25,364

[α]Total organic carbon (TOC) for organic functionalized iron oxide nanocrystals (10 mg/L Fe).
[β]Number of amine groups per carbon of PEI coated IONCs was obtained by considering repeat unit of multi branched PEI structure.
[γ]Number of amine groups per carbon of CTAB functionalized IONCs was obtained based on an assumption of full surfactant encapsulation.

All batch sorption isotherms were well matched with a Langmuir adsorption model (**Table 4.2**) with the corresponding sorption constant (k) for PFOA calculated to be much higher than that of PFOS regardless of sorbent. Further, for comparison, we also modeled sorption data with a Freundlich isotherm as well (**Table 4.2**). Interestingly, PFOS is observed to have higher maximum sorption density (Q_{max}) compared to PFOA, for all material combinations explored. For example, the k and Q_{max} values on Fe_3O_4@PEI25k are 657 L/mmol and 18.3 mmol/g for PFOA, and 4.22 L/mmol and 88.8 mmol/g for PFOS, respectively. This difference indicates that PFAS functional head group(s) contribute to the sorption behavior as PFOA and PFOS having similar fluorine saturated tail structures. With regard to functional group acidity, PFOS, has a lower pKa value (< 0) than PFOA (0.5-3.8), in addition to higher affinity for octanol (a model non-aqueous phase, log K_{OW} = 5.43) compared to PFOA (log K_{OW} = 5.11).[142, 221-223] As discussed by others, amine–sulfonic interactions typically have a more negative enthalpy (ΔH) value (-42.81 kJ/mol) compared to amine–carboxyl interactions (-21.41 kJ/mol), which also likely contributes to (more) favorable adsorption.[224, 225] These property differences may also impact association sterics, in terms of average geometrical orientation of the sorption event, which is further explored and discussed below.

Table 4.2 Sorption isotherm constants and regression data for Langmuir and Freundlich adsorption isotherm models.

Target	Adsorbents	Langmuir Isotherm			Freundlich Isotherm		
		q_{max} (mmol/g)	k (L/mmol)	R^2	K_f [α]	n	R^2
PFOA	Fe_3O_4@PEI25k	18.3	657	0.99	41.9	4.28	0.88
	Fe_3O_4@PEI10k	11.9	148	0.95	29.9	2.92	0.98
	Fe_3O_4@CTAB	3.14	112	0.99	4.16	5.36	0.90
	Fe_3O_4@OA	1.83	16.5	0.70	3.60	1.94	0.89
PFOS	Fe_3O_4@PEI25k	88.8	4.22	0.99	98.6	1.73	0.99
	Fe_3O_4@PEI10k	83.5	9.27	0.99	88.5	3.20	0.95
	Fe_3O_4@CTAB	6.58	16.3	0.99	7.02	3.10	0.97
	Fe_3O_4@OA	5.30	6.89	0.61	16.0	1.17	0.75

[α]Unit of K_f is (mmol/g) $(L/mmol)^{1/n}$.

4.1.2 Real Time Analysis of PFAS Sorption via QCM-D

To better understand fundamental sorption dynamics, a quartz crystal microbalance with dissipation (QCM-D) monitoring technique was developed to observe real time, in situ sorption behavior of PFAS. For this, we arrange a stable, monolayer of IONPs at the sensor interface – whereby varied aqueous solutions can be introduced sequentially and equilibrated, including changes in water chemistry and PFAS concentration/type (**Figure 4.4**). **Figure 4.5** shows the kinetics (slope of frequency shift) of IONP deposition and sensor surface saturation (i.e. monolayer coverage) at or above 5 mg/L of concentration of NPs. Once stabilized IONPs demonstrate relative fast responses upon introducing PFAS solutions and reached equilibrium within minutes. These results are consistent with the batch sorption isotherm and kinetic tests for both PFOA and PFOS using IONPs (**Figure 4.6**). To further understand PFAS sorption kinetics on IONPs, the slope of the frequency shift (f_{slope}) was calculated from the data obtained during QCM-D sorption experiments. Since the frequency shift (Δf) is proportional to a change in mass (Δm) on the crystal surface, the rate of Δf change is equivalent to the rate of mass change on the crystal surface (i.e., the rate of PFAS attachment or release).[226, 227] Hence, the PFAS sorption rate (kinetics) can be determined by calculating the slope of frequency shift (f_{slope}). As shown in **Figure 4.7**, Fe_3O_4@CTAB NPs showed the highest value of f_{slope}, followed by Fe_3O_4@PEI10k and Fe_3O_4@PEI25k, which is inversely proportional to the hydrodynamic diameter of IONPs. We expected the thicker PEI (and denser) surface coating layer requires more time for PFAS to fully sorb, which is likely due to mass transfer limitations, while showing overall higher sorption densities due to relatively more binding sites.

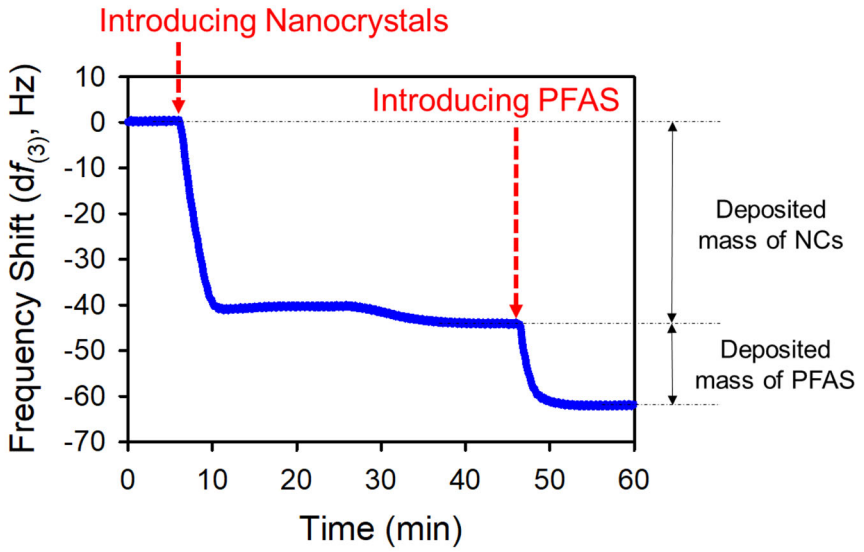


Figure 4.4 Real time frequency responses of QCM-D for PFAS sorption on organic functionalized iron oxide nanoparticles (IONPs) coated Q-sensor.

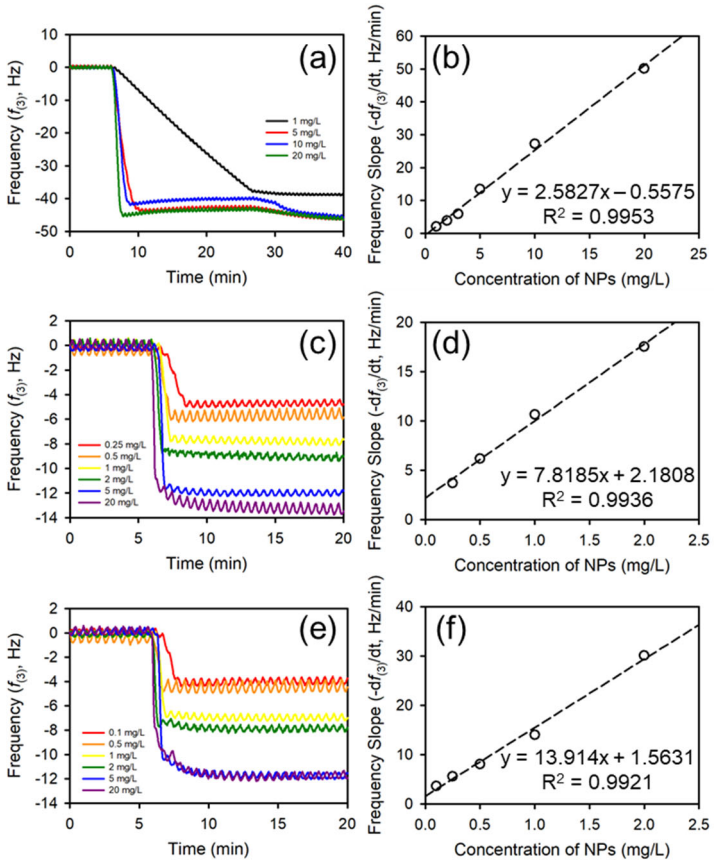


Figure 4.5 Frequency shift and slope with respect to the different concentration of IONCs with various surface coating; (a, b) CTAB, (c, d) PEI25k, and (e, f) PEI10k, respectively.

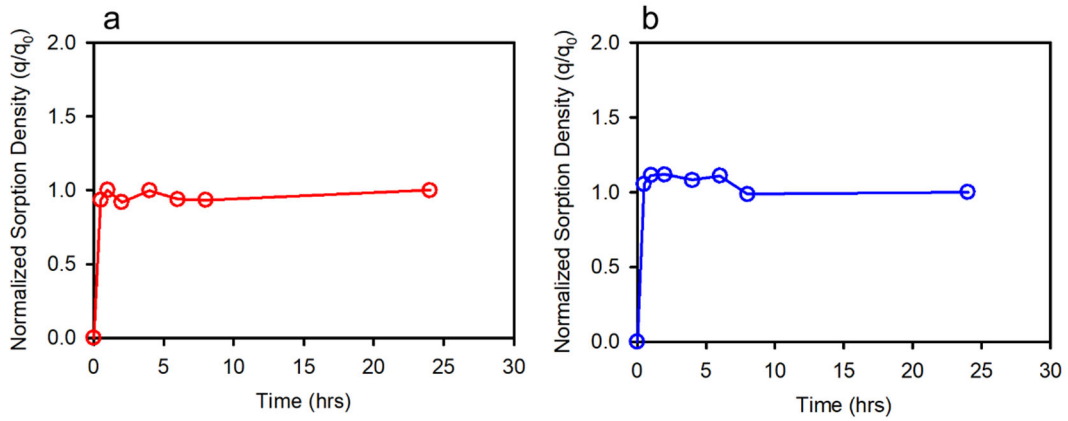


Figure 4.6 Time dependent normalized sorption density of PEI coated IONPs (Fe_3O_4@PEI25k) for 0.6 mmol/L of (a) PFOA and (b) PFOS.

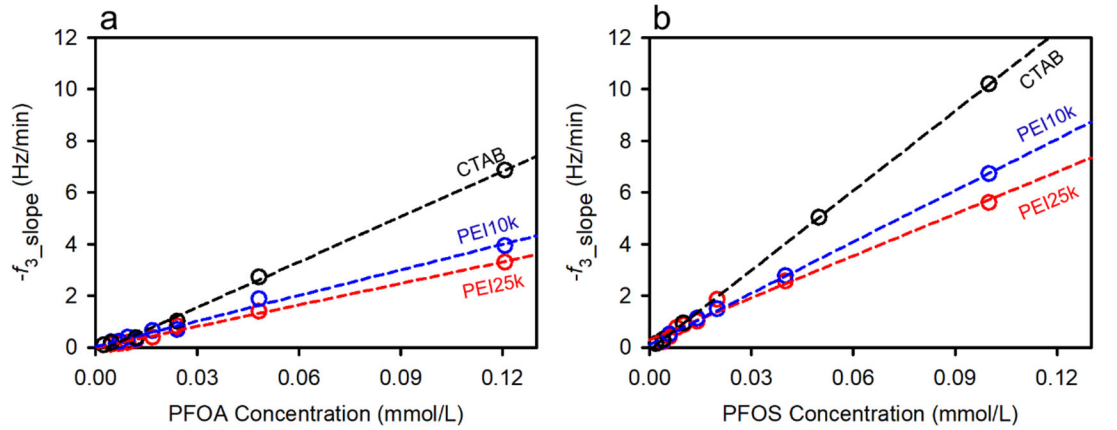


Figure 4.7 Real time deposition rates ($-f_{3_slope}$) of (a) PFOA and (b) PFOS on IONPs with respect to the different surface coating (PEI25k, PEI10k, and CTAB).

Based on both frequency shifts from flowing IONPs and PFAS solutions to Q-sensor, we determined both PFOA and PFOS sorption density of IONPs using deposited mass via the Sauerbrey equation.[228] We confirmed no PFAS was directly attached to quartz crystal sensor without IONPs (**Figure 4.8**), thus any observed frequency shift in the presence of PFAS is due to its association with IONCs. **Figure 4.9** details sorption isotherms for both PFOA and PFOS for IONPs with different surface coatings (PEI25k, PEI10k, and CTAB) as calculated by mass per IONP (mass) via QCM-D. The initial calculated sorption density obtained from QCM-D showed relatively lower values than those from batch sorption tests. Based on our previous research, frequency shifts can be observed with the release of sorbed water associated with certain polymers, thus complicating sorbate association measurements.[229] To address this issue, we developed a correction factor based on calculated mass of water associated with IONCs. In **Figure 4.10**, we present PFAS sorption isotherms on IONPs determined by both batch sorption and QCM-D methods with such correction factors. Overall, corrected sorption data from QCM-D (dotted line) experiments are similar to batch sorption trends and values, which highlights QCM-D as a powerful tool to quantify and compare relative sorption behavior(s) in real time.

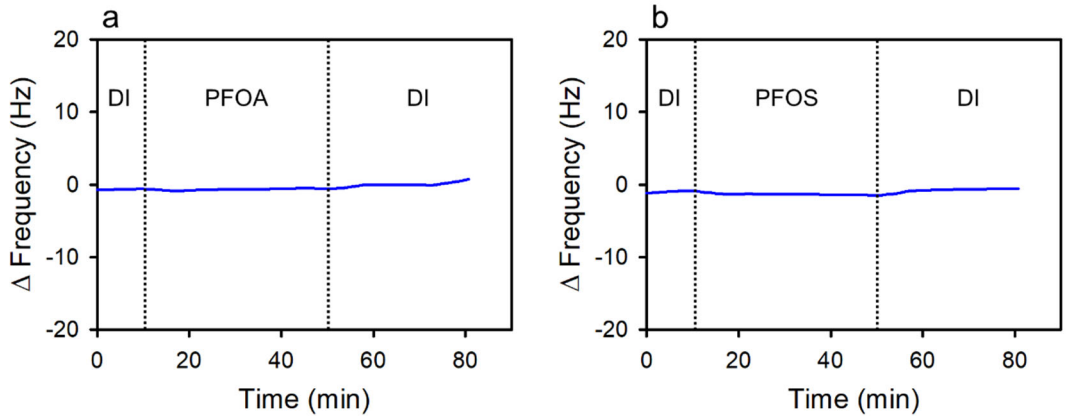


Figure 4.8 Frequency shift of quartz crystal sensor (overtone = 3) with 0.6 mmol/L of (a) PFOA and (b) PFOS solutions at pH 7.

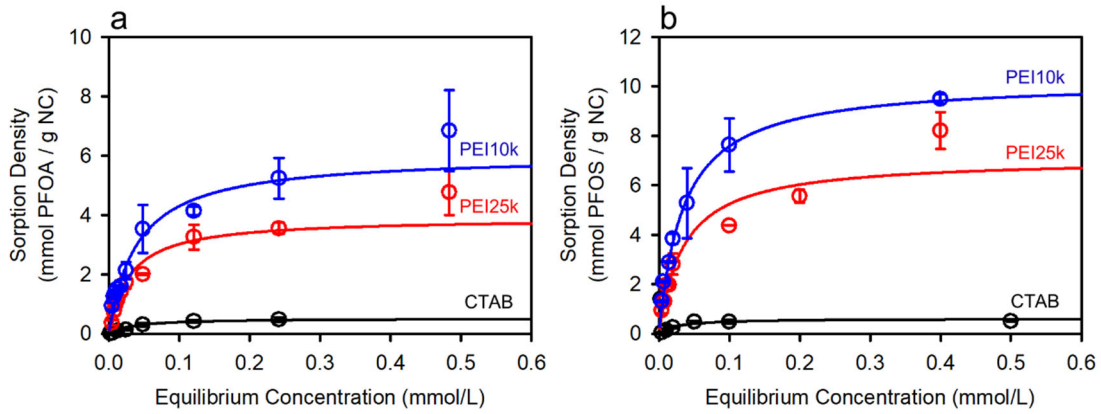


Figure 4.9 (a) PFOA and (b) PFOS sorption isotherm on iron oxide nanocrystals (IONCs) obtained from mass of IONCs deposited on Q-sensor and mole of PFAS attached to IONCs via QCM-D. Note that no correction factor is applied here to consider water sorption.

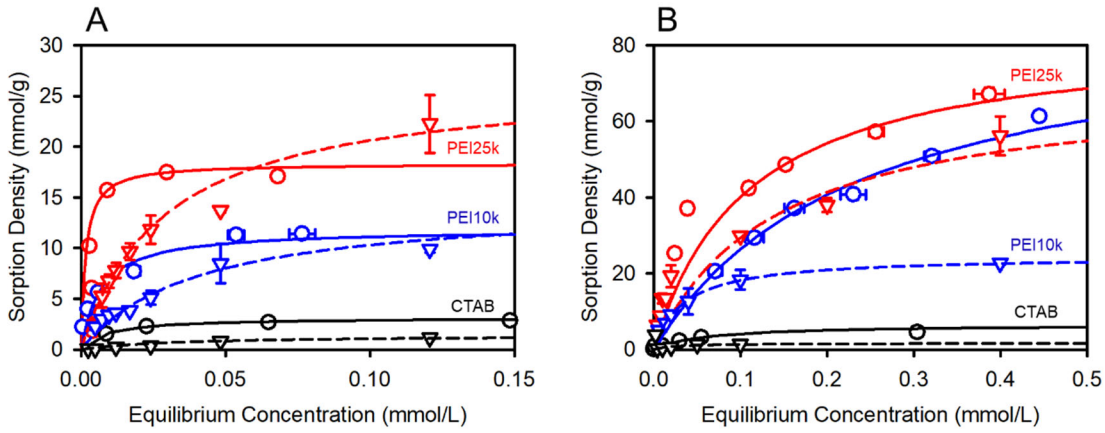


Figure 4.10 (a) PFOA and (b) PFOS sorption isotherm on IONPs obtained via batch (circle dot and solid line) and QCM-D (reverse triangle dot and dotted line) methods. Data for batch sorption is replotted from Figure 1 for direct comparison. QCM-D results are obtained by multiplying QCM-D correction factor with sorption density.

4.1.3 Competitive Sorption of PFAS: Multi-Sorbate System

Multi-sorbate tests considering both PFOA and PFOS were performed to determine competitive effects on isotherm behavior(s) using Fe_3O_4@PEI25k NPs (highest performing material). Sorption isotherms for multi-sorbate systems (both PFOA and PFOS with a molar ratio of 1:1) and single-sorbate are presented in **Figure 4.11a, b**. For these conditions, we observed PFOA sorption was significantly hindered in the presence of PFOS, for which maximum sorption capacity was 18.3 mmol g^{-1} (PFOA as the single sorbate) and 7.0 mmol g^{-1} for multi-sorbate systems, respectively. The sorption density for PFOS was also considerably decreased in the presence of PFOA (88.8 mmol g^{-1} for single (PFOS as single sorbate) and 20.4 mmol g^{-1} for multi-sorbate systems, respectively). For both, sorption capacities in multi-sorbate system were lower than that of single-sorbate test, which is likely due to not only differences in free energy of association, but also steric hindrance(s), among other complicating factors in a competitive, multi-sorbate system.[163, 230] Sorption density of PFOA on IONCs in the multi-sorbate system also decreased at higher equilibrium concentrations (above 0.1 mmol/L), indicating that PFOA molecules adsorbed on IONCs are favorably exchanged, to some degree, by PFOS.

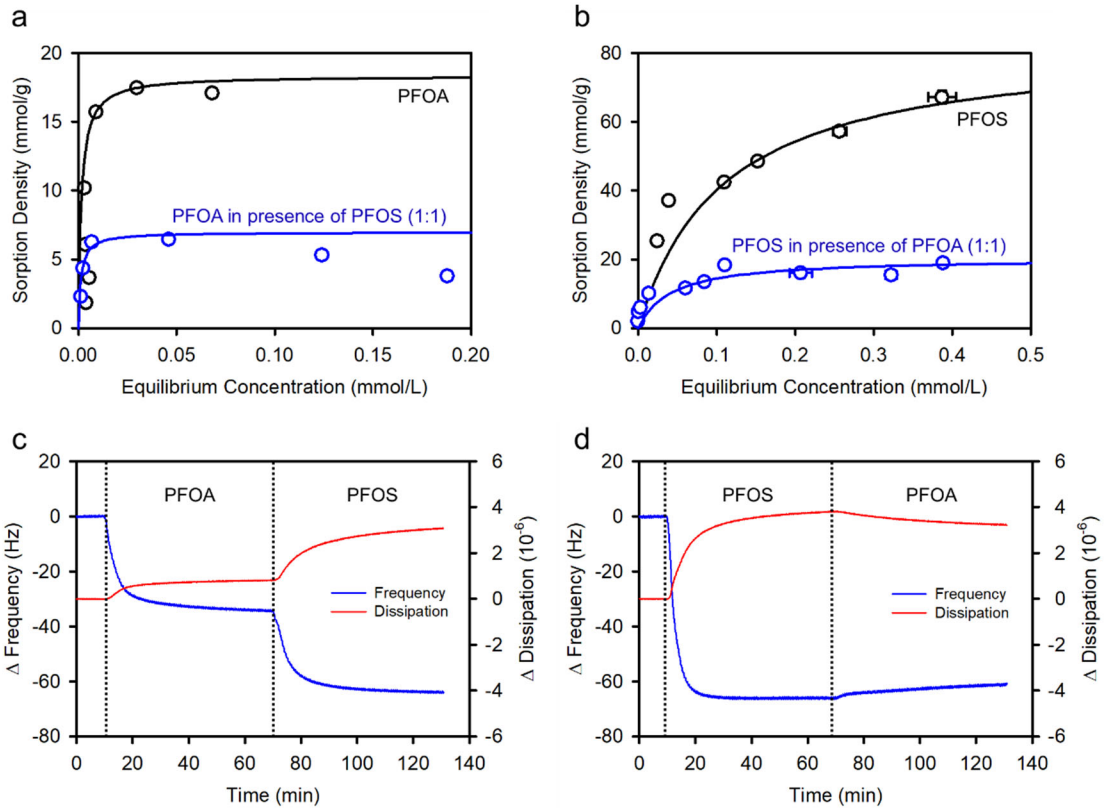


Figure 4.11 Single- and multi-sorption isotherms on PEI coated IONCs for (a) PFOA and (b) PFOS; single-sorbate systems (black line) and multi-sorbate systems (PFOA and PFOS (blue line)). Multi-sorption tests were performed with the same initial concentration of both PFOA and PFOS from 0.02 to 0.1 mmol/L at pH 7. (c-d) Time dependent frequency and dissipation shift (overtone n = 3) of the IONPs coated Q-sensor with introducing both PFOA and PFOS sequentially, and vice versa, by QCM-D analysis.

To further evaluate sorption preference between PFOA and PFOS, real time sorption behavior was evaluated using the QCM-D method described above. To do this, we introduced either 0.6 mmol/L of PFOA or PFOS solutions over IONPs coated Q-sensor sequentially. As shown in **Figure 4.11c, d**, frequency and dissipation shifts associated with PFOA and PFOS sorption events were observed, indicating attachment (sorption) of PFAS on IONPs. After stabilization, we then switched the solutions from PFOA to PFOS and PFOS to PFOA, respectively. We observed additional frequency and dissipation shifts in the system with newly introduced PFOS, indicating molecular exchange and/or additional sorption (**Figure 4.11c**), while no changes in both frequency and/or dissipation were observed when PFOA was introduced to a system with PFOS previously sorbed (**Figure 4.11d**). These observations support batch results, described above, further implicating the key role of the PFAS head group with regard to sorption behavior.

4.1.4 Critical Role of Functional Groups of PFAS on Sorption Behavior

PFOA with carboxylic head group shows a higher affinity to positively charged IONPs than PFOS, resulting in higher Langmuir adsorption constants (k). In comparison, the sulfonic group of PFOS results in a relatively lower k value due to lower bulk affinity compared PFOA; however, PFOS has three different resonance structure(s) which, when taken together, allows for overall more favorable interactions. To explore this directly, we demonstrated the thickness of PFAS layer, as a function of PFAS type, using the Voigt model via QCM-D analysis. With all variables held constant (IONP, water chemistry, etc.) except for PFAS type, **Figure 4.12** shows that a difference between PFOA and PFOS sorbed layers is about 5 angstrom (Å), indicating the orientation of sorbed PFAS is different based on the functional head groups. For these, on average PFOS is likely more vertically aligned on the surface of IONPs due to the resonance structure of sulfonic group, while PFOA aligns in a more horizontal fashion (on average), which is also supported by the maximum sorption values observed (i.e., higher sorption density is possible with vertically oriented PFOS). Differences in sorbed orientation between PFOA and PFOS may also contribute to the relative recalcitrance of PFOS relating to steric hindrance and/or active site distance from a reactive material surface(s).

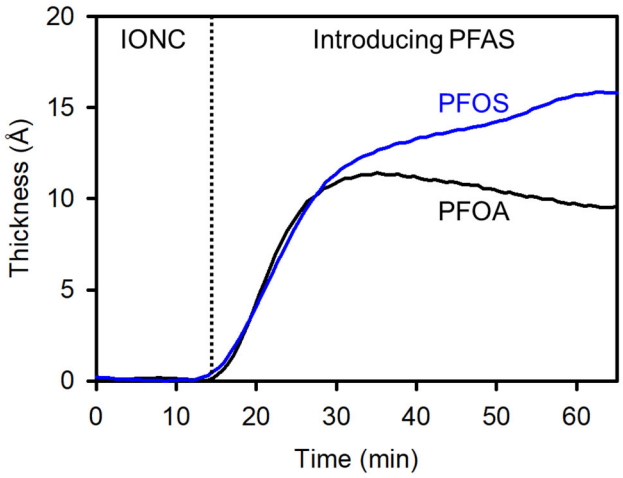


Figure 4.12 Thickness of the attached layer of PFOA and PFOS on the IONC coated Q-sensor obtained as calculated by the Voigt model via frequency shift (*f*) and dissipation (*D*) during PFAS sorption.

4.1.5 Effect of Water Chemistry on PFAS Sorption Behavior

To understand how water chemistry affects PFAS sorption behavior, we evaluated PFAS sorption using Fe_3O_4@PEI25k as a function of solution pH, ionic strength and type, and NOM in water. **Figure 4.13a, b** shows that higher sorption densities were observed under both acidic (pH 4.0) and neutral (pH 7.0) conditions, compared to basic conditions (pH 10.0), as expected. The maximum sorption capacity was 14.7 mmol g^{-1} at pH 4.0, 18.3 mmol g^{-1} at pH 7.0, and 9.2 mmol g^{-1} at pH 10.0 for PFOA, and 58.8 mmol g^{-1} at pH 4.0, 83.5 mmol g^{-1} at pH 7.0, and 38.5 mmol g^{-1} at pH 10.0 for PFOS, respectively. The observed decrease in sorption at higher pH values was attributed to a decrease in surface zeta potential, and thus, a lower electrostatic affinity for negatively charged PFAS molecules (**Figure 4.14**). We also observed a decrease in maximum sorption capacity at lower pH (pH 4) compared to neutral pH (pH 7). As reported by others, acidic conditions can affect PFAS sorption.[162] Here, a net decrease in zeta potential (ca. 14% from pH 7 to pH 4) likely contributes to a lower (maximum) sorption capacity at pH 4.

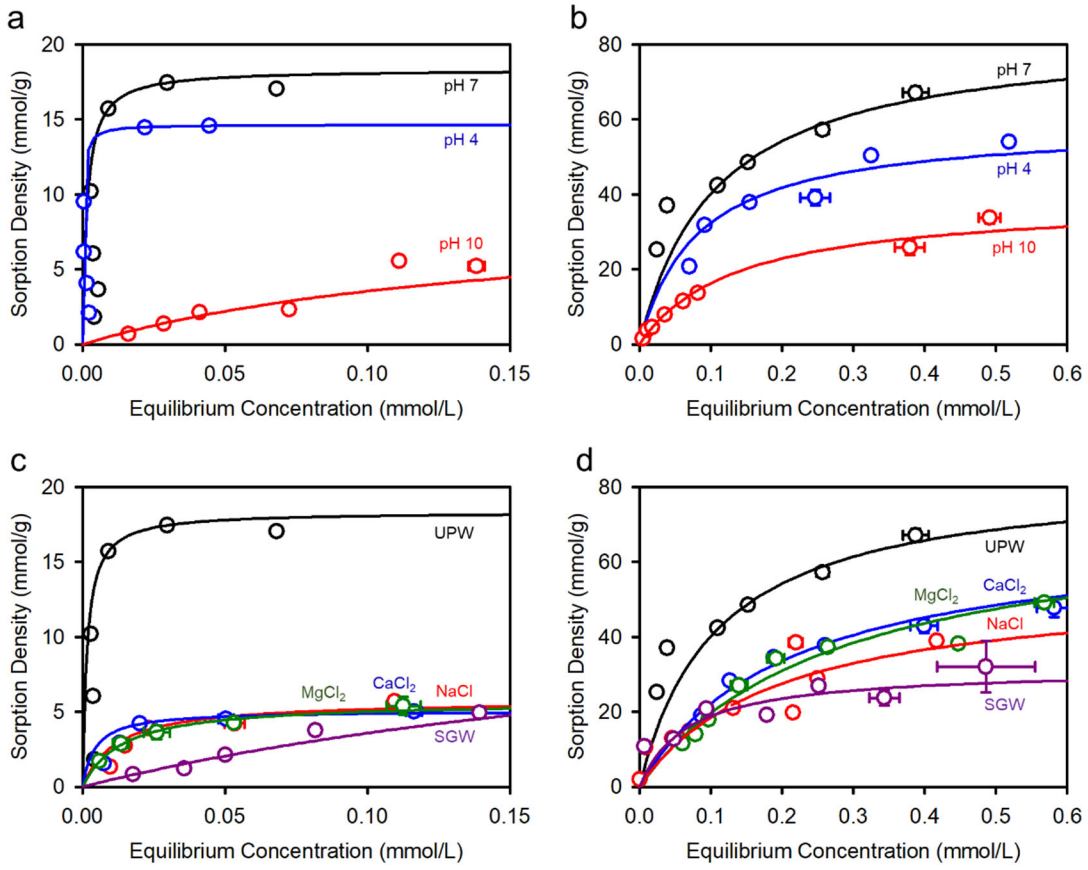


Figure 4.13 (a) PFOA and (b) PFOS sorption isotherm on PEI-coated IONPs (Fe_3O_4@PEI25k) as a function of pH (4.0 (blue), 7.0 (black), and 10.0 (red)). Sorption isotherm for (c) PFOA and (d) PFOS with different water chemistry of ultrapure water (UPW, black), NaCl (red), $CaCl_2$ (blue), $MgCl_2$ (green), and synthetic groundwater (SGW, purple), respectively. Total ionic strength for all solutions was adjusted to be identical with SGW.

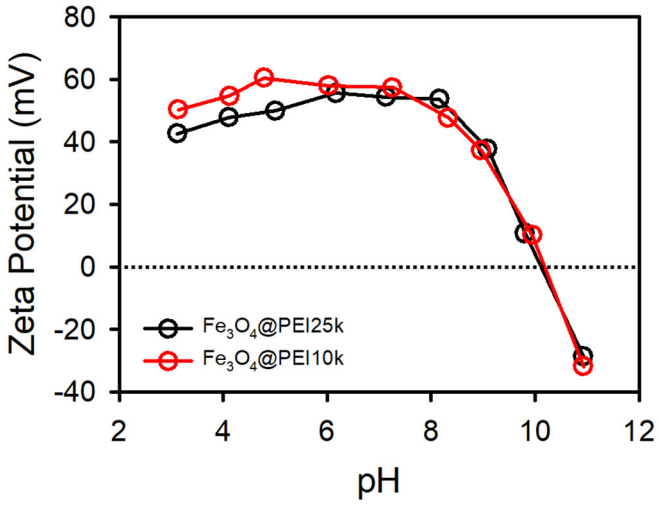


Figure 4.14 Zeta potential of PEI coated IONCs with different molecular weight (25k and 10k) as a function of solution pH.

The effect of ionic strength and type on PFAS sorption was also evaluated using Fe_3O_4@PEI25k NCs via batch sorption experiments at pH 7. Here NaCl, $CaCl_2$, $MgCl_2$, were evaluated along with a synthetic groundwater (SGW) and compared with ultrapure water (UPW). Synthetic groundwater was prepared as described by others,[231] and the composition is summarized in **Table 4.3**. As shown in **Figure 4.13c–d**, sorption capacities for both PFOA and PFOS decreased in the presence of all salts evaluated and the synthetic groundwater. The maximum sorption densities for PFOA were observed to be 18.3, 5.7, 5.1, 5.7, and 14.3 mmol g^{-1} for ultrapure water, NaCl, $CaCl_2$, $MgCl_2$, and synthetic groundwater, respectively, and 83.5, 54.3, 69.0, 73.7, and 31.5 mmol g^{-1} for PFOS for ultrapure water, NaCl, $CaCl_2$, $MgCl_2$, and synthetic groundwater, respectively. We observed competitive effects of ionic species on PFAS sorption performance, with similar or higher hindrance observed for NaCl compared to $CaCl_2$ and $MgCl_2$. This is likely due to the competitive effect(s) of counterions, here as anions, on positively charged IONPs in which concentration of counter ion (Cl^-) in NaCl is higher than divalent cations ($CaCl_2$ and $MgCl_2$) for identical ionic strengths. Despite these interferences, material performance under real world conditions remains considerably higher than other reported sorbents which only considered pure water (i.e., best case scenario), **Table 2.1**. For all suspensions evaluated, no IONP aggregation was observed under any condition evaluated (**Figure 4.15**), thus minimizing the loss of surface area as a confounding performance factor.

Table 4.3 Ionic composition of synthetic groundwater.

Ion	Na^+	Ca^{2+}	Mg^{2+}	HCO^{3-}	Cl^-	HPO_4^{2-}	SiO_3^{2-}
Conc. (mmol/L)	10.4	2.5	1.6	8.2	8.2	0.1	1

PFAS sorption capacities also decreased in the presence of NOM (0–0.5 mg/L). To quantify this process, we evaluated the role of humic acid (HA) concentration on sorption density via QCM-D analysis. As shown in **Figure 4.16**, sorption densities decreased with increase of HA concentration. HA, with a large cation exchange capacity, readily competes in bulk with positively active sites on IONPs for PFAS sorption, as observed by others for negatively charged pollutants.[232, 233]

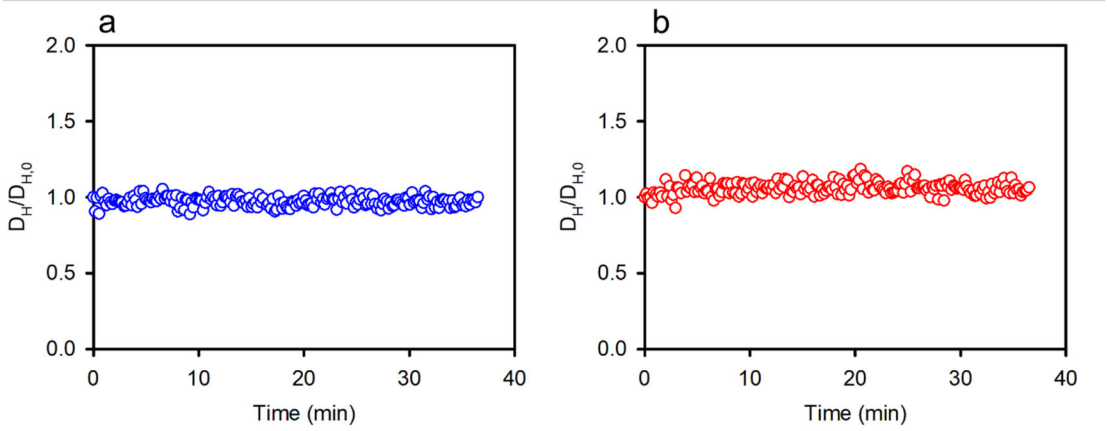


Figure 4.15 Aggregation profile of Fe_3O_4@PEI25k NCs in the presence of (a) 1000 mmol/L of NaCl and (b) 1000 mmol/L of $CaCl_2$ concentrations at pH 7.

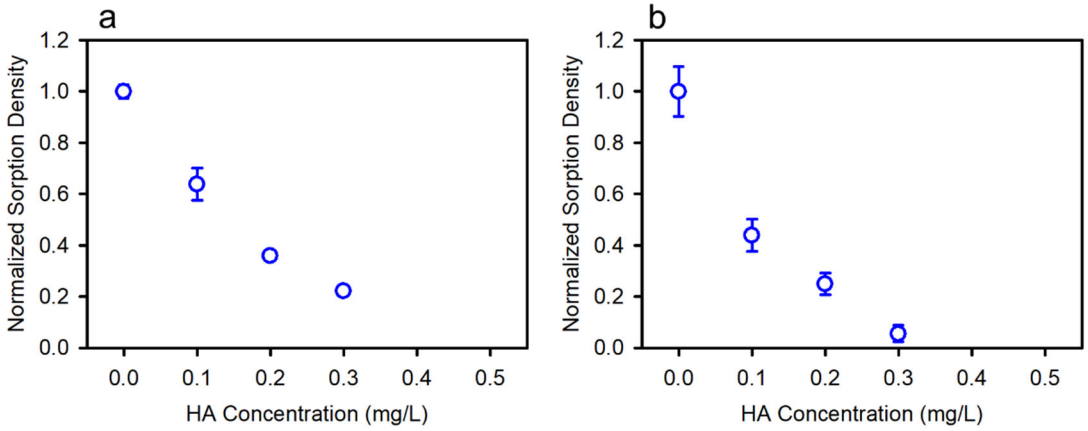


Figure 4.16 Normalized sorption density for (a) PFOA and (b) PFOS on Fe_3O_4@PEI25k NCs as a function of humic acid (HA) concentrations via QCM-D method.

4.1.6 Sequestration of PFOA and PFOS in Column Studies

To demonstrate application potential, effluent breakthrough curves obtained following the injection of solutions containing PFOA or PFOS into columns packed IONC treated Ottawa sand are shown in **Figure 4.17**. For the PFOA column study, a solution containing 100 µg/L PFOA in 10 mmol/L NaCl was introduced for 10 pore volumes (PVs), with no detectable levels of PFOA observed in effluent samples. To assess the limiting adsorptive capacity of the IONP-treated sand, the influent concentration of PFOA was then increased to 10 mg/L (considered as a very high environmental PFAS concentration), which resulted in detection of PFOA after approximately 31

PVs. The concentration of PFOA increased steadily to a relative concentration (C/C_0) of 0.83 after 39 PVs, and reached the influent concentration ($C/C_0 = 1$) at 49 PVs (**Figure 4.17a**). Over the course of the experiment, a total of 5.16 mg of PFOA were retained, which corresponds to 5.37 mmol/L PFOA per g of IONC (2.34 mg total IONP in the column), consistent with batch sorption results.

For the PFOS column study, a solution containing 100 µg/L PFOS in 10 mmol/L NaCl was introduced for approximately 10 PVs with no detectable levels of PFOS observed in the column effluent. Similar to the PFOA column study, the concentration of PFOS in the influent solution was then increased to 10 mg/L and PFOS was subsequently detected in the effluent after approximately 23 PVs, and increased steadily to the influent concentration ($C/C_0 = 1$) after 39 PVs (**Figure 4.17b**). Overall, a total of 6.34 mg of PFOS was retained in the IONP-treated column, which corresponds to 5.18 mmol/L PFOS per g of IONPs (2.45 mg total in the column), also in line with batch studies. When compared to control columns conducted with clean 40-50 mesh Ottawa sand, retention, thus treatment, of PFOA or PFOS in IONP-treated columns increased by more than three orders of magnitude, suggesting potential as a new sorbent material for in situ treatment processes.

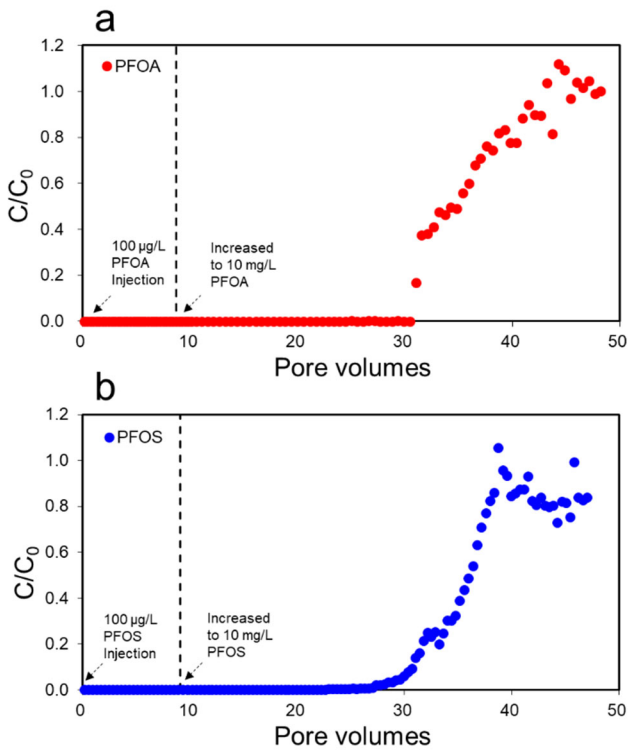


Figure 4.17 Effluent breakthrough curves for (a) PFOA and (b) PFOS in columns packed with IONCs (2.9 mg) treated 40-50 mesh Ottawa Sand (80 g).

4.2 Enhanced Photocatalytic Oxidation of PFOA with Functionalized Metal Organic Framework (MOF) Composite Materials

4.2.1 PFOA Degradation by TiO2/MOF Composites

MOF encapsulation and/or incorporation procedure was demonstrated with 20 nm titanium dioxide (TiO_2) nanoparticles (NPs) with zeolitic imidazoleframework−8 (ZIF−8) materials. Typically, synthesis included zinc nitrate (Zn) and 2−methylimidazole mixed in methanol and desired amount of TiO_2 NPs (20, 50, 100, 500, and 1000 mg) with continuous magnetic stirring at room temperature for 24 h. **Figure 4.18** showed SEM images of TiO_2/ZIF−8 composite materials with varied concentration of TiO_2 NPs. With these materials, we studied the photocatalytic degradation of PFOA under UV−C (254 nm) irradiation (**Figure 4.19a**). When the amount of TiO_2 NPs increased from 20 to 100 mg (10 mg/L PFOA), the reaction rate constants and conversion efficiency increased, while negligible or negative effects observed over 100 mg. **Figure 4.20** shows the concentration evolution(s) of related byproducts, which is in accordance with observed rate constants for PFOA degradation. To further alter MOF particle and pore size, we varied the ratio of precursor concentrations as described in the above procedure (zinc nitrate solution (zinc nitrate hexahydrate (Zn) and 2−methylimidazole solution). **Figure 4.19b** shows degradation of PFOA using different concentrations of TiO_2 (100 and 500 mg) on modified ZIF−8 synthesized with 1:1 ratio of precursors. For these, we observed slight increase in conversion efficiency using ZIF−8 with 1:1 ratio, which showed larger crystalline structure(s) compared to ZIF−8 with 1:6.7 precursor ratio(s).

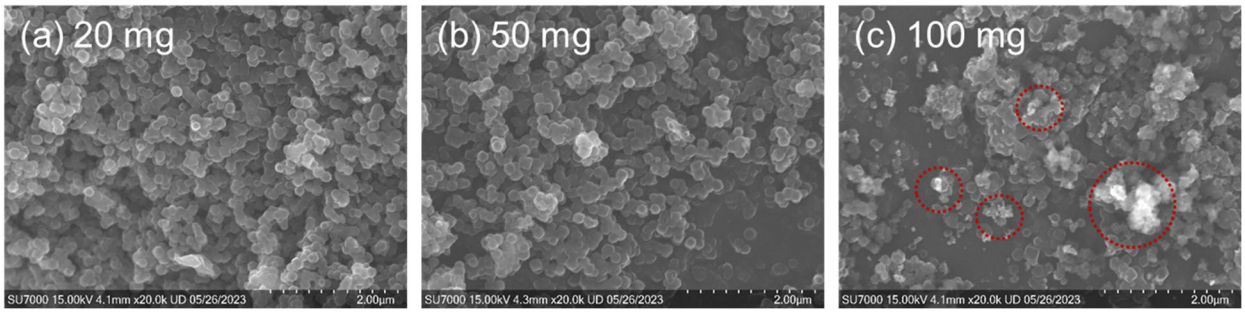


Figure 4.18 SEM images of TiO_2/ZIF−8 composite materials with varied concentration of TiO_2 NPs.

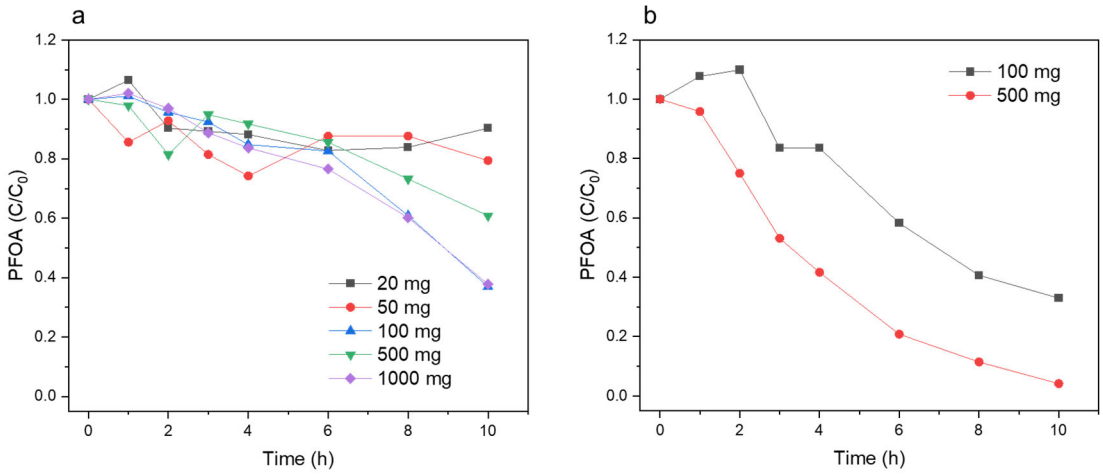


Figure 4.19 Concentration-time profiles for PFOA degradation using ZIF−8 synthesized with different ratios of precursor ratios of (a) 1:6.7 and (b) 1:1. All experiments were performed at pH 3 under UVC irradiation. Initial concentration of PFOA is 10 mg/L.

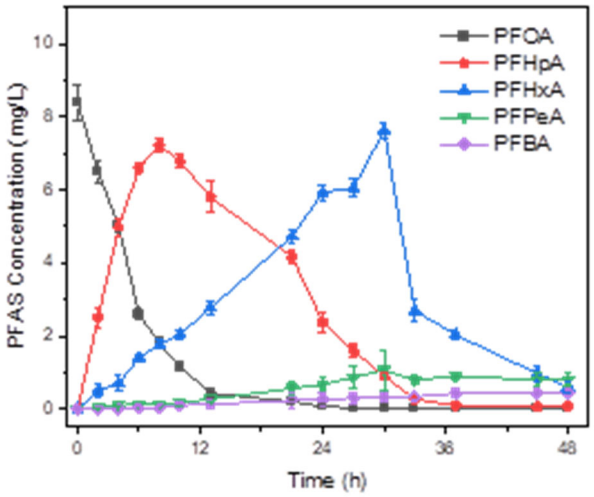


Figure 4.20 Concentration profiles of related byproducts, which is in accordance with observed rate constants for PFOA degradation

4.2.2 Enhancing MOF Composite Photocatalytic Activity

Building on results presented above, we further functionalized ZIF−8 (MOF) materials with surface amine groups through both *in−situ* and post synthesis procedures to improve removal efficiency for PFOA. The crystalline structure of functionalized TiO_2/ZIF−8 composite materials was determined via XRD analysis (**Figure 4.21a**). The NH_2−TiO_2/ZIF−8 prepared with a methanol-based method showed consistent peaks with TiO_2/ZIF−8, while no ordered (crystalline) structure was observed using a solvothermal method(s), indicating that the crystalline structure of

ZIF−8 can be disrupted during functionalization. **Figure 4.21b** shows PFOA degradation performance with pristine and functionalized TiO_2/ZIF−8 composite materials, where enhanced reactivity is achieved with the methanol-based method; PFOA transformation was observed at 67, 85, and 62% for pristine, methanol, and solvothermal-based methods over for 10h, respectively (10 mg/L PFOA, UVC light, pH 3). For these, amine functionalization not only enhances PFOA sorption affinity via electrostatic interactions, providing more/stronger adsorbing sites, but also likely affecting (net) material band gap(s).

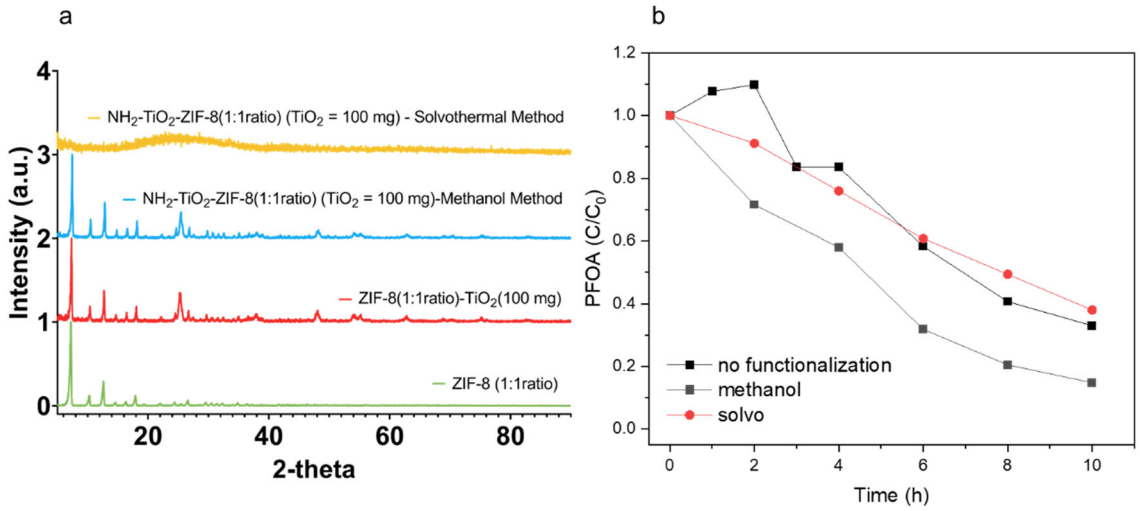


Figure 4.21 (a) XRD analysis for various materials including ZIF−8, TiO_2/ZIF−8, functionalized TiO_2/ZIF−8 via methanol and solvothermal methods. (b) Concentration−time profiles for PFOA degradation using TiO_2/ZIF−8, functionalized TiO_2/ZIF−8 via methanol-based and solvothermal-based methods. Initial concentration of PFOA is 10 mg/L and 200 mg/L of each materials were applied.

4.2.3 Proposed Reaction Mechanisms

To further explore the PFOA reaction mechanism for MOF-based materials, we conducted radical scavenging experiments using (dissolved) methanol and tert-butyl alcohol (TBA). As shown in **Figure 4.22a**, transformation rates significantly decreased with both methanol (only 14%), and TBA (36%), compared to 85% transformation without any scavenger(s) for 10 h reaction. To further evaluate the role of potential radical species, we tested PFOA degradation using hydrogen peroxide (H_2O_2), peroxymonosulfate (PMS), and peroxydisulfate (PDS) (for generation of hydroxyl and sulfate radicals). As shown in **Figure 4.22b**, we observed little transformation in the presence of both radical scavengers.

To further understand PFOA reaction pathway(s), the concentration profiles of PFHpA, PFHxA, PFPeA, and PFBA were evaluated over longer term reaction experiment (48 h) are shown in **Figure 4.23**. The temporal profiles of PFHpA, PFHxA show a stepwise evolution from longer chain to shorter chain PFCAs, in agreement with a chain shortening (oxidative) mechanism, which is similar to what has been proposed by others.[181, 234, 235]

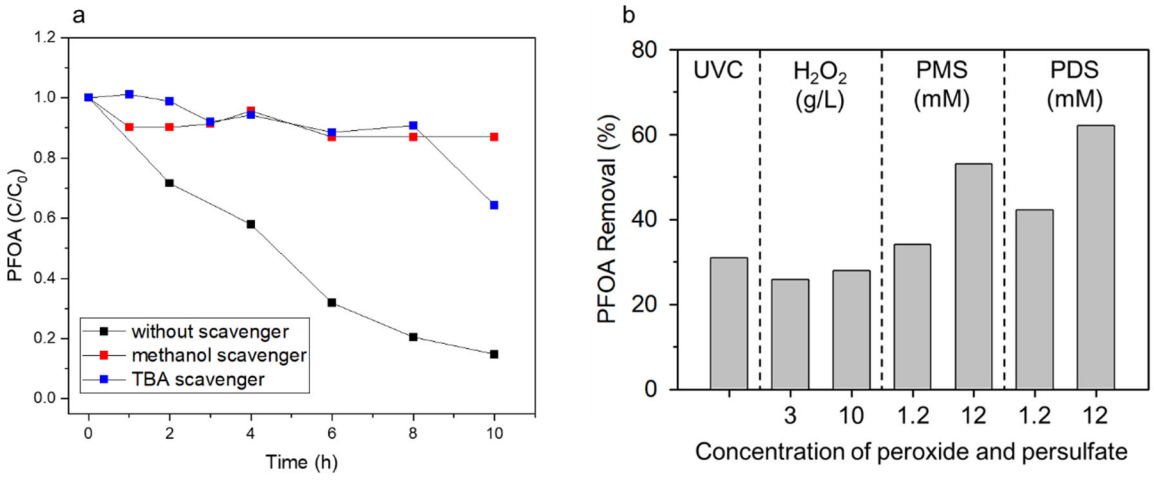


Figure 4.22 (a) PFOA degradation in the presence of various scavengers including methanol and TBA compared to no scavenger (1:1, methanol-based modified ZIF-8 and TiO_2). (b) PFOA removal with different concentrations of hydrogen peroxide (H_2O_2, 3 and 10 g/L), peroxymonosulfate (PMS, 1.2 and 12 mM), and peroxydisulfate (PDS, 1.2 and 12 mM) under UVC irradiation (254 nm) for 24 h. Initial PFOA concentration is 10 mg/L for all.

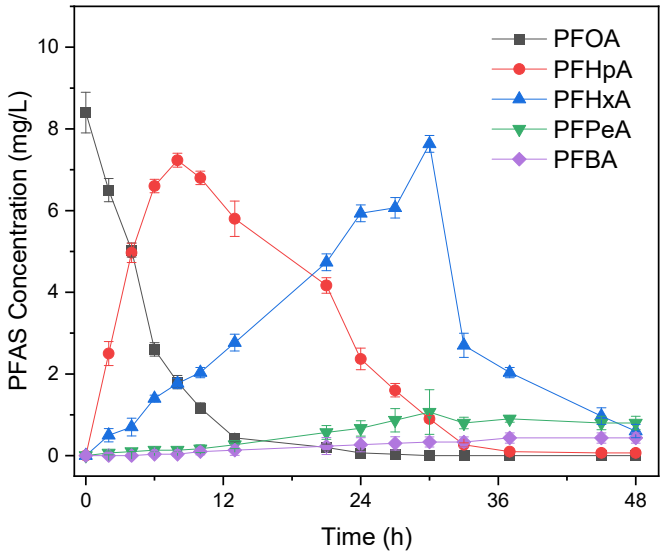


Figure 4.23 Concentration profiles of PFOA, PFHpA, PFHxA, PFPeA, and PFBA using 200 mg/L of functionalized TiO_2/ZIF−8 composite materials under UVC irradiation. Initial concentration of PFOA is 10 mg/L and all experiments conducted at pH 3 under UVC irradiation.

4.3 Development of Novel Electrochemical Oxidation Reaction for PFOS Transformation

4.3.1 Morphological Features and Characterization of CNTs−NF Electrodes

CNT-based heterostructure electrodes were synthesized on Ni foam (NF) via a CVD process (at 700℃ in a tube furnace). In situ CNT growth was enhanced by metallic Pt catalysts on top of the pure Ni foam surface, as shown in **Figure 4.24**. FE−SEM images of CNTs−NF 'films' in **Figure 4.25a, b** show full CNT coverage while being a highly interconnected structure of porous nickel foam after the CVD process. The selected area electron diffraction (SAED) pattern of CNTs-NF shows arrays of hexagonal symmetrical diffraction spots that are indicative of highly crystalline CNTs structures (**Figure 4.25d**). The presence of another hexagonal lattice structure, forming cylindrical nanostructures assisted by the Pt catalysts, was misaligned with the innermost pattern, which suggests the CNTs were grown on the NF film itself. The FE-SEM image (**Figure 4.25a, b**) and TEM images in **Figure 4.25c** show multiple-walled CNTs which are 5–10 nm in diameter and several micrometers in length. Growing high-density carbon nanotubes (CNTs) directly on bare nickel foam is challenging due to the difficulty of diffusion of the carbon onto the nickel substrate during the high-temperature CVD processes, especially when no barrier layers are present. Here, we employed graphene as an anti-diffusion layer against the Pt catalyst, supporting CNT growth via the formation of a favorable interface (between graphene and CNTs). Such an interface not only offers substantial surface area but also facilitates a smooth, conductive electrical path, enhancing electron flow/transfer. FE-SEM images presented in **Figure 4.26**, reveal the intricate porous architecture inherent to a pristine NF template. Additionally, it is evident that the surface is adorned with nickel grains that differ markedly in both size and morphology. In spite of these disparities, the G-NF and NG-NF samples maintain features that are suggestive of the open-cell NF template, as demonstrated in **Figure 4.26c, e**.

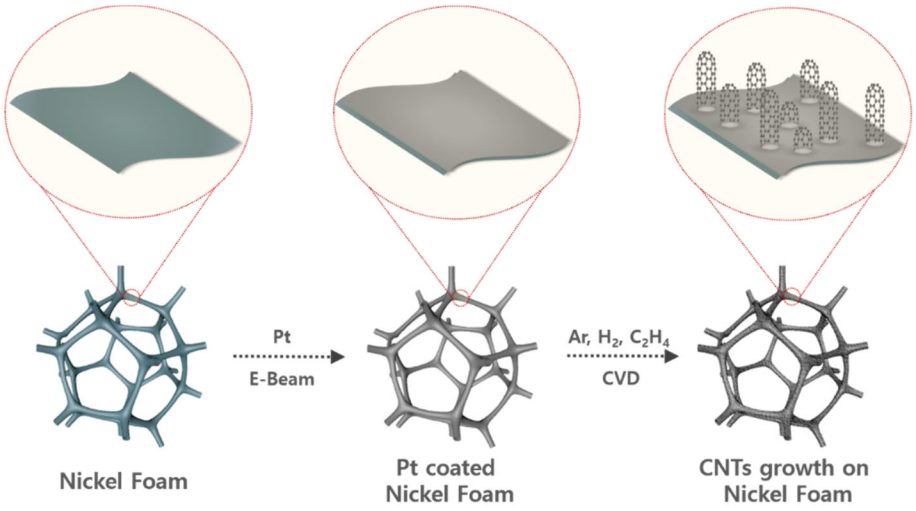


Figure 4.24 Scheme of CVD process of CNTs-NF electrode.

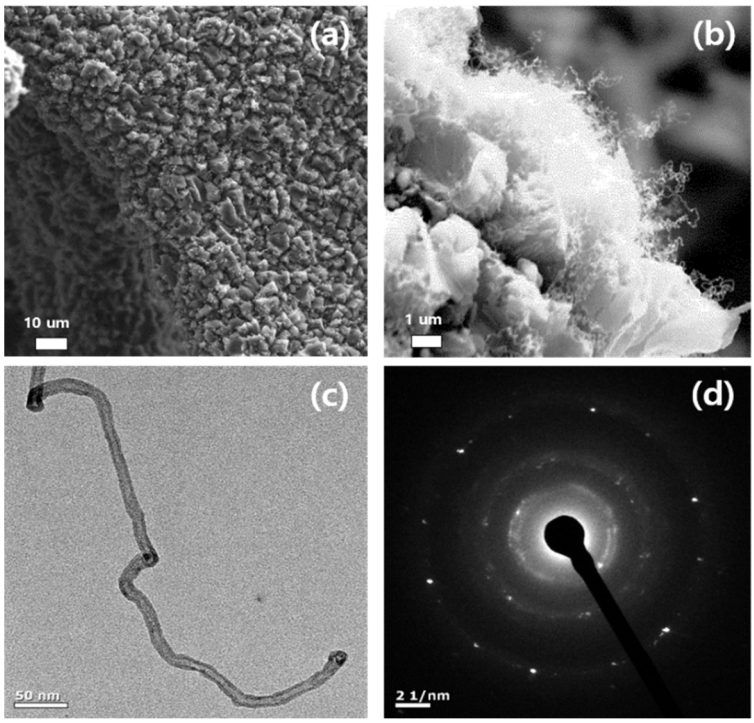


Figure 4.25 FE-SEM images of CNTs-NF with (a) low resolution, (b) high resolution, HR-TEM images of (c) CNTs-NF, and (d) SAED patterns, respectively.

Three major diffraction peaks, indexed as the (111), (200), and (220) lattice planes of pure Ni (JCPDS card no. 04-0850), are observed in the XRD patterns of pristine NF, G-NF, NG-NF, and CNTs-NF[236]. The growth of CNTs via CVD show a broad peak at $2\theta = 26.7°$ that corresponds to the (002) plane of graphitic-like structures (**Figure 4.27c**), indicating the presence of multiple CNTs on the NF template. Further structural studies on the CNTs-NF electrode were conducted by Raman spectroscopy. Given the lack of homogeneity of (MW)CNTs, spectra were collected from 10 random sample spots to obtain an average spectrum. For these, two major bands are observed, corresponding to D and G bands of carbon. The G band at 1585 cm^{-1} corresponds to the vibrations of sp^2 bonded carbon atoms as part of two-dimensional hexagonal lattices, confirming crystalline graphite phase(s). The observed D band appears at 1345 cm^{-1}, which is typically associated with carbon atoms with dangling bond, which arise at plane termination(s) of disordered graphite, or in the presence of amorphous carbon[237].

Figure 4.27 shows XPS survey spectrum of pristine NF, G-NF, NG-NF, and CNTs-NF electrodes. The peak at 856.34 eV is due to the oxidized Ni species arising from the superficial oxidation of Ni_2P via Ni−POx formation.[15] The satellite peak at 861.5 eV and the peak at 873.1 eV can be assigned to NiO, arising from the surface oxidation of NF electrode.[238]. Successful surface loading of graphitic carbon is confirmed by the C 1s XPS spectra of the G-NF, NG-NF, and CNTs-NF samples prepared, for which characteristic of sp^2 carbon peak is observed at 284.7 eV.[239] A comparison of the XPS survey spectra of G-NF and NG-NF show the explicit incursion of nitrogen atoms into the carbon lattice, indicating that NH_3 serves as a nitrogen source introduced concurrently with the carbon precursor. Successful surface loading of graphitic carbon via the exposure of NF to the CVD process was confirmed by the C 1s XPS spectra of the G-NF, NG-NF,

and CNTs-NF samples (Figure 4.3.3), for which the peak characteristic of sp^2 carbon is observed at 284.7 eV. The C 1s XPS peak had an asymmetric tail toward the higher binding energy, implying the presence of mono-oxidized fraction (as a minor component).

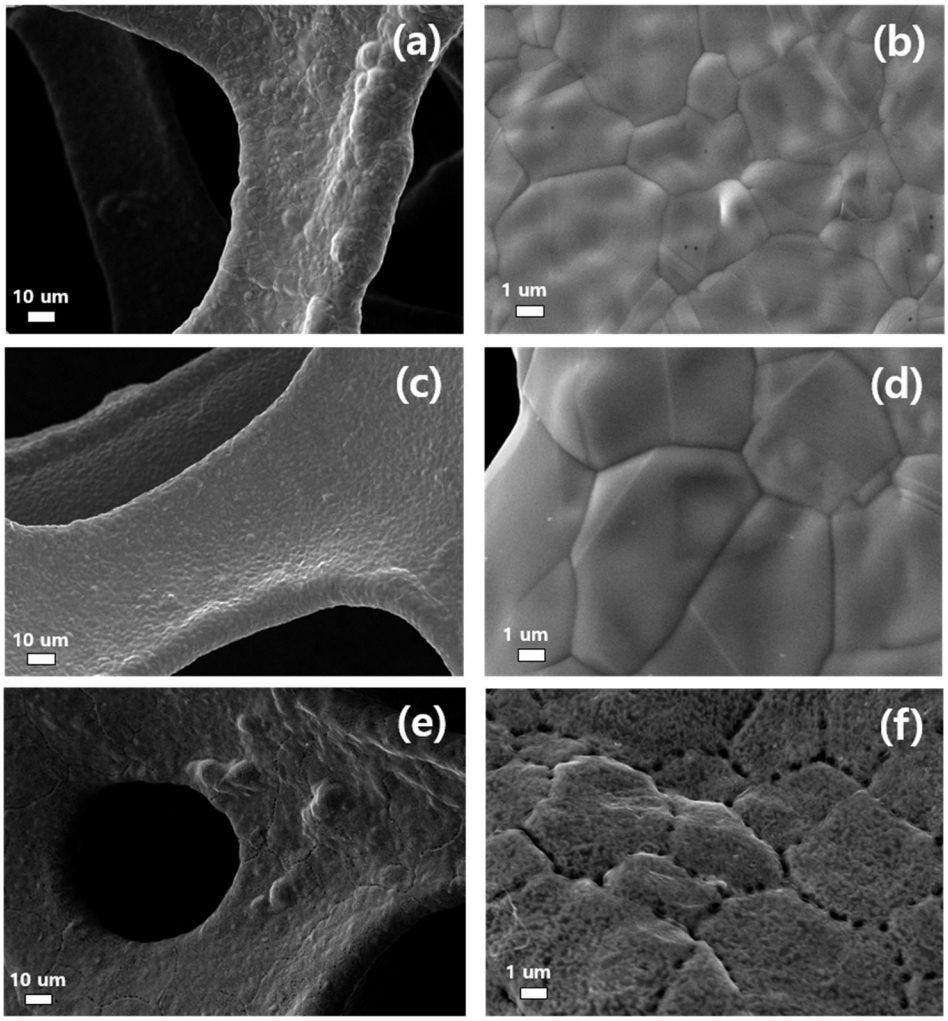


Figure 4.26 FE-SEM images of (a-b) pristine Ni, (c-d) G-Ni, (e-f) NG-NF, and (g-h) CNTs-Ni.

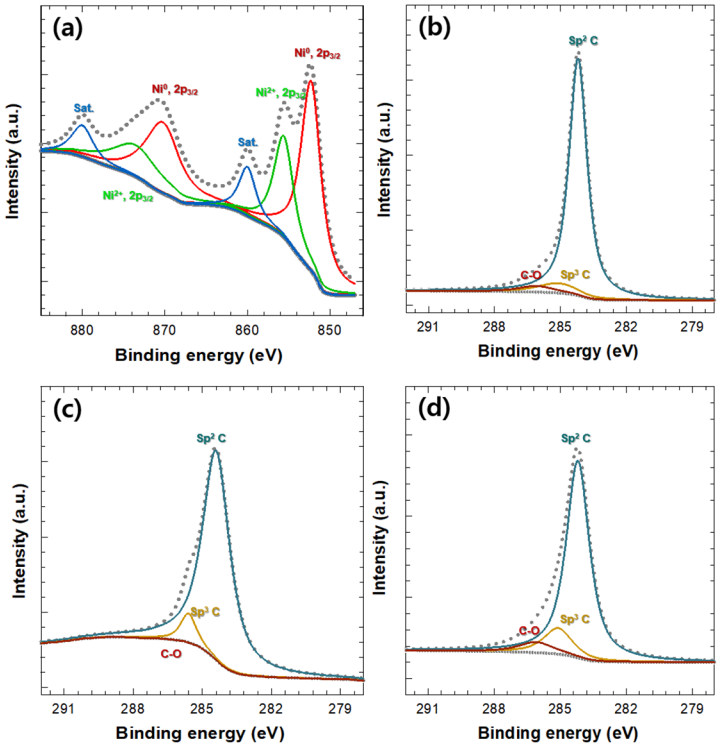


Figure 4.27 XPS spectra of (a) Pristine NF, (b) G-NF, (c) NG-NF, and (d) CNTs-NF, respectively.

4.3.2 Enhanced PFOS Degradation with Carbon-based NF Cathodes

To understand the primary role of $^{\bullet}OH$ and $SO_4^{\bullet-}$ based reactions for PFOS degradation, we assessed transformation efficiency using UV-based advanced oxidation processes (UV-AOPs) with the addition of H_2O_2 and peroxydisulfate (PDS) oxidants (10 mM) as controls. Exposure of PFOS to sulfate and OH radicals resulted in minimal PFOS breakdown and no fluoride release during 1 hour of UV photolysis (254 nm radiation at 6.4 W/cm^2). This suggests that, as dissolved, $^{\bullet}OH$ and $SO_4^{\bullet-}$ are relatively unreactive with PFOS alone, as seen in **Figure 4.28** (transformation rate comparison). For the electrochemical oxidation (EO) system employing a BDD anode and CNTs-based cathode, high degradation rate of PFOS was observed (0.0753 min^{-1}) with SO_4^{2-} electrolyte. In contrast, when using NaCl, NaOH, and KOH electrolyte solutions, degradation rates of PFOS were markedly lower at 0.0073, 0.0039 and 0.0036 min^{-1}, respectively (**Figure A.29**). We also evaluated the electrochemical activation efficiency of BDD with different carbon composite electrodes for PFOS degradation. As shown in **Figure 4.28**, the CNTs-NF electrode demonstrated a markedly higher removal rate compared to pristine NF, G-NF, and NG-NF (which gave rate constants of 0.0125, 0.0138, and 0.0278 min^{-1}, respectively). The efficiency of PFOS degradation correlates with the evolution of fluoride ion (F^-) release (from PFOS defluorination). This observation indicates that the reduction in PFOS concentrations can be attributed both to the physical properties of CNTs such as their vast surface areas electrical properties (which enhance active sites for pollutant adsorption); and to their ability to generate surface-bound reactive sulfate radicals when reacting with anodically-produced PDS during the electrolysis period (60 min). As shown in Figure S17, we note a sequential increase in PDS concentration in the following order: CNTs-NF > NG-NF > G-NF > Pristine NF. This indicates a higher generation of sulfate radicals

in the BDD/CNTs-NF configuration within a standard cell, enhancing the PFOS degradation efficiency.

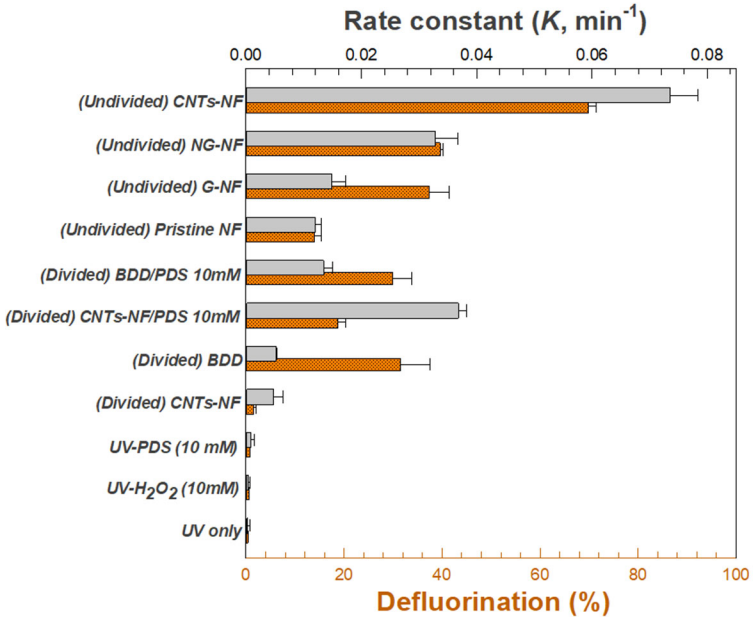


Figure 4.28 Comparative results of PFOS removal efficiency through the use of different electrode types under different conditions ($[PFOS]_0$ = 20 mg/L, $[Na_2SO_4]_0$ = 100 mM, [Applied current density] = 50 mA/cm^2, $[pH]_i$ = 6).

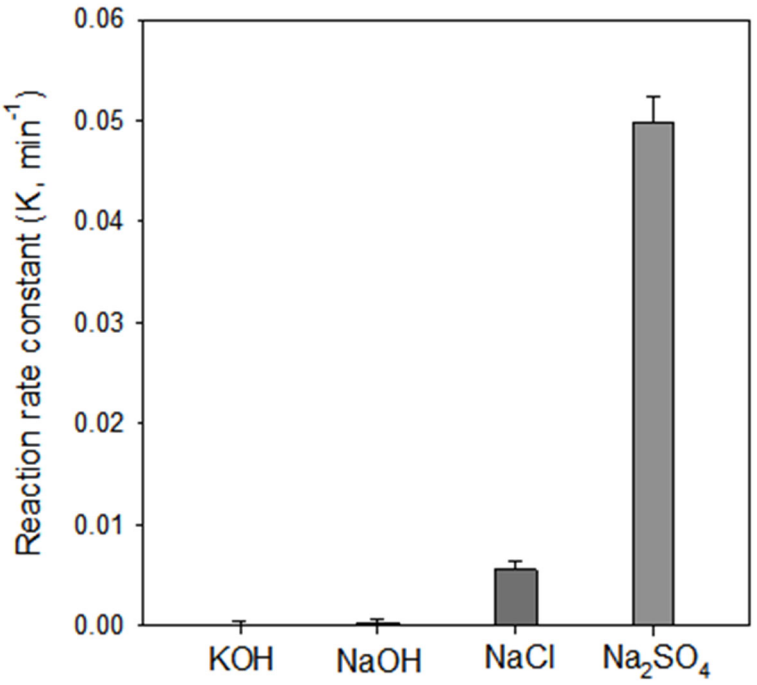


Figure 4.29 PFOS removal efficiency in different types of electrolyte ($[PFOS]_0$ = 20 mg/L, [KOH, NaOH, NaCl, $Na_2SO_4]_0$ = 100 mM, [Applied current] = 50 mA/cm^2, $[pH]_i$ = 6).

Building on these findings, we further explored the electrochemical interaction between PDS and the CNTs-NF cathode. For this, we intentionally introduced PDS (10 mM) to the CNTs-NF cathode chamber in a divided cell configuration and monitored the PFOS removal efficiency. When using the carbon-coated NF electrode, there was a marked decomposition of PFOS following the addition of PDS. This is likely attributed to a synergetic effects of enhanced PFOS adsorption via large surface of CNTs and the generation of surface-bound sulfate radicals[240]. Together, such interfaces can kinetically accelerate the reductive transformation of PDS to $SO_4^{\bullet-}$ on sp^2 carbon surfaces[241]. Conversely, when in direct contact with NF, there was a noticeable decrease in reactivity with PDS, resulting in fewer radical species being generated during cathode reduction in a split cell mode.

4.3.3 Mechanistic Investigation Based on Surface of CNTs-bound Sulfate Radicals

To investigate how CNTs-NF function as an reactive cathode facilitating PFOS oxidation via PDS activation, we monitored the concentration profiles of PFOS and PDS over a 1-hour electrolysis period. We used various cathodes for this study, including pristine NF, G-NF, NG-NF, and CNTs-NF. EPR spectra from the BDD anode showed the presence of •OH and $SO_4^{\bullet-}$ radicals, highlighting the key role of electrolyte-derived oxidants in the electrochemical oxidation process. The generation of these radicals, stemming from the one-electron oxidation of SO_4^{2-} at the BDD anode and their subsequent activation by anodically produced PDS, was further corroborated by EPR observations during electrolytic oxidation in an aqueous SO_4^{2-} solution.

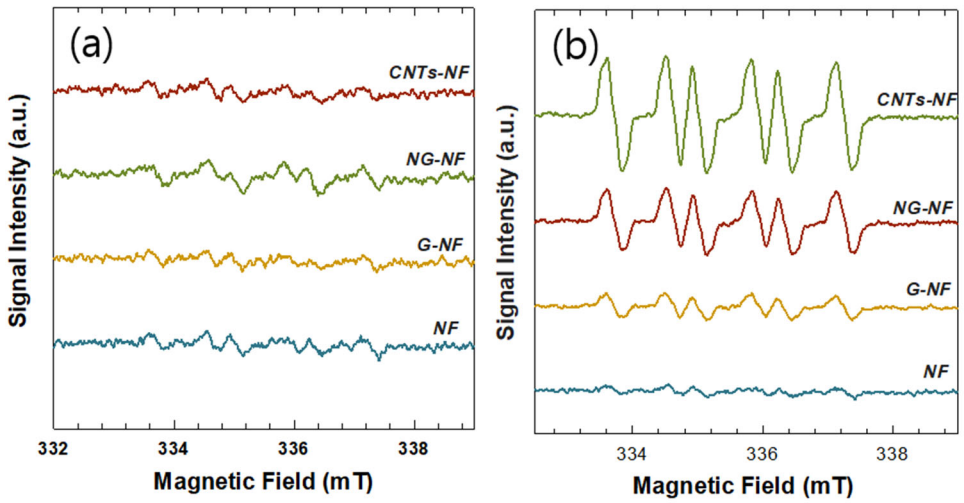


Figure 4.30 EPR spectra observed (a) in the absence of PDS, and (b) observed in the presence of PDS with a cathode in a divided cell ($[PDS]_0 = 10$ mM, $[Na_2SO_4]_0 = 100$ mM, [Applied current density] = 50 mA/cm^2, $[pH]_i = 6$).

The EPR spectra (**Figure 4.30)** recorded under BDD anode assigned to the •OH and $SO_4^{\bullet-}$, implying that electrolyte derived oxidants contribute to the overall electrochemical oxidation process. The formation of $SO_4^{\bullet-}$ due to the one-electron oxidation of SO_4^{2-} on the BDD anode and activation with anodically generated PDS was further evidenced by EPR spectra during electrolytic oxidation in the aqueous SO_4^{2-} solution. The CNTs-NF cathode in divided cell mode showed no spectral features indicative of radical species (•OH or $SO_4^{\bullet-}$), suggesting that ROS does not play a part in the carbocatalytic PDS activation. On the other hand, the formation of $SO_4^{\bullet-}$, resulting from the one-electron reduction from anodically generated PDS on the CNTs-NF cathode was evident

when PDS (10 mM) was present in the electrochemical oxidation process. This phenomenon was observed during electrochemical reduction along with PDS solution on the side of CNTs-NF cathode in separate chamber, illustrating potential PFOS oxidation through a series of electrolysis reactions, thereby highlighting the reactivity of the surface-bound sulfate radicals. To demonstrate the role of surface-bound sulfate radicals on the hydrophobic CNTs coated on the NF electrode, we examined the effects of various scavengers based on their hydrophilic and hydrophobic properties (**Figure 4.31**). This classification provided insight into how different scavengers interact with the sulfate radicals on the CNTs-NF electrode surface. Hydrophilic scavengers exhibited rare scavenging effects on PFOS removal; the rate constants were 0.04 ± 0.0041 min^{-1} for MeOH, 0.0435 ± 0.0056 min^{-1} for T-Butanol, and 0.053 ± 0.0028 for thiosulfate, respectively. This indicated limited radical reduction due to the low(er) probability of reacting with the sulfate radicals generated on the surface, which was mainly responsible for transforming PFOS attached on the CNTs-NF in the divided cell. In contrast, hydrophobic scavengers including dimethyl sulfoxide (DMSO), humic acid, and alginate significantly reduced the rate constant (e.g., DMSO (0.0114 min^{-1}), HA (0.0079 min^{-1}), and alginate (0.0028 min^{-1})), serving as surface bound $SO_4^{-\bullet}$ scavengers that showed the rate constant for PFOS was reduced by more than 10 times. This suggests that the hydrophobic interactions between the scavengers and the CNTs-NF cathode influence the surface-bound sulfate radical interactions, prompting hydrophobic components to engage with PFOS degradation.

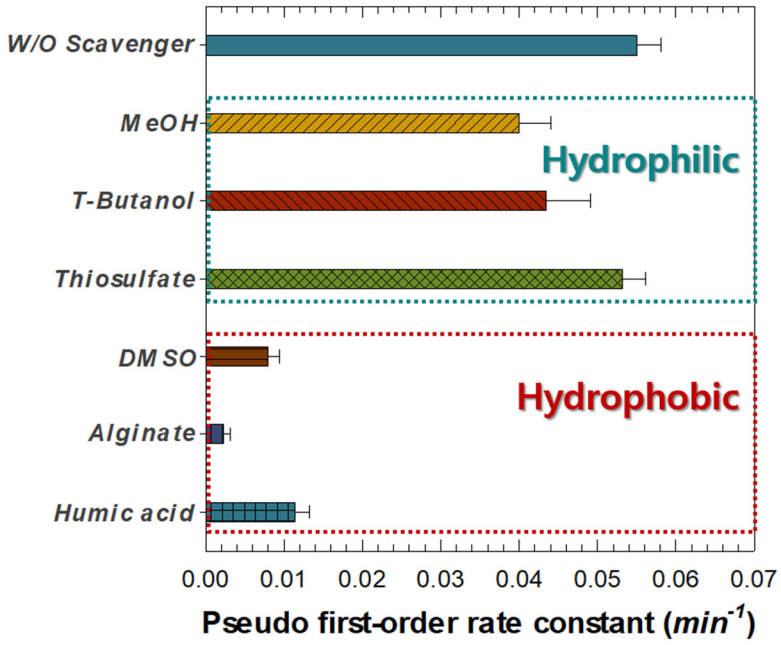


Figure 4.31 Influences of hydrophilic and hydrophobic scavengers on surface-bound radicals on the CNTs-NF electrode ($[PFOS]_0$ = 20 mg/L, $[Na_2SO_4]_0$ = 100 mM, [Scavengers]$_0$ = 200 mM, [Applied current density] = 50 mA/cm^2, $[pH]_I$ = 6).

Statistical analyses were conducted to quantify the intermediate products formed during treatment with a BDD anode and a CNTs-NF cathode, utilizing a divided cell with the addition of 10 mM PDS, under the same operational conditions. Utilizing the Elbow method based on the inertia plot, we identified 25 target intermediates from PFOS oxidation and discerned three optimal clusters (C 3.64, C 8, and C 4), which were organized based on the number of carbon atoms present according

to **Figure 4.32**. Significantly, a distinct cluster become a clue among intermediates containing BDD anode with a C2 group, demonstrating a marked increase in density. In contrast, the group associate with CNTs-NF cathodes predominantly displayed elevated values linked to the C1 group and diminished values correlated with the C3 group. This suggests a potential divergence in intermediate formation tendencies between direct oxidation stemming from the BDD anode and indirect oxidation involving reactions with sulfate radicals.

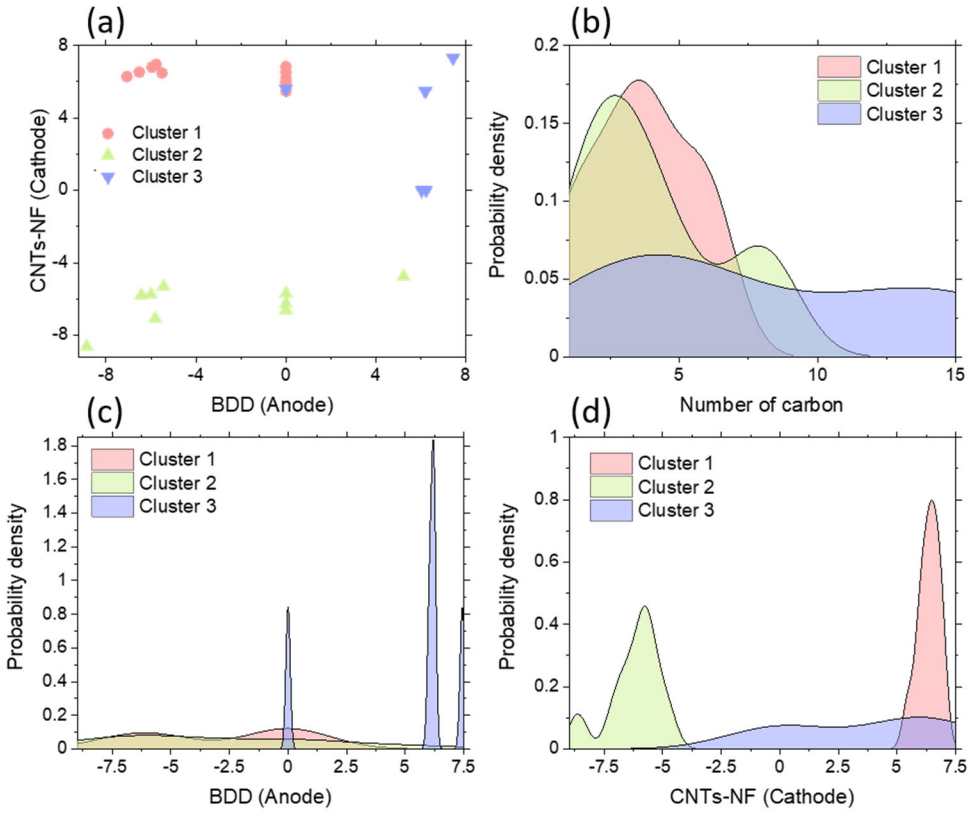


Figure 4.32 The intermediate analysis of PFOS oxidation in BDD anode and CNTs-NF cathode using K-mean cluster algorithm.

4.3.4 Mechanistic investigation of Adsorption Capacity of CNTs-NF Electrodes

The electrochemically active surface area (ECSA) of an electrode is crucial for determining its adsorption capacity and electrocatalytic performance. It typciallyshows a positive correlation with double-layer capacitance (Cdl). To evaluate and compare ECSA across catalysts, we first examined their Cdl values. As depicted in **Figure 4.33**, the CNTs-NF possesses the most extensive surface area, with an ECSA value (0.148) that is significantly higher than those of NG-NF, G-NF, and pristine NF, which have values of 0.0196, 0.0075, and 0.0011, respectively. This result indicates that the larger the surface area of graphitic carbon such as CNTs, the better their ability to capture PFOS compounds. In other words, their unique structure and chemical characteristics should contribute to making CNTs-NF electrodes particularly effective at binding PFOS during the electrolysis[242].

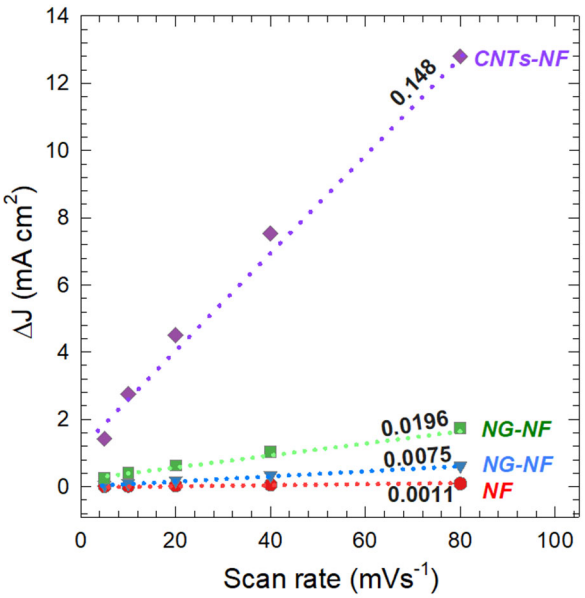


Figure 4.33 A comparison of the electrochemically active surface area using pristine NF, G-NF, NG-NF, and CNTs-NF electrodes.

To explore the impact of PDS on electro-sorption of PFOS on carbon-based electrodes, we conducted PFOS adsorption tests using pristine NF and carbon-based NF electrodes, with the aid of electrochemical assistance and in the presence of 10 mM PDS. **Figure 4.34** presents the resulting adsorption capacities, revealing an increase in these capacities with the addition of 10 mM PDS to carbon-based cathode chamber. Specifically, electro-sorption capacities for CNTs-NF, NG-NF, and G-NF electrodes were recorded at 0.9912, 0.2889, 0.2823, and 0.0252 mg/g for PFOS, respectively. Notably, these capacities elevated to 1.3793, 0.4699, 0.5574, and 0.0282 mg/g for PFOS when PDS was present, suggesting that PDS might alter the carbon surface, generating additional active sites. This, in turn, augments the adsorption capacity for PFOS. In contrast, the pristine NF exhibited minimal change in electro-sorption capacities for PFOS for systems with and without PDS, suggesting that functional groups or charge sites on pure NF have limited potential to interact with PFOS nor PDS molecules.

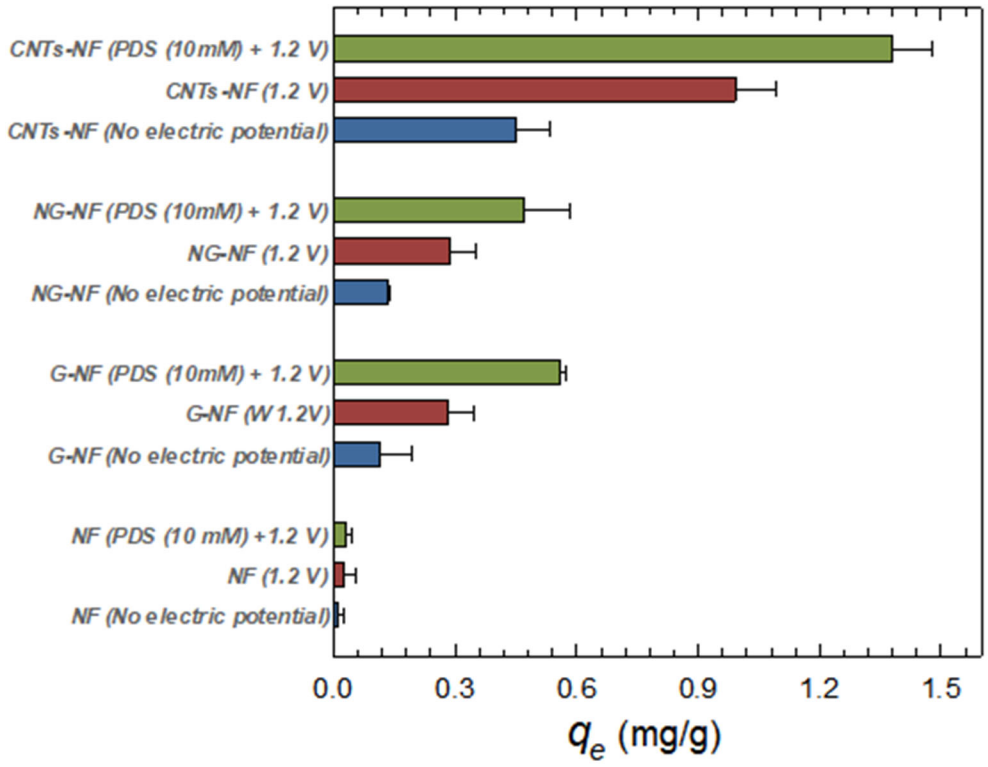


Figure 4.34 The equilibrium adsorption capacity of PFOS at 1.2 V using various types of electrodes ($[PFOS]_0$ = 10 mg/L, $[Na_2SO_4]_0$ = 100 mM, [Applied potential] = 1.2V, $[pH]_i$ = 6).

We performed pH dependent PFOS degradation tests using CNTs-NF electrode. The rate constants for PFOS degradation decreased under basic conditions: 0.049, 0.0549, 0.0714, 0.0425, and 0.0279 min^{-1} for solution pH of 3, 5, 7, 9, and 11, respectively (**Figure 4.35a**). The pH dependent activity observed in CNTs-NF suggests that its carbon layer serves as a protective shield, potentially influencing its surface charge. As indicated by the changing zeta potentials with the initial pH (see **Figure 4.35b**), CNTs-NF begins to display a negative surface charge when the pH surpasses 7. This charge prevents anionic PDS molecules from accessing the bimetal surface due to repulsive interactions, thereby limiting the generation of radical species that react with PDS[243].

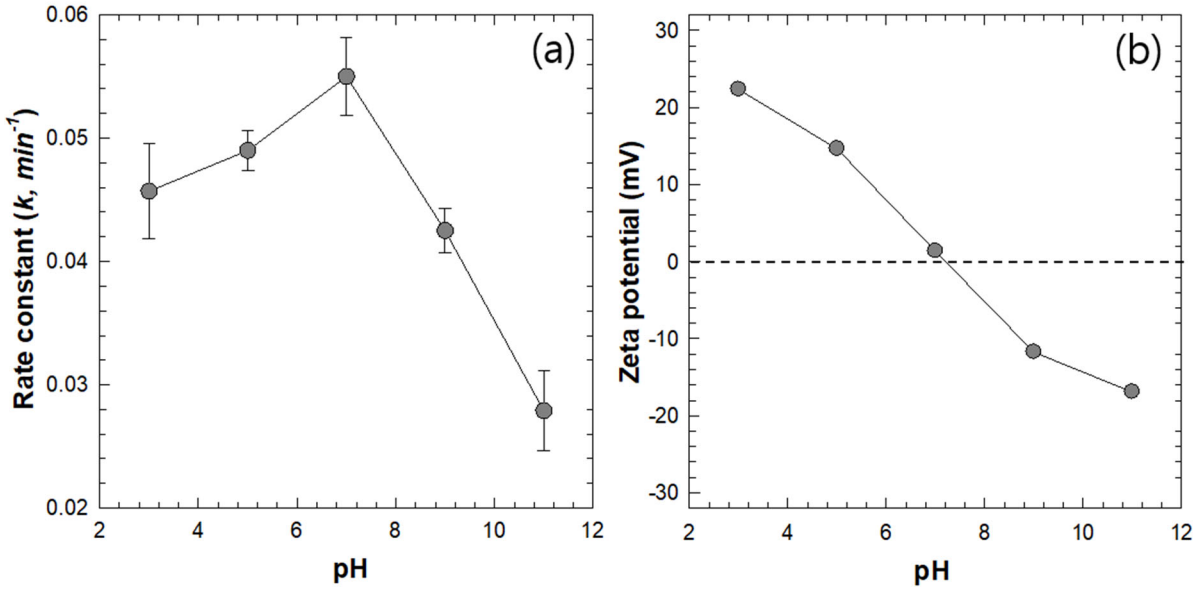


Figure 4.35 pH effects on (a) PFOS rate constants and (b) zeta potential on CNTs-NF ((a)$[PFOS]_0$ = 20 mg/L, $[Na_2SO_4]_0$ = 100 mM, [Applied current density] = 50 mA/cm^2, $[pH]_i$ = 6 and (b) $[PFOS]_0$=20 mg/L, $[Na_2SO_4]_0$=100 mM, $[pH]_i$ = 3, 5, 7, 9, and 11).

4.3.5 Stability Tests for Repeated PFOS Oxidation and Defluorination

To evaluate the cycling efficiency of cathodic persulfate activation during the electrolysis process, we monitored PFOS oxidation and defluorination rates over ten cycles, using CNTs-NF as the cathode (**Figure 4.36**). In every cycle, PFOS was completely degraded within an hour, regardless of electric current application. The result indicate substantial PFOS oxidative degradation was maintained during the consistent electrochemical activation of PDS by CNTs-NF. This highlights the utility of CNTs-NF as the cathode, which facilitates both the anodic reactions with PDS generation and PFOS degradation with surface bound sulfate radicals. There was a very minor, consistent decrease in PFOS treatment efficiency through both anodic oxidation and carbocatalytic PDS activation over the cycles, highlighting the durability of CNTs-NF for (these) continuous redox reactions.

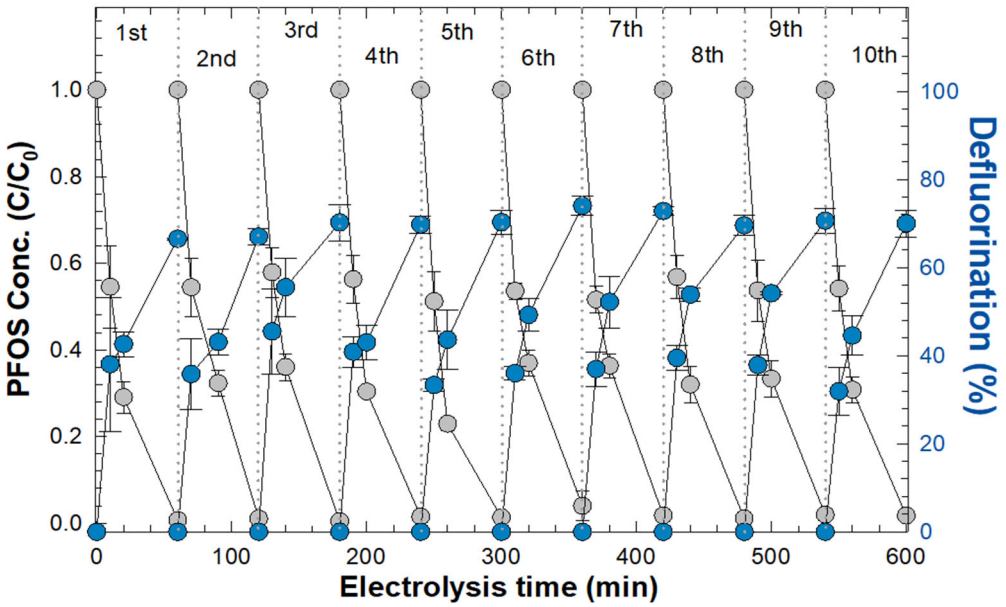


Figure 4.36 Repeated PFOS degradation along with defluorination by BDD/CNTs-NF electrode system over 10 cycles ($[PFOS]_0 = 20$ mg/L, $[Na_2SO_4]_0 = 100$ mM, [Applied current density] = 50 mA/cm^2, $[pH]_i = 6$).

To further evaluate the long-term durability, we utilized the chronoamperometry method, tracking the cell current density's behavior at a consistent 5 V across 100 hours of electrolysis **(Figure 4.37**). Throughout this operating time, the CNTs-NF cathode steadily maintained its peak current, at a density of 2.1 mA cm^{-2}. This cathode showcased significant electrochemical resilience, with a 98% current retention over 100 hours. This emphasizes their superior catalytic activity and robustness, highlighting suitability for efficient electrochemical destruction of persistent organic contaminants (including PFAS)..

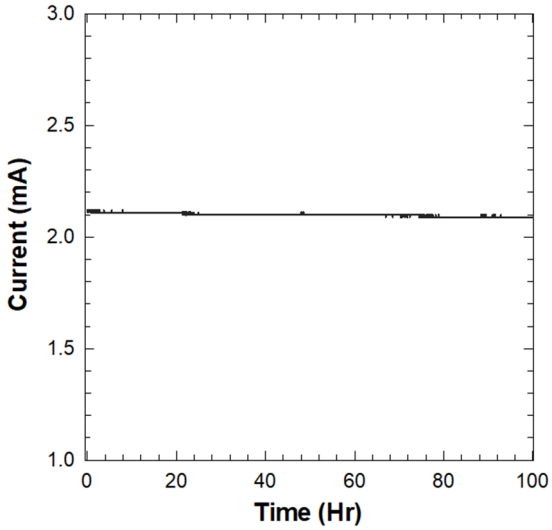


Figure 4.37 Stability analysis of the CNTs-NF electrode using the chronoamperometric technique (0.1M Na_2SO_4 solution with an applied voltage of 5V over a 100-hour electrolysis duration).

4.4 Biotic Batch Reactors and Microcosoms

4.4.1 Impacts of PFAAs on MRD in the Absence of Soil

In batch reactors, the time to transform PCE and TCE to daughter products was the same or faster at all PFAA concentrations tested (up to 101 mg/L) when compared to reactors without PFAAs. The biodegradation time, i.e., time until TCE was not detected (TCE<0.18 mg/L [0.0014 mM]), averaged 6.0 (±0.0) days in reactors without PFAAs (**Figure 4.38**). In reactors with PFAAs, average biodegradation time was 5.3 (±0.94) days, demonstrating that PFAAs did not impede biodegradation of PCE and TCE to *cis*-DCE.

MRD of *cis*-DCE to VC and VC to ethene, however, required additional time in reactors with PFAAs when compared to control reactors. In batch reactors without PFAAs, *cis*-DCE was no longer detected (<0.15 mg/L [0.0016 mM]) after 32.0 (±0.0) days and VC was no longer detected (<0.10 mg/L [0.0016 mM]) after 34.7 (±1.9) days, while reactors with 11.7 mg/L PFAAs required 17% more time (37.3±1.9 days) until *cis*-DCE was not detected, and 15% more time (40.0±0.0 days) until VC was not detected (**Figure 4.38**). Similarly, the time until cis-DCE was not detected was 38% (44.0±0.0 days), 56% (50.0±2.8 days), 81% (58.0±5.7 days), and 194% (94.0±5.7 days) longer in reactors with 26.5, 49.8, 61.7, and 101 mg/L PFAAs, respectively. The time until VC was not detected was 35% (46.7 ±1.9 days), 44% (50.0 ±2.8 days), 67% (58.0±5.7 days), and 249% (121±8.8 days) longer in reactors with 26.5, 49.8, 61.7, and 101 mg/L PFAAs, respectively, when compared with reactors containing 0 mg/L PFAAs (**Figure 4.38**).

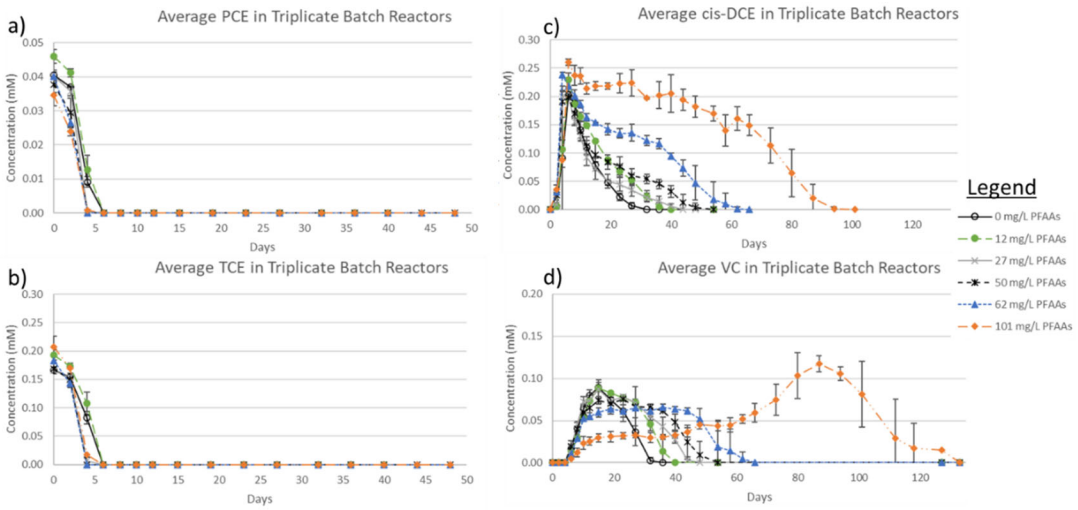


Figure 4.38 Transformation of chlorinated ethenes in batch reactor experiments. Symbols represent average **a)** PCE **b)** TCE **c)** cis-DCE and **d)** VC concentrations in triplicate batch reactors. Vertical error bars represent one standard deviation.

In all cases, however, PCE and TCE were fully transformed to ethene; ethene concentrations are shown in **Figure 4.39**a. The additional time required to fully transform *cis*-DCE to ethene in reactors with PFAAs indicates that MRD by *Dhc* was impeded by PFAAs in batch reactor experiments. MRD of PCE and TCE to *cis*-DCE was likely facilitated by *Geobacter* species, which

comprise a larger proportion of the dechlorinating community when PCE and TCE are present [34, 244]. While PCE and TCE were present, *Geobacter lovleyi* strain *SZ (GeoSZ)* abundance increased similarly in batch reactor experiments regardless of PFAA concentration (see **Table 4.4**). Specifically, *GeoSZ* abundance increased 610-, 307-, 272-, 275-, 219-, and 290-fold in reactors containing 0, 11.7, 26.5, 49.8, 61.7, and 101 mg/L PFAAs, respectively. Similarly, *GeoSZ* abundance increased 2.35-, 7.64-, 7.39-, and 4.62-fold in reactors containing 0, 9.52, 19.4, and 38.7 mg/L PFAAs, respectively, in microcosms (**Table 4.5**). Total *GeoSZ* abundance increased by the same order of magnitude in experiments prepared with PFAAs (219- to 307-fold and 3.86- to 7.64- fold in batch reactors and microcosms, respectively) as in experiments prepared without PFAAs (610-fold and 2.35-fold in batch reactors and microcosms, respectively). These results suggest that *GeoSZ* are not likely to be inhibited by PFAA concentrations that inhibit *Dhc* MRD past *cis*-DCE. There was no evidence of PFAA transformation in the batch reactors. Although measured concentrations of total PFAAs varied -13% to + 0% over the course of the experiments (**Table A.2, Figure A.1**), there was no downward trend with time and fluoride was not detected (<0.01 mM).

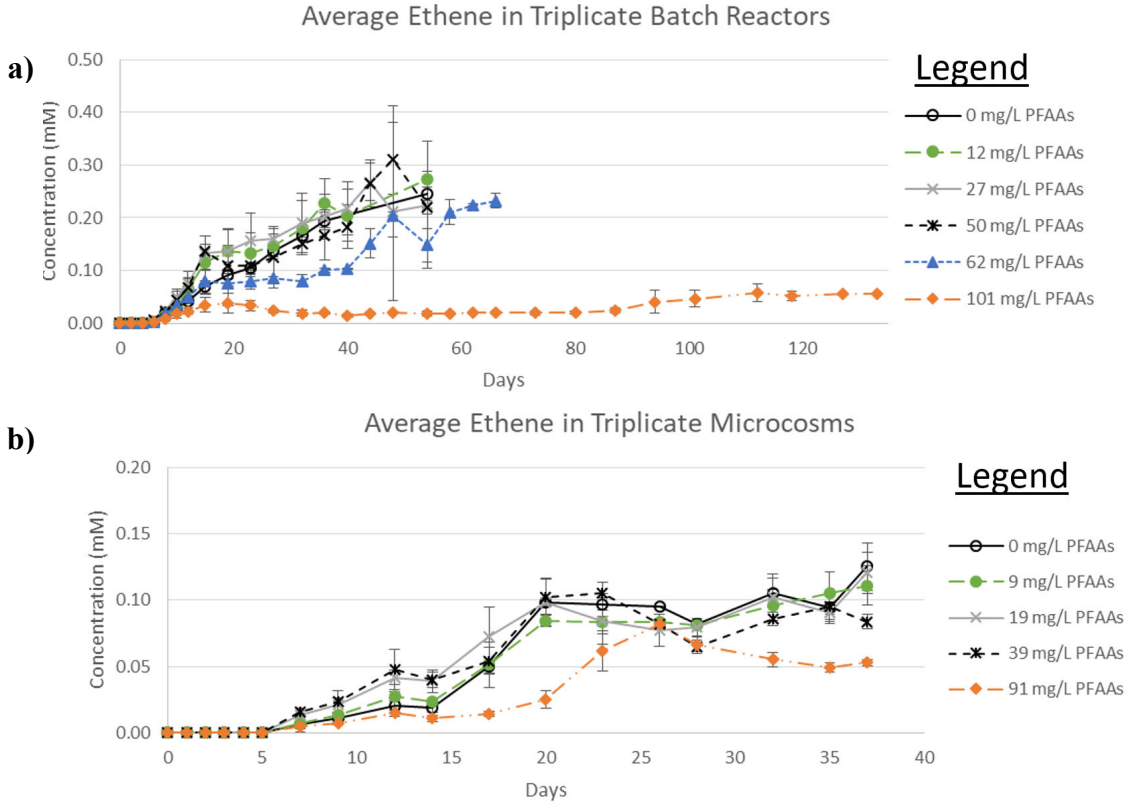


Figure 4.39 Average aqueous ethene concentrations over time in **a)** triplicate batch reactor and **b)** triplicate microcosm experiments. Vertical error bars represent one standard deviation between triplicate batch reactors. Note that the aqueous volume decreased over time due to sampling, and thus, the ratio of dissolved to gaseous ethene is not constant over time.

Table 4.4 Mean of triplicate measurements of initial and final *GeoSZ* abundances in gene copies/mL in batch reactors. Initial abundances were calculated using the measured abundance in inoculum and mass of inoculum added.

PFAA Concentration (mg/L)	**Mean initial *GeoSZ* abundance (±st. dev.)**	**Mean final *GeoSZ* abundance (±st. dev.)**
0	1.36×10^{7} ($\pm7.64\times10^{6}$)	8.30×10^{9} ($\pm1.59\times10^{9}$)
11.7	1.36×10^{7} ($\pm7.64\times10^{6}$)	4.18×10^{9} ($\pm1.09\times10^{9}$)
26.5	1.37×10^{7} ($\pm7.68\times10^{6}$)	3.77×10^{9} ($\pm2.69\times10^{9}$)
49.8	1.38×10^{7} ($\pm7.73\times10^{6}$)	3.02×10^{9} ($\pm2.27\times10^{9}$)
61.7	1.31×10^{7} ($\pm7.40\times10^{6}$)	3.81×10^{9} ($\pm2.23\times10^{9}$)
101	1.40×10^{7} ($\pm7.85\times10^{6}$)	3.80×10^{9} ($\pm2.26\times10^{9}$)

Table 4.5 Mean of triplicate measurements of initial and final *GeoSZ* abundances in gene copies/mL in microcosms. Initial abundances were calculated using the measured abundance in inoculum and mass of inoculum added.

PFAA Concentration (mg/L)	Mean initial *GeoSZ* abundance (±st. dev.)	Mean final *GeoSZ* abundance (±st. dev.)
0	2.54×10^{9} ($\pm8.25\times10^{8}$)	5.96×10^{9} ($\pm2.19\times10^{9}$)
9.52	1.43×10^{9} ($\pm5.27\times10^{8}$)	1.09×10^{10} ($\pm4.08\times10^{9}$)
19.4	1.43×10^{9} ($\pm5.26\times10^{8}$)	1.06×10^{10} ($\pm8.26\times10^{9}$)
38.7	1.43×10^{9} ($\pm5.28\times10^{8}$)	6.62×10^{9} ($\pm3.28\times10^{9}$)
91.3	3.15×10^{9} ($\pm6.68\times10^{8}$)	9.25×10^{9} ($\pm8.83\times10^{9}$)

Chlorinated ethenes were not transformed in abiotic batch reactor experiments, but concentrations declined due to diffusion into the stopper and losses to the environment as modeled above (**Figure 4.3**) and due to a decrease in the ratio of aqueous phase to gaseous phase due to sampling.

4.4.2 Modeling MDR in Batch Reactors

Abiotic batch reactor model fitting revealed that a simple first-order diffusive mass loss term, R_i^s in **equation 3.1**, underestimated the chlorinated ethene mass in reactors over time (see **Figure A.4**). To avoid potential Monod kinetic parameter estimation bias, an improved method for estimating chlorinated ethene mass loss into the rubber stopper was implemented [198]. This approach used time superposition of an analytical solution for planar diffusion of a chemical compound i from an aqueous phase at concentration C_i^a into a semi-infinite solid rubber phase [245]:

$$C_i^r(x,t) = K_i^{ra} C_i^a \operatorname{erfc}\left(\frac{x}{2\sqrt{D_i t}}\right) \qquad (4.1)$$

Here, C_i^r is the molar concentration in the rubber phase [M/L^3], x is distance from the aqueous-rubber interface [L], t is time, K_i^{ra} is a dimensionless rubber-aqueous linear partitioning coefficient dictating rubber phase chlorinated ethene concentrations at $x = 0$ [(rubber molarity)/(aqueous molarity)], and D_i is the diffusion coefficient of compound i in the rubber phase [L^2/T]. After estimating D_i and K_i^{ra} for PCE and TCE using abiotic batch reactor data and literature values [246, 247], correlations based on molecular size [248, 249], and the octanol-water partitioning coefficient [250, 251] were applied to estimate D_i and K_i^{ra}, respectively, for *cis*-DCE, VC, and ethene (see **Appendix A.3**).

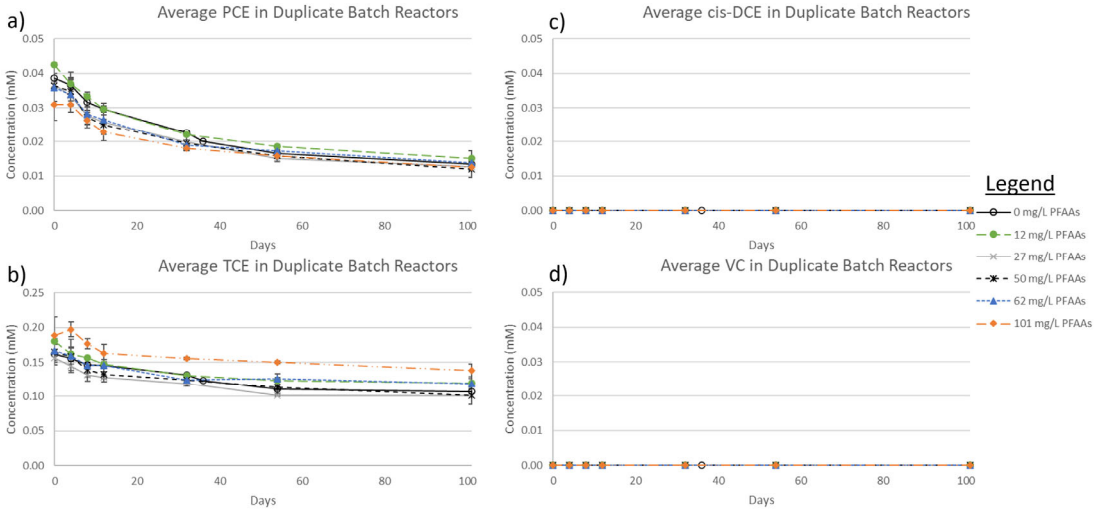


Figure 4.40 Average **a)** PCE **b)** TCE **c)** *cis*-DCE and **d)** VC concentrations in duplicate abiotic batch reactors. Vertical error bars represent one standard deviation between duplicate batch reactors.

To explore the potential inhibition of chlorinated ethene MRD by PFAAs, the numerical model was used to fit $k_{max,i}$ to experimental data from reactors with and without PFAAs. Weighted least squares regression of the MRD model to biotic control reactors using all Monod parameters as fitting parameters reproduced the magnitudes and temporal trends of chlorinated ethene and qPCR measurements (McFadden pseudo R^2 value (R^2) [252] of 0.951, see **Table A.5**, **Figure A.6**). Subsequent model fits to reactors containing PFAAs also demonstrated good agreement with experimental measurements (R^2 from 0.779-0.951), despite the lower number of fitting parameters (four $k_{max,i}$ only) (**Figure A.7**). Average fitted $k_{max,i}$ values for reactors amended with various PFAA concentrations are presented in **Figure 4.41** and **Table A.6**.

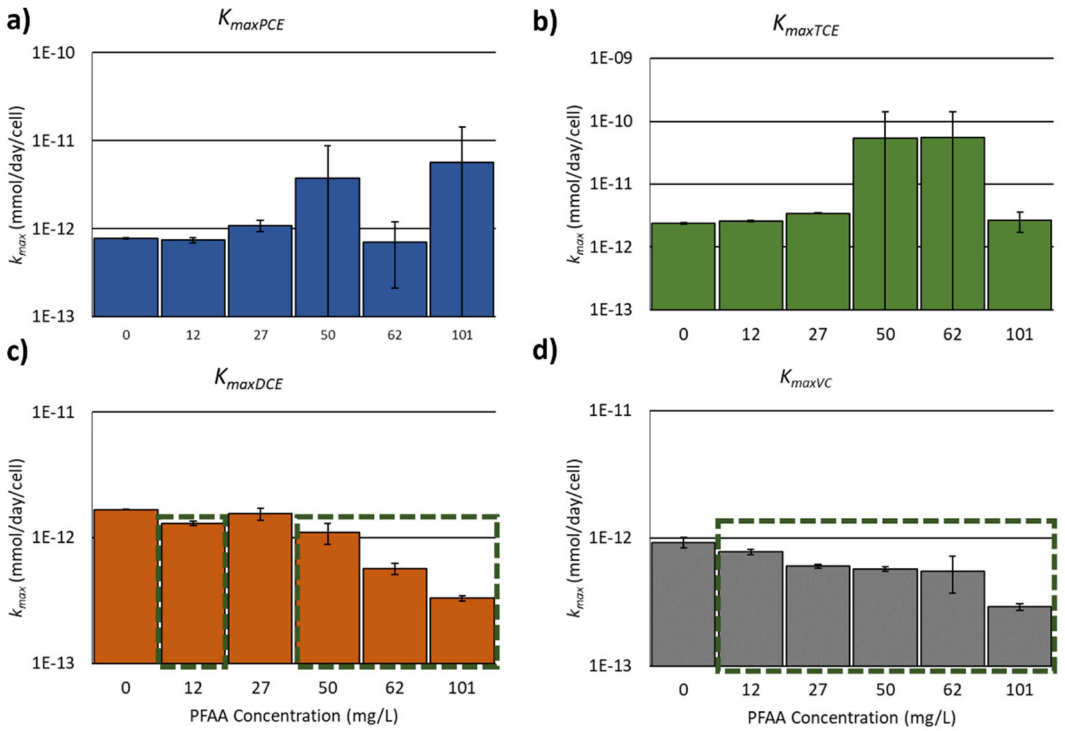


Figure 4.41 Average maximum substrate utilization rates (k_{max}) for **a)** PCE degradation, **b)** TCE degradation, **c)** cis-DCE degradation, and **d)** vinyl chloride degradation. Each bar represents the value fit to each set of triplicate batch reactors in units of mmol/day/cell and error bars represent the standard deviation. Values within dashed rectangles are significantly lower than the average for the 0 mg/L reactor set ($p<0.05$).

The average fitted $k_{max,PCE}$ and $k_{max,TCE}$ values for reactors containing PFAAs were either higher or not statistically lower than the fitted $k_{max,PCE}$ and $k_{max,TCE}$ values for those without PFAAs (p=0.18-0.42), demonstrating that PFAAs did not reduce (inhibit) PCE and TCE biodegradation rates for all PFAA concentrations tested (≤101 mg/L). Average fitted $k_{max,DCE}$ values (representing *cis*-DCE biodegradation), however, were significantly smaller (p=0.00002-0.02) in reactor sets with PFAA concentrations ≥49.8 mg/L, when compared with the average $k_{max,DCE}$ value for reactors without PFAAs (**Figure 4.41**, **Table A.6**). The average fitted $k_{max,DCE}$ for the 11.7 mg/L PFAA reactor set was also significantly (p=0.003) lower, but the rate fit to the 26.5 mg/L PFAA reactor set was not (p=0.17) (**Figure 4.41**, **Table A.6**). These differences suggest that *cis*-DCE to VC biodegradation was inhibited at PFAA concentrations of 49.8 mg/L and higher but may or may not be inhibited at PFAA concentrations of 11.7 and 26.5 mg/L. The average $k_{max,VC}$ values (representing VC biodegradation) were significantly lower (p=0.001-0.034) when fit to reactor sets containing PFAAs at all concentrations tested when compared to fits to the reactor set without PFAAs, indicating that VC to ethene biodegradation is inhibited at total PFAA concentrations ≥11.7 mg/L.

To quantify the empirical relationship between PFAA concentration and MRD inhibition, a log-logistic dose-response model [253, 254] was fit to the $k_{max,i}$ values (see **Appendix A.3**). This empirical model is used to describe inhibition of microbial processes by toxic compounds where

the rate of the microbial process is largely uninhibited until the concentration of the compound(s) reaches a threshold, after which the rate decreases and is formulated as:

$$k_{\text{inh},i} = \frac{k_{\text{max},i}}{1 + \exp\left[b_i \log\left(\frac{C^a_{\text{inh}}}{C^a_{50,i}}\right)\right]} \quad \textbf{(4.2)}$$

where, $k_{\text{inh},i}$ is the inhibited $k_{max,i}$ [M/T/cell], $k_{\text{max},i}$ is the uninhibited $k_{max,i}$ [M/T/cell], C^a_{inh} is the aqueous concentration of the substance(s) inhibiting the microbial process (i.e., total PFAA concentration [mg/L]), $C^a_{50,i}$ is the substance(s) concentration at which the rate is halved [mg/L], and b_i is a dimensionless parameter describing the rate of decrease around the threshold concentration (C^a_{50}). The relationship between $k_{max,DCE}$ and $k_{max,VC}$ values and PFAA concentration was well-captured by this model (R^2=0.801 and 0.728, respectively; **Figure 4.42**). $C^a_{50,i}$ was 57.0 and 60.0 mg/L for *cis*-DCE and VC degradation, respectively. The best-fit values for b_{DCE} and b_{VC} were 6.78 and 2.15, respectively. These parameter values indicate that *cis*-DCE and VC biodegradation are both inhibited at similar PFAA concentrations, but the impact on the *cis*-DCE biodegradation rate is greater than on the VC biodegradation rate at a specific PFAA concentration. These differences in magnitude of inhibition may be related to impacts of PFAAs on specific *Dhc* strains as discussed below.

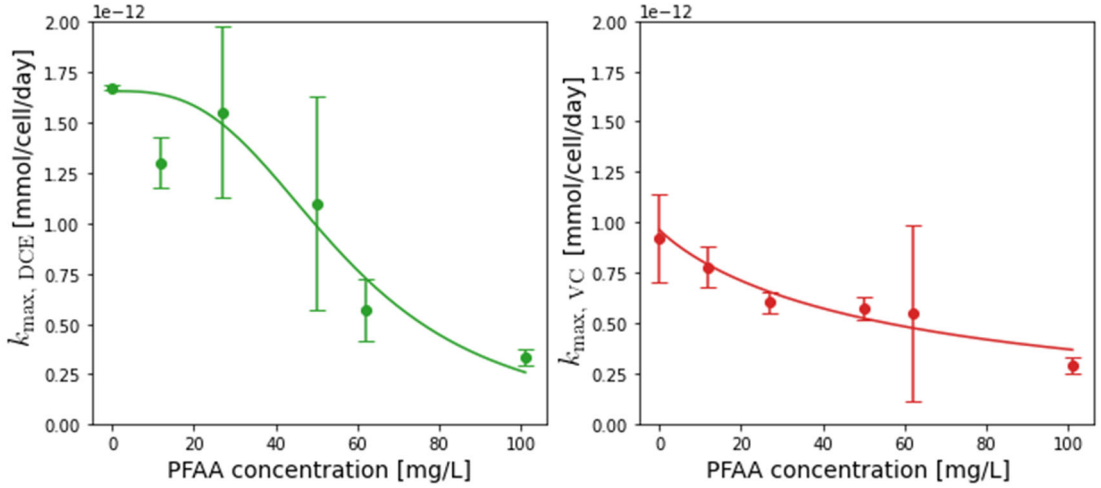


Figure 4.42 Estimated maximum substrate utilization rates for batch reactor experiments conducted with varying concentrations of total PFAAs. Plotted curves show fit of log-logistic dose-response model for inhibition of MRD by PFAA. Points represent the mean of three k_{max} estimates and each error bar indicates the corresponding 95% confidence interval.

4.4.3 Modeling MDR in Microcosms

Comparisons between microcosm (with porous media) and batch reactor (without porous media) experiments were used to assess the influence of a solid phase on the effect of PFAAs on MRD of chlorinated ethenes. In the microcosm experiments, there was a lag of approximately 4 days between bioaugmentation and the rapid onset of PCE and TCE biotransformation. This lag is likely due to differences in the microbial cultures used for bioaugmentation. The initial *Dhc* 16S rRNA and *tceA* abundances in the microcosm inoculums were 88% and 77% lower, respectively, than the batch reactor inoculums (see **Table 3.2**). Due to these differences, the comparison between

microcosm and batch reactors was limited to comparing the PFAA concentrations that may cause inhibition rather than comparing transformation rates directly.

In microcosms, similar to batch reactors, there was no difference in the time to dechlorinate PCE and TCE to *cis*-DCE at any of the PFAA concentrations tested. TCE was not detected 9 days after bioaugmentation in all microcosms (**Figure 4.43**). The time until *cis*-DCE was not detected was 26.3 (±1.7) days in all bioaugmented microcosms with 0.0,9.25, 19.4 or 38.7 mg/L PFAAs, and only reactors containing 91.3 mg/L PFAAs required additional time (6% longer, 28.0±0.0 days) until *cis*-DCE was not detected. Similarly, the same amount of time (33.8±3.2 days) was required until VC was no longer detected in microcosms with PFAA concentrations ≤38.7 mg/L, and only the microcosms with 91.3 mg/L PFAAs required additional time (9% longer; 37.0±0.0 days) until VC was no longer detected. As in the batch reactors, PCE and TCE were fully transformed to ethene in microcosms; ethene concentrations are shown in **Figure 4.39**b. Sorption of chlorinated ethenes is not expected to vary between microcosm experiments as the same solid-liquid ratios were used in each; therefore, sorption does not explain the differences in degradation times between microcosms. Microcosm experiments were not modeled because potential inhibition of MRD by PFAAs was only observed in the highest concentration microcosms containing 91.3 mg/L PFAAs.

The difference between batch reactor results, in which additional time was required to transform *cis*-DCE and VC at PFAA concentrations of 11.7 mg/L, and microcosm results, in which no additional time was required to transform *cis*-DCE and VC at PFAA concentrations as high as 38.7 mg/L, indicates that the presence of a solid phase reduced the inhibition of *cis*-DCE and VC MRD by PFAAs. Sorption of chlorinated ethenes to the solid phase in microcosms was minimal and does not explain the difference between inhibitory concentrations in batch reactor and microcosm experiments (**Appendix A.4**). A better explanation for this difference is protective microenvironments and/or biofilms around solid particles [104, 255]. In previous studies, the presence of certain porous media, even at low solid to liquid ratios (10 g soil to 100 mL aqueous phase), prevented complete inhibition of dechlorination at low pH [255]. The authors attributed this phenomenon to more favorable pH conditions at the solid-aqueous interface; similarly, cells attached to soil particles may not be exposed to the same detrimental effects of PFAAs as those in the bulk aqueous phase.

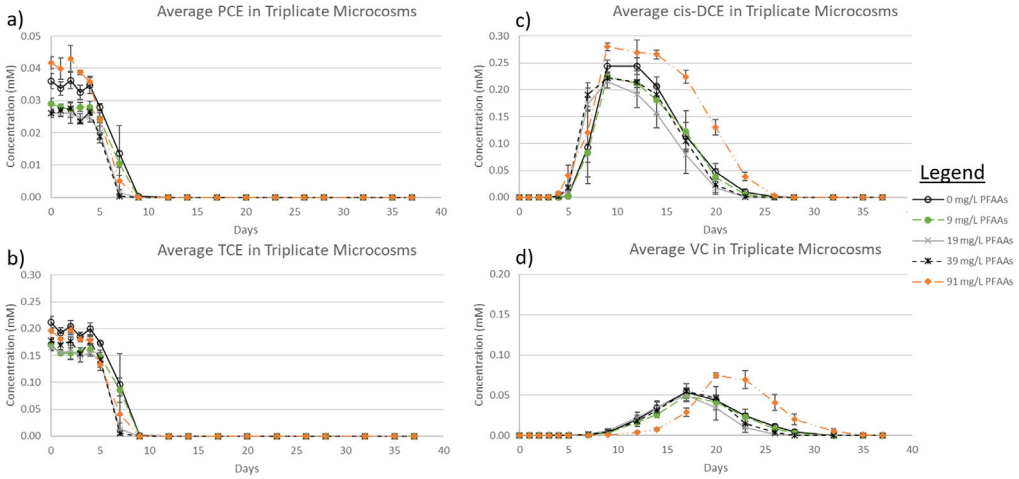


Figure 4.43 Average **a)** PCE **b)** TCE **c)** cis-DCE and **d)** VC concentrations in triplicate microcosms. Vertical error bars represent one standard deviation.

In addition to the protection of soil microenvironments, solid-phase sorption of PFAAs reduced the aqueous PFAA concentration and changed the composition of the PFAA mixture over time. PFAA concentrations in microcosms decreased over the first 20 days, then remained constant, within the variability of the analytical methods (**Table A.3**, **Figure A.2**). Due to the sorption of PFAAs, microcosms are referred to using their final total PFAA concentrations and all conclusions assumed that observed effects, if any, correlate to this lower, final PFAA concentration. Decreases in aqueous total PFAA concentrations was not observed in batch reactors (without solid phase), therefore, losses cannot be attributed to sorption to the glass or rubber stopper (**Table A.2**, **Figure A.1**) [256-258]. Because concentrations dropped in both inactivated and bioaugmented microcosms and fluoride was not detected, it is unlikely that PFAAs were transformed or degraded. Total PFAA concentrations dropped to 72%-75% of their initial values while concentrations of individual compounds remained constant or decreased to as low as 37% of their initial values (**Table A.3**, **Figure A.2**). The greatest declines were observed for PFDA and PFOS, which averaged 39% and 59% of initial concentrations, respectively (**Table A.3**, **Figure A.2**). These larger decreases were anticipated, based upon the affinity of longer carbon chain PFAS for organic carbon, as indicated by their higher organic carbon partitioning coefficients (K_{oc}) [203, 205, 259].

In microcosms prepared without bioaugmentation, the porous media was the only source of microbes. The terminal transformation product of PCE and TCE was cis-DCE, indicating that the native microbes responsible for PCE and TCE biodegradation were not microbial strains capable of cis-DCE MRD (see **Figure 4.43**). Numerous microbial species, including GeoSZ, are capable of PCE and TCE MRD but the specific species in the porous media were not quantified. Biodegradation of PCE and TCE to cis-DCE occurred similarly in microcosms with and without PFAAs, suggesting that these species were not negatively impacted by PFAAs.

4.4.4 Total and Strain-specific Growth of Dhc in Batch reactors and Microcosms

Total *Dhc* growth, measured via qPCR of the *Dhc* 16S rRNA gene, was quantified for batch reactor and microcosm experiments in the presence and absence of PFAAs. Based on the differences in inoculum bottles used to prepare reactor sets (**Section 3.1**), the results from batch reactors are directly compared with one another based on PFAA concentrations but cannot be compared with the results from microcosms. Similarly, results from microcosms can be directly compared with one another but not with the results from batch reactors. Although the microcosms containing 91.3 mg/L PFAAs were prepared with a different inoculum bottle than the other microcosms, the initial abundances of *GeoSZ* 16S rRNA, *Dhc* 16S rRNA, *tceA,* and *vcrA* were not significantly different between the inoculum bottles (**Table 3.2**). The abundance of *bvcA* was significantly different ($p=0.05$) between the inoculums and this difference was considered in data interpretation. In batch reactors, average *Dhc* abundance increased significantly ($p=0.02$) from 7.59×10^6 ($\pm1.73\times10^5$) gene copies/mL initially to 1.94×10^8 ($\pm6.92\times10^7$) gene copies/mL at the time when all chlorinated ethenes had been transformed to ethene (day 32-101 depending on PFAA concentration; **Figure 4.44**). In microcosms, *Dhc* abundance increased from 1.21×10^6 ($\pm3.59\times10^5$) gene copies/mL to 4.97×10^7 ($\pm3.36\times10^7$) gene copies/mL over the first 28 days of the experiments (while chlorinated ethenes were present; **Figure 4.45**). This increase was less significant ($p=0.06$) than the increase in batch reactors. In batch reactors, *Dhc* abundance increased 17-, 39-, 15-, 18-, 24-, and 19-fold in reactors containing 0, 11.7, 26.5, 49.8, 61.7, and 101 mg/L PFAAs, respectively. Similarly, in microcosms, *Dhc* abundance increased 25-, 21-, 22-, 26- and 235-fold in reactors containing 0, 9.25, 19.4, 38.7, and 86.3 mg/L PFAAs, respectively. These data demonstrate that total *Dhc* abundance increased similarly in experiments prepared with PFAAs (15- to 39-fold and 21- to 235-

fold in batch reactors and microcosms, respectively) and in experiments prepared without PFAAs (17-fold and 25-fold in batch reactors and microcosms, respectively). The microcosms containing 86.3 mg/L PFAS were bioaugmented from a different inoculum bottle, therefore, the -fold increases measured for these microcosms are not directly comparable to the other microcosm results.

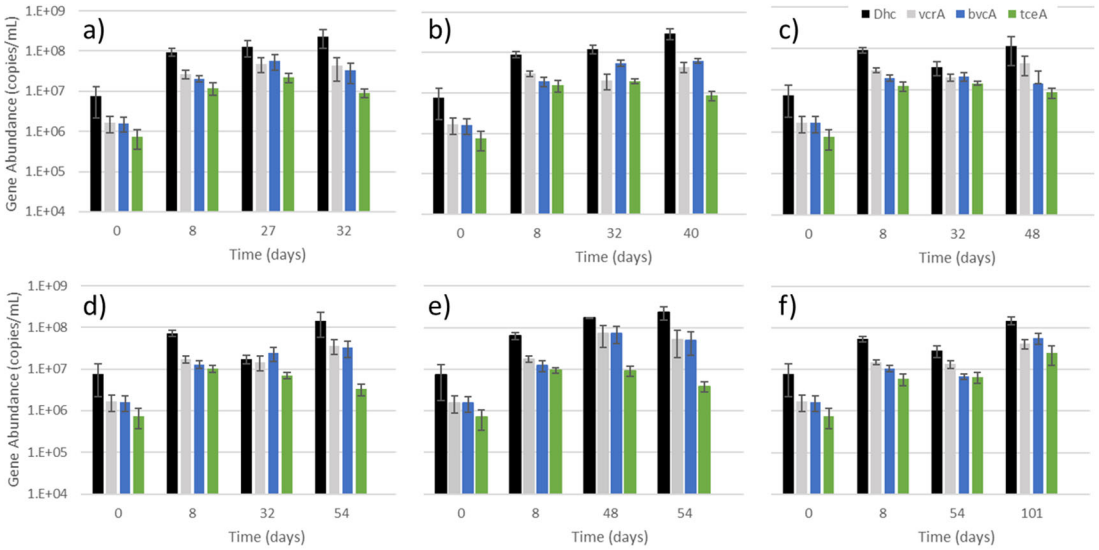


Figure 4.44 *Dhc* 16S rRNA and RDase gene abundance in batch reactor experiments containing concentrations of **a)** 0 mg/L, **b)** 12 mg/L, **c)** 27 mg/L, **d)** 50 mg/L, **e)** 62, and **f)** 101 mg/L PFAAs. Each bar represents the average of 3 replicates with one standard deviation represented with error bars. The time 0 abundances are based on the composition of the inoculum used in each batch reactor set.

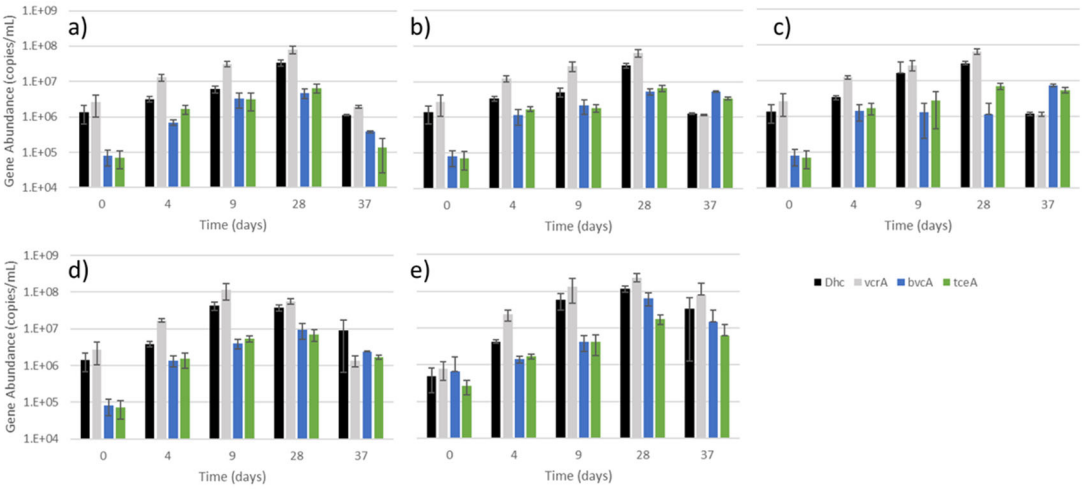


Figure 4.45 *Dhc* 16S rRNA and RDase gene abundance in microcosm experiments containing final concentrations of **a)** 0 mg/L, **b)** 9 mg/L, **c)** 19 mg/L, **d)** 39 mg/L, and **e)** 91 mg/L PFAAs. Each bar represents the average of 3 replicates with one standard deviation represented with error bars. The time 0 abundances are based on the composition of the inoculum used in each microcosm set.

Both batch reactor and microcosm experiments demonstrated differential *Dhc* strain growth when PFAAs were present. At the time of complete dechlorination (day 32 to 101), *vcrA*, *bvcA*, and *tceA* genes comprised 50.2%, 39.0%, and 10.8% of total RDase genes, respectively, in batch reactors without PFAAs (a). In reactors with PFAAs, average proportions of *vcrA*, *bvcA*, and *tceA* genes were 45.8%, 45.3%, and 8.9%, respectively (**Figure 4.46**a). The proportion of *vcrA* genes was lower in batch reactors containing PFAAs (33.6%-50.1%), but this was not significantly different (p=0.21) from the proportion in reactors without PFAAs. The proportion of *bvcA* genes was significantly higher (p=0.018) in batch reactors containing PFAAs than in reactors without PFAAs (42.0%-47.2% of the RDase genes). The proportion of *tceA* genes in reactors with PFAAs (3.7%-20.3%) were not consistently higher or lower than the proportion in reactors without PFAAs. The average proportion of *tceA* genes in reactors with PFAAs was not significantly different (p=0.35) than in reactors without PFAAs. At the highest PFAA concentration tested in batch reactors (101 mg/L), the proportion of *vcrA* harboring cells was 32% lower compared to reactors containing lower PFAA concentrations. Similarly, in microcosm experiments the proportion of *vcrA* harboring cells was 11% lower in reactors with the highest PFAA concentration (91.3 mg/L) than in reactors with lower PFAA concentrations. This suggests a strain-specific impact of PFAAs that may only be observable at high PFAA concentrations. The abundance of *Dhc* 16S rRNA and RDase genes in batch reactor experiments over time are shown in **Figure 4.44**.

At the time of complete dechlorination in microcosms, the *vcrA*, *bvcA*, and *tceA* genes comprised an average of 87.8%, 5.11%, and 7.09% of total RDase genes, respectively, without PFAAs (**Figure 4.43**b). In microcosms with 9.25 and 19.4 mg/L PFAAs, the composition at the end of dechlorination was similar (**Figure 4.43**b) and the average abundance of RDase genes was not significantly different (p=0.059-0.20) than in reactors without PFAAs. In microcosms with higher PFAA concentrations (38.7 and 91.3mg/L), however, the average proportion of *vcrA* genes was significantly lower (p=0.006), 77.2% and 74.2%, respectively, than in those with no PFAAs or low PFAA concentrations (0, 9.25, and 19.4 mg/L; 87.8%, 83.4%, 84.5% *vcrA,* respectively). The proportions of *bvcA* genes were significantly higher (p=0.026) in microcosms containing high PFAA concentrations (38.7 and 91.3 mg/L; 12.3% and 20.3% *bvcA* gene) than in microcosms with no PFAAs or low PFAA concentrations (0, 9.25 and 19.4 mg/L; 5.11%, 7.40%, 6.33% *bvcA* gene, respectively). The proportion of *tceA* genes was not significantly different (p=0.28) between microcosms containing high PFAA concentrations (38.7 and 91.3 mg/L; 9.54% and 5.48% *tceA* gene) and microcosms with no PFAAs or low PFAA concentrations (0, 9.25 and 19.4 mg/L; 7.09%, 9.21%, 9.21% *tceA* gene, respectively). As in the batch reactors, the largest difference in RDase composition was observed at the highest PFAA concentration tested (91.3 mg/L). Although the inoculum used in the 86.3 mg/L microcosm contained a higher initial abundance of *bvcA,* the 38.7 mg/L microcosms were inoculated from the same bottles as the other microcosms and also contained a higher proportion of *bvcA* (relative to microcosms with lower PFAA concentrations) at the end of the experiment. The abundance of *Dhc* 16S rRNA and RDase genes in microcosm experiments over time are shown in **Figure 4.46**.

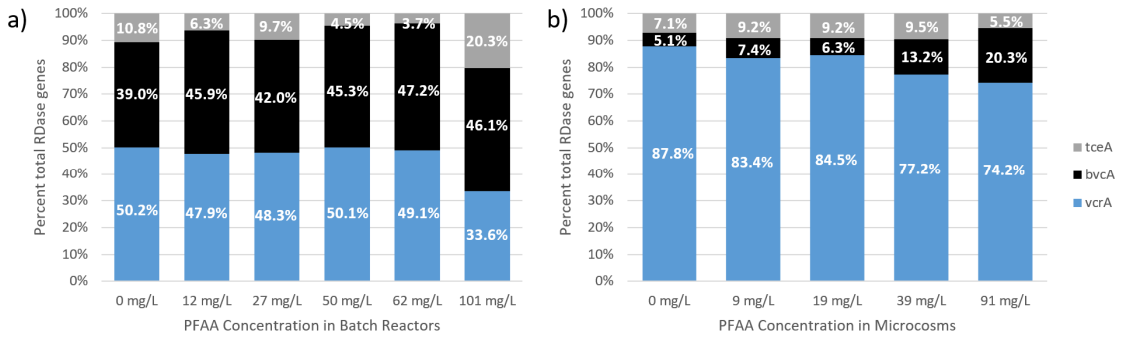


Figure 4.46 Proportion of RDase genes in a) batch reactor and b) microcosm experiments at the end of dechlorination. End of dechlorination in batch reactors varied from day 32 to 101 depending on PFAA concentration. In microcosms, end of dechlorination occurred at day 28 at all PFAA concentrations.

In batch reactors, the proportion of each RDase gene did not correlate strongly (R^2<0.70) with PFAA concentration (**Figure 4.47 a, c**). The slight downward trend in the proportion of *vcrA* genes (R^2=0.58) was the result of the measurement of *vcrA* at the highest PFAA concentration. The proportion of *bvcA* genes trended slightly upward (R^2=0.44) with PFAA concentration. Although there was a slight upward trend in the proportion of *tceA* genes with PFAA concentration (R^2=0.21), this trend was also the result of the proportion of *tceA* in the highest PFAA concentration experiment. In microcosms (**Figure 4.47 b, d**), the proportions of *vcrA* and *bvcA* genes were strongly correlated with PFAA concentrations (R^2=0.89 and 0.85, respectively) but the proportion of *tceA* genes did not correlate strongly with PFAA concentration (R^2=0.58). These correlations suggest that PFAA concentrations may preferentially impact *Dhc* strains containing the *vcrA* gene by lowering the relative proportion in the overall population, especially at high PFAA concentrations (≥38.7 mg/L).

These analyses revealed a potential change in the *Dhc* strain responsible for ethene formation from cells harboring the *vcrA* gene in the absence of PFAAs to cells harboring the *bvcA* gene at high PFAA concentrations. The change in *Dhc* strain was observed in the highest concentration batch reactors (101 mg/L PFAS) and in microcosms with final PFAA concentrations of 38.7 mg/L and 91.3 mg/L. Differential strain-specific *Dhc* growth may contribute to the variable impact of PFAAs revealed in the log-logistic dose-response inhibition model. *Dhc* strains harboring the *bvcA* gene are capable of transforming VC to ethene, but there is less evidence that they transform DCE isomers to VC, while transformation of DCE isomers to VC by *Dhc* strains harboring *vcrA* is well documented [98, 260]. Slower growth of *vcrA* gene-harboring strains at high PFAA concentrations results in more inhibition of *cis*-DCE biodegradation than VC biodegradation at the same PFAA concentration.

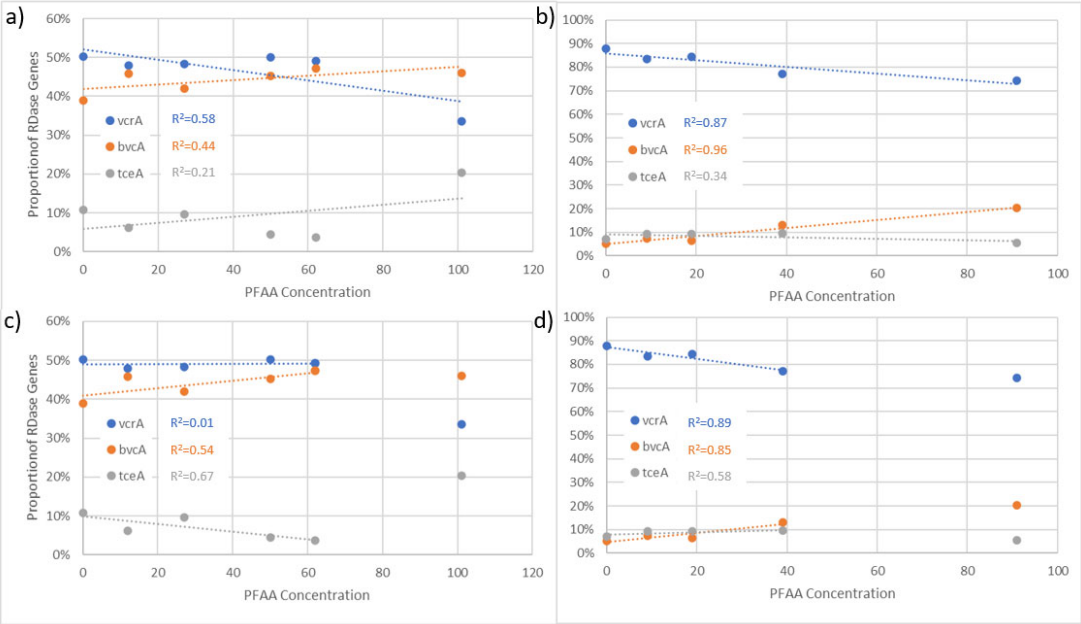


Figure 4.47 Proportion of RDase genes vs PFAA concentration at the end of experiment with linear regression fit to all data in **a)** batch reactor (day 32 to 101) and **b)** microcosm (day 28) experiments and with linear regression fit to all data except highest PFAA concentration data in **c)** batch reactor (day 32 to 101) and **d)** microcosm (day 28) experiments.

4.5 Batch Reactors and Microcosoms

4.5.1 Single and Coupled Column Experiments for Mixed Chlorinated Ethenes and PFAA Treatment

In comparison to a series of single-solute adsorption experiments (based on unpublished data), both PCE/TCE and PFAAs displayed earlier breakthroughs in this study, indicating the occurrence of competitive adsorption. Both adsorptive materials (IONP and S-PAC) columns exhibited adsorption preference for PCE over TCE. The breakthrough orders for the 10 PFAAs in all the adsorptive columns (both IONP and S-PAC) in four sets of experiments in this study were consistent and similar to the unpublished multi-solute column data from the Pennell Lab at Brown University and their prior studies on various adsorptive materials [35, 118]. However, the amount of chlorinated ethenes and PFAAS retained in each experiment set was different.

4.5.1.1 Set 1: Single IONP column experiment

During the 42.1 PVs operation, 0.05 ± 0.01 mM of PCE and 0.11 ± 0.01 mM of TCE were constantly introduced into the single IONP column. In the effluent, PCE and TCE were first detected at 4.2 PV and 2.2 PV, respectively (**Figure 4.48**). Earlier breakthrough of TCE than PCE suggested that PCE has a higher adsorption affinity to IONPs than TCE. The effluent concentrations of PCE and TCE gradually increased and reached a steady state of 0.03 mM at 13.0 PV and 0.09 mM at 9.7 PV, respectively (**Figure 4.48**). Unexpected microbial degradation resulted in the production of *cis*-DCE after 19.4 PV. To inhibit microbial activity, 1 g/L sodium azide was added to the influent solution after 25 PV. After 28 PV, the concentrations of PCE and TCE returned to the steady-state concentrations, and no more *cis*-DCE was detected (**Figure 4.48**).

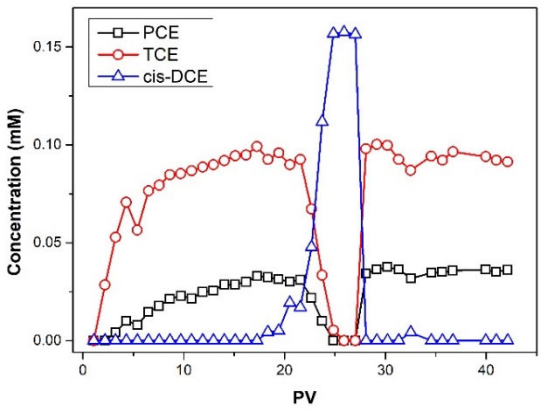


Figure 4.48 Concentrations of PCE/TCE and cis-DCE in the effluent during an injection of influent solution containing a mixture of PFAAs and PCE/TCE for 42.1 PVs in set 1 experiment (single IONP column).

The retention and breakthrough of 10 PFAAs in the single IONP column is illustrated in **Figure 4.49.** PFBA, PFPeA, PFHxA, and PFBS were the first to be detected at 1.1 PV, followed by PFHpA and PFOA, which appeared in the effluent at 2.2 PV. Breakthrough of PFHxS and PFNA were observed at 3.2 PV and 6.5 PV, respectively. PFDA and PFOS, the last two to emerge in the column effluent, exhibited breakthroughs at 18.4 PV. The effluent concentrations of PFBS, PFHxS, and all PFCAs except for PFDA, underwent a gradual increase, with a complete breakthrough ($C/C_0 \geq 1$) between 14 to 22 PV. In comparison, the longest chain PFCA and PFSA tested in this study, PFDA and PFOS did not reach to $C/C_0 \geq 1$ until 28.1 PV and 40.0 PV, respectively (**Figure 4.49**). The order of complete breakthrough for the 10 PFAAs indicates a distinct adsorption preference, with the sequence being PFOS > PFDA > PFNA > PFHxS > PFOA > PFHpA > PFBS > PFHxA > PFPeA > PFBA.

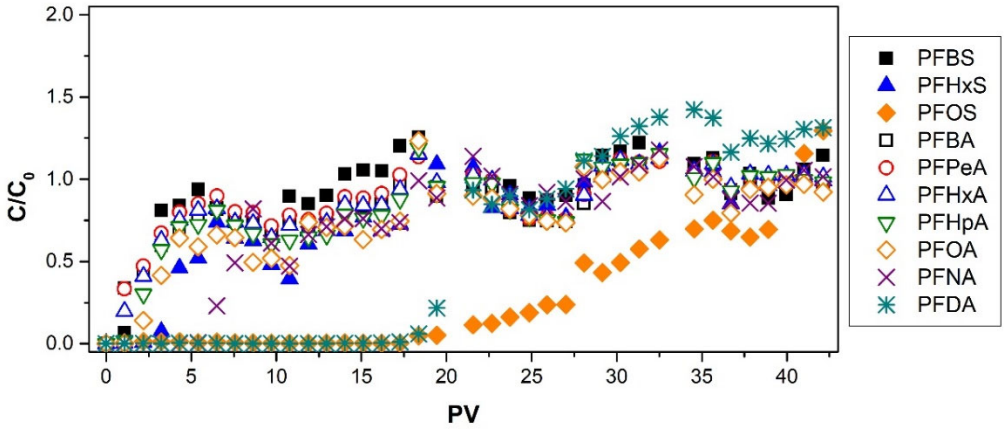


Figure 4.49 Breakthrough of 10 PFAAs, during an injection of influent solution containing a mixture of PFAAs and PCE/TCE for 42.1 PVs in set 1 experiment (single IONP column).

4.5.1.2 Set 2: Single S-PAC column experiment

Throughout the 87.5 PVs of operation, 0.05 ± 0.00 mM of PCE and 0.12 ± 0.01 mM of TCE were continuously introduced to the single S-PAC column. Similar to the results in the single IONP column, the breakthrough of TCE (6.5 PV) preceded that of PCE (14.0 PV) (**Figure 4.50**), indicating a higher adsorption affinity of PCE to S-PAC compared to TCE. The effluent concentrations of both PCE and TCE increased over time, with a complete breakthrough at 30.3 PV and 15.1 PV, respectively (**Figure 4.50**).

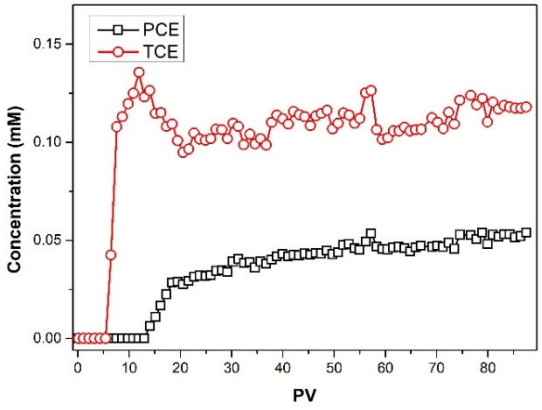


Figure 4.50 Concentrations of PCE and TCE in the effluent during an injection of influent solution containing a mixture of PFAAs and PCE/TCE for 87.5 PVs in set 2 experiment (single S-PAC column).

In the effluent of the single S-PAC column experiment, the breakthrough of PFBA and PFPeA was observed at 1.1 PV. Subsequently, PFBS, PFHxA, and PFHpA were detected in sequence between 3.2 and 5.4 PVs. In comparison, PFHxS and PFOA were not detected until 9.8 PV, while PFNA appeared in the effluent at 19.5 PV. The breakthrough of PFDA and PFOS was latest at 42.1 and 46.4 PVs, respectively. For the majority of these PFAAs, their effluent concentrations rapidly increased to the applied concentration following breakthrough. However, PFOS, PFNA, and PFDA took approximately 10 PVs to gradually reach $C/C_0 \geq 1$ (**Figure 4.51**). In the set 2 S-PAC column experiment, a complete breakthrough of 10 PFAAs was observed, with the order being PFOS > PFDA > PFNA > PFHxS > PFOA > PFHpA > PFHxA > PFBS > PFPeA > PFBA.

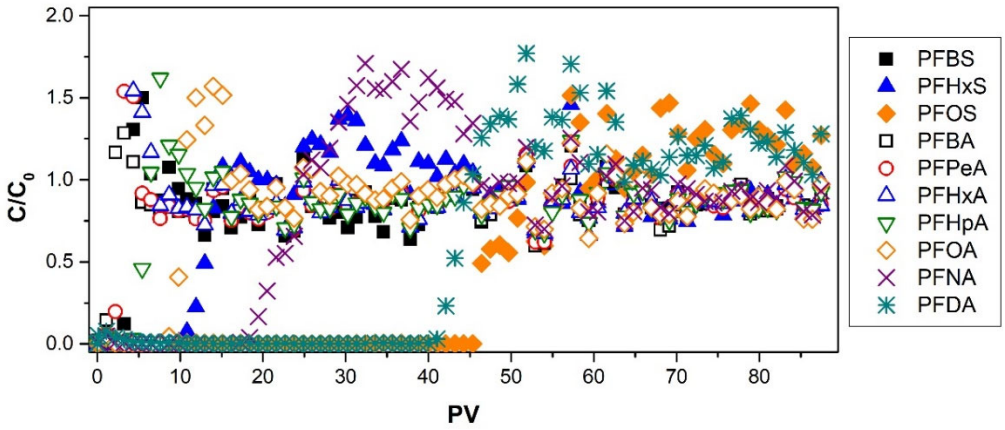


Figure 4.51 Breakthrough curves of 10 PFAAs, during an injection of influent solution containing a mixture of PFAAs and PCE/TCE for 87.5 PVs in set 2 experiment (single S-PAC column).

4.5.1.3 Set 3: Coupled bioactive and IONP columns experiment

An average of 0.06 ± 0.01 mM PCE and 0.11 ± 0.01 mM TCE was continuously introduced into the upgradient bioactive column during the 42.1 PVs operation. With a residence time of 2.2 days, nearly all PCE and TCE were degraded to non-toxic ethene (0.13 ± 0.03 mM) by the dechlorinating consortium in bioactive columns (**Figure 4.52** a). Low levels of VC (<0.03 mM) and *cis*-DCE (0.01 mM) were sporadically detected in the effluent of bioactive columns (**Figure 4.52)**. However, a further detoxicification of VC and *cis*-DCE was observed in the downgradient IONP sorptive columns; no *cis*-DCE and VC was detected in the effluent, except for a small amount of VC at 8.6 PV (**Figure 4.52**). The synergistic detoxification observed in IONP columns could be due to a further microbial dechlorination of VC and *cis*-DCE by dechlorinating bacteria flowing into the IONP columns. Additionally, VC and *cis*-DCE could be adsorbed on IONPs; the sorption of ethene was appreciated, as a slightly lower concentration of ethene was measured in the effluent of IONP column (0.10 ± 0.02 mM) compared to the influent (0.13 ± 0.03 mM).

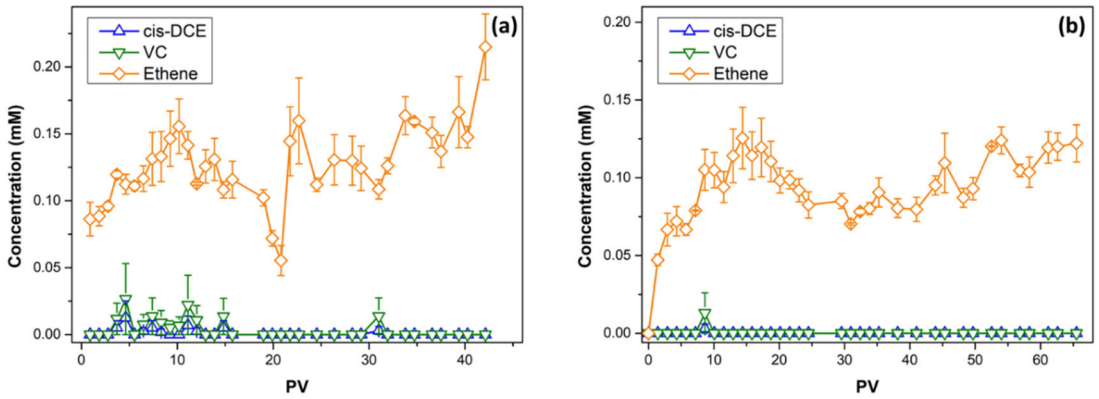


Figure 4.52 Average concentrations of PCE and TCE dechlorinated transformation products (cis-DCE, VC, and ethene) in the effluent of (a) the upgradient bioactive columns (n = 2) and (b) the

downgradient adsorptive (IONP) columns (n = 2) during a 42.1/65.5-PV injection of influent solution containing a mixture of PFAAs and PCE/TCE in set 3 experiment (coupled bioactive and IONP columns).

The effluent concentrations of all 10 PFAAs remained relatively stable and were similar to those in the influent of the bioactive columns during the operation. This is expected given the recalcitrance of PFAAs to microbial degradation, and 60 PVs injection of column influent to bioactive columns prior to initiation of the set 3 experiment. These 10 PFAAs with constant concentrations then entered the IONP columns. As shown in **Figure 4.53**, during the 65.5 PVs operation of downgradient IONP columns, PFBA, PFPeA, PFHxA, PFBS, and PFHpA were initially detected at 1.4 PV, whereas PFOA, PFHxS, and PFNA were detected initially at 4.3 PV, 7.2 PV, and 14.4 PV, respectively. Following their initial breakthrough, most PFAAs, except for PFOS and PFDA, showed rapid increases in concentration, reaching a plateau before 24.5 PV. In contrast, breakthroughs of PFOS and PFDA were not observed until 36.7-38.2 PV, with their concentrations gradually reaching influent levels ($C/C_0 = 1$) at 55.4-56.9 PV. The breakthrough order of the 10 PFAAs was consistent with the set 1 single IONP column, with PFDA and PFOS exhibiting the highest adsorption preference, followed by PFNA, PFHxS, PFOA, PFHpA, PFBS, PFHxA, PFPeA, and PFBA.

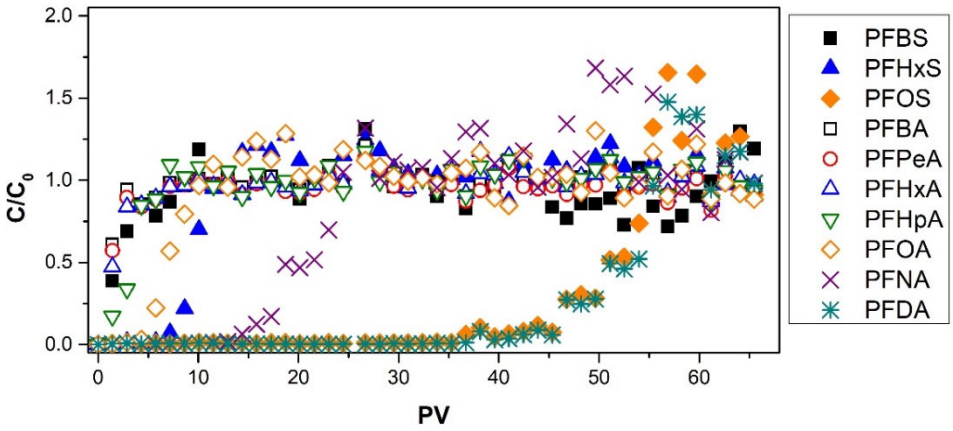


Figure 4.53 Breakthrough curves of 10 PFAAs in the IONP columns (n = 2), during a 42.1/65.5-PV injection of influent solution containing a mixture of PFAAs and PCE/TCE in set 3 experiment (coupled bioactive and IONP columns).

4.5.1.4 Set 4: Coupled bioactive and S-PAC columns experiment

Upon the completion of set 3 experiment, two downgradient IONPs columns were replaced with S-PAC sorptive columns to initiate Set 4 experiment. The same upgradient bioactive columns exhibited stable and improved microbial dechlorination performance. A complete microbial detoxification of PCE and TCE was achieved after passing through the bioactive columns; 0.05 ± 0.01 mM PCE and 0.12 ± 0.01 mM TCE were all degraded into ethene (0.14 ± 0.06 mM). A slightly lower ethene concentration (0.12 ± 0.06 mM) was measured in the effluent of downgradient S-PAC columns, due to the possible sorption (**Figure 4.54**). In addition, a large variation in ethene concentrations was measured in the

effluent of Set 4 experiment. Ethene formation in gas phase was visible along the bioactive columns, and it is hypothesized that the discontinuity of each gas phase could temporarily delay ethene elution at one sampling point, resulting in transient accumulation and "inflated" release of ethene at a subsequent sampling point. A similar phenomenon was documented in a previous study [213].

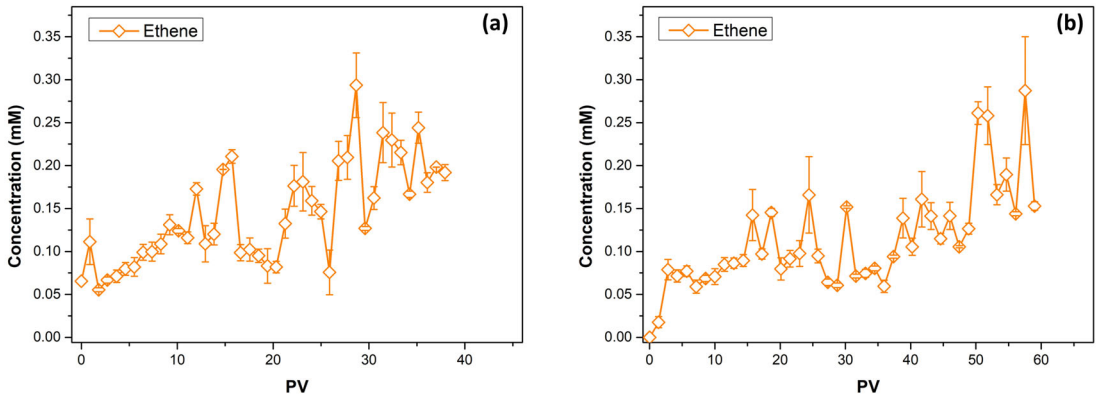


Figure 4.54 Average concentrations of PCE and TCE dechlorinated transformation products (cis-DCE, VC, and ethene) in the effluent of (a) the upgradient bioactive columns (n = 2) and (b) the downgradient adsorptive (S-PAC) columns (n = 2) during a 38.0/59.0-PV injection of influent solution containing a mixture of PFAAs and PCE/TCE in set 4 experiment (coupled bioactive and S-PAC columns).

Similar to the Set 3 experiment, the concentrations of all 10 PFAAs remained stable in the effluent of bioactive columns (i.e., influent of S-PAC columns) in the Set 4 experiment. As illustrated in **Figure 4.55**, in the effluent of S-PAC columns, PFBA was initially detected at 2.8 PV, and PFPeA and PFHxA were detected initially at 4.2 PV. Between 5.7-15.8 PV, PFBS, PFHpA, PFOA, PFHxS, and PFNA were then detected in sequence. Following the breakthrough, the relative concentrations of these PFAAs rapidly increased to $C/C_0 = 1$. PFDA was eluted at 47.5 PV, while the breakthrough of PFOS was not observed after 59 PVs operation of S-PAC columns. The breakthrough order of the 10 PFAAs was consistent with that in the set 2 single S-PAC column, indicating that PFOS had the highest adsorption preference, followed by PFDA, PFNA, PFHxS, PFOA, PFHpA, PFBS, PFHxA, PFPeA, and PFBA.

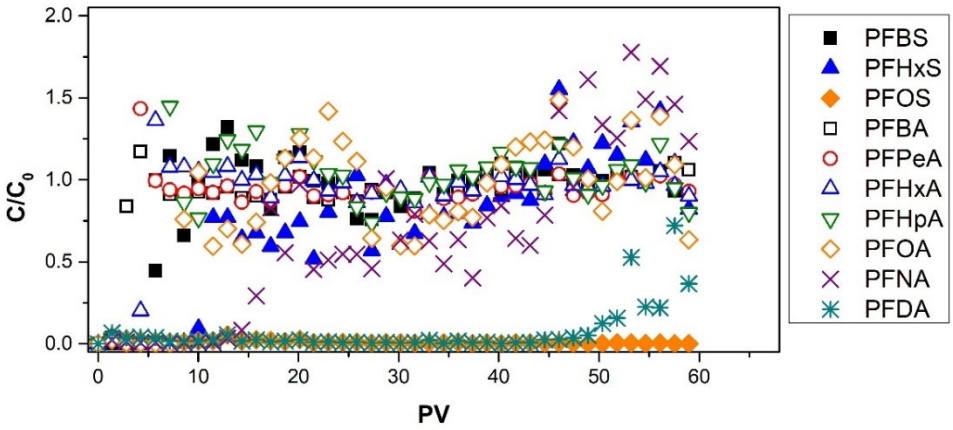


Figure 4.55 Breakthrough curves of 10 PFAAs in the S-PAC columns (n = 2), during a 38.0/59.0-PV injection of influent solution containing a mixture of PFAAs and PCE/TCE in set 4 experiment (coupled bioactive and S-PAC columns).

4.2.5 Enhanced sequestration of PFAAs in coupled bioactive and adsorptive columns

In addition to microbial detoxification of PCE and TCE achieved in the coupled bioactive and adsorptive columns, an obvious enhanced sequestration of long-chain PFAAs was observed in the IONP and S-PAC columns of set 3 and set 4 experiments, compared to the ones in set 1 and set 2 experiments. For example, breakthroughs of PFDA and PFOS occurred at 18.4 PV in the single IONP column (**Figure 4.49**), while they did not occur until 36.7-38.2 PV in the IONP column downgradient of bioactive columns (**Figure 4.53**). Likewise, breakthroughs of PFDA and PFOS were observed at 42.1-46.4 PVs in the single S-PAC column (**Figure 4.51**), whereas PFDA was first detected at 47.5 PV and no PFOS was detected at 59 PV in the S-PAC column downgradient from the bioactive columns (**Figure 4.55**). **Table 4.6** summarizes the calculated mass of PCE, TCE, and 10 PFAAs sequestrated in the IONP and S-PAC column at the conclusion of each experiment set. It was challenging to calculate the adsorption contribution of the small amounts of *cis*-DCE and VC generated in the coupled column experiment and the unexpected *cis*-DCE formed in the single adsorptive column, which, therefore, are not included. In the IONP columns within the coupled bioactive and IONP columns system, a larger mass of total PFAAs was retained (437.3 μg) compared to the single IONP column (394.0 μg). It took longer for the IONP columns in the coupled system (~57 PVs) to reach their adsorption capacity compared to the single IONP column (~40 PVs). Similarly, although the adsorption capacity of the S-PAC columns within the coupled column system has not been exhausted since PFOS and PFDA have not yet reached their applied concentrations, a greater mass of total PFAAs has already been retained in the S-PAC columns within the coupled system (601.24 μg) compared to the single S-PAC column (622.38 μg). These results suggested that with reductive dechlorination in bioactive columns upgradient, the adsorptive columns (both IONP and S-PAC) exhibited enhanced sequestration of PFAAs.

Table 4.6 Retained mass of PFAAs and PCE/TCE in adsorptive columns in all four sets of column experiments (PFAAs in μg, PCE/TCE in mg)

	IONP column in Set 1 (42.1 PVs)	**Avg. IONP columns in Set 3 (65.5 PVs)**	**S-PAC column in Set 2 (87.5 PVs)**	**Avg. S-PAC columns in Set 4 (59.0 PVs)**
PFBS	9.9 (11.2%)	7.2 (10.8%)	9.1 (4.7%)	14.9 (11.7%)
PFHxS	65.9 (23.1%)	59.6 (30.7%)	102.2(16.7%)	104.0 (27.7%)
PFOS	140.6 (67.5%)	195.3 (75.6%)	261.8 (59.2%)	**> 239.1** (98.9%)
PFBA	18.5 (13.4%)	8.6 (8.8%)	5.9 (2.1%)	10.8 (6.2%)
PFPeA	25.3 (11.3%)	12.8 (8.1%)	14.5 (3.0%)	23.6 (7.5%)
PFHxA	34.1 (11.8%)	20.9 (10.0%)	28.6 (4.6%)	37.8 (9.6%)
PFHpA	22.5 (17.0%)	12.3 (13.3%)	17.7 (6.1%)	22.4 (12.4%)
PFOA	28.3 (20.7%)	22.7 (24.0%)	34.1 (11.6%)	35.7 (19.1%)
PFNA	14.5 (23.4%)	26.2 (60.9%)	36.7 (26.8%)	41.4 (48.9%)
PFDA	34.4 (42.1%)	72.0 (76.1%)	90.7 (50.1%)	**> 92.7** (93.9%)
PCE	2.6 (48.2%)		4.8 (31.7%)	
TCE	2.2 (23.7%)		2.7 (10.2%)	

Note: The numbers in the parentheses represent the retained mass as a percentage of the total injected mass into the columns at the conclusion of the experiments.

The adsorption capacities of PFAAs and PCE/TCE in the adsorptive columns across all four sets of column experiments is shown in **Table 4.6**. The findings reveal a distinct trend in adsorption based on the perfluorinated carbon chain length, with longer-chain PFAAs exhibiting a higher adsorption capacity compared to their shorter-chain counterparts. Notably, perfluoroalkane sulfonic acids (PFSAs) demonstrated a greater adsorption capacity than perfluoroalkyl carboxylic acids (PFCAs) of the same chain length. Intriguingly, the single IONP column excelled in sequestering PFBA, PFPeA, PFHxA, and PFHpA, while the coupled bioactive and IONP columns were more effective at retaining PFOS, PFNA, and PFDA. This discrepancy can potentially be attributed to the presence of PCE and TCE in the single adsorptive column, which may have competed with the longer-chain PFAAs. Although the single S-PAC column and the coupled bioactive S-PAC columns displayed similar adsorption capacities for all PFAAs, it is noteworthy that PFOS and PFDA have not yet reached their applied concentrations at the conclusion of the set 4 experiment. This observation suggests the possibility of competitive adsorption between PCE/TCE and longer-chain PFAAs, like PFOS and PFDA.

Table 4.7 Adsorption capacity of PFAAs and PCE/TCE in adsorptive columns in all four sets of column experiments (retained mass per gram adsorptive material, in unit mg/g Fe or C)

	IONP column in Set 1 (42.1 PVs)	**Avg. IONP columns in Set 3 (65.5 PVs)**	**S-PAC column in Set 2 (87.5 PVs)**	**Avg. S-PAC columns in Set 4 (59.0 PVs)**
PFBS	1.8	1.3	0.3	0.4
PFHxS	12.0	10.8	3.3	2.9
PFOS	25.52	35.5	8.3	6.7
PFBA	3.4	1.6	0.2	0.3
PFPeA	4.6	2.3	0.5	0.7
PFHxA	6.2	3.8	1.0	1.1
PFHpA	4.1	2.2	0.6	0.6
PFOA	5.1	4.1	1.1	1.0
PFNA	2.6	4.8	1.2	1.2
PFDA	6.2	13.1	2.9	2.6
PCE	473.9		153.4	
TCE	397.6		86.5	

4.6 Evaluation of S-PAC as a Permeable Adsorptive Barrier

The goals of these studies were to (a) develop stable aqueous suspensions of powdered activated carbon (S-PAC), (b) evaluate the delivery and retention of S-PAC, and (c) quantify the ability of S-PAC to sorb PFOA and PFOS under dynamic conditions. Preliminary studies demonstrated that a cationic polymer, polydiallyldimethylammonium (polyDADMAC), which has also been shown enhance PFAS sorption by soils [261, 262] was able to effectively stabilize DARCO® 100-mesh PAC in aqueous solutions. Batch reactor experiments were conducted to determine the adsorption capacity of DARCO® 100-mesh PAC for PFOS and PFOA. A series of column studies was then performed to evaluate the delivery and retention of PAC in water-saturated Ottawa sand, and subsequently, to assess the sorption of PFOA and PFOS by PAC-treated sand. To further evaluate the performance of S-PAC under more realistic conditions, a heterogeneous laboratory-scale aquifer cell study was completed to assess the S-PAC injection and subsequent retention of PFOS.

4.6.1 S-PAC Batch Adsorption Results

The results of batch adsorption tests conducted with ground PAC (DARCO®, 100 mesh, < 149 µm) and either PFOA or PFOS are shown in **Figure 4.56**. Using a non-linear least squares regression procedure, the adsorption data were fit to the Freundlich adsorption model;

$$C_s = K_F C_w^n \quad (\mathbf{4.1})$$

where C_s is the solid-phase concentration, K_F is the Freundlich distribution coefficient, C_w is the concentration in water, and n is a Freundlich exponent. The Freundlich model is based on the premise that a range of adsorption sites exist with varying free energies, resulting nonlinear behavior. The fitted values of K_F (135 and 629 L/g^{-n}) and n (0.54 and 0.30) obtained for PFOA and PFOS are similar to those reported in the literature for PAC [206, 263].

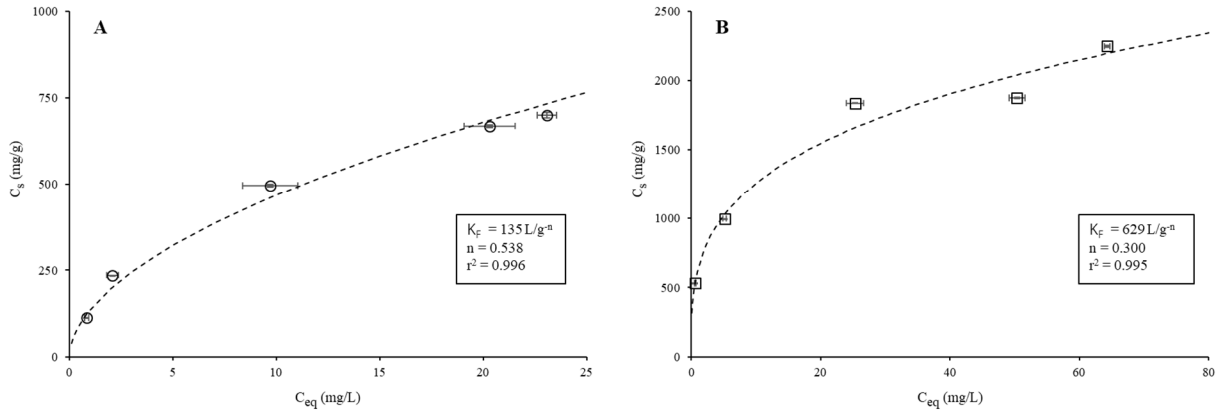


Figure 4.56 Adsorption of PFOA (A) and PFOS (B) on 100-mesh PAC and corresponding fits to the Freundlich adsorption model. Error bars represent standard deviation of mean for three replicates.

4.6.2 S-PAC Column Results

After each column was packed with 40-50 mesh Ottawa sand and completely saturated with water, a non-reactive tracer test was performed assess hydrodynamic dispersion and confirm the pore volume, which was approximately 20 mL. A representative effluent breakthrough curve (BTC) for the tracer test is shown in **Figure 4.57**. Preliminary column experiments were undertaken to

evaluate the injection of S-PAC (3.5 PV of 1,000 mg/L PAC + 5,000 mg/L polyDADMAC) and subsequent distribution of retained PAC after flushing with 3.5 PV of background solution (10 mM NaCl) at a flow rate of 0.12 mL/min (pore-water velocity ~ 1 m/day). Representative photographs of the S-PAC injection sequence are shown in **Figure 4.58**, while the resulting PAC retention profile after flushing with the background solution are shown in **Figure 4.59**. Dynamic light scattering indicated that the particle size of the PAC ranged from approximately 70 nm to greater than 1 μm, with an average diameter of 225 nm (**Figure 4.60**). The total amount of PAC measured in each column ranged from 17.6 to 23.5 mg, equivalent to 24 to 32% of the injected PAC was retained. Based on the measured PAC carbon content of 85%, these values correspond to an average solid phase carbon content of 0.19 to 0.25 mg C/g dry sand. To further evaluate PAC retention by the solid phase, grains of quartz sand were collected from S-PAC treated and untreated (control) columns for SEM-EDS analysis. As shown in **Figure 4.61**, PAC was deposited in localized regions on the mineral surface, leading to a nonuniform or "patchy" coverage.

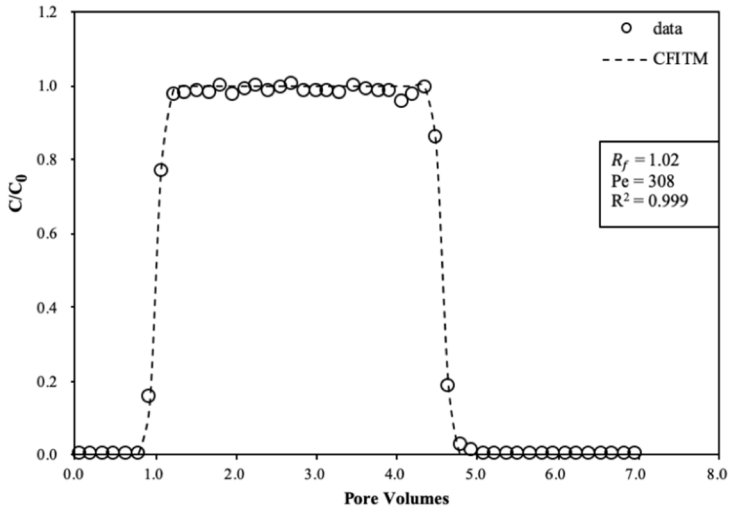


Figure 4.57 Representative bromide tracer breakthrough curve (BTC) obtained for a water-saturated column containing untreated 40-50 mesh Ottawa sand. The pore volume was approximately 20 mL, and the 10 mM NaBr solution was introduced at a flow rate of 0.12 mL/min, yielding a residence time of approximately 2.75 h. Experimental data were fit to a one-dimensional form of the advective-dispersive transport equation using the CXTFIT program.

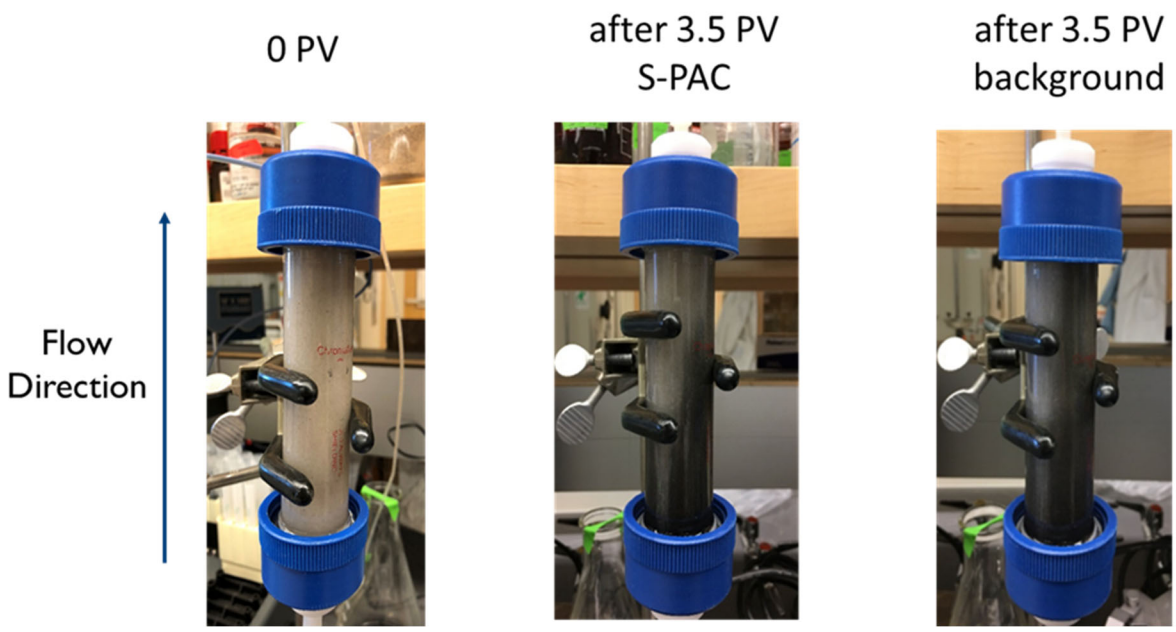


Figure 4.58 Photographs showing the injection of S-PAC and retention PAC (dark color) in a water-saturated column packed with 40-50 mesh Ottawa sand. Approximately 3.5 PV of S-PAC were injected followed by 3.5 PV of background solution (10 mM NaCl) at a flow rate was 0.12 mL/min.

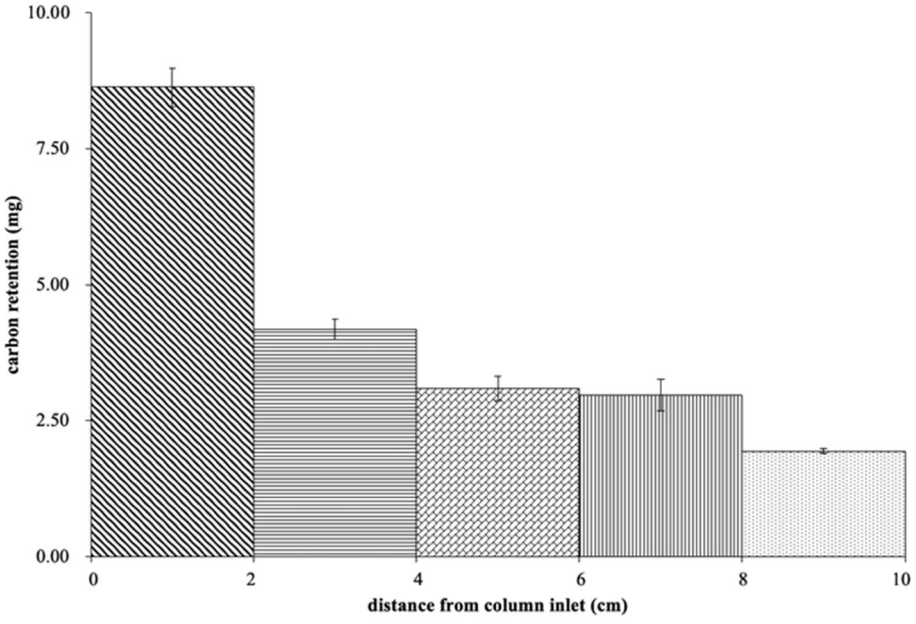


Figure 4.59 Distribution of retained carbon after the injection of 3.5 pore volumes of S-PAC into a column packed with water-saturated 40-50 mesh Ottawa sand followed by 3.5 pore volumes of background electrolyte solution (10 mM NaCl) at a flow rate of 0.12 mL/min.

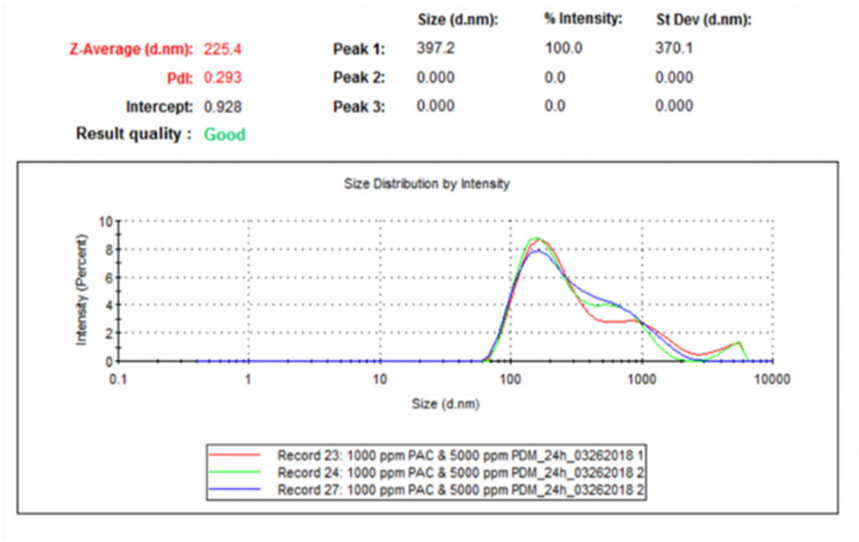


Figure 4.60 Particle size distribution of stabilized PAC obtained by dynamic light scattering using a Zetasizer Nano ZS Analyzer operated in back-scattering mode at an angle of 173º.

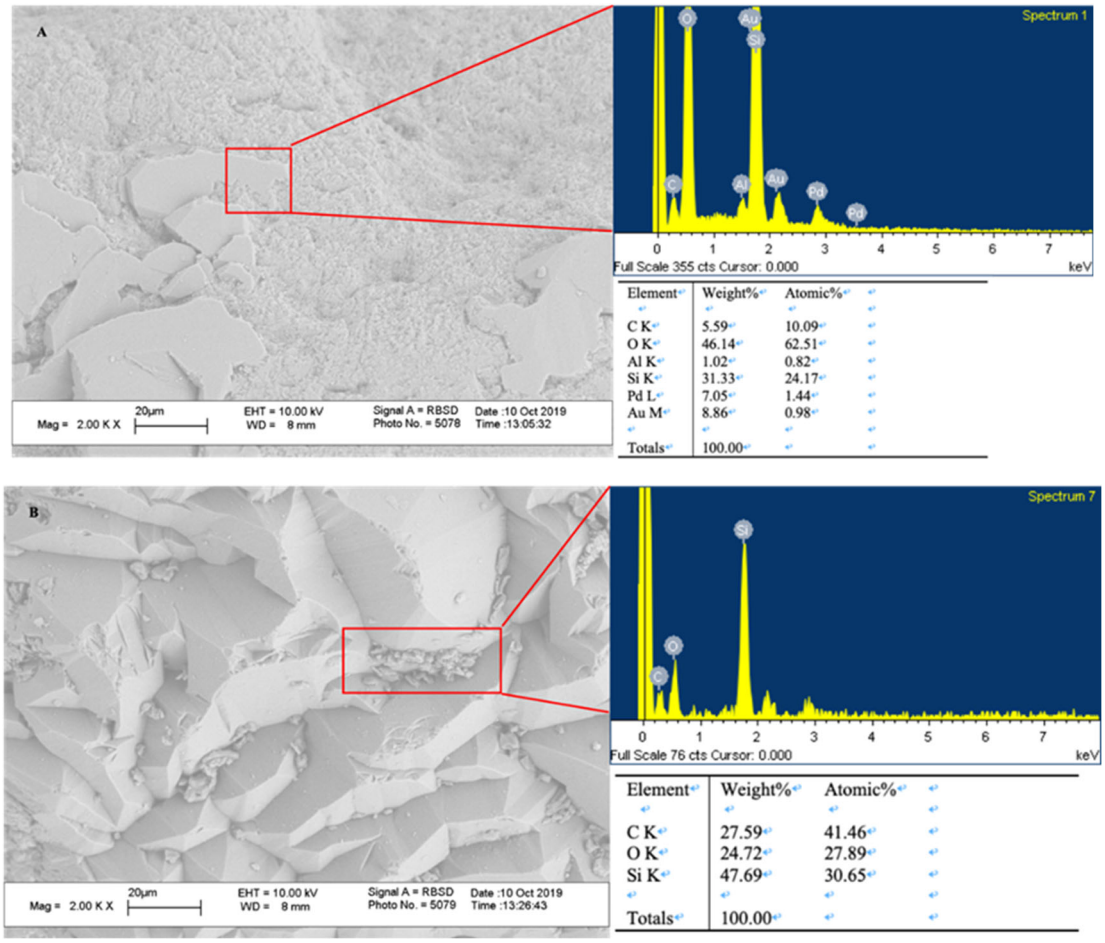


Figure 4.61 Images of 40-50 mesh Ottawa sand (A) before and (B) after treatment with S-PAC obtained using a Zeiss Leo 1530 VP SEM-EDS.

Following the establishment of retained PAC within each column, an aqueous solution containing either PFOA or PFOS was introduced at a flow rate 0.12 mL/min, which corresponds to a residence time of approximately 2.75 h. The resulting PFOA and PFOS effluent breakthrough curves (BTCs) are shown in Figure 3. Initially, the injected solution contained 100 µg/L of PFOA or PFOS in 10 mM NaCl, but no breakthrough was observed after approximately 15 PVs. Therefore, the influent concentration was increased to 20 mg/L PFOA or PFOS to evaluate the overall adsorptive capacity of S-PAC treated columns. For PFOA, breakthrough occurred at approximately 30 PVs, while PFOS breakthrough occurred after approximately 40 PVs. In contrast, breakthrough of PFOA and PFOS occurred after only 1 and 3 PVs in columns packed with untreated 40-50 mesh Ottawa sand (negative control) at a similar flow rate (0.12 mL/min) and influent concentration (100 µg/L) (**Figure 4.62**). Based upon the difference between the mass of PFOA or PFOS injected and the amount measured in the column effluent, a total of 6.57 mg of PFOA and 10.30 mg of PFOS were retained within the S-PAC treated columns (**Figure 4.63**). Thus, the addition of PAC with polyDADMAC increased PFOA and PFOS retention by three orders of magnitude compared to the untreated 40-50 mesh Ottawa sand. In these columns, 17.3 to 20.8 mg of PAC were retained, yielding overall adsorption capacities for PFOA and PFOS of 379.8 mg/g and 495.2 mg/g, respectively. In prior work, Aly et al. (Aly et al., 2018, 2019) reported that treating of 40-50 mesh Ottawa sand with a 5,000 mg/L polyDADMAC solution increased the retention of PFOA or PFOS by 6 to 10 times, while treating a natural soil with a 5,000 mg/L polyDADMAC solution increased the retention of PFOA or PFOS by 4 to 6 times, respectively. Based on the results shown in **Figure 4.63**, injection of a solution containing 100 µg/L PFOA or PFOS into an S-PAC treated column would not be expected to result in breakthrough until 4,060 and 6,360 PVs, respectively, representing more than a 3 order of magnitude increase in retention capacity compared to untreated Ottawa sand or a polyDADMAC treatment alone.

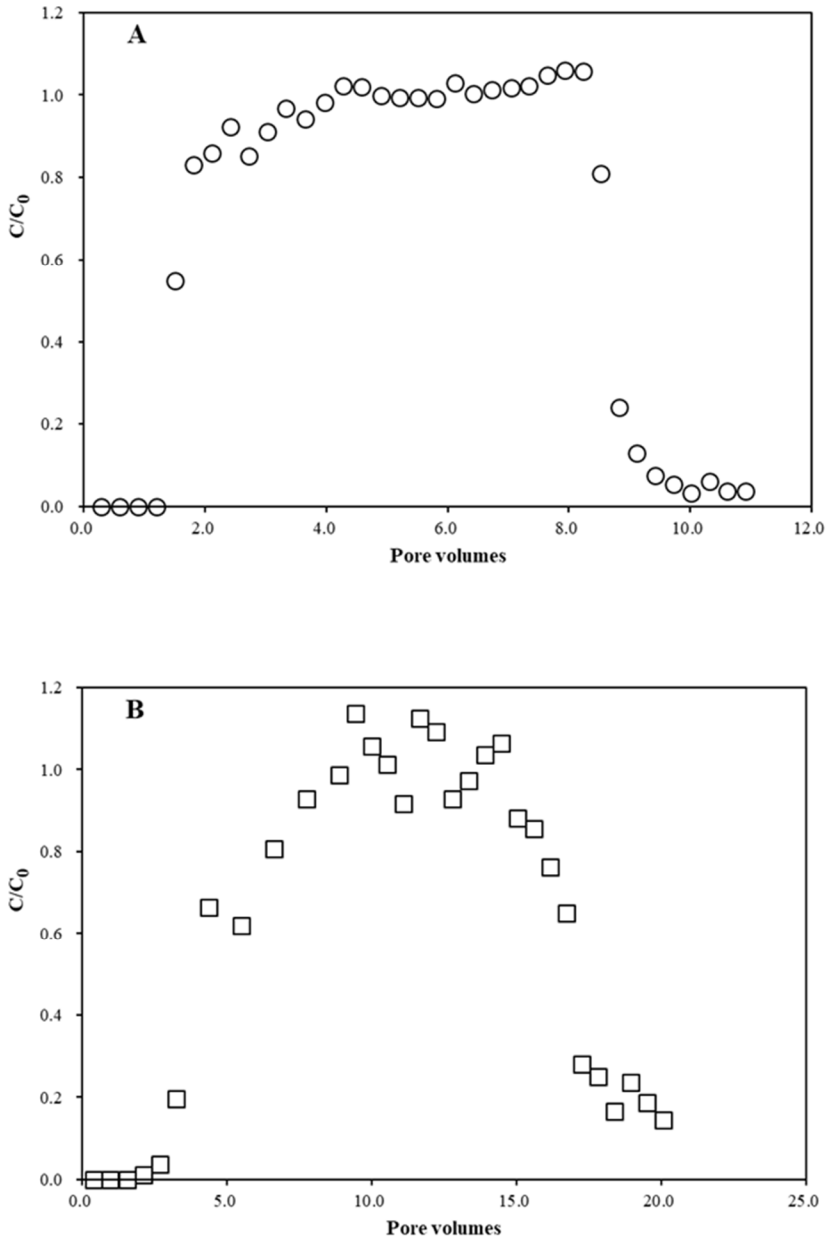


Figure 4.62 Effluent breakthrough curves obtained for pulse injections of aqueous solutions containing either (A) PFOA (100 µg/L) or (B) PFOS (100 µg/L) in water-saturated columns containing untreated 40-50 mesh Ottawa sand at a flow rate of 0.12 mL/min (pore-water velocity of 1 m/day).

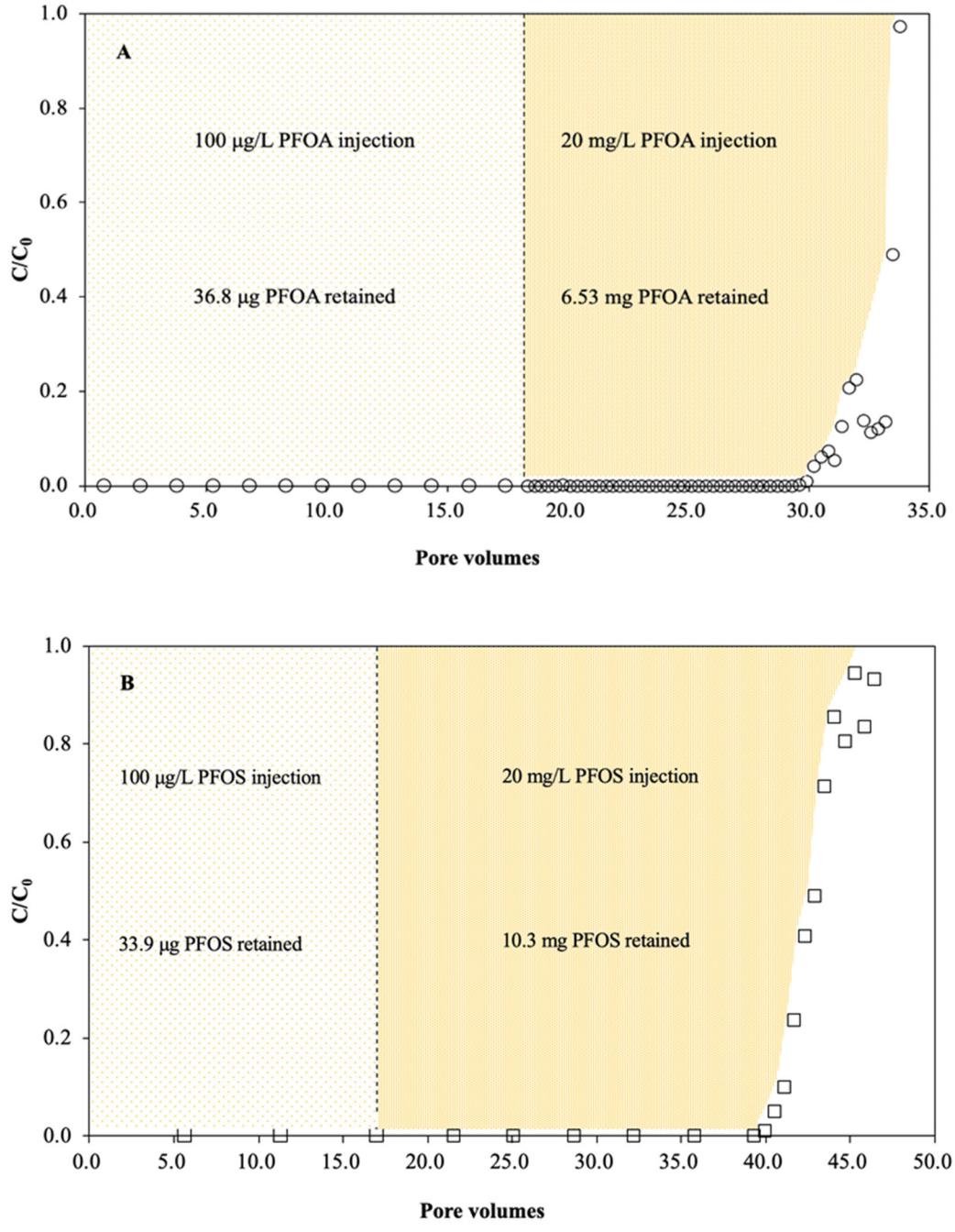


Figure 4.63 Effluent breakthrough curves obtained for the injection of either (A) PFOA or (B) PFOS (100 µg/L then 20 mg/L) in water-saturated columns containing S-PAC treated 40-50 mesh Ottawa sand. Shaded areas show the amount of PFOA or PFOS retained in the columns. The pore volume of each column was approximately 20 mL and the flow rate was 0.12 mL/min, yielding a residence time of 2.75 h.

4.6.3 S-PAC Aquifer Cell Results

The aquifer cell was configured to represent a heterogeneous formation with regions of high- and low-permeability porous media. In this scenario, the S-PAC suspension was injected into the lower high-permeability zone (ports 8 and 9) with the goal of reducing PFOA and PFOS mass flux from the cell, while causing minimal alteration to the local permeability field (**Figure 4.64 and Figure 4.65**). A solution containing 50 µg/L PFOS, 50 µg/L PFOA and 10 mM NaBr was introduced immediately upgradient of the upper control region (port 2) and the lower S-PAC treated region (port 4), and down-gradient side-port and effluent well samples were collected over a period of 70 h or approximately 7 total PVs. In the untreated upper region of the aquifer cell, both PFOA and PFOS appeared in the down-gradient sampling ports (6 and 7) within 5 and 10 h after injection (**Figure 4.66**), respectively, and approached the injection concentration of 50 µg/L, consistent with appearance the non-reactive tracer in ports 6 and 7, which was injected simultaneously (**Figure 4.67**). Immediately down gradient of the S-PAC treated region of the aquifer cell, PFOA and PFOS concentrations were greatly reduced, with a maximum of 0.23 µg/L PFOS detected in sampling port 12 at 24 h. Maximum PFOA concentrations of 1.36 µg/L and 0.63 µg/L were detected in samples ports 13 and 18 at 24 h, respectively (**Figure 4.66 c**). Based on the effluent data collected over time, 85.5 and 99.2% of the injected PFOA and PFOS was retained, respectively. Despite the appearance of low concentrations of PFOA and PFOS in the effluent, the aquifer cell experiment demonstrated the ability of the S-PAC to create an *in situ* adsorptive zone in the higher permeability regions of a heterogeneous domain with minimal bypassing.

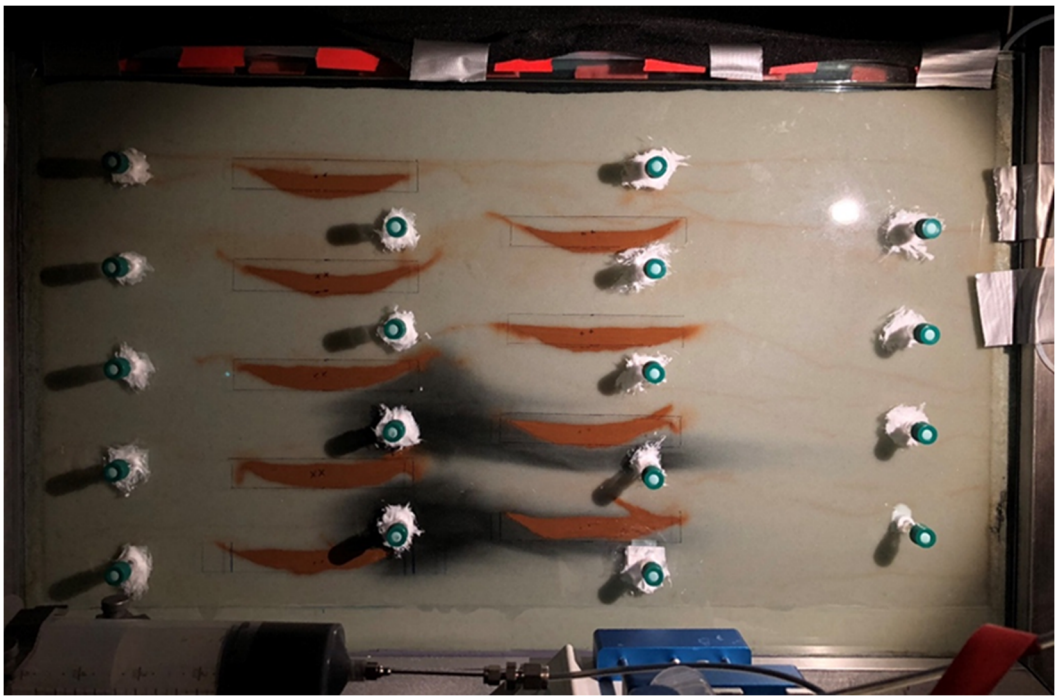


Figure 4.64 Photograph showing retained PAC (dark color) following the injection of 80 mL of S-PAC into side-ports 8 and 9 of the aquifer cell at a flow rate of 0.08 mL/min.

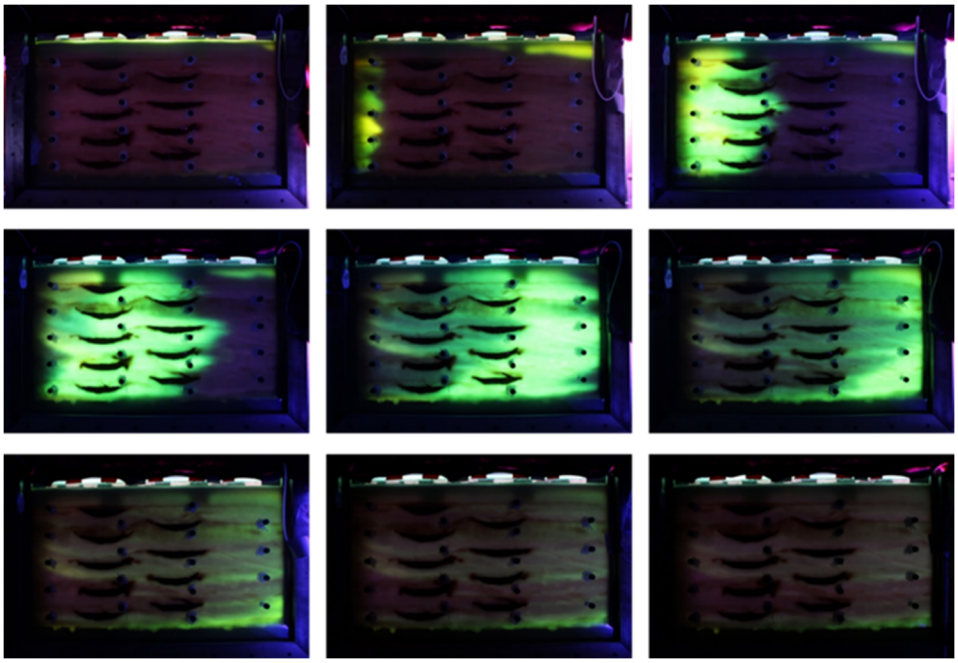


Figure 4.65 Fluorescein tracer test (0.5 PV pulse injection) conducted in the aquifer cell prior to injection of S-PAC at a flow rate of 2.4 mL/min. Images collected at intervals of 0.26 PV.

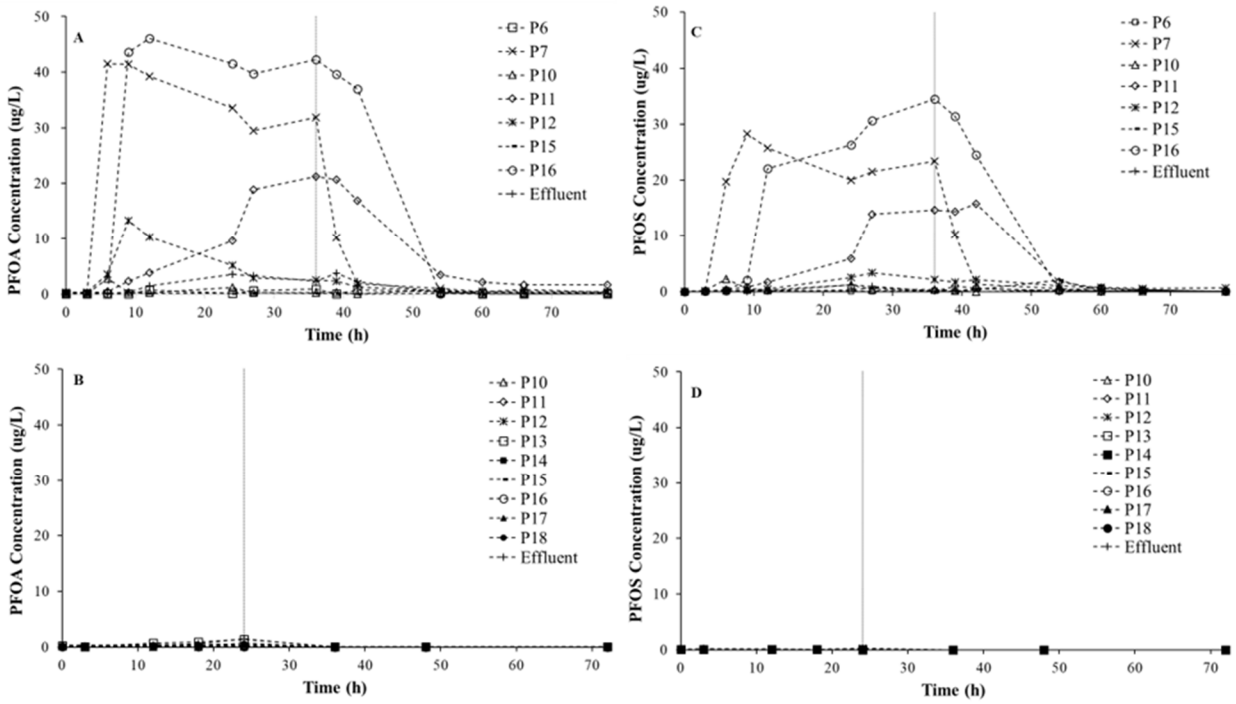


Figure 4.66 Aquifer cell side-port and effluent samples for PFOA in (A) upper untreated control region and (B) lower S-PAC treated region, and for PFOS in (C) upper untreated control region and (D) lower S-PAC treated region. A 260 mL pulse of solution containing 50 µg/L PFOS, 50 µg/L PFOA, and 10 mM NaBr (tracer) was injected through ports 2 and 4 immediately up-gradient from the control and S-PAC treated regions of the aquifer cell, respectively.

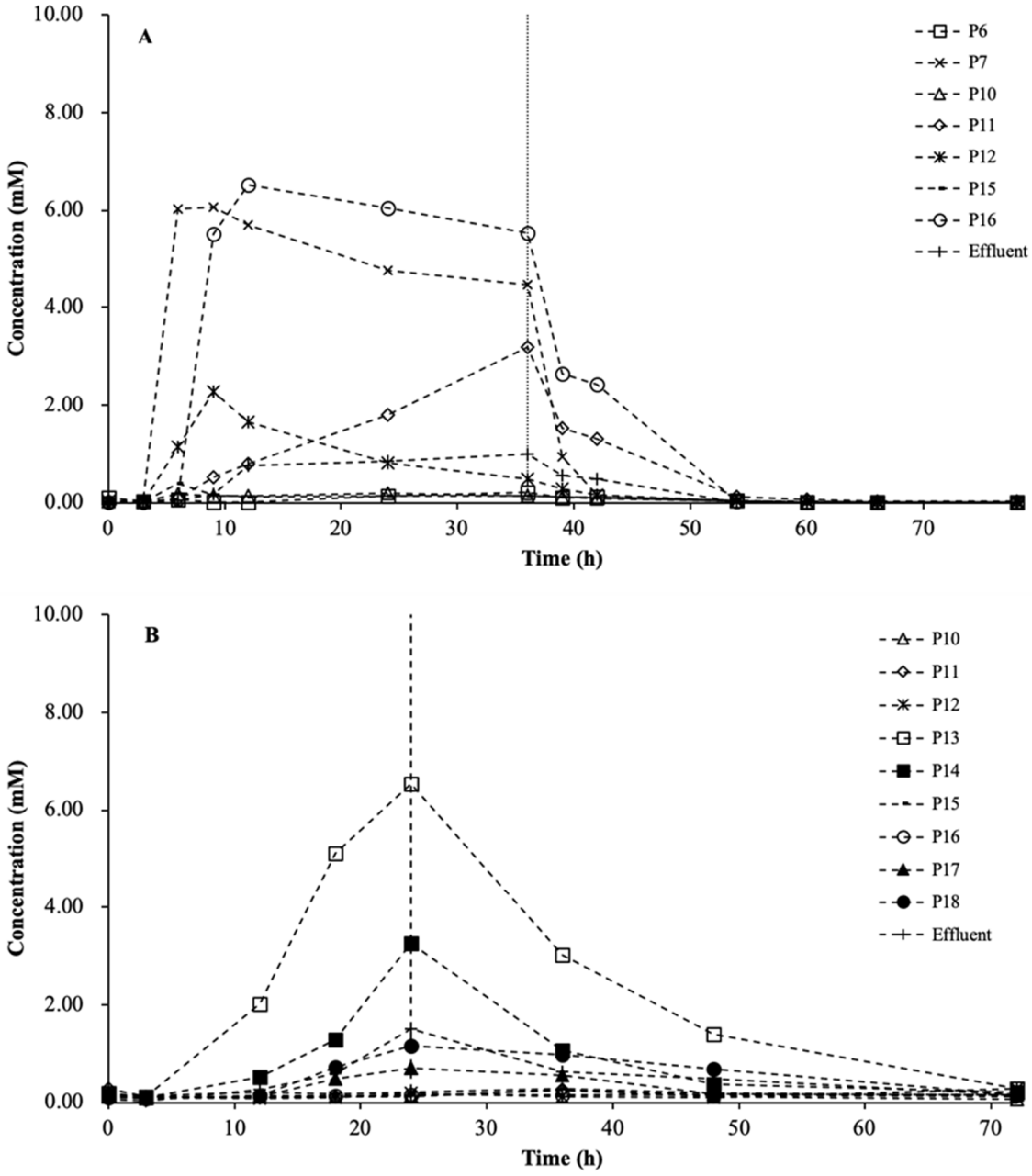


Figure 4.67 Aquifer cell side-port and effluent samples for PFOA in (A) upper untreated control region and (B) lower S-PAC treated region, and for PFOS in (C) upper untreated control region and (D) lower S-PAC treated region. A 260 mL pulse of solution containing 50 µg/L PFOS, 50 µg/L PFOA, and 10 mM NaBr (tracer) was injected through ports 2 and 4 immediately up-gradient from the control and S-PAC treated regions of the aquifer cell, respectively.

4.7 Evaluation of S-IXR as a Permeable Adsorptive Barrier

One potential strategy for *in situ* remediation of PFAS-impacted groundwater involves the injection of particulate amendments into the subsurface to create a permeable adsorptive barrier (PAB) that acts to sequester PFAS, with the goal of concentrating contaminant mass and limiting subsequent migration. In the studies described above, an aqueous suspension consisting of powdered activated carbon (PAC) stabilized by polydiallyldimethylammonium chloride (polyDADMAC) was injected into a column containing water-saturated quartz sand to create an adsorptive zone that increased PFOA and PFOS adsorption by more than 3 orders-of-magnitude compared to untreated control columns [35]. Similarly, in a pilot-scale field study, injection of colloidal activated carbon was shown to reduce the concentrations of PFOA and PFOS in groundwater from 3.26 µg/L and 1.45 µg/L, respectively, to below 30 ng/L [264].

Based on the desire to achieve greater adsorption capacity for a broader range of PFAS, the goal of this work was to develop a polymer-stabilized suspension of ion exchange resin (S-IXR) that can be injected to porous media to create a permeable adsorptive zone. Amberlite® IRA910 was selected as the anion exchange resin due to its demonstrated adsorption capacity for PFAS, pH independent adsorption resulting from quaternary ammonium functional groups, and potential for regeneration with sulfate radical-based oxidation [171, 211, 265, 266]. The matrix of IRA910 is macroreticular crosslinked polystyrene and the functional group is dimethyl ethanol ammonium. The total exchange capacity of IRA 910 is ≥ 1.00 eq/L (Cl^- form). Pluronic® F-127, a non-ionic polymer (molecular weight of approximately 12,500 Da), was selected as the stabilizing polymer due to its low toxicity, low viscosity (1.01 cP at 1,500 mg/L 25°C) and ability to effectively stabilize resin particles in preliminary experiments. Due to their inclusion on the U.S. EPA third Unregulated Contaminant Monitoring Rule (UCMR 3), the following six PFAS were evaluated: PFOS, PFOA, perfluorononanoic acid (PFNA), perfluorohexanesulphonic acid (PFHxS), perfluoroheptanoic acid (PFHpA), and perfluorobutanesulfonic acid (PFBS). A combination of batch reactor and column studies were performed to (a) obtain adsorption isotherms for individual PFAS and multi-solute mixtures, (b) assess the delivery and retention of S-IXR in a quartz sand, and (c) determine the adsorption capacity of the S-IXR treated sand for PFOA, PFOS and a mixture of the six PFAS under dynamic conditions.

4.7.1 S-IXR batch adsorption results for individual PFAS

The results of single-solute batch adsorption experiments conducted with ground Amberlite® IRA910 beads and each of the six PFAS (PFOS, PFOA, PFNA, PFHxS, PFHpA, or PFBS) are shown in **Figure 4.68**. In the low concentration range (1 to 100 µg/L), all six PFAS exhibited linear sorption. The corresponding linear adsorption coefficient (K_D) values obtained for PFOS, PFOA, PFNA, PFHxS, PFHpA and PFBS are shown in **Table 4.8**. In the higher concentration range (10 to 500 mg/L), all the PFAS adsorption isotherms were non-linear over the concentration range evaluated, and were therefore fit to the Freundlich model: $C_s = K_F C_{eq}^{n}$, where C_s is the solid-phase concentration, C_{eq} is the aqueous phase concentration, K_F is the Freundlich distribution coefficient and n is the adsorption constant. The Freundlich adsorption parameters obtained for PFOS, PFOA, PFNA, PFHxS, PFHpA, and PFBS are shown in **Table 4.9**. When comparing among the six PFAS tested, adsorption was greater for longer C-F chain length sulphonates or carboxylates (i.e., PFOS>PFHxS>PFBS and PFNA>PFOA>PFHpA). For PFAS of equal C-F chain length, sulphonates exhibited stronger adsorption than carboxylates (e.g., PFOS > PFNA). These adsorption trends are consistent with previous studies, which reported adsorption capacities ranging from 900 to 1,750 mg/g for PFOS and PFOA on ion exchange resins under similar

conditions, and are approximately three times greater than adsorption capacities reported for granular activated carbon [29, 205, 206, 211, 267], and similar to those reported for powdered activated carbon [35].

Table 4.8 Linear adsorption coefficient (K_D) values obtained for individual PFAS and mixture of the six PFAS in completely mixed batch reactors in the low concentration range (1 to 100 μg/L).

Adsorption of Individual PFAS						
	PFOS	PFOA	PFNA	PFHxS	PFHpA	PFBS
K_D (L/g)	194.19	9.51	12.95	60.52	5.34	15.88
R^2	1.00	1.00	1.00	1.00	0.99	1.00
Adsorption from Mixtures of Six PFAS						
	PFOS	PFOA	PFNA	PFHxS	PFHpA	PFBS
K_D (L/g)	184.25	8.51	15.43	56.62	4.04	14.30
R^2	0.98	0.99	0.99	0.99	0.99	0.99

Table 4.9 Freundlich adsorption parameters (K_F and n) obtained for individual PFAS in completely mixed batch reactors in the high concentration range (10 to 500 mg/L).

Adsorption of Individual PFAS						
	PFOS	PFOA	PFNA	PFHxS	PFHpA	PFBS
K_F (L/g)	543.40	316.81	287.12	365.17	143.41	136.64
n	0.25	0.25	0.29	0.26	0.24	0.29
R^2	0.99	0.95	0.98	0.96	0.97	0.98

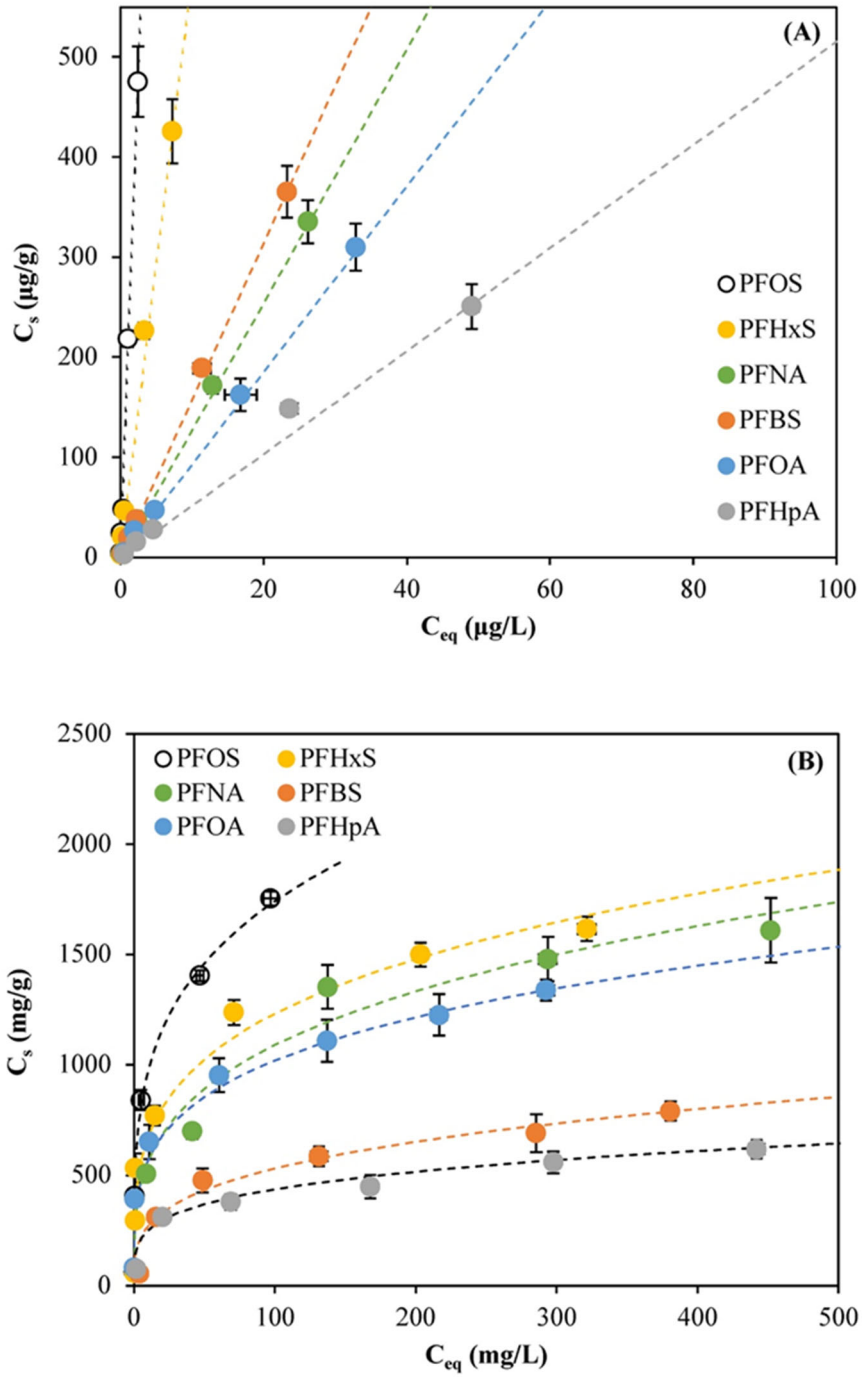


Figure 4.68 Sorption of PFOS, PFOA, PFNA, PFHxS, PFHpA, or PFBS on Amberlite® IRA910 in single-solute experiments over a concentration range of (A) 1 to 100 µg/L and (B) 10 to 500 mg/L with corresponding fits (dashed lines) to (A) linear and (B) Freundlich adsorption model.

4.7.2 S-IXR batch adsorption results for mixtures of PFAS

The results of multi-solute batch adsorption experiments conducted with ground Amberlite® IRA910 beads and aqueous solutions containing equal concentration mixtures of PFOS, PFOA, PFNA, PFHxS, PFHpA, or PFBS are shown in **Figure 4.69**. For the low concentration range (1 to 100 µg/L each), all six PFAS exhibited linear sorption behavior. The linear adsorption coefficient (K_D) values are shown in **Table 4.8**. Similar to the behavior observed in the single-solute experiments, PFAS with longer C-F chain length exhibited greater adsorption than shorter chain length species, and sulfonates exhibited greater adsorption compared to carboxylates of equal C-F chain length. The isotherms for all 6 PFAS were similar to the isotherms obtained in single-solute experiments as shown in **Figure 4.70**. The K_D values obtained in multi-solute experiments are within 75.72% to 119.21% of the K_D values obtained in single-solute experiments. The K_D values for both individual and PFAS mixture experiments are summarized in **Table 4.8**. Thus, at these environmental relevant concentration levels (< 100 µg/L), the influence of competitive adsorption on the six PFAS was negligible.

For the higher concentration range (2 to 100 mg/L), non-linearity was again observed with varying trends among the six PFAS. For PFOS the adsorption isotherm obtained in the multi-solute experiment was similar but slightly lower than the isotherm for PFOS in the single-solute experiment as shown in **Figure 4.71**. The following Freundlich adsorption parameters were obtained for PFOS in the mixture (K_F = 404 L/g, n = 0.232, R^2 = 0.95). In contrast, the adsorbed concentrations of PFNA and PFHxS initially increased at low equilibrium aqueous concentrations (< 5 mg/L), remained relatively constant (within 23.6% for PFHxS and 3.89% for PFNS) over an aqueous concentration range of 5 to 40 mg/L, and then declined gradually at higher equilibrium aqueous concentrations (40 to 100 mg/L). The adsorbed concentrations of PFOA, PFHpA and PFBS also increased to 192.15 mg/g, 160.45 mg/g and 222.66 mg/g, respectively, at the low equilibrium aqueous concentrations (< 10 mg/L) but then decreased markedly as the equilibrium concentrations increased above 10 mg/L. At the highest equilibrium aqueous concentrations, the adsorbed concentrations of PFOA, PFHpA and PFBS decreased to 29.95 mg/g, 27.00 mg/g and 5.48 mg/g, which were reduced by 84.4%, 83.2% and 97.54 when compared to their highest adsorbed concentrations, respectively.

When compared to single-solute experiments, the adsorbed amounts of all six PFAS were lower in the multi-solute system as shown in **Figure 4.71**. The divergence between adsorption isotherms in single-solute and multi-solute experiments was exacerbated at higher initial concentrations. At an initial concentration of 100 mg/L each, PFOS was the least affected by competitive adsorption with the amount adsorbed decreasing from 94.2% of the initial applied mass in single solute experiment to 81.8% in multi-solute experiment, while the adsorption of the other PFAS decreased to less than 20% of the initial applied mass in multiple solute experiment as shown in **Figure 4.72**. The observed competitive adsorption behavior described above was consistent with data reported in literature for IXR as well as other adsorbents in the rank of competitive adsorption (PFOS > PFNA > PFHxS > PFOA > PFBS > PFHpA)[211, 268, 269].

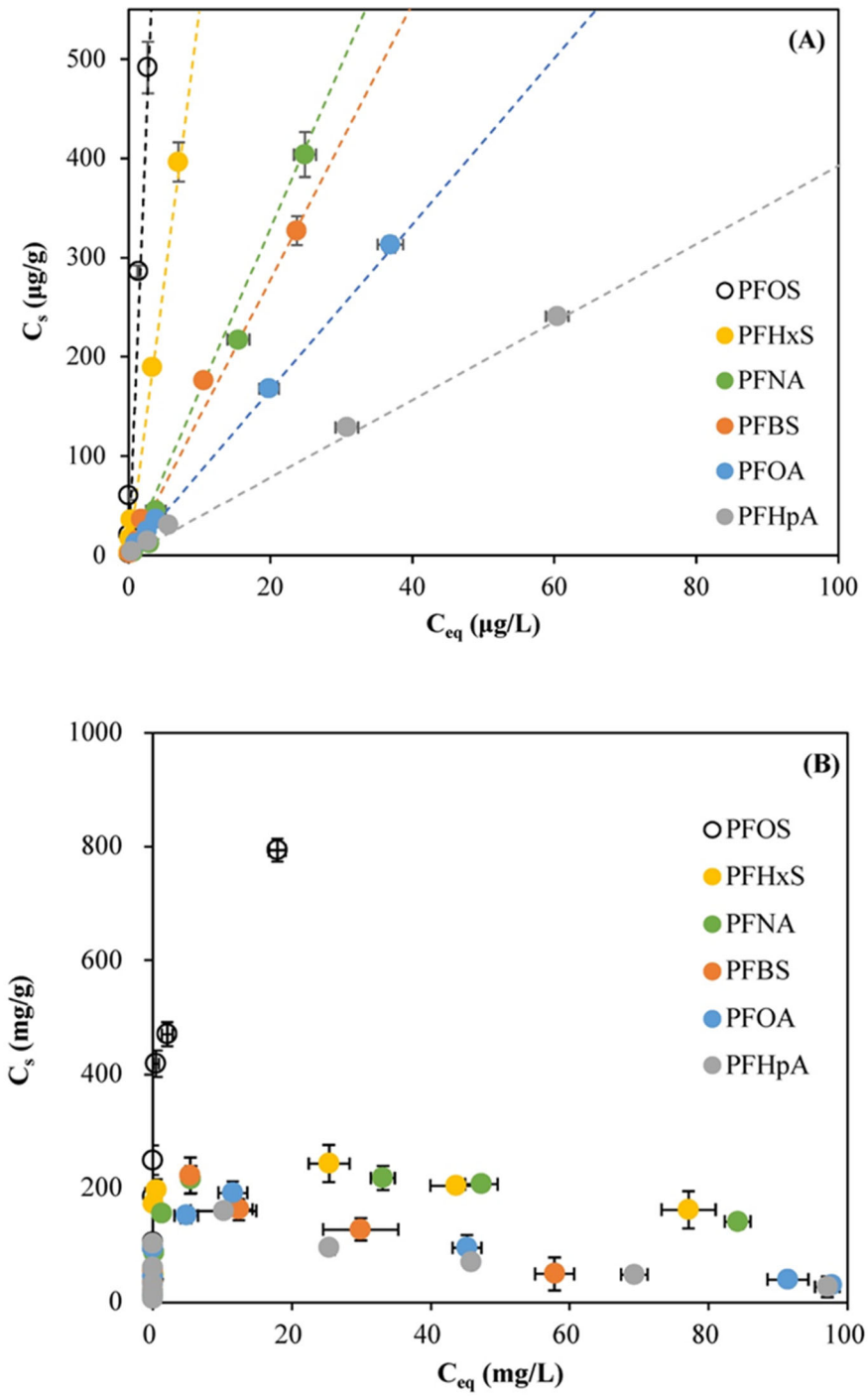


Figure 4.69 Sorption of mixtures of PFOS, PFOA, PFNA, PFHxS, PFHpA, and PFBS on Amberlite® IRA910 over a concentration range of (A) 1 to 100 µg/L and (B) 2 to 100 mg/L.

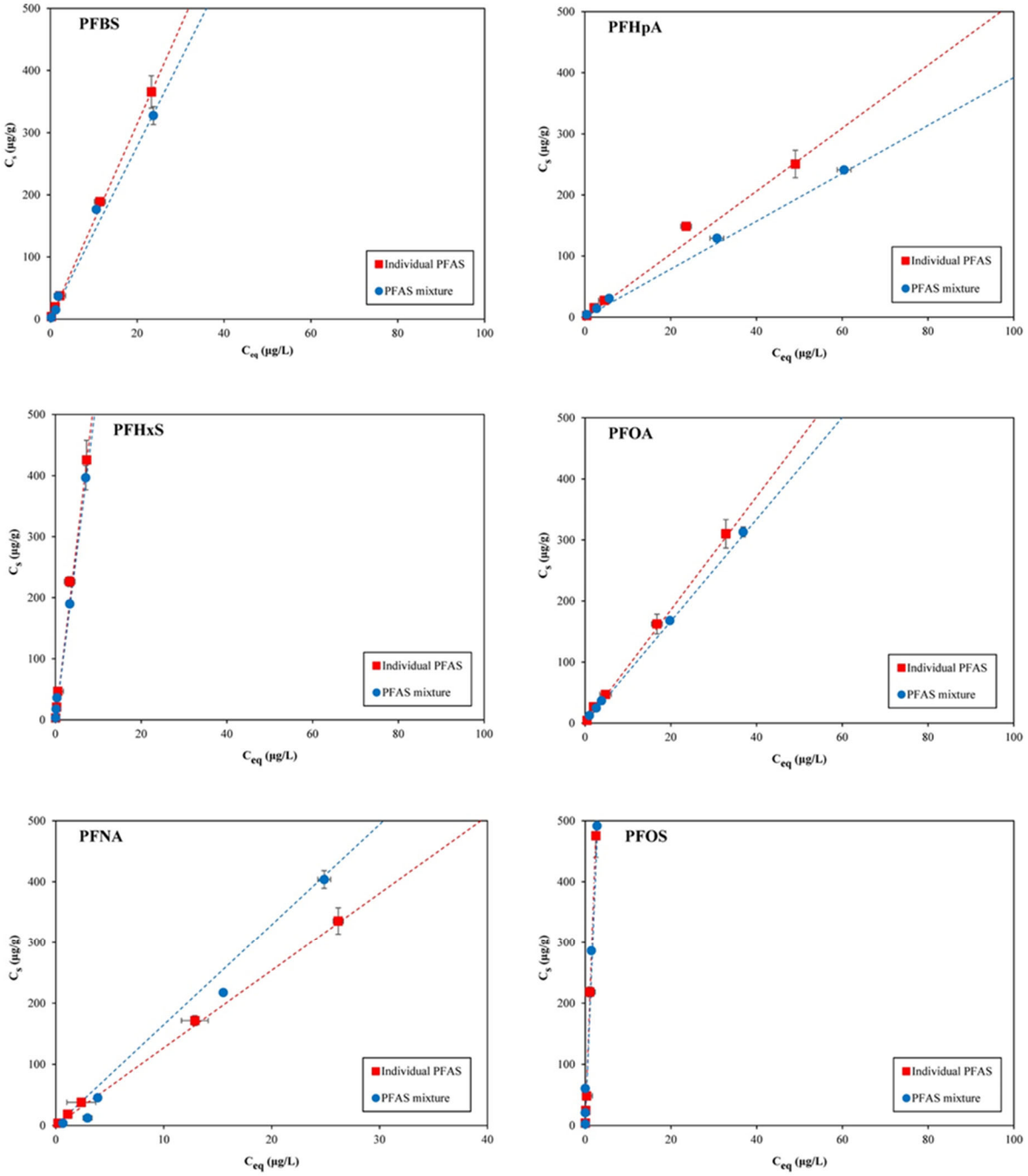


Figure 4.70 Sorption of mixtures of PFOS, PFOA, PFNA, PFHxS, PFHpA, and PFBS on Amberlite® IRA910 over a concentration range of 1 to 100 µg/L in single solute or multiple solute batch experiments.

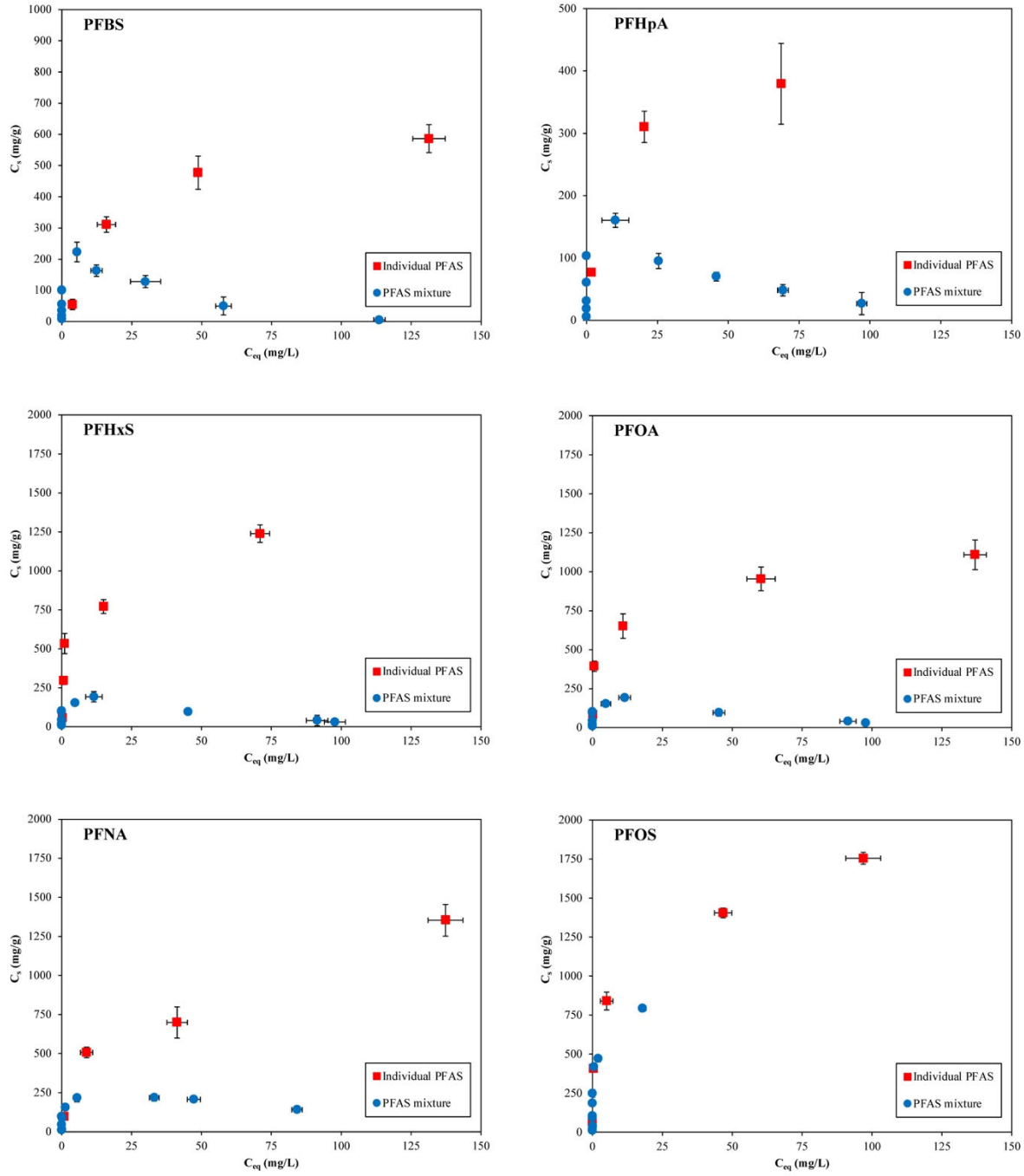


Figure 4.71 Sorption of mixtures of PFOS, PFOA, PFNA, PFHxS, PFHpA, and PFBS on Amberlite® IRA910 over a concentration range of 1 to 100 mg/L in single solute or multiple solute batch experiments.

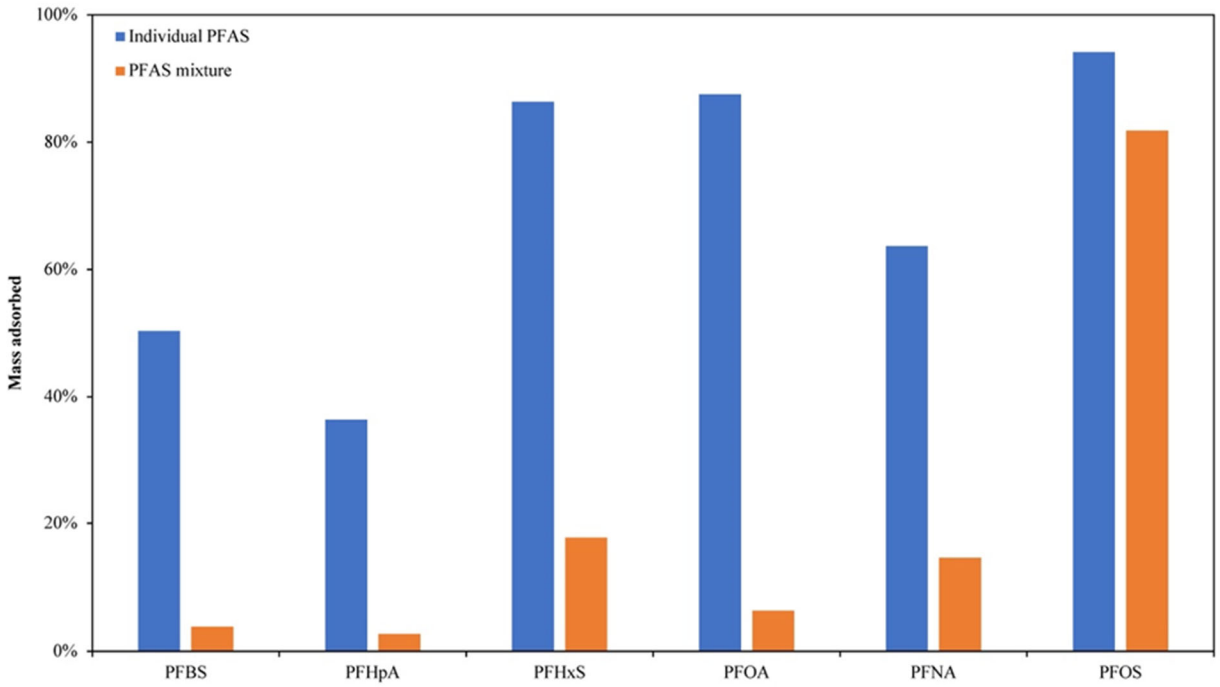


Figure 4.72 Comparison of PFBS, PFHpA, PFHxS, PFOA, PFNA and PFOS adsorption on 10 mg Amberlite® IRA910 in single and multi-solute batch experiments at an initial concentration of 100 mg/L each.

4.7.3 Delivery and Retention of S-IXR

Based on the DLS analysis, the S-IXR suspension contained resin particles with a mean hydrodynamic diameter of 219 nm and zeta potential of +96.7 mV (**Figure 4.73**). The viscosity of the S-IXR suspension was 1.02 cP at 20 °C, which makes it relatively easy to inject. Preliminary column experiments conducted with a 3.5 PV injection of S-IXR to assess the delivery and retention capacity of S-IXR yielded a uniform distribution of retained IXR (**Figure 4.74**) with organic carbon contents ranging from 0.479 to 0.678 mg/g along the length of the column. Sand grains imaged using SEM-EDS showed that surfaces of S-IXR treated sand were covered with resin particle clusters ranging from 0.1 to 10 µm in diameter, whereas the surfaces of untreated sand were smooth and clean (**Figure 4.75**). Evaluation of EDS spectra indicated that the amount of carbon on the treated sand was substantially higher than untreated sand (**Figure 4.76**), with elemental carbon accounting for 32.7% by weight and 54.9% by atom, compared to values of 5.59% by weight and 10.1% by atom for untreated sand. Thus, the EDS data provide confirmation that particle clusters observed in SEM images of S-IXR treated sand were in fact retained resin particles.

		Size (d.nm):	% Intensity:	St Dev (d.n...
Z-Average (d.nm): 219.4	Peak 1:	227.2	90.1	109.9
PdI: 0.374	Peak 2:	4682	9.9	789.0
Intercept: 0.936	Peak 3:	0.000	0.0	0.000
Result quality : Good				

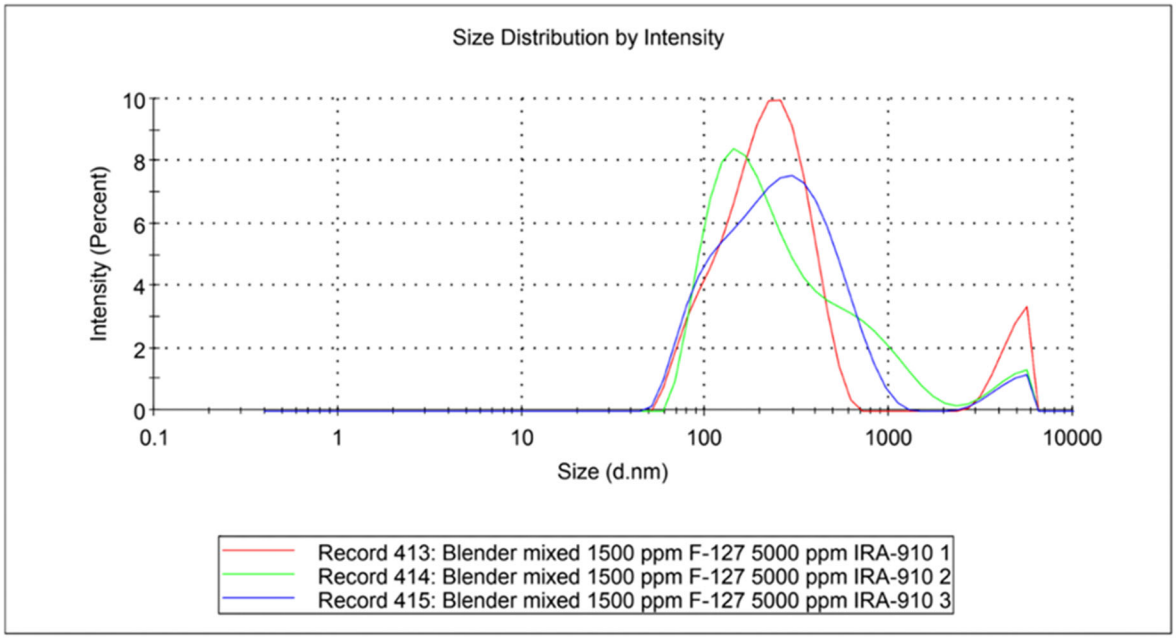


Figure 4.73 Particle size distribution of S-IXR obtained by dynamic light scattering using a Zetasizer Nano ZS Analyzer operated in back-scattering mode at an angle of 173°.

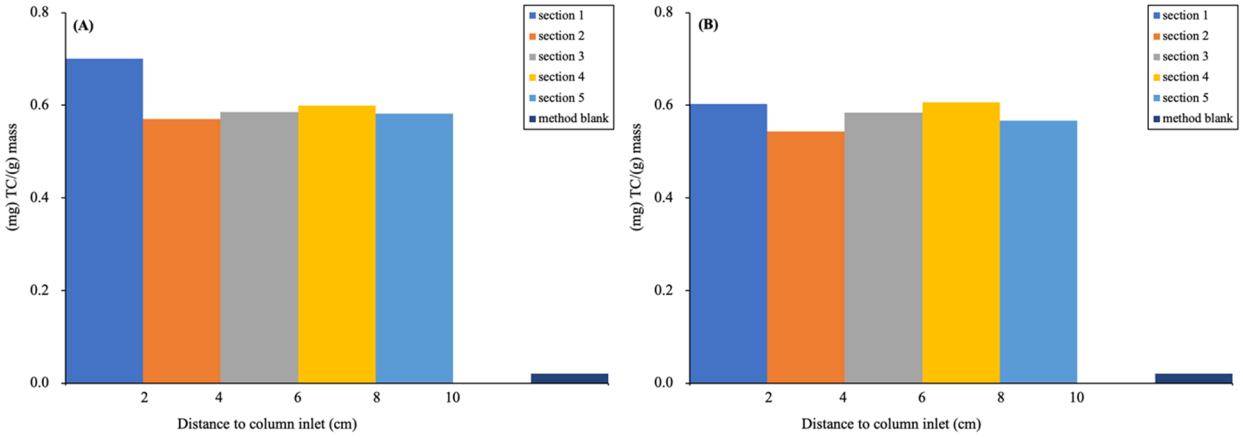


Figure 4.74 Distribution of retained carbon after the injection of 3.5 pore volumes of S-IXR into a column packed with water-saturated 40-50 mesh Ottawa sand followed by 3.5 pore volumes of background electrolyte solution (10 mM NaCl) at a flow rate of 0.12 mL/min prior to (A) PFOA injection and (B) PFOS injection, where 67.1 mg of IRA910 was retained in (A) and 61.3 mg of IRA910 was retained in (B).

4.7.4 Sequestration of PFOA or PFOS by S-IXR Treated Sand

Following injection of a solution containing 100 µg/L of PFOA in 10 mM NaCl, no breakthrough of PFOA was measured after approximately 7 PVs (**Figure 4.77 a**). Since the residence time in the column was approximately 2.8 h, these data indicate rapid uptake of PFOA. The influent PFOA concentration was then increased from 100 µg/L to 100 mg/L to assess the adsorptive capacity of S-IXR treated sand. PFOA breakthrough occurred at approximately 60.7 PV (or 54.0 PVs after the increase to 100 mg/L PFOA), which corresponds to the retention of 112.4 mg of PFOA (**Figure 4.77 a**) calculated from the mass of PFOA introduced into the column prior to breakthrough. Based on the amount of IXR coating the sand (67.1 mg IRA 910, **Figure 4.74**), the PFOA retention capacity was approximately 1,675 mg PFOA/g IRA 910 (4.06 mmol/g), which is consistent the single solute batch adsorption data. Similar results were observed for PFOS, where no breakthrough of PFOS was detected after introducing approximately 7 PV of 100 µg/L PFOS (**Figure 4.77 b**). After the influent PFOS concentration was increased to 100 mg/L, PFOS breakthrough occurred at approximately 52.9 PVs (46.1 PVs after the increase to 100 mg/L PFOS). By the end of the injection period (75.9 PV), 120 mg of PFOS were retained by the S-IXR treated sand, which correspond to adsorption capacity of approximately 1,961 mg PFOS/g IRA 910 (3.93 mmol/g), consistent the single solute batch adsorption data (**Figure 4.68)**. In untreated 40-50 mesh Ottawa sand columns, breakthrough of PFOA and PFOS was observed after only 1.2 PV and 2.5 PV, respectively, at an influent concentration at 100 µg/L (**Figure 4.78**). Thus, the S-IXR treatment increased the PFOA and PFOS retention by more than 5 orders-of-magnitude relative to untreated control columns. If the influent concentration had been maintained at 100 µg/L PFOA or PFOS, the S-IXR treated columns would be effective for more than 5,900 and 9,240 PVs, respectively, based on the batch adsorption data (**Figure 4.68**, **Table 4.8**) and the retained mass of resin.

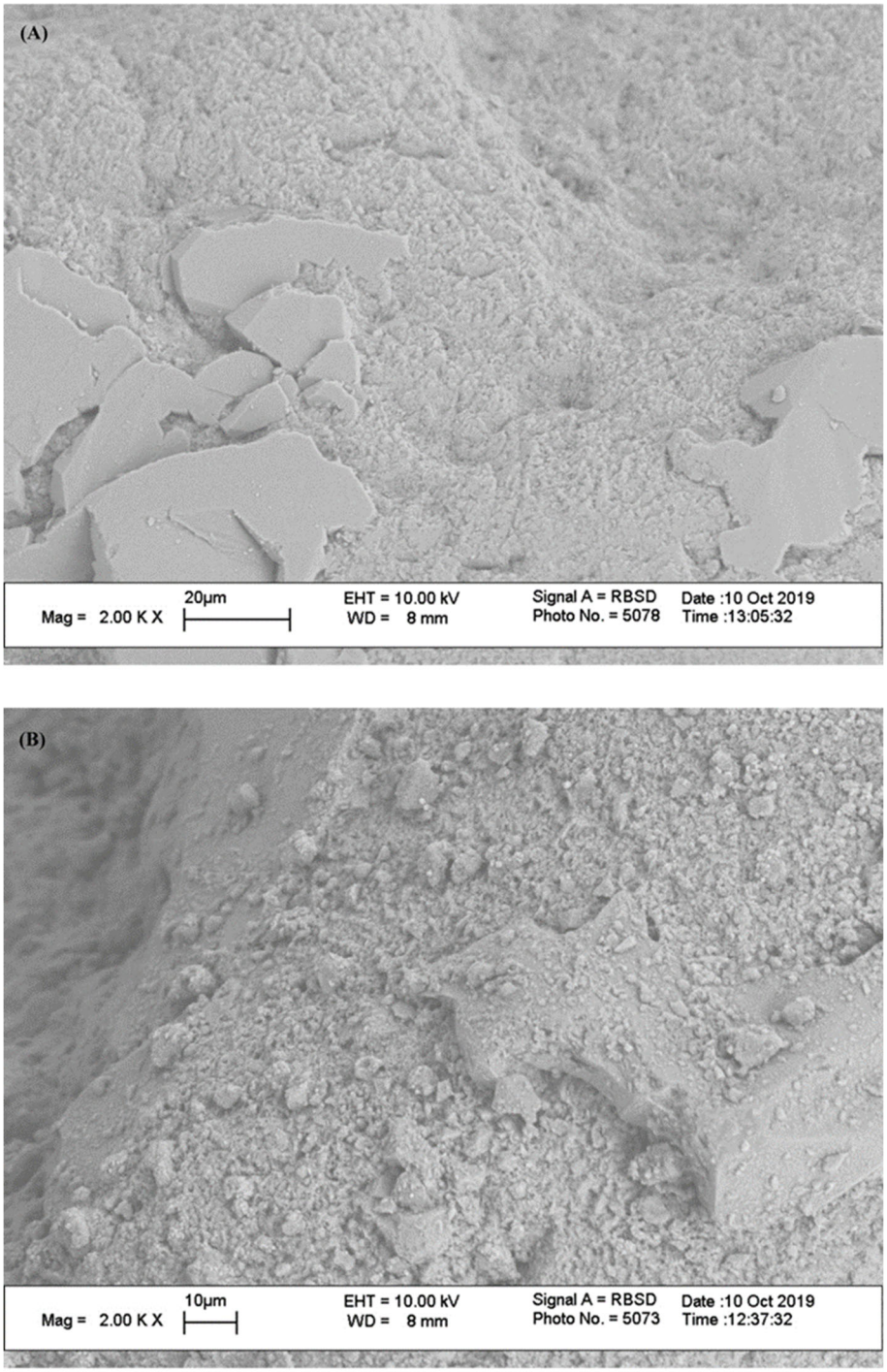
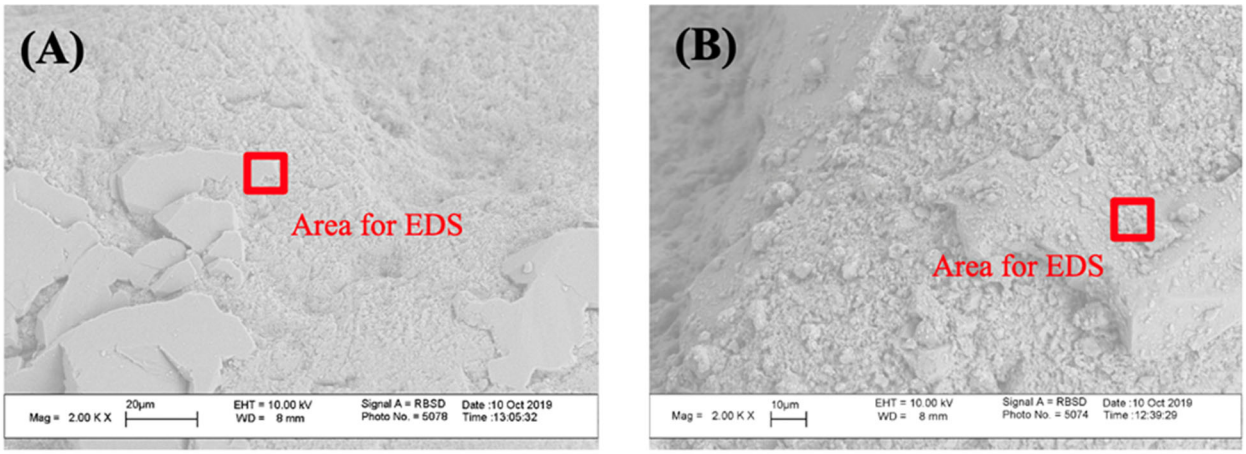
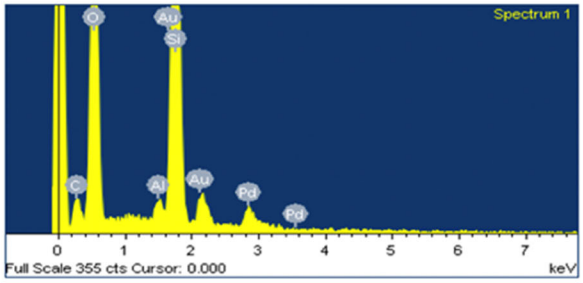
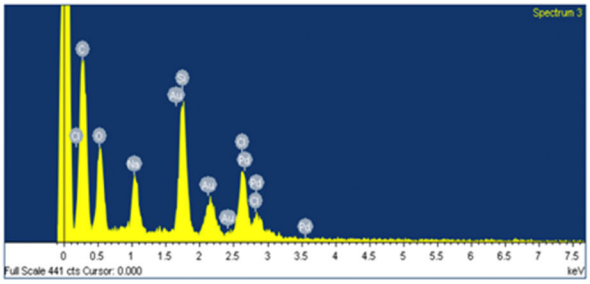


Figure 4.75 Images of 40-50 mesh Ottawa sand (a) before and (b) after treatment with S-IXR obtained using a Zeiss Leo 1530 VP Scanning Electron Microscope (SEM).





Element	Weight%	Atomic%
C K	5.59	10.09
O K	46.14	62.51
Al K	1.02	0.82
Si K	31.33	24.17
Pd L	7.05	1.44
Au M	8.86	0.98
Totals	100.00	



Element	Weight%	Atomic%
C K	32.65	54.85
O K	18.22	22.99
Na K	4.62	4.05
Si K	12.13	8.72
Cl K	11.43	6.51
Pd L	8.48	1.61
Au M	12.48	1.28
Totals	100.00	

Figure 4.76 Images of 40-50 mesh Ottawa sand (A) before and (B) after treatment with S-IXR obtained using a Zeiss Leo 1530 VP Scanning Electron Microscope (SEM) coupled with an Oxford Instruments 7426 Energy Dispersive Spectrometer (EDS).

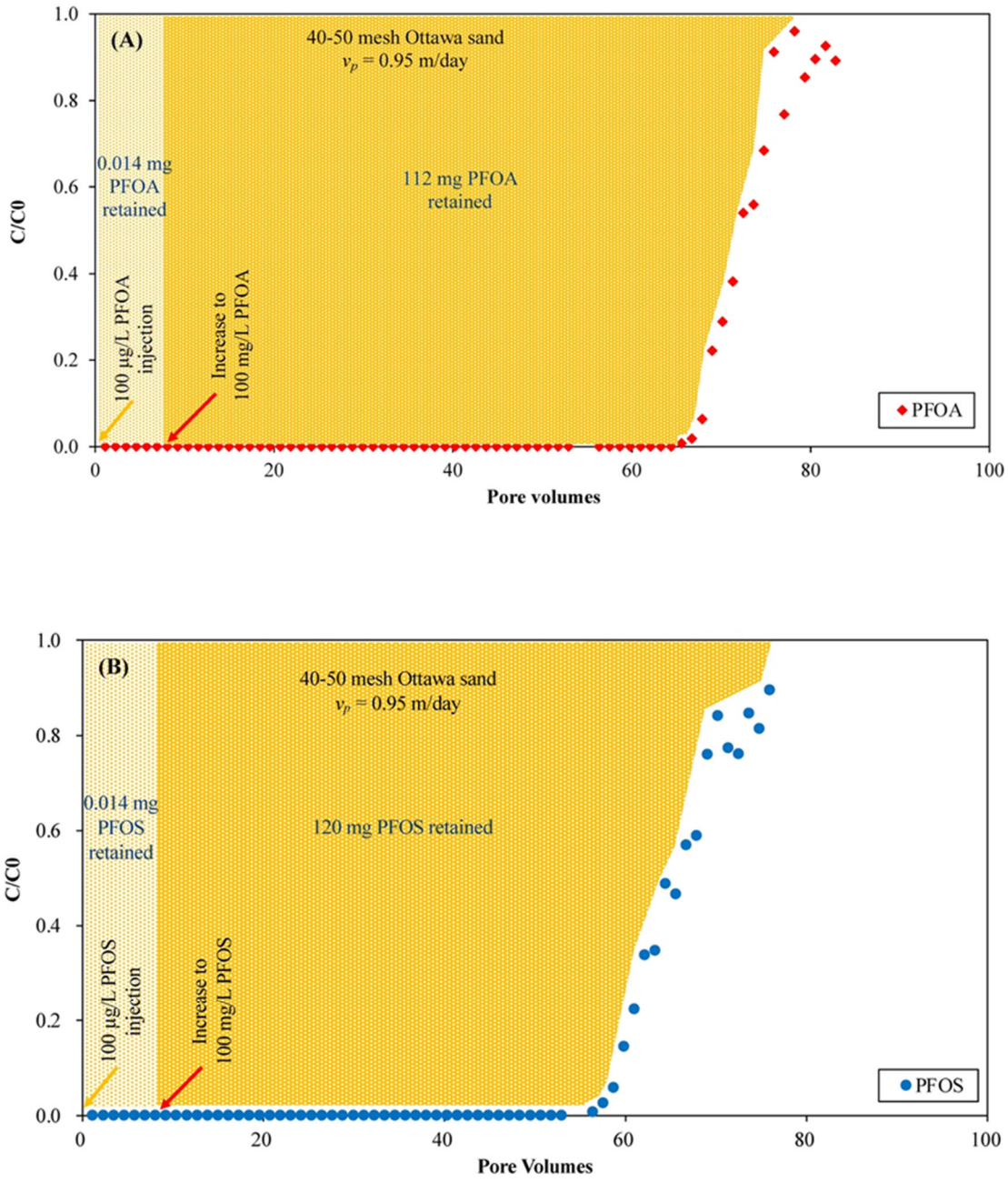


Figure 4.77 Effluent breakthrough curves for (a) PFOA and (b) PFOS in a water-saturated column containing S-IXR treated 40-50 mesh Ottawa sand. Shaded areas show the amount of retained PFOS or PFOA for injected concentrations of 100 µg/L and 100 mg/L.

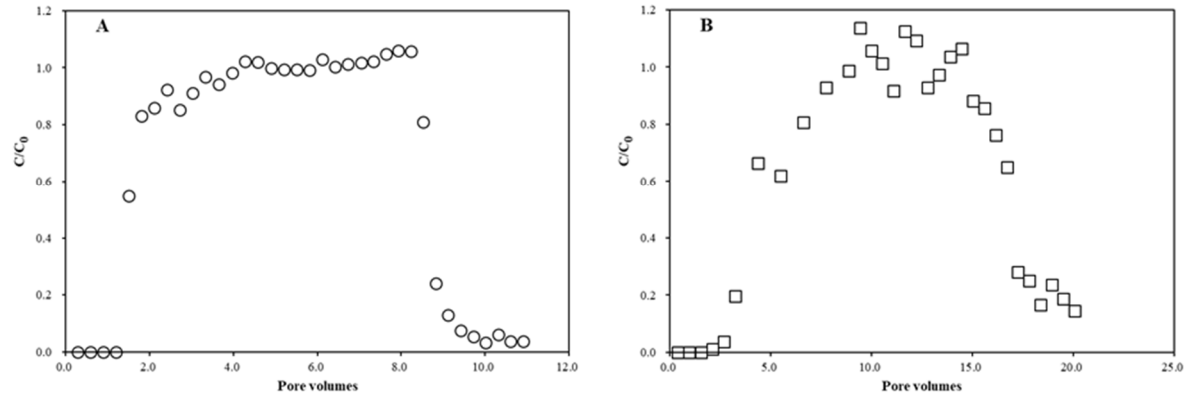


Figure 4.78 Effluent breakthrough curves obtained for pulse injections of aqueous solutions containing either (a) PFOA (100 µg/L) or (b) PFOS (100 µg/L) in water-saturated columns containing untreated 40-50 mesh Ottawa sand. The flow rate was 0.12 mL/min (pore-water velocity of 0.88 m/day), yielding a residence time of approximately 2.77 h. The pore volume of each column was approximately 20 mL.

4.7.5 Sequestration of a PFAS Mixture by S-IXR Treated Sand

For the multi-solute column experiment, a 60 µg/L mixture of PFOS, PFOA, PFNA, PFHxS, PFHpA, and PFBS (10 µg/L each) in 10 mM NaCl was introduced into a S-IXR treated column at a pore-water velocity of 0.96 m/day. After 14 PVs, no PFAS were detected in the column effluent; therefore, the total PFAS influent concentration was increased to 60 mg/L (10 mg/L each). PFHpA was the first PFAS detected in the column effluent (29.13 PV) and the relative concentration increased rapidly to applied concentration ($C/C_0 = 1$) after 32.5 PV. Breakthrough of PFHpA was followed by PFBS (32.47 PV), PFOA (35.85 PV), PFHxS (41.49 PV) and PFNA (44.05 PV). Similar to PFHpA, the effluent concentrations of these PFAS increased rapidly to the applied concentration following breakthrough. PFOS was the last species to appear in the column effluent (55.50 PV), and the relative concentration increased gradually to 0.21 after 79.42 PV, at which point the experiment was terminated (**Figure 4.79**). The order of breakthrough observed for the six PFAS was consistent with multi-solute batch adsorption data (**Figure 4.68 b**), which showed an adsorption preference of PFOS > PFNA > PFHxS > PFOA > PFBS > PFHpA at aqueous phase concentrations of 10 mg/L each. At the conclusion of the mixed-solute column study (65.38 PV), the following amounts of PFAS were retained by the S-IXR treated sand: PFHpA (3.84 mg); PFBS (4.63 mg); PFOA (5.80 mg); PFHxS (6.92 mg); PFNA (8.48 mg); PFOS (14.07 mg). The retained amounts of PFAS compared to the total amounts injected were: PFHpA (30.51%); PFBS (34.13%); PFOA (41.77%); PFHxS (50.47%); PFNA (56.82%); PFOS (96.44%). Although PFOS exhibited the greater adsorption than other 5 PFAS, a considerable amount of the shorter C-F chain length PFAS were still retained despite competitive adsorption effects at the higher applied concentration. If the influent concentration had been maintained at 60 µg/L (10 µg/L for each), the S-IXR treated columns would be effective for more than 14,200 PVs for PFHpA, 10,600 PVs for PFBS, 29,700 PVs for PFOA, 32,600 PVs for PFHxS, 22,800 PVs for PFNA and 51,100 PVs for PFOS, under these experimental conditions. When compared to the control column containing untreated sand (**Figure 4.80**), the amounts of PFAS retained in the S-IXR treated column were four to six orders-

of-magnitude greater: PFHpA (8,872 times); PFBS (116,321 times); PFOA (10,282 times); PFHxS (13,6103 times); PFNA (9,138 times); PFOS (29,796 times). Prior research suggests a correlation between hydrophobicity and the extent of PFAS retention by ion exchange resins[171, 206]. However, based on the K_{ow} values of the six PFAS (**Table 3.6)** this trend was not consistent with column effluent data. For example, PFOA has a greater K_{ow} value than PFHxS but exhibited less adsorption in both batch and column studies. These data suggest that both hydrophobic interactions and ion exchange reactions contributed to PFAS adsorption by the resin.

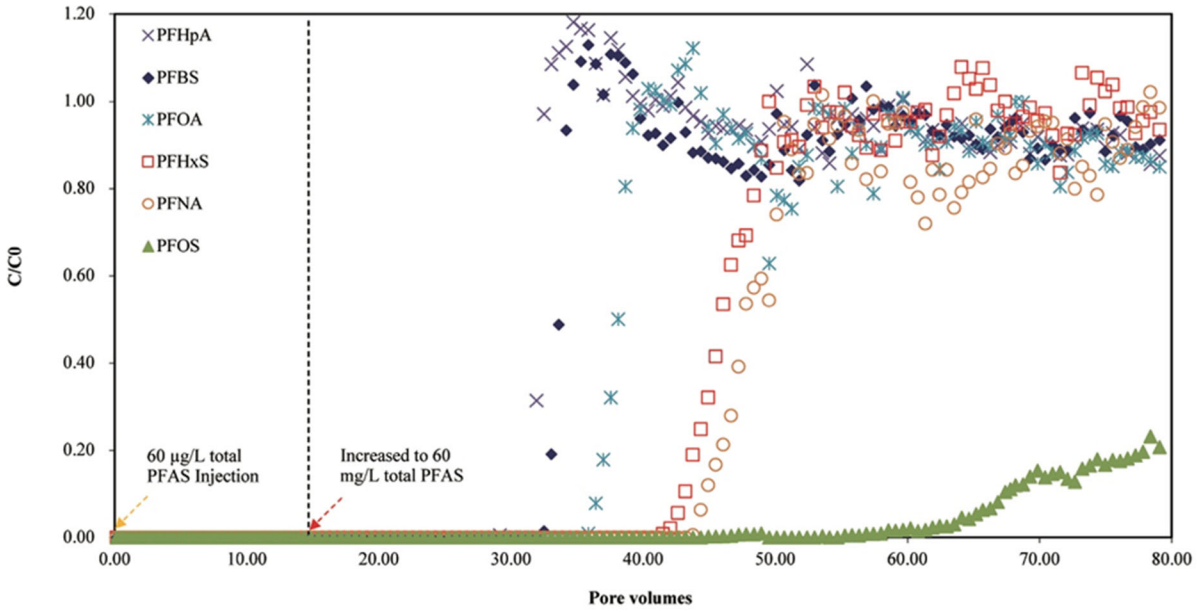


Figure 4.79 Effluent breakthrough curves obtained for a mixture of PFBS, PFHpA, PFHxS, PFOA, PFOS, and PFNA (60 ug/L and 60 mg/L) applied to a water-saturated column containing S-IXR treated 40-50 mesh Ottawa sand.

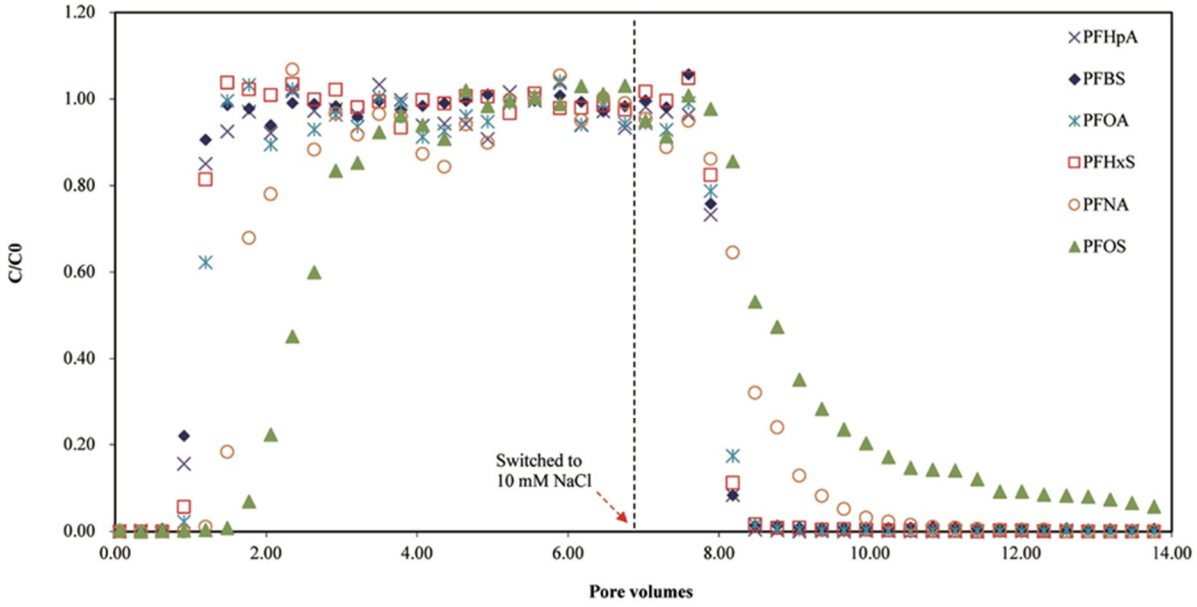


Figure 4.80 Effluent breakthrough curves obtained for pulse injections of aqueous solutions containing a 600 µg/L mixture of PFHpA, PFBS, PFOA, PFHxS, PFNA and PFOS (100 µg/L each) in a water-saturated column containing untreated 40-50 mesh Ottawa sand. The flow rate was 0.12 mL/min (pore-water velocity of 1.03 m/day), yielding a residence time of approximately 2.57 h. The pore volume of the column was 18.52 mL.

5. Conclusions and Implications

5.1 Development of sorptive and reactivce materials

We demonstrate ultra-high sorption performance for PFOA and PFOS using amine-based, organic functionalized superparamagnetic iron oxide nanocrystals (IONCs) via both batch sorption and novel QCM-D studies. We achieved higher sorption performance using higher PEI MW compared to other organic coatings (CTAB and OA), indicating the grafting density and polymer structure of surface coating are key factors for enhanced PFAS sorption behavior. We developed a novel QCM-D based method to achieve real time sorption analysis, quantifying not only PFAS sorption affinity/behavior, but also competitive sorption effects between different PFAS molecules. These data describe the critical role of the PFAS head group as it relates to (sorbed) molecular orientation. We observed dynamic sorption processes as a function of water chemistry, including solution pH, ionic strength/type, and NOM in water. Data obtained from column studies further demonstrates the high potential of IONC-based platform materials to provide effective in situ sequestration of PFOA and PFOS under dynamic flow conditions.

Further, we investigated the function and efficacy of CNTs under electric current within the CNTs-NF cathode system to facilitate the oxidation of PFOS. The remarkable conductivity coupled with the extensive surface area of CNTs makes them as ideal catalysts for PFOS removal. The process is facilitated by the electrochemical activation of persulfate that anodically generated PDS. Electrically stimulated CNTs have the potential to enhance the mass transfer of PFOS onto the CNTs surface, particularly in the presence of persulfate (PDS), thereby enhancing the electro-adsorptive capacity for PFOS. Conversely, as pH levels rise, the surfaces of the CNTs gain additional negative charges, leading to increased electrostatic repulsion that diminishes the overall effectiveness of PFOS removal. The major oxidation pathway of PFOS by the BDD anode is commonly known as electron transfer on its surface during electrochemical oxidation. On the other hand, the CNTs-NF cathode system displays a different pathway, effectively generating surface-bound sulfate radicals via electrolysis with PDS. This facilitates the decomposition of PFOS substances adsorbed on the CNTs-NF surface. The sulfate radical adducts (DMPO-SO4) in CNTs-NF cathode system were investigated using EPR spectra, and further studied by hydrophobic quenching experiments for elucidating the PFOS oxidation pathway. It is noted that the hydrophobic substances have a stronger impact on sulfate radical scavenging compared to hydrophilic substances, owing to their higher affinity for CNTs. Significantly, the analysis of intermediates using anodic oxidation with a BDD electrode and electrically activated CNTs-NF in the presence of PDS reveals distinct different profiles of oxidation products. Consistently across repeated processing cycles, a series of PFOS oxidation reactions was systematically initiated, accompanied by quantifiable analysis (?) of defluorination, all of which were enabled by the electrochemical activation of persulfate. Observations over 10 repeated cycles test revealed that the electro-treatment efficiency maintained a relatively steady rate, unaffected by continuous performance, or sustained electric current. By employing carbon-based activators to alter the surface of cathode materials, we establish electrochemical pathways conducive to persulfate activation that not only enable the generation of surface-bound radicals through heterolytic dissociation of PDS but also enhance adsorption capabilities. As a result, this methodology significantly promotes the removal of PFOS during the electrolysis process under effective cathodic stability, suggesting a new potential application for the efficient removal of PFOS.

5.2 Impacts of PFAS on organohalide respiration

Total PFAA concentrations of 11.7 mg/L and higher partially inhibited MRD of *cis*-DCE to VC and ethene by *Dhc* strains harboring the *vcrA* and *bvcA* genes in batch reactors. In the presence of a solid phase, however, rates of MRD of PCE and TCE to ethene were not reduced in microcosms with total final PFAAs concentrations of 38.7 mg/L or lower (53.5 mg/L initial). This protection was attributed to a combination of PFAA sorption to the solid phase, decreasing the total aqueous concentration by approximately 30%, and microenvironments around solid particles that may protect microbial cells from the high concentrations in the bulk liquid, as has been observed in low pH conditions [255]. Environmentally relevant PFAA concentrations, even in AFFF source areas, are expected to be lower than the concentrations used in these experiments (0.124-7.09 mg/L [270]) and, therefore, will not inhibit MRD.

Although a previous study did not observe inhibition of MRD of TCE to ethene by *Dhc* strain 195 in experiments performed with 22 mg/L PFAAs, the discrepancy is likely caused by PFAA mixture composition [103]. Previous 22 mg/L PFAA experiments contained equal concentrations of each PFAA (i.e., 2 mg/L PFOS) [103], while in this study concentrations of each PFAA were unequal (i.e., 20.0%, 5.7 mg/L PFOS). These results suggest that individual PFAAs at specific concentration thresholds may inhibit MRD even if the total PFAA concentration is less than that that previously shown to cause inhibition. For example, perfluorosulfonic acids (e.g. PFOS) were shown to exhibit greater toxicity to soil microorganisms than perfluorocarboxylic acids with the same number of carbons (e.g. PFOA) and longer-chain PFAAs (e.g., PFOS, PFOA) were shown to be more toxic than their shorter-chain analogues (e.g., PFBS and PFBA), attributed to the longer hydrophobic chain resulting in higher bioaccumulation and stronger interactions with proteins [271]. Preliminary batch reactor experiments performed with PFOS alone (not shown) revealed a lag in the time to transform all chlorinated ethenes (PCE, TCE, *cis*-DCE, and VC) at PFOS concentrations of 2 mg/L and higher. There was no correlation with increasing PFOS concentration, however, and additional investigation is necessary to determine the impact of single PFAAs on MRD.

PFAAs did not impede total *Dhc* growth in batch reactor or microcosm experiments, but the composition of the population was altered with *bvcA* gene-harboring *Dhc* strains comprising a larger proportion of the ethene-producing *Dhc* population in experiments with high PFAA concentrations (101 mg/L in batch reactors and 38.7 mg/L and 91.3 mg/L in microcosms). Similar resilience of *bvcA* gene-harboring *Dhc* strains has been observed in populations exposed to elevated temperatures (35°C) [213], suggesting these strains are more resilient to conditions typically considered non-ideal for *Dhc* growth and activity.

This study documents the complete dechlorination of PCE to ethene by a microbial consortium containing multiple strains of *Dhc* even with PFAA concentrations as high as 91.3 mg/L (120 mg/L before sorption) when the selected solid phase is present. This suggests that MRD is a suitable treatment for chlorinated ethenes in groundwater, even if PFAAs are present, as there will be a solid phase that could protect microorganisms from high aqueous concentrations, and because PFAA concentrations are expected to be lower than those used in these experiments [270]. The shift in the *Dhc* strains capable of metabolically transforming *cis*-DCE to ethene, from *vcrA*-harboring cells to *bvcA*-harboring cells at high PFAA concentrations, demonstrates the advantage of maintaining a diverse *Dhc* population containing multiple strains.

5.3 Injectable particulate amendments for permeable adsorptive barriers

The results obtained from batch and column studies clearly demonstrate that polymer-stabilized powdered activated carbon (S-PAC) and ion exchange resin (S-IXR) can be introduced into a quartz sand to create a permeable adsorption zone or barrier that is capable of effectively removing both individual PFAS and PFAS mixtures. At environmentally relevant applied concentrations (< 100 ug/L total) that are typical of most groundwater contamination scenarios, competitive adsorption of PFAS was not observed. However, at higher concentrations (60 mg/L total) preferential adsorption of longer-chain length PFAS, especially PFOS, was evident in both batch reactor and column studies. For field applications of this technology, it will be important to perform treatability tests using site specific aquifer materials and groundwater to address potential impacts of natural organic matter (NOM) and inorganic ions on the adsorption performance of the emplaced resins [272]. In addition, further studies are needed to assess the long-term viability of S-IXR treated aquifer materials to retain PFAS over a range of environmental conditions, and to understand the long-term fate of the adsorbed PFAS when competitive adsorption effects are relevant.

There are several important limitations of this work, however, that require further study, including assessments of long-term performance of the injectable particulate amendments, effects of co-contaminants (e.g., PFAS mixtures, natural organic matter) on the adsorption capacity and desorption/release of PFAS from carbons and resins, effects of solution conditions including pH and ionic species, and delivery and retention of S-PAC and S-IXR in lower permeability and heterogeneous porous media.

5.4 Coupled treatment systems for groundwater containing chlorinated ethenes and PFAS

Overall, the coupled bioactive and sorptive column system showed the advantage of complete detoxification of PCE and TCE to ethene and greater performance in adsorption of PFAAs within the same timeframe, making it a promising option for treating co-occurring PFAAs and chlorinated ethenes.

The results of this study are consistent with previous work [35, 118] and unpublished multi-solute column data from the Pennell Lab at Brown University using various adsorptive materials that suggest PFSA exhibits higher adsorption than PFCA of the same C-F chain length for both IONP and S-PAC. Additionally, longer chain PFAAs were found to have greater adsorption than shorter chain PFAAs. These findings suggest that both electrostatic interactions and hydrophobicity play a role in PFAA adsorption by IONP and S-PAC. Notably, this study observed competitive adsorption between chlorinated ethenes and PFAAs, highlighting the importance of site-specific information in evaluating the adsorption capacity for mixed PFAS and chlorinated ethenes groundwater plumes.

The study advanced our understanding of the synergistic benefits associated with sequential treatment of complex groundwater contamination scenarios involving mixtures of PFAS and chlorinated ethenes, which will be useful to site managers, regulators, and environmental engineers dealing with recalcitrant compounds co-mingled with chlorinated ethenes. Nonetheless, further research is needed to address the limitations of this study, such as the long-term fate and transport of nanoparticles, effects of natural organic matter and other co-contaminants, the impacts of

solution conditions like pH and ionic species on adsorption capacity, and the long-term impacts on the local biogeochemical conditions.

6. Literature Cited

1. Usepa, *Interim Drinking Water Health Advisory: Perfluorooctanoic Acid (PFOA) CASRN 335-67-1.* United States Environmental Protection (EPA), Office of Water, 0000: p. EPA/822/R-22/003.
2. Usepa, *Proposed PFAS National Primary Drinking Water Regulation.* United States Environmental Protection (EPA), 2023: p. EPA-HQ-OW-2022-0114.
3. MassDep, *Massachusetts Drinking Water Standard and Health Information*. 2020.
4. Nhdes, *Update on New Hampshire PFAS Drinking Water Standards (MCLs)*. 2020.
5. Njdep, *PFAS Standards, Criteria, and Guidance*. 2020.
6. Guelfo, J.L. and D.T. Adamson, *Evaluation of a national data set for insights into sources, composition, and concentrations of per- and polyfluoroalkyl substances (PFASs) in U.S. drinking water.* Environmental Pollution, 2018. **236**: p. 505-513.
7. Giesy, J.P. and K. Kannan, *Global Distribution of Perfluorooctane Sulfonate in Wildlife.* Environmental Science & Technology, 2001. **35**(7): p. 1339-1342.
8. Lanza, H.A., et al., *Temporal monitoring of perfluorooctane sulfonate accumulation in aquatic biota downstream of historical aqueous film forming foam use areas.* Environmental Toxicology and Chemistry, 2017. **36**(8): p. 2022-2029.
9. Moody, C.A. and J.A. Field, *Perfluorinated Surfactants and the Environmental Implications of Their Use in Fire-Fighting Foams.* Environmental Science & Technology, 2000. **34**(18): p. 3864-3870.
10. Navarro, I., et al., *Uptake of perfluoroalkyl substances and halogenated flame retardants by crop plants grown in biosolids-amended soils.* Environmental Research, 2017. **152**: p. 199-206.
11. Michigan, P.A.R.T., *PFAS Sites*. 2019.
12. DeWitt, J.C. and others, *Toxicological effects of perfluoroalkyl and polyfluoroalkyl substances*. 2015: Springer.
13. Anderko, L. and E. Pennea, *Exposures to per-and polyfluoroalkyl substances (PFAS): Potential risks to reproductive and children's health.* Current Problems in Pediatric and Adolescent Health Care, 2020. **50**(2): p. 100760-100760.
14. Atsdr, *Toxicological Profile for Perfluoroalkyls:Draft for public comment*. 2018.
15. Barry, V., A. Winquist, and K. Steenland, *Perfluorooctanoic Acid (PFOA) Exposures and Incident Cancers among Adults Living Near a Chemical Plant.* Environmental Health Perspectives, 2013. **121**(11-12): p. 1313-1318.
16. Pelch, K.E., et al., *PFAS health effects database: Protocol for a systematic evidence map*. 2019, Elsevier Ltd. p. 104851-104851.
17. Sunderland, E.M., et al., *A review of the pathways of human exposure to poly- and perfluoroalkyl substances (PFASs) and present understanding of health effects*. 2019, Nature Publishing Group. p. 131-147.
18. Vuong, A.M., et al., *Prenatal and childhood exposure to poly- and perfluoroalkyl substances (PFAS) and cognitive development in children at age 8 years.* Environmental Research, 2019. **172**: p. 242-248.
19. Death, C., et al., *Per- and polyfluoroalkyl substances (PFAS) in livestock and game species: a review.* Science of The Total Environment, 2021. **774**: p. 144795-144795.
20. Xiang, L., et al., *Food Safety Concerns: Crop Breeding as a Potential Strategy to Address Issues Associated with the Recently Lowered Reference Doses for Perfluorooctanoic Acid*

and Perfluorooctane Sulfonate. Journal of Agricultural and Food Chemistry, 2020. **68**(1): p. 48-58.
21. Usepa, *EPA's PFAS Action Plan*. 2019.
22. Newell, C.J., et al., *Comparing PFAS to other groundwater contaminants: Implications for remediation.* Remediation Journal, 2020. **30**(3): p. 7-26.
23. Stroo, H.F., et al., *Chlorinated ethene source remediation: lessons learned.* Environ Sci Technol, 2012. **46**(12): p. 6438-47.
24. Parsons, J.R., et al., *Biodegradation of perfluorinated compounds*, in *Reviews of Environmental Contamination and Toxicology Vol 196*. 2008, Springer. p. 53-71.
25. Vecitis, C.D., et al., *Treatment technologies for aqueous perfluorooctanesulfonate (PFOS) and perfluorooctanoate (PFOA).* Frontiers of Environmental Science & Engineering in China, 2009. **3**(2): p. 129-151.
26. Liu, C., et al., *Effect of temperature on oxidative transformation of perfluorooctanoic acid (PFOA) by persulfate activation in water.* Separation and Purification Technology, 2012. **91**: p. 46-51.
27. Mitchell, S.M., et al., *Degradation of perfluorooctanoic acid by reactive species generated through catalyzed H2O2 propagation reactions.* Environmental Science & Technology Letters, 2013. **1**(1): p. 117-121.
28. Kothawala, D.N., et al., *Influence of dissolved organic matter concentration and composition on the removal efficiency of perfluoroalkyl substances (PFASs) during drinking water treatment.* Water Research, 2017. **121**: p. 320-328.
29. McCleaf, P., et al., *Removal efficiency of multiple poly- and perfluoroalkyl substances (PFASs) in drinking water using granular activated carbon (GAC) and anion exchange (AE) column tests.* Water Research, 2017. **120**: p. 77-87.
30. Xiao, X., et al., *Sorption of Poly- and Perfluoroalkyl Substances (PFASs) Relevant to Aqueous Film-Forming Foam (AFFF)-Impacted Groundwater by Biochars and Activated Carbon.* Environmental Science & Technology, 2017. **51**(11): p. 6342-6351.
31. Gagliano, E., et al., *Removal of poly- and perfluoroalkyl substances (PFAS) from water by adsorption: Role of PFAS chain length, effect of organic matter and challenges in adsorbent regeneration*. 2020, Elsevier Ltd. p. 115381-115381.
32. Weathers, T.S., et al., *Perfluoroalkyl acids inhibit reductive dechlorination of trichloroethene by repressing Dehalococcoides.* Environmental Science & Technology, 2016. **50**(1): p. 240-248.
33. Duhamel, M., K. Mo, and E.a. Edwards, *Characterization of a Highly Enriched Dehalococcoides -Containing Culture That Grows on Vinyl Chloride and.* Applied Environmental Microbiology, 2004. **70**(9): p. 5538-5545.
34. Duhamel, M., et al., *Comparison of anaerobic dechlorinating enrichment cultures maintained on tetrachloroethene, trichloroethene, cis-dichloroethene and vinyl chloride.* Water Research, 2002. **36**(17): p. 4193-4202.
35. Liu, C., et al., *In Situ Sequestration of Perfluoroalkyl Substances Using Polymer-Stabilized Powdered Activated Carbon.* Environmental Science & Technology, 2020. **54**(11): p. 6929-6936.
36. Lee, J., et al., *Ultra-high capacity, multifunctional nanoscale sorbents for PFOA and PFOS treatment.* npj Clean Water, 2023. **6**(1): p. 62.

37. Hnatko, J.P., et al., *Microbial Reductive Dechlorination by a Commercially Available Dechlorinating Consortium Is Not Inhibited by Perfluoroalkyl Acids (PFAAs) at Field-Relevant Concentrations.* Environmental Science & Technology, 2023.
38. Harding-Marjanovic, K.C., et al., *Effects of Aqueous Film-Forming Foams (AFFFs) on Trichloroethene (TCE) Dechlorination by a Dehalococcoides mccartyi-Containing Microbial Community.* Environmental Science and Technology, 2016. **50**(7): p. 3352-3361.
39. Kissa, E., *Fluorinated surfactants: synthesis, properties, applications*. Surfactant science series. 1994, New York: M. Dekker %@ 978-0-8247-9011-0 %U http://www.gbv.de/dms/bowker/toc/9780824790110.pdf.
40. Usepa, *EPA's Per- and Polyfluoroalkyl Substances (PFAS) Action Plan.* 2019.
41. Oecd, *Toward a new comprehensive global database of per-and polyfluoroalkyl substances (PFASs): Summary report on updating the OECD 2007 list of per-and polyfluoroalkyl substances (PFASs)*. 2018, OECD Environment Directorate, Environment, Health and Safety Division Paris ….
42. Darwin, R., *Estimated quantities of aqueous film forming foam (AFFF) in the United States.* Baltimore, MD: Aug, 2004. **2004**.
43. D'Agostino, L.A. and S.A. Mabury, *Identification of Novel Fluorinated Surfactants in Aqueous Film Forming Foams and Commercial Surfactant Concentrates.* Environmental Science and Technology, 2013. **48**(1): p. 121-129.
44. Barzen-Hanson, K.A., et al., *Sorption of Fluorotelomer Sulfonates, Fluorotelomer Sulfonamido Betaines, and a Fluorotelomer Sulfonamido Amine in National Foam Aqueous Film-Forming Foam to Soil.* Environmental Science & Technology, 2017. **51**(21): p. 12394-12404.
45. Barzen-Hanson, K.A. and J.A. Field, *Discovery and Implications of C 2 and C 3 Perfluoroalkyl Sulfonates in Aqueous Film-Forming Foams and Groundwater.* Environmental Science & Technology Letters, 2015. **2**(4): p. 95-99.
46. Dauchy, X., et al., *Per- and polyfluoroalkyl substances in firefighting foam concentrates and water samples collected near sites impacted by the use of these foams.* Chemosphere, 2017. **183**: p. 53-61.
47. SERDP-ESTCP. *SERDP Core FY 2018 Solicitation: Improved Understanding of Per- and Polyfluoroalkyl Substance Source Zones*. 2018 5/22/23]; Available from: https://serdp-estcp.org/workingwithus/callforproposal?id=e9783b3b-0222-45ab-91cb-0d6c04ae152e.
48. Backe, W.J., T.C. Day, and J.A. Field, *Zwitterionic, cationic, and anionic fluorinated chemicals in aqueous film forming foam formulations and groundwater from US military bases by nonaqueous large-volume injection HPLC-MS/MS.* Environmental Science & Technology, 2013. **47**(10): p. 5226-5234.
49. McGuire, M.E., et al., *Evidence of Remediation-Induced Alteration of Subsurface Poly- and Perfluoroalkyl Substance Distribution at a Former Firefighter Training Area.* Environmental Science & Technology, 2014. **48**(12): p. 6644-6652.
50. Moody, C.A. and J.A. Field, *Determination of Perfluorocarboxylates in Groundwater Impacted by Fire-Fighting Activity.* Environmental Science & Technology, 1999. **33**(16): p. 2800-2806.
51. Hu, X.C., et al., *Detection of Poly- and Perfluoroalkyl Substances (PFASs) in U.S. Drinking Water Linked to Industrial Sites, Military Fire Training Areas, and Wastewater Treatment Plants.* Environmental Science & Technology Letters, 2016. **3**(10): p. 344-350.

52. Houtz, E.F., *Oxidative Measurement of Perfluoroalkyl Acid Precursors: Implications for urban runoff management and remediation of AFFF-contaminated groundwater and soil.* 2013.
53. Darrow, L.A., C.R. Stein, and K. Steenland, *Serum perfluorooctanoic acid and perfluorooctane sulfonate concentrations in relation to birth outcomes in the Mid-Ohio Valley, 2005–2010.* Environmental health perspectives, 2013. **121**(10): p. 1207-1213.
54. Lopez-Espinosa, M.-J., et al., *Thyroid function and perfluoroalkyl acids in children living near a chemical plant.* Environmental health perspectives, 2012. **120**(7): p. 1036-1041.
55. Steenland, K., et al., *Ulcerative colitis and perfluorooctanoic acid (PFOA) in a highly exposed population of community residents and workers in the mid-Ohio valley.* Environmental health perspectives, 2013. **121**(8): p. 900-905.
56. Anderson-Mahoney, P., et al., *Self-reported health effects among community residents exposed to perfluorooctanoate.* New Solutions: A journal of environmental and occupational health policy, 2008. **18**(2): p. 129-143.
57. Dong, G.-H., et al., *Serum polyfluoroalkyl concentrations, asthma outcomes, and immunological markers in a case–control study of Taiwanese children.* Environmental health perspectives, 2013. **121**(4): p. 507-513.
58. Erickson, H.P., *Size and shape of protein molecules at the nanometer level determined by sedimentation, gel filtration, and electron microscopy.* Biological Procedures Online, 2009. **11**(1): p. 32--51.
59. Fitz-Simon, N., et al., *Reductions in serum lipids with a 4-year decline in serum perfluorooctanoic acid and perfluorooctanesulfonic acid.* Epidemiology (Cambridge, Mass.), 2013. **24**(4): p. 569-569.
60. Humblet, O., et al., *Perfluoroalkyl chemicals and asthma among children 12–19 years of age: NHANES (1999–2008).* Environmental health perspectives, 2014. **122**(10): p. 1129-1133.
61. Min, J.-Y., et al., *Perfluorooctanoic acid exposure is associated with elevated homocysteine and hypertension in US adults.* Occupational and environmental medicine, 2012. **69**(9): p. 658-662.
62. Nelson, J.W., E.E. Hatch, and T.F. Webster, *Exposure to polyfluoroalkyl chemicals and cholesterol, body weight, and insulin resistance in the general US population.* Environmental health perspectives, 2010. **118**(2): p. 197-202.
63. Shankar, A., J. Xiao, and A. Ducatman, *Perfluorooctanoic acid and cardiovascular disease in US adults.* Archives of Internal Medicine, 2012. **172**(18): p. 1397-1403.
64. Rappazzo, K.M., E. Coffman, and E.P. Hines, *Exposure to perfluorinated alkyl substances and health outcomes in children: a systematic review of the epidemiologic literature.* International journal of environmental research and public health, 2017. **14**(7): p. 691-691.
65. Di Nisio, A., et al., *Perfluorooctanoic acid alters progesterone activity in human endometrial cells and induces reproductive alterations in young women.* Chemosphere, 2020. **242**: p. 125208-125208.
66. Fei, C., et al., *Maternal levels of perfluorinated chemicals and subfecundity.* Human reproduction, 2009. **24**(5): p. 1200-1205.
67. Johnson, P.I., et al., *The Navigation Guide—evidence-based medicine meets environmental health: systematic review of human evidence for PFOA effects on fetal growth.* Environmental health perspectives, 2014. **122**(10): p. 1028-1039.

68. Koustas, E., et al., *The Navigation Guide—evidence-based medicine meets environmental health: systematic review of nonhuman evidence for PFOA effects on fetal growth.* Environmental health perspectives, 2014. **122**(10): p. 1015-1027.
69. Savitz, D.A., et al., *Perfluorooctanoic acid exposure and pregnancy outcome in a highly exposed community.* Epidemiology (Cambridge, Mass.), 2012. **23**(3): p. 386-386.
70. Stein, C.R., D.A. Savitz, and M. Dougan, *Serum levels of perfluorooctanoic acid and perfluorooctane sulfonate and pregnancy outcome.* American journal of epidemiology, 2009. **170**(7): p. 837-846.
71. Vélez, M.P., T.E. Arbuckle, and W.D. Fraser, *Maternal exposure to perfluorinated chemicals and reduced fecundity: the MIREC study.* Human reproduction, 2015. **30**(3): p. 701-709.
72. Usepa, *The third unregulated contaminant monitoring rule (UCMR 3): data summary.* EPA, Washington DC, 2013.
73. Usepa, *Drinking Water Health Advisory for Perfluorooctanoic Acid (PFOA)*. United States Environmental Protection (EPA), Office of Water, 0000: p. 822-R-16-005.
74. Agency, U.S.E.P. *Proposed PFAS National Primary Drinking Water Regulation*. 2023 03/28/2023]; Available from: https://www.epa.gov/sdwa/and-polyfluoroalkyl-substances-pfas.
75. Oecd, *WORKING TOWARDS A GLOBAL EMISSION INVENTORY OF PFASS: FOCUS ON PFCAS-STATUS QUO AND THE WAY FORWARD*. 2015.
76. Wang, Z., et al., *Fluorinated alternatives to long-chain perfluoroalkyl carboxylic acids (PFCAs), perfluoroalkane sulfonic acids (PFSAs) and their potential precursors.* Environment International, 2013. **60**: p. 242-248.
77. Barzen-Hanson, K.A., et al., *Discovery of 40 Classes of Per- and Polyfluoroalkyl Substances in Historical Aqueous Film-Forming Foams (AFFFs) and AFFF-Impacted Groundwater.* Environmental Science & Technology, 2017. **51**: p. 2047-2057.
78. Sun, M., et al., *Legacy and Emerging Perfluoroalkyl Substances Are Important Drinking Water Contaminants in the Cape Fear River Watershed of North Carolina.* Environmental Science and Technology Letters, 2016. **3**(12): p. 415-419.
79. Wang, Z., et al., *Hazard assessment of fluorinated alternatives to long-chain perfluoroalkyl acids (PFAAs) and their precursors: status quo, ongoing challenges and possible solutions.* Environment international, 2015. **75**: p. 172-179.
80. Cao, Y., et al., *1000-fold preconcentration of per-and polyfluorinated alkyl substances within 10 minutes via electrochemical aerosol formation.* Analytical chemistry, 2019. **91**(22): p. 14352-14358.
81. Meng, P., et al., *Role of the air-water interface in removing perfluoroalkyl acids from drinking water by activated carbon treatment.* Journal of Hazardous Materials, 2020. **386**: p. 121981.
82. Vecitis, C., et al., *Enhancement of perfluorooctanoate and perfluorooctanesulfonate activity at acoustic cavitation bubble interfaces.* The Journal of Physical Chemistry C, 2008. **112**(43): p. 16850-16857.
83. Lyu, Y., et al., *Adsorption of PFOA at the air–water interface during transport in unsaturated porous media.* Environmental Science & Technology, 2018. **52**(14): p. 7745-7753.

84. Lyu, Y. and M.L. Brusseau, *The influence of solution chemistry on air-water interfacial adsorption and transport of PFOA in unsaturated porous media.* Science of the Total Environment, 2020. **713**: p. 136744.
85. Anderson, R.H., et al., *Occurrence of select perfluoroalkyl substances at US Air Force aqueous film-forming foam release sites other than fire-training areas: Field-validation of critical fate and transport properties.* Chemosphere, 2016. **150**: p. 678-685.
86. Xiao, F., et al., *Perfluorooctane sulfonate (PFOS) and perfluorooctanoate (PFOA) in soils and groundwater of a US metropolitan area: migration and implications for human exposure.* Water Research, 2015. **72**: p. 64-74.
87. Anderson, R.H., D.T. Adamson, and H.F. Stroo, *Partitioning of poly-and perfluoroalkyl substances from soil to groundwater within aqueous film-forming foam source zones.* Journal of Contaminant Hydrology, 2019. **220**: p. 59-65.
88. Høisæter, Å., A. Pfaff, and G.D. Breedveld, *Leaching and transport of PFAS from aqueous film-forming foam (AFFF) in the unsaturated soil at a firefighting training facility under cold climatic conditions.* Journal of Contaminant Hydrology, 2019. **222**: p. 112-122.
89. Shinoda, K. and T. Nomura, *Miscibility of fluorocarbon and hydrocarbon surfactants in micelles and liquid mixtures. Basic studies of oil repellent and fire extinguishing agents.* The Journal of Physical Chemistry, 1980. **84**(4): p. 365-369.
90. Downes, N., G. Ottewill, and R. Ottewill, *An investigation of the behaviour of ammonium perfluoro-octanoate at the air/water interface in the absence and presence of salts.* Colloids and Surfaces A: Physicochemical and Engineering Aspects, 1995. **102**: p. 203-211.
91. Brusseau, M.L., et al., *Comprehensive retention model for PFAS transport in subsurface systems.* Water Research, 2019. **148**: p. 41-50.
92. Hill, C., et al., *Surface and bulk properties of surfactants used in fire-fighting.* Journal of Colloid and Interface Science, 2018. **530**: p. 686-694.
93. USEPA, *Superfund Remedy Report 15th Edition*. 2017.
94. Huang, B., et al., *Chlorinated volatile organic compounds (Cl-VOCs) in environment - sources, potential human health impacts, and current remediation technologies.* Environment International, 2014. **71**: p. 118-138.
95. Futagami, T., M. Goto, and K. Furukawa, *Biochemical and genetic bases of dehalorespiration.* Chemical Record, 2008. **8**(1): p. 1-12.
96. Yan, J., et al., *Respiratory Vinyl Chloride Reductive Dechlorination to Ethene in TceA-Expressing Dehalococcoides mccartyi.* Environmental Science & Technology, 2021. **55**(8): p. 4831-4841.
97. Löffler, F.E., K.M. Ritalahti, and S.H. Zinder, *Dehalococcoides and Reductive Dechlorination of Chlorinated Solvents*, in *Bioaugmentation for Groundwater Remediation*, H.F. Stroo, et al., Editors. 2013: New York, NY. p. 39-88.
98. Patil, S.S., E.M. Adetutu, and A.S. Ball, *Microbiology of chloroethene degradation in groundwater.* Microbiology Australia, 2014: p. 211-214.
99. Im, J., et al., *Biotic and Abiotic Dehalogenation of 1,1,2-Trichloro-1,2,2-trifluoroethane (CFC-113): Implications for Bacterial Detoxification of Chlorinated Ethenes.* Environmental Science and Technology, 2019. **53**(20): p. 11941-11948.
100. Maymó-Gatell, X., I. Nijenhuis, and S.H. Zinder, *Reductive dechlorination of cis-1,2-dichloroethene and vinyl chloride by "Dehalococcoides ethenogenes".* Environmental Science and Technology, 2001. **35**(3): p. 516-521.

101. Mayer-Blackwell, K., et al., *1,2-Dichloroethane Exposure Alters the Population Structure, Metabolism, and Kinetics of a Trichloroethene-Dechlorinating Dehalococcoides mccartyi Consortium.* Environmental Science and Technology, 2016. **50**(22): p. 12187-12196.
102. Wen, L.L., et al., *Effects of 1,1,1-trichloroethane and triclocarban on reductive dechlorination of trichloroethene in a TCE-reducing culture.* Frontiers in Microbiology, 2017. **8**(AUG): p. 1-10.
103. Weathers, T.S., et al., *Perfluoroalkyl Acids Inhibit Reductive Dechlorination of Trichloroethene by Repressing Dehalococcoides.* Environmental Science and Technology, 2016. **50**(1): p. 240-248.
104. Cápiro, N.L., F.E. Löffler, and K.D. Pennell, *Spatial and temporal dynamics of organohalide-respiring bacteria in a heterogeneous PCE-DNAPL source zone.* Journal of Contaminant Hydrology, 2015. **182**: p. 78-90.
105. Yang, Y., et al., *Resilience and recovery of Dehalococcoides mccartyi following low pH exposure.* FEMS Microbiology Ecology, 2017. **93**(12): p. 1-9.
106. Tang, Z., et al., *Effects of co-occurrence of PFASs and chlorinated aliphatic hydrocarbons on microbial communities in groundwater: A field study.* Journal of Hazardous Materials, 2022. **435**(April).
107. McKenzie, E.R., et al., *The influence of a non-aqueous phase liquid (NAPL) and chemical oxidant application on perfluoroalkyl acid (PFAA) fate and transport.* Water Research, 2016. **92**: p. 199-207.
108. McKenzie, E.R., et al., *Effects of Chemical Oxidants on Perfluoroalkyl Acid Transport in One-Dimensional Porous Media Columns.* Environmental Science & Technology, 2015. **49**(3): p. 1681-1689.
109. Guo, B., J. Zeng, and M.L. Brusseau, *A mathematical model for the release, transport, and retention of per-and polyfluoroalkyl substances (PFAS) in the vadose zone.* Water Resources Research, 2020. **56**(2): p. e2019WR026667.
110. Silva, J.A.K., J. Šimůnek, and J.E. McCray, *A modified HYDRUS model for simulating PFAS transport in the vadose zone.* Water, 2020. **12**(10): p. 2758.
111. Silva, J.A., et al., *Simulated leaching of PFAS from land-applied municipal biosolids at agricultural sites.* Journal of Contaminant Hydrology, 2022. **251**: p. 104089.
112. Šimůnek, J., M.T. Van Genuchten, and M. Šejna, *Recent developments and applications of the HYDRUS computer software packages.* Vadose Zone Journal, 2016. **15**(7).
113. Zeng, J., M.L. Brusseau, and B. Guo, *Model validation and analyses of parameter sensitivity and uncertainty for modeling long-term retention and leaching of PFAS in the vadose zone.* Journal of Hydrology, 2021. **603**: p. 127172.
114. Zeng, J. and B. Guo, *Multidimensional simulation of PFAS transport and leaching in the vadose zone: Impact of surfactant-induced flow and subsurface heterogeneities.* Advances in Water Resources, 2021. **155**: p. 104015.
115. Wallis, I., et al., *Model-based identification of vadose zone controls on PFAS mobility under semi-arid climate conditions.* Water Research, 2022. **225**: p. 119096.
116. Huang, S. and P.R. Jaffé, *Defluorination of Perfluorooctanoic Acid (PFOA) and Perfluorooctane Sulfonate (PFOS) by Acidimicrobium sp. Strain A6.* Environmental Science & Technology, 2019. **53**(19): p. 11410-11419.
117. Yu, Y., et al., *Microbial Cleavage of C-F Bonds in Two C6Per- And Polyfluorinated Compounds via Reductive Defluorination.* Environmental Science and Technology, 2020. **54**(22): p. 14393-14402.

118. Liu, C., et al., *In-situ sequestration of perfluoroalkyl substances using polymer-stabilized ion exchange resin.* Journal of Hazardous Materials, 2022. **422**: p. 126960.
119. Aly, Y.H., et al., *Enhanced adsorption of perfluoro alkyl substances for in situ remediation.* Environmental Science: Water Research & Technology, 2019. **5**(11): p. 1867-1875.
120. Hakimabadi, S.G., A. Taylor, and A.L.-T. Pham, *Factors Affecting the Adsorption of Per- and Polyfluoroalkyl Substances (PFAS) by Colloidal Activated Carbon.* Water Research, 2023: p. 120212.
121. Carey, G.R., et al., *Longevity of colloidal activated carbon for in situ PFAS remediation at AFFF-contaminated airport sites.* Remediation Journal, 2022. **33**(1): p. 3-23.
122. Jasmann, J.R., et al., *Synergistic treatment of mixed 1, 4-dioxane and chlorinated solvent contaminations by coupling electrochemical oxidation with aerobic biodegradation.* Environmental Science & Technology, 2017. **51**(21): p. 12619-12629.
123. Chen, H., et al., *Simultaneous dissipation of trichloroethene and arsenic from co-contaminated groundwater by coupling biodechlorination and biodetoxification with assistance of biochar.* Biochar, 2022. **4**(1): p. 69.
124. McGregor, R. and Y. Zhao, *The in situ treatment of TCE and PFAS in groundwater within a silty sand aquifer.* Remediation Journal, 2021. **31**(2): p. 7-17.
125. Favreau, P., et al., *Multianalyte profiling of per-and polyfluoroalkyl substances (PFASs) in liquid commercial products.* Chemosphere, 2017. **171**: p. 491-501.
126. Herzke, D., E. Olsson, and S. Posner, *Perfluoroalkyl and polyfluoroalkyl substances (PFASs) in consumer products in Norway – A pilot study.* Chemosphere, 2012. **88**(8): p. 980-987.
127. Houtz, E.F., et al., *Persistence of Perfluoroalkyl Acid Precursors in AFFF-Impacted Groundwater and Soil.* Environmental Science & Technology, 2013. **47**(15): p. 8187-8195.
128. Lee, H., J. D'eon, and S.A. Mabury, *Biodegradation of polyfluoroalkyl phosphates as a source of perfluorinated acids to the environment.* Environmental Science & Technology, 2010. **44**(9): p. 3305-3310.
129. Wang, N., et al., *6: 2 Fluorotelomer sulfonate aerobic biotransformation in activated sludge of waste water treatment plants.* Chemosphere, 2011. **82**(6): p. 853-858.
130. Dasu, K., J. Liu, and L.S. Lee, *Aerobic soil biodegradation of 8: 2 fluorotelomer stearate monoester.* Environmental Science & Technology, 2012. **46**(7): p. 3831-3836.
131. Liou, J.-C., et al., *Investigating the biodegradability of perfluorooctanoic acid.* Chemosphere, 2010. **80**(2): p. 176-183.
132. Liu, J., et al., *6-2 Fluorotelomer alcohol aerobic biodegradation in soil and mixed bacterial culture.* Chemosphere, 2010. **78**(4): p. 437-444.
133. Royer, L.A., et al., *Microbial transformation of 8: 2 fluorotelomer acrylate and methacrylate in aerobic soils.* Chemosphere, 2015. **129**: p. 54-61.
134. Wang, N., et al., *8-2 Fluorotelomer alcohol aerobic soil biodegradation: Pathways, metabolites, and metabolite yields.* Chemosphere, 2009. **75**(8): p. 1089-1096.
135. Dinglasan, M.J.A., et al., *Fluorotelomer Alcohol Biodegradation Yields Poly- and Perfluorinated Acids.* Environmental Science & Technology, 2004. **38**(10): p. 2857-2864.
136. Harding-Marjanovic, K.C., et al., *Aerobic biotransformation of fluorotelomer thioether amido sulfonate (Lodyne) in AFFF-amended microcosms.* Environmental Science & Technology, 2015. **49**(13): p. 7666-7674.

137. Zhang, S., et al., *6:2 and 8:2 Fluorotelomer Alcohol Anaerobic Biotransformation in Digester Sludge from a WWTP under Methanogenic Conditions.* Environmental Science & Technology, 2013. **47**(9): p. 4227-4235.
138. Zhang, S., et al., *Biotransformation potential of 6: 2 fluorotelomer sulfonate (6: 2 FTSA) in aerobic and anaerobic sediment.* Chemosphere, 2016. **154**: p. 224-230.
139. Lange, C., *The aerobic biodegradation of N-EtFOSE alcohol by the microbial activity present in municipal wastewater treatment sludge.* For 3M Company, 2000.
140. Rhoads, K.R., et al., *Aerobic biotransformation and fate of N-ethyl perfluorooctane sulfonamidoethanol (N-EtFOSE) in activated sludge.* Environmental Science & Technology, 2008. **42**(8): p. 2873-2878.
141. Benskin, J.P., et al., *Biodegradation of N -Ethyl Perfluorooctane Sulfonamido Ethanol (EtFOSE) and EtFOSE-Based Phosphate Diester (SAmPAP Diester) in Marine Sediments.* Environmental Science & Technology, 2013. **47**(3): p. 1381-1389.
142. Park, M., et al., *Adsorption of perfluoroalkyl substances (PFAS) in groundwater by granular activated carbons: Roles of hydrophobicity of PFAS and carbon characteristics.* Water Research, 2020. **170**: p. 115364.
143. Chen, W., et al., *Sorption of perfluorooctane sulfonate and perfluorooctanoate on polyacrylonitrile fiber-derived activated carbon fibers: in comparison with activated carbon.* RSC Advances, 2017. **7**(2): p. 927-938.
144. Cao, F., et al., *Synthesis and application of a highly selective molecularly imprinted adsorbent based on multi-walled carbon nanotubes for selective removal of perfluorooctanoic acid.* Environmental Science: Water Research & Technology, 2018. **4**(5): p. 689-700.
145. Zaggia, A., et al., *Use of strong anion exchange resins for the removal of perfluoroalkylated substances from contaminated drinking water in batch and continuous pilot plants.* Water Research, 2016. **91**: p. 137-146.
146. Wang, W., et al., *Adsorption behavior and mechanism of emerging perfluoro-2-propoxypropanoic acid (GenX) on activated carbons and resins.* Chemical Engineering Journal, 2019. **364**: p. 132-138.
147. Ching, C., et al., *β-Cyclodextrin Polymers with Different Cross-Linkers and Ion-Exchange Resins Exhibit Variable Adsorption of Anionic, Zwitterionic, and Nonionic PFASs.* Environmental Science & Technology, 2020. **54**(19): p. 12693-12702.
148. Yang, A., et al., *Cyclodextrin Polymers with Nitrogen-Containing Tripodal Crosslinkers for Efficient PFAS Adsorption.* ACS Materials Letters, 2020. **2**(9): p. 1240-1245.
149. Ateia, M., et al., *Cationic polymer for selective removal of GenX and short-chain PFAS from surface waters and wastewaters at ng/L levels.* Water Research, 2019. **163**: p. 114874.
150. Ateia, M., et al., *Rapid Removal of Poly- and Perfluorinated Alkyl Substances by Poly(ethylenimine)-Functionalized Cellulose Microcrystals at Environmentally Relevant Conditions.* Environmental Science & Technology Letters, 2018. **5**(12): p. 764-769.
151. Campos-Pereira, H., et al., *The Adsorption of Per- and Polyfluoroalkyl Substances (PFASs) onto Ferrihydrite Is Governed by Surface Charge.* Environmental Science & Technology, 2020. **54**(24): p. 15722-15730.
152. Zhang, Y., et al., *Sorption of Perfluoroalkyl Acids to Fresh and Aged Nanoscale Zerovalent Iron Particles.* Environmental Science & Technology, 2018. **52**(11): p. 6300-6308.

153. Du, Z., et al., *Selective and Fast Adsorption of Perfluorooctanesulfonate from Wastewater by Magnetic Fluorinated Vermiculite.* Environmental Science & Technology, 2017. **51**(14): p. 8027-8035.
154. Meng, P., et al., *Superhigh adsorption of perfluorooctane sulfonate on aminated polyacrylonitrile fibers with the assistance of air bubbles.* Chemical Engineering Journal, 2017. **315**: p. 108-114.
155. Xiang, J., et al., *Thermally Driven Separation of Perfluoroalkyl Substances with High Efficiency.* ACS Applied Materials & Interfaces, 2020. **12**(36): p. 40759-40767.
156. Ali, M., et al., *Capture of Perfluorooctanoic Acid Using Oil-Filled Graphene Oxide–Silica Hybrid Capsules.* Environmental Science & Technology, 2020. **54**(6): p. 3549-3558.
157. Stebel, E.K., et al., *Absorption of short-chain to long-chain perfluoroalkyl substances using swellable organically modified silica.* Environmental Science: Water Research & Technology, 2019. **5**(11): p. 1854-1866.
158. Gong, Y., et al., *Removal of aqueous perfluorooctanoic acid (PFOA) using starch-stabilized magnetite nanoparticles.* Science of The Total Environment, 2016. **562**: p. 191-200.
159. Rattanaoudom, R., C. Visvanathan, and S.K. Boontanon, *Removal of concentrated PFOS and PFOA in synthetic industrial wastewater by powder activated carbon and hydrotalcite.* J. Water Sustain, 2012. **2**(4): p. 245-258.
160. Deng, S., et al., *Enhanced adsorption of perfluorooctane sulfonate and perfluorooctanoate by bamboo-derived granular activated carbon.* Journal of Hazardous Materials, 2015. **282**: p. 150-157.
161. Wang, B., et al., *Covalent triazine-based framework: A promising adsorbent for removal of perfluoroalkyl acids from aqueous solution.* Environmental Pollution, 2016. **216**: p. 884-892.
162. Niu, H. and Y. Cai, *Preparation of Octadecyl and Amino Mixed Group Modified Titanate Nanotubes and Its Efficient Adsorption to Several Ionic or Ionizable Organic Analytes.* Analytical Chemistry, 2009. **81**(24): p. 9913-9920.
163. Maimaiti, A., et al., *Competitive adsorption of perfluoroalkyl substances on anion exchange resins in simulated AFFF-impacted groundwater.* Chemical Engineering Journal, 2018. **348**: p. 494-502.
164. Yu, Q., et al., *Sorption of perfluorooctane sulfonate and perfluorooctanoate on activated carbons and resin: Kinetic and isotherm study.* Water Research, 2009. **43**(4): p. 1150-1158.
165. Xu, C., H. Chen, and F. Jiang, *Adsorption of perflourooctane sulfonate (PFOS) and perfluorooctanoate (PFOA) on polyaniline nanotubes.* Colloids and Surfaces A: Physicochemical and Engineering Aspects, 2015. **479**: p. 60-67.
166. Deng, S., et al., *Highly efficient sorption of perfluorooctane sulfonate and perfluorooctanoate on a quaternized cotton prepared by atom transfer radical polymerization.* Chemical Engineering Journal, 2012. **193-194**: p. 154-160.
167. Deng, S., et al., *Adsorption of perfluorinated compounds on aminated rice husk prepared by atom transfer radical polymerization.* Chemosphere, 2013. **91**(2): p. 124-130.
168. Chen, M.-J., et al., *Influence of crystal topology and interior surface functionality of metal-organic frameworks on PFOA sorption performance.* Microporous and Mesoporous Materials, 2016. **236**: p. 202-210.
169. Chen, X., et al., *A comparative study on sorption of perfluorooctane sulfonate (PFOS) by chars, ash and carbon nanotubes.* Chemosphere, 2011. **83**(10): p. 1313-1319.

170. Gao, Y., et al., *Adsorptive removal of emerging polyfluoroalky substances F-53B and PFOS by anion-exchange resin: A comparative study.* Journal of Hazardous Materials, 2017. **323**: p. 550-557.
171. Deng, S., et al., *Removal of perfluorooctane sulfonate from wastewater by anion exchange resins: Effects of resin properties and solution chemistry.* Water Research, 2010. **44**(18): p. 5188-5195.
172. Yu, Q., S. Deng, and G. Yu, *Selective removal of perfluorooctane sulfonate from aqueous solution using chitosan-based molecularly imprinted polymer adsorbents.* Water Research, 2008. **42**(12): p. 3089-3097.
173. Zhang, Q., et al., *Removal of perfluorooctane sulfonate from aqueous solution by crosslinked chitosan beads: Sorption kinetics and uptake mechanism.* Bioresource Technology, 2011. **102**(3): p. 2265-2271.
174. Luo, Q., et al., *A Porous Aromatic Framework Constructed from Benzene Rings Has a High Adsorption Capacity for Perfluorooctane Sulfonate.* Scientific Reports, 2016. **6**(1): p. 20311.
175. Jin, T., M. Peydayesh, and R. Mezzenga, *Membrane-based technologies for per- and poly-fluoroalkyl substances (PFASs) removal from water: Removal mechanisms, applications, challenges and perspectives.* Environment International, 2021. **157**: p. 106876.
176. Qian, L., F.-D. Kopinke, and A. Georgi, *Photodegradation of Perfluorooctanesulfonic Acid on Fe-Zeolites in Water.* Environmental Science & Technology, 2021. **55**(1): p. 614-622.
177. Duan, L., et al., *Efficient Photocatalytic PFOA Degradation over Boron Nitride.* Environmental Science & Technology Letters, 2020. **7**(8): p. 613-619.
178. Rao, U., et al., *Structural Dependence of Reductive Defluorination of Linear PFAS Compounds in a UV/Electrochemical System.* Environmental Science & Technology, 2020. **54**(17): p. 10668-10677.
179. Bao, Y., et al., *Degradation of PFOA Substitute: GenX (HFPO–DA Ammonium Salt): Oxidation with UV/Persulfate or Reduction with UV/Sulfite?* Environmental Science & Technology, 2018. **52**(20): p. 11728-11734.
180. Zhang, W., et al., *Destruction of Perfluoroalkyl Acids Accumulated in Typha latifolia through Hydrothermal Liquefaction.* ACS Sustainable Chemistry & Engineering, 2020. **8**(25): p. 9257-9262.
181. Bentel, M.J., et al., *Degradation of Perfluoroalkyl Ether Carboxylic Acids with Hydrated Electrons: Structure–Reactivity Relationships and Environmental Implications.* Environmental Science & Technology, 2020. **54**(4): p. 2489-2499.
182. Kim, T.-H., et al., *Decomposition of perfluorooctane sulfonate (PFOS) using a hybrid process with electron beam and chemical oxidants.* Chemical Engineering Journal, 2019. **361**: p. 1363-1370.
183. Singh, R.K., et al., *Removal of Poly- and Per-Fluorinated Compounds from Ion Exchange Regenerant Still Bottom Samples in a Plasma Reactor.* Environmental Science & Technology, 2020. **54**(21): p. 13973-13980.
184. Olatunde, O.C., A.T. Kuvarega, and D.C. Onwudiwe, *Photo enhanced degradation of polyfluoroalkyl and perfluoroalkyl substances.* Heliyon, 2020. **6**(12): p. e05614.
185. Fang, C., M. Megharaj, and R. Naidu, *Electrochemical Advanced Oxidation Processes (EAOP) to degrade per- and polyfluoroalkyl substances (PFASs).* Journal of Advanced Oxidation Technologies, 2017. **20**(2).

186. Yu, W.W., et al., *Synthesis of monodisperse iron oxide nanocrystals by thermal decomposition of iron carboxylate salts.* Chemical Communications, 2004(20): p. 2306-2307.
187. Prakash, A., et al., *Bilayers as Phase Transfer Agents for Nanocrystals Prepared in Nonpolar Solvents.* ACS Nano, 2009. **3**(8): p. 2139-2146.
188. Sperling, R.A. and W.J. Parak, *Surface modification, functionalization and bioconjugation of colloidal inorganic nanoparticles.* Philosophical Transactions of the Royal Society A: Mathematical, Physical and Engineering Sciences, 2010. **368**(1915): p. 1333-1383.
189. Dunér, G., E. Thormann, and A. Dėdinaitė, *Quartz Crystal Microbalance with Dissipation (QCM-D) studies of the viscoelastic response from a continuously growing grafted polyelectrolyte layer.* Journal of colloid and interface science, 2013. **408**: p. 229-234.
190. Thompson, J.A., et al., *Tunable CO2 Adsorbents by Mixed-Linker Synthesis and Postsynthetic Modification of Zeolitic Imidazolate Frameworks.* The Journal of Physical Chemistry C, 2013. **117**(16): p. 8198-8207.
191. J. McCord, S. Newton, and M. Strynar, *Validation of quantitative measurements and semi-quantitative estimates of emerging perfluoroethercarboxylic acids (PFECAs) and hexfluoroprolyene oxide acids (HFPOAs).* J. Chromatogr. A, 2018. **1551**: p. 52-58.
192. E.-T. Yun, et al., *Exploring the role of persulfate in the activation process: radical precursor versus electron acceptor.* Environ. Sci. Technol., 2017. **51**(17): p. 10090-10099.
193. Löffler, F.E., R.A. Sanford, and K.M. Ritalahti, *Enrichment, cultivation, and detection of reductively dechlorinating bacteria.* Methods in Enzymology, 2005. **397**(1996): p. 77-111.
194. OECD, *Hazard Assessment of Perfluorooctane Sulfonate (PFOS) and Its Salts*. 2002.
195. Yan, J., et al., *Guided cobalamin biosynthesis supports Dehalococcoides mccartyi reductive dechlorination activity.* Philosophical Transactions of the Royal Society B: Biological Sciences, 2013. **368**(1616): p. 20120320.
196. Lichstein, H.C. and M.H. Soule, *Studies of the Effect of Sodium Azide on Microbic Growth and Respiration.* Journal of Bacteriology, 1944. **47**(3): p. 253-257.
197. Virtanen, P., et al., *SciPy 1.0: fundamental algorithms for scientific computing in Python.* Nature Methods, 2020. **17**(3): p. 261-272.
198. Elsey, J.L., J.A. Christ, and L.M. Abriola, *Quantifying Impacts of Microcosm Mass Loss on Kinetic Constant Estimation.* Environmental Science & Technology, 2021. **55**(20): p. 13822-13833.
199. Yang, L., et al., *Exploration of processes governing microbial reductive dechlorination in a heterogeneous aquifer flow cell.* Water Research, 2021. **193**.
200. Chambon, J.C., et al., *Review of reactive kinetic models describing reductive dechlorination of chlorinated ethenes in soil and groundwater.* Biotechnology and Bioengineering, 2013. **110**(1): p. 1-23.
201. Van den Bos, A., *Parameter Estimation for Scientists and Engineers*. 2007, Hoboken, NJ, USA.
202. McNamara, J.D., et al., *Comparison of activated carbons for removal of perfluorinated compounds from drinking water.* Journal-American Water Works Association, 2018. **110**(1): p. E2--E14.
203. Ochoa-Herrera, V. and R. Sierra-Alvarez, *Removal of perfluorinated surfactants by sorption onto granular activated carbon, zeolite and sludge.* Chemosphere, 2008. **72**(10): p. 1588-1593.

204. Senevirathna, S.T., et al., *A comparative study of adsorption of perfluorooctane sulfonate (PFOS) onto granular activated carbon, ion-exchange polymers and non-ion-exchange polymers.* Chemosphere, 2010. **80**(6): p. 647-651.
205. Xiao, X., et al., *Sorption of Poly- and Perfluoroalkyl Substances (PFASs) Relevant to Aqueous Film-Forming Foam (AFFF)-Impacted Groundwater by Biochars and Activated Carbon.* Environmental Science and Technology, 2017. **51**(11): p. 6342-6351.
206. Yu, Q., et al., *Sorption of perfluorooctane sulfonate and perfluorooctanoate on activated carbons and resin: Kinetic and isotherm study.* Water Res, 2009. **43**(4): p. 1150-1158.
207. Zhang, D., et al., *Sorption of perfluorooctanoic acid, perfluorooctane sulfonate and perfluoroheptanoic acid on granular activated carbon.* Chemosphere, 2016. **144**: p. 2336-2342.
208. Usepa, *Office of the Federal Register.* Washington DC, 2012. **vol. 77**: p. pp. 26071-26101.
209. Hidalgo, A. and N. Mora-Diez, *Novel approach for predicting partition coefficients of linear perfluorinated compounds.* Theoretical Chemistry Accounts, 2016. **135**: p. 18-18.
210. Deng, S., et al., *Sorption mechanisms of perfluorinated compounds on carbon nanotubes.* Environmental Pollution, 2012. **168**: p. 138-144.
211. Maimaiti, A., et al., *Competitive adsorption of perfluoroalkyl substances on anion exchange resins in simulated AFFF-impacted groundwater.* Chemical Engineering Journal, 2018. **348**(May): p. 494-502.
212. McCord, J., S. Newton, and M. Strynar, *Validation of quantitative measurements and semi-quantitative estimates of emerging perfluoroethercarboxylic acids (PFECAs) and hexfluoroprolyene oxide acids (HFPOAs).* Journal of Chromatography A, 2018. **1551**: p. 52-58.
213. Marcet, T.F., et al., *Impacts of low-temperature thermal treatment on microbial detoxification of tetrachloroethene under continuous flow conditions.* Water research, 2018. **145**: p. 21-29.
214. Szostek, B., K.B. Prickett, and R.C. Buck, *Determination of fluorotelomer alcohols by liquid chromatography/tandem mass spectrometry in water.* Rapid Communications in Mass Spectrometry, 2006. **20**(19): p. 2837-2844.
215. Williams, A.J., et al., *The CompTox Chemistry Dashboard: a community data resource for environmental chemistry.* Journal of Cheminformatics, 2017. **9**(1): p. 61.
216. Wishart, D.S., et al., *BioTransformer 3.0—a web server for accurately predicting metabolic transformation products.* Nucleic Acids Research, 2022: p. gkac313.
217. Schymanski, E.L., et al., *Identifying Small Molecules via High Resolution Mass Spectrometry: Communicating Confidence.* Environmental Science & Technology, 2014. **48**(4): p. 2097-2098.
218. Kim, C., et al., *Engineered superparamagnetic nanomaterials for arsenic(v) and chromium(vi) sorption and separation: quantifying the role of organic surface coatings.* Environmental Science: Nano, 2018. **5**(2): p. 556-563.
219. Goss, K.-U., *The pKa Values of PFOA and Other Highly Fluorinated Carboxylic Acids.* Environmental Science & Technology, 2008. **42**(2): p. 456-458.
220. Ji, W., et al., *Removal of GenX and Perfluorinated Alkyl Substances from Water by Amine-Functionalized Covalent Organic Frameworks.* Journal of the American Chemical Society, 2018. **140**(40): p. 12677-12681.
221. Brooke, D., A. Footitt, and T. Nwaogu, *Environmental risk evaluation report: Perfluorooctanesulphonate (PFOS).* 2004.

222. Burns, D.C., et al., *Experimental pKa Determination for Perfluorooctanoic Acid (PFOA) and the Potential Impact of pKa Concentration Dependence on Laboratory-Measured Partitioning Phenomena and Environmental Modeling.* Environmental Science & Technology, 2008. **42**(24): p. 9283-9288.
223. Cheng, J., et al., *Acid Dissociation versus Molecular Association of Perfluoroalkyl Oxoacids: Environmental Implications.* The Journal of Physical Chemistry A, 2009. **113**(29): p. 8152-8156.
224. Sha, B., et al., *Adsorption of organic amines from wastewater by carboxyl group-modified polyacrylonitrile fibers.* Journal of applied polymer science, 2013. **128**(6): p. 4124-4129.
225. Wang, L. and J. Song, *Enhanced NH3 sensing properties of carboxyl functionalized carbon nanocoil.* Materials Research Express, 2020. **7**(7): p. 075014.
226. Fatisson, J., et al., *Deposition of TiO2 Nanoparticles onto Silica Measured Using a Quartz Crystal Microbalance with Dissipation Monitoring.* Langmuir, 2009. **25**(11): p. 6062-6069.
227. Quevedo, I.R., A.L.J. Olsson, and N. Tufenkji, *Deposition Kinetics of Quantum Dots and Polystyrene Latex Nanoparticles onto Alumina: Role of Water Chemistry and Particle Coating.* Environmental Science & Technology, 2013. **47**(5): p. 2212-2220.
228. Sauerbrey, G., *Verwendung von Schwingquarzen zur Wägung dünner Schichten und zur Mikrowägung.* Zeitschrift für physik, 1959. **155**(2): p. 206-222.
229. Kim, C. and J.D. Fortner, *Surface-Engineered Nanomaterials in Water: Understanding Critical Dynamics of Soft Organic Coatings and Relative Aggregation Density.* Environmental Science & Technology, 2020. **54**(21): p. 13548-13555.
230. Kim, C., et al., *Surface functionalized nanoscale metal oxides for arsenic(v), chromium(vi), and uranium(vi) sorption: considering single- and multi-sorbate dynamics.* Environmental Science: Nano, 2020. **7**(12): p. 3805-3813.
231. Müller, S., T. Behrends, and C.M. van Genuchten, *Sustaining efficient production of aqueous iron during repeated operation of Fe(0)-electrocoagulation.* Water Research, 2019. **155**: p. 455-464.
232. Esfandiar, N., R. Suri, and E.R. McKenzie, *Competitive sorption of Cd, Cr, Cu, Ni, Pb and Zn from stormwater runoff by five low-cost sorbents; Effects of co-contaminants, humic acid, salinity and pH.* Journal of Hazardous Materials, 2022. **423**: p. 126938.
233. Genç-Fuhrman, H., P.S. Mikkelsen, and A. Ledin, *Simultaneous removal of As, Cd, Cr, Cu, Ni and Zn from stormwater using high-efficiency industrial sorbents: Effect of pH, contact time and humic acid.* Science of The Total Environment, 2016. **566-567**: p. 76-85.
234. Wen, Y., et al., *Integrated photocatalytic reduction and oxidation of perfluorooctanoic acid by metal–organic frameworks: key insights into the degradation mechanisms.* Journal of the American Chemical Society, 2022. **144**(26): p. 11840-11850.
235. Sansotera, M., et al., *Decomposition of perfluorooctanoic acid photocatalyzed by titanium dioxide: Chemical modification of the catalyst surface induced by fluoride ions.* Applied Catalysis B: Environmental, 2014. **148-149**: p. 29-35.
236. B. Lu, et al., *Porous Ni Foams Filled by N-Doped Carbon Nanotubes Coated with N-Doped Ni3P and Ni Nanoparticles for Catalytic Water Splitting.* ACS Appl. Nano Mater., 2021. **4**(7): p. 7443-7453.
237. A. Reina, et al., *Large Area, Few-Layer Graphene Films on Arbitrary Substrates by Chemical Vapor Deposition.* Nano Lett., 2009. **9**(1): p. 30-35.

238. W. Hu, et al., *CoNi2S4 Nanosheet Arrays Supported on Nickel Foams with Ultrahigh Capacitance for Aqueous Asymmetric Supercapacitor Applications.* ACS Appl. Mater. Interfaces., 2014. **6**(21): p. 19318-19326.
239. Y.-H. Chang, et al., *Highly efficient electrocatalytic hydrogen production by MoSx grown on graphene-protected 3D Ni foams.* Adv. Mater., 2013. **25**(5): p. 756-760.
240. A. Peigney, et al., *Specific surface area of carbon nanotubes and bundles of carbon nanotubes.* Carbon, 2001. **39**(4): p. 507-514.
241. W. Ren, et al., *Electro-Induced Carbon Nanotube Discrete Electrodes for Sustainable Persulfate Activation.* Environ. Sci. Technol., 2022. **56**(19): p. 14019-14029.
242. D. Q. Zhang, W. L. Zhang, and Y. N. Liang, *Adsorption of perfluoroalkyl and polyfluoroalkyl substances (PFASs) from aqueous solution-A review. Sci. Total Environ.*, 2019. **694**: p. 133606.
243. E.-T. Yun, et al., *Identifying the Nonradical Mechanism in the Peroxymonosulfate Activation Process: Singlet Oxygenation Versus Mediated Electron Transfer.* Environ.Sci.Technol., 2018. **52**(12): p. 7032-7042.
244. Amos, B.K., et al., *Spatial and temporal distributions of Geobacter lovleyi and Dehalococcoides spp. during bioenhanced PCE-NAPL dissolution.* Environmental Science and Technology, 2009. **43**(6): p. 1977-1985.
245. Crank, J., *The Mathematics of Diffusion*. 1979.
246. Göbel, R., et al., *Investigation of Different Polymers as Coating Materials for IR/ATR Spectroscopic Trace Analysis of Chlorinated Hydrocarbons in Water.* Applied Spectroscopy, 1994. **48**(6): p. 678-683.
247. Göbel, R., et al., *Infrared attenuated total reflection spectroscopic investigations of the diffusion behaviour of chlorinated hydrocarbons into polymer membranes.* Vibrational Spectroscopy, 1995. **8**(2): p. 141-149.
248. Chung, T.H., et al., *Generalized multiparameter correlation for nonpolar and polar fluid transport properties.* Industrial & Engineering Chemistry Research, 1988. **27**(4): p. 671-679.
249. Teplyakov, V. and P. Meares, *Correlation aspects of the selective gas permeabilities of polymeric materials and membranes.* Gas Separation & Purification, 1990. **4**(2): p. 66-74.
250. Kim, J.Y., J.K. Park, and T.B. Edil, *Sorption of Organic Compounds in the Aqueous Phase onto Tire Rubber.* Journal of Environmental Engineering, 1997. **123**(9): p. 827-835.
251. Zhu, T., et al., *A novel method for measuring polymer–water partition coefficients.* Chemosphere, 2015. **138**: p. 973-979.
252. McFadden, D., *Conditional logit analysis of qualitative choice behavior*, in *Frontiers in Econometrics*, P. Zarembka and P. Zarembka, Editors. 1973. p. 105-142.
253. Doelman, P. and L. Haanstra, *Short- and long-term effects of heavy metals on phosphatase activity in soils: An ecological dose-response model approach.* Biology and Fertility of Soils, 1989. **8**(3): p. 235-241.
254. Haest, P.J., D. Springael, and E. Smolders, *Dechlorination kinetics of TCE at toxic TCE concentrations: Assessment of different models.* Water Research, 2010. **44**(1): p. 331-339.
255. Yang, Y., et al., *Organohalide Respiration with Chlorinated Ethenes under Low pH Conditions.* Environmental Science and Technology, 2017. **51**(15): p. 8579-8588.
256. Bräunig, J., et al., *Fate and redistribution of perfluoroalkyl acids through AFFF-impacted groundwater.* Science of the Total Environment, 2017. **596-597**: p. 360-368.

257. Field, J.A., D.L. Sedlak, and L. Alvarez-Cohen, *Characterization of the Fate and Biotransformation of Fluorochemicals in AFFF-Contaminated Groundwater at Fire / Crash Testing Military Sites (ER-2128)*. 2017.
258. Higgins, C.P. and R.G. Luthy, *Sorption of perfluorinated surfactants on sediments.* Environmental Science and Technology, 2006. **40**(23): p. 7251-7256.
259. Hansen, M.C., et al., *Sorption of perfluorinated compounds from contaminated water to activated carbon.* Journal of Soils and Sediments, 2010. **10**(2): p. 179-185.
260. Krajmalnik-Brown, R., et al., *Genetic Identification of a Putative Vinyl Chloride Reductase in strain BAV1.* Applied and Environmental Microbiology, 2004. **70**(10): p. 6347-6351.
261. Aly, Y.H., et al., *In Situ Remediation Method for Enhanced Sorption of Perfluoro-Alkyl Substances onto Ottawa Sand.* Journal of Environmental Engineering, 2018. **144**(9): p. 4018086-4018086.
262. Aly, Y.H., et al., *Enhanced adsorption of perfluoro alkyl substances for: In situ remediation.* Environmental Science: Water Research and Technology, 2019. **5**(11): p. 1867-1875.
263. Hansen, K.J., et al., *Compound-specific, quantitative characterization of organic fluorochemicals in biological matrices.* Environmental science & technology, 2001. **35**(4): p. 766-770.
264. McGregor, R., *In Situ treatment of PFAS-impacted groundwater using colloidal activated Carbon.* Remediation, 2018. **28**(3): p. 33-41.
265. Chularueangaksorn, P., et al., *Batch and column adsorption of perfluorooctane sulfonate on anion exchange resins and granular activated carbon.* Journal of Applied Polymer Science, 2014. **131**(3): p. 39782-39782.
266. Gao, P., J. Cui, and Y. Deng, *Direct regeneration of ion exchange resins with sulfate radical-based advanced oxidation for enabling a cyclic adsorption – regeneration treatment approach to aqueous perfluorooctanoic acid (PFOA).* Chemical Engineering Journal, 2021. **405**: p. 126698-126698.
267. Appleman, T.D., et al., *Treatment of poly-and perfluoroalkyl substances in US full-scale water treatment systems.* Water research, 2014. **51**: p. 246-255.
268. Park, M., et al., *Adsorption of perfluoroalkyl substances (PFAS) in groundwater by granular activated carbons: Roles of hydrophobicity of PFAS and carbon characteristics.* Water Research, 2020. **170**: p. 115364-115364.
269. Xiao, F., et al., *Effects of monovalent cations on the competitive adsorption of perfluoroalkyl acids by kaolinite: Experimental studies and modeling.* Environmental Science and Technology, 2011. **45**(23): p. 10028-10035.
270. Moody, C.A. and J.A. Field, *Determination of Perfluorocarboxylates in Groundwater Impacted by Fire-Fighting Activity Determination of Perfluorocarboxylates in Groundwater Impacted by Fire-Fighting Activity.* Environmental Science and Technology, 1999. **33**(16): p. 2800-2806.
271. Cai, Y., et al., *Toxicity of perfluorinated compounds to soil microbial activity: Effect of carbon chain length, functional group and soil properties.* Science of the Total Environment, 2019. **690**: p. 1162-1169.
272. Dixit, F., et al., *Performance of the HSDM to predict competitive uptake of PFAS, NOM and inorganic anions by suspended ion exchange processes.* Environmental Science: Water Research & Technology, 2021.

273. Ritalahti, K.M., et al., *Quantitative PCR targeting 16S rRNA and reductive dehalogenase genes simultaneously monitors multiple Dehalococcoides strains.* Applied and Environmental Microbiology, 2006. **72**(4): p. 2765-2774.
274. Amos, B.K., et al., *Experimental evaluation and mathematical modeling of microbially enhanced tetrachloroethene (PCE) dissolution.* Environmental Science and Technology, 2007. **41**(3): p. 963-970.
275. Holliger, C., G. Wohlfarth, and G. Diekert, *Reductive dechlorination in the energy metabolism of anaerobic bacteria.* FEMS Microbiology Reviews, 1998. **22**(5): p. 383-398.
276. Liu, C. and J.M. Zachara, *Uncertainties of Monod Kinetic Parameters Nonlinearly Estimated from Batch Experiments.* Environmental Science & Technology, 2001. **35**(1): p. 133-141.
277. Ticknor, J.L., et al., *Simplified Analysis of Chlorinated Ethenes in Water Samples by Gas Chromatography with Flame Ionization Detection.* Environmental Engineering Science, 2013. **30**(1): p. 30-37.
278. Seshadri, R., et al., *Genome sequence of the PCE-dechlorinating bacterium Dehalococcoides ethenogenes.* Science, 2005. **307**(5706): p. 105-108.
279. Storn, R. and K. Price, *Differential Evolution – A Simple and Efficient Heuristic for global Optimization over Continuous Spaces.* Journal of Global Optimization, 1997. **11**(4): p. 341-359.
280. Friis, A.K., et al., *Temperature dependence of anaerobic TCE-dechlorination in a highly enriched Dehalococcoides-containing culture.* Water Research, 2007. **41**(2): p. 355-364.
281. Kube, M., et al., *Genome sequence of the chlorinated compound-respiring bacterium Dehalococcoides species strain CBDB1.* Nature Biotechnology, 2005. **23**(10): p. 1269-1273.
282. Levenberg, K., *A method for the solution of certain non-linear problems in least squares.* Quarterly of Applied Mathematics, 1944. **2**(2): p. 164-168.
283. Marquardt, D.W., *An Algorithm for Least-Squares Estimation of Nonlinear Parameters*, in *J. Soc. INDUST. APPL. MATH*. 1963.
284. Mackay, D., et al., *Handbook of physical-chemical properties and environmental fate for organic chemicals*. 2nd ed ed, ed. D. Mackay, et al. 2006, Boca Raton, FL.

Appendix A: Supporting Information

A.1 Biological Analytical Methods

Aqueous biomass samples (1 mL) were prepared by centrifugation at 15,000 rpm (21,130×g) for 15 minutes using an Eppendorf 5424 centrifuge with 5424R rotor (Eppendorf; Hamburg, Germany). After removing the supernatant, pellets were stored at -20°C. Microbial genomic DNA was extracted from the pellets using the QIAamp DNA Mini Kit (Qiagen; Hilden, Germany) and following the manufacturer's protocol. Extracted DNA was stored at -20°C until qPCR analysis.

Dhc strain abundance was quantified by qPCR analysis targeting the *Dhc* 16S rRNA gene with additional analysis targeting the *tceA, vcrA, and bvcA* RDase genes. All qPCR analyses were measured in triplicate using a Step One Plus Real-Time PCR System (Applied Biosystems; Foster City, CA) under standard operating conditions and TaqMan-based chemistry [273]. *Geo*SZ 16S rRNA gene copies were measured using SYBR Green detection chemistry according to previously described protocols [274] with modifications by others [244]. Primers and probes were obtained from IDT Technologies (Coralville, IA) or ThermoFisher and the TaqMan and SYBR Green Universal PCR Master Mixes from Applied Biosystems (Foster City, CA).

For each analysis, a standard curve was generated using 10-fold serial dilutions of a stock solution containing a known concentration of plasmid DNA with a single copy of the target gene [273]. DNA for standard curves were extracted from pure-cultures of *E. coli* containing a plasmid with a single *GeoSZ* 16S rRNA gene copy or a single copy of the *Dhc* 16S rRNA, *tceA, vcrA,* and *bvcA* genes. DNA was extracted from the plasmid using the QIAprep Miniprep Kit (Qiagen; Hilden, Germany) and following the manufacturer's protocol. DNA in the extracted solution was quantified using a Qubit 2.0 fluorometer with the dsDNA BR assay kit (ThermoFisher Scientific; Waltham, MA). This known quantity of DNA was diluted to a concentration of 1 ng/L using DNA free water. The number of template gene copies in the standard 1 ng/L was calculated using the length of the plasmid sequences [273] and was diluted in a series of 10-fold serial dilutions to produce 6 or 7 standard concentrations. Calibration curve slopes, intercepts, and correlation coefficients (R^2), as well as the standard concentrations used to calculate the linear range are included as **Table A.1**.

All TaqMan PCR analyses contained a forward primer, a reverse primer, a 6-carboxyfluorescein (FAM) probe as a reporter fluorophore on the 5' end, and an N,N,N',N'-tetramethyl-6-carboxyrhodamine (TAMRA) quencher on the 3' end using published sequences [273]. Each reaction contained 10 µL of 2x concentration TaqMan Universal PCR Master Mix (Applied Biosystems; Foster City, CA), 6.74 µL of DNA-free water, 0.06 µL of probe (at 100 µM concentration), 0.6 µL of forward primer (at 100 µM concentration), 0.6 µL of reverse primer (at 100 µM concentration), and 2 µL of extracted DNA solution to achieve the target concentration of 300 nM for primers and probes. PCRs were carried out at 50°C for 2 minutes, 95°C for 10 minutes, and 40 cycles of 95°C for 15 seconds and 52°C for 60 seconds.

All SYBR PCR analyses contained a forward primer and a reverse primer using published sequences [274]. Each reaction contained 10 µL of 2x concentration SYBR Green Universal PCR Master Mix (Applied Biosystems; Foster City, CA), 6.8 µL of DNA-free water, 0.6 µL of forward primer (at 100 µM concentration), 0.6 µL of reverse primer (at 100 µM concentration), and 2 µL of extracted DNA solution to achieve the target concentration of 300 nM for probes. PCRs were

carried out at 50°C for 2 minutes, 95°C for 15 minutes, and 40 cycles of 94°C for 30 seconds, 50°C for 30 seconds, and 72°C for 30 seconds. After this sequence, a melt curve analysis was performed using the default system settings from 67°C to 95°C.

PCRs were run in batches of 96 reactions including 21 standards/positive controls, 3 negative controls (containing primers, probes, and DNA free water), and 72 reactions containing extracted DNA from experiments. All reactions were performed in triplicate during each batch and the average and one standard deviation of each set of reactions was calculated. Because samples were from laboratory experiments with known conditions, rather than environmental samples, the potential for inhibition was considered minimal. When amplification was measured in negative controls, samples with a cycle threshold (C_T) number within 3 of the lowest C_T number of a negative controls were rejected as false positives. All quantification was performed automatically by the Step One Plus software (Applied Biosystems; Foster City, CA). For PCRs run using SYBR chemistry, the melt temperatures were consistent for each sample run with averages of 81.4 (±0.182), 81.5 (±0.182), 81.6 (±0.292), 81.4 (±0.422), 81.3 (±0.121), and 81.6 (±0.180) for runs 1, 2, 3, 4, 5, and 6, respectively.

Table A.1 qPCR target gene, chemistry, calibration curve parameters, and standard linear range for each analytical run

Run Number	Target Gene	Chemistry	Calibration Curve Slope	Calibration Curve Intercept	Calibration Curve R^2	Gene copies in highest standard	Gene copies in lowest standard
1	*GeoSZ* 16S rRNA	SYBR	-4.002	49.777	0.988	$8.22x10^8$	822
2	*GeoSZ* 16S rRNA	SYBR	-5.769	61.453	0.975	$8.22x10^8$	822
3	*GeoSZ* 16S rRNA	SYBR	-5.182	58.517	0.988	$8.22x10^8$	822
4	*GeoSZ* 16S rRNA	SYBR	-5.248	61.237	0.916	$8.22x10^8$	822
5	*GeoSZ* 16S rRNA	SYBR	-6.386	67.720	0.984	$8.22x10^8$	822
6	*GeoSZ* 16S rRNA	SYBR	-3.851	47.221	0.858	$8.22x10^8$	822
7	*Dhc* 16S rRNA	TaqMan	-3.84	44.548	0.997	$3.38x10^8$	33.8
8	*Dhc* 16S rRNA	TaqMan	-4.074	46.970	0.963	$3.80x10^8$	38
9	*Dhc* 16S rRNA	TaqMan	-4.837	55.069	0.943	$3.80x10^8$	38
10	*Dhc* 16S rRNA	TaqMan	-4.628	53.948	0.949	$3.38x10^8$	338
11	*Dhc* 16S rRNA	TaqMan	-2.843	43.077	0.963	$3.38x10^8$	338

12	*Dhc* 16S rRNA	TaqMan	-2.865	43.341	0.936	$3.38x10^8$	338
13	*Dhc* 16S rRNA	TaqMan	-4.019	46.030	0.985	$3.38x10^8$	338
14	*bvcA* RDase	TaqMan	-3.522	41.487	0.991	$3.38x10^8$	33.8
15	*bvcA* RDase	TaqMan	-4.595	47.880	0.979	$3.80x10^8$	38
16	*bvcA* RDase	TaqMan	-4.858	50.850	0.957	$3.80x10^8$	38
17	*bvcA* RDase	TaqMan	-3.838	44.677	0.998	$3.38x10^8$	338
18	*bvcA* RDase	TaqMan	-3.983	43.623	0.984	$3.38x10^8$	338
19	*bvcA* RDase	TaqMan	-4.313	47.560	0.96	$3.38x10^8$	338
20	*tceA* RDase	TaqMan	-3.339	40.407	0.989	$3.38x10^8$	33.8
21	*tceA* RDase	TaqMan	-4.560	48.173	0.978	$3.80x10^8$	38
22	*tceA* RDase	TaqMan	-4.866	51.469	0.962	$3.38x10^8$	338
23	*tceA* RDase	TaqMan	-3.947	43.954	0.997	$3.38x10^8$	338
24	*tceA* RDase	TaqMan	-3.902	45.438	0.987	$3.38x10^8$	338
25	*tceA* RDase	TaqMan	-4.225	46.748	0.951	$3.38x10^8$	338
26	*vcrA* RDase	TaqMan	-3.570	41.688	0.999	$3.38x10^8$	33.8
27	*vcrA* RDase	TaqMan	-4.652	47.168	0.982	$3.80x10^8$	38
28	*vcrA* RDase	TaqMan	-5.047	53.169	0.968	$3.80x10^8$	38
29	*vcrA* RDase	TaqMan	-3.800	41.050	0.996	$3.38x10^8$	338
30	*vcrA* RDase	TaqMan	-3.891	45.455	0.988	$3.38x10^8$	338
31	*vcrA* RDase	TaqMan	-3.851	45.412	0.942	$3.38x10^8$	338

A.2 Chemical Analytical Methods

Samples for chlorinated ethene and ethene analysis were placed into headspace analysis vials immediately after collection and analyzed within 24-hours. Chlorinated ethene and ethene concentrations were measured using an Agilent 7890B GC system with a DB-625 column and an FID (Agilent Technologies; Santa Clara, CA). Samples were introduced to the GC by a Telemark HT3 headspace autosampler (Teledyne Technologies; Thousand Oaks, CA) using a constant heating program. Chlorinated ethene concentrations in methanol were measured using an Agilent 7890B VC system with a DB-5 column and micro electron capture detector (μECD) (Agilent Technologies; Santa Clara, CA).

Targeted analysis of PFAS was based on a modification of EPA Method 537 that employs large volume injection (LVI). Quantification was achieved using a Waters Xevo TQ-S triple quadrupole mass spectrometer equipped with a Waters Acquity ultra high performance liquid chromatograph (uHPLC). To achieve analyte separation, a Waters BEH C-18 column (1.7 μm dia., 2.1 × 50 mm) was operated at a flow rate of 0.4 mL/min with an eluent gradient consisting of 2 mM ammonium acetate in water or methanol. The mass spectrometer was operated in negative electrospray ionization and multiple reaction monitoring modes. The method is able to detect 40 PFAS, precursors, and C-13 labeled standards with a total run time of approximately 10 min and detection limits ranging from 5 to 20 ng/L. LVI (50 μL) were used to improve sensitivity without the use of solid phase extraction.

The PFAA concentrations measured using this method are provided in **Table A.2** and **Table A.3** for batch reactor and microcosm experiments, respectively. Plots of total PFAA concentrations over time are included as **Figure A.1** and **Figure A.2**. In batch reactor experiments, total and individual PFAA concentrations varied slightly over time, but did not display a consistent upward or downward trend (**Table A.1**, **Figure A.1**). In microcosms, total and individual PFAA concentrations declined initially due to soil sorption, but concentrations then stabilized (**Table A.3**, **Figure A.2**).

VFA and fluoride concentrations were measured by IC using a Dionex ICS-2100 IC system with IonPac AS-18 Fast column (Thermo Scientific; Waltham, MA). Batch reactor and microcosm pH was measured using an Orion 3 Star pH meter with a glass pH probe (Thermo Scientific; Waltham, MA) by placing the probe into a polypropylene centrifuge tube (various manufacturers) containing approximately 3mL of sample. The average pH in batch reactor and microcosm experiments is shown in **Figure A.3**.

Table A.2 PFAS concentrations (mg/L) in batch reactors. For each entry, the average value of 5 batch reactor measurements is shown. The standard deviation is provided in parenthesis and the proportion of total PFAAs by mass for each PFAA is shown as a percentage. PFBA= perfluorobutrycic acid, PFPeA=perfluoropentanoic acid, PFBS=perfluorobutane sulfonic acid, PFHxA=perfluorohexanoic acid, PFHpA= perfluoroheptanoic acid, PFHxS=perfluorohexane sulfonic acid, PFOA=perfluorooctanoic acid, PFNA=perfluorononanoic acid, PFOS= perfluorooctane sulfonic acid, and PFDA=perfluorodecanoic acid.

	PFBA	PFPeA	PFBS	PFHxA	PFHpA	PFHxS	PFOA	PFNA	PFOS	PFDA	Total
11.7 mg/L total PFAA batch reactors											
Initial	0.90 (±0.03)	1.88 (±0.08)	0.40 (±0.25)	0.93 (±0.64)	0.81 (±0.04)	2.20 (±0.10)	1.16 (±0.04)	0.45 (±0.02)	2.54 (±0.10)	0.37 (±0.04)	11.7 (±0.57)
	8%	16%	3%	8%	7%	19%	10%	4%	22%	3%	
Day 2	0.71 (±0.09)	1.79 (±0.06)	0.35 (±0.32)	1.11 (±0.47)	0.76 (±0.03)	2.18 (±0.18)	1.13 (±0.04)	0.40 (±0.01)	2.61 (±0.16)	0.39 (±0.03)	11.4 (±0.57)
	6%	16%	3%	10%	7%	19%	10%	4%	23%	3%	
Day 9	0.58 (±0.13)	1.83 (±0.06)	0.63 (±0.31)	0.97 (±0.60)	0.79 (±0.03)	2.07 (±0.21)	1.12 (±0.04)	0.44 (±0.03)	2.45 (±0.28)	0.36 (±0.05)	11.2 (±1.19)
	5%	16%	6%	9%	7%	18%	10%	4%	22%	3%	
Day 19	0.71 (±0.04)	1.83 (±0.06)	0.63 (±0.28)	1.11 (±0.51)	0.75 (±0.06)	2.12 (±0.20)	1.13 (±0.05)	0.47 (±0.05)	2.27 (±0.34)	0.37 (±0.00)	11.4 (±0.87)
	6%	16%	6%	10%	7%	19%	10%	4%	20%	3%	
Final	0.60 (±0.21)	1.85 (±0.07)	0.68 (±0.19)	1.08 (±0.51)	0.76 (±0.06)	2.02 (±0.17)	1.13 (±0.05)	0.46 (±0.03)	2.44 (±0.24)	0.36 (±0.01)	11.4 (±1.00)
	7%	15%	6%	11%	6%	18%	9%	4%	21%	3%	7%
26.5 mg/L total PFAA batch reactors											
Initial	1.82 (±0.24)	3.98 (±0.53)	1.00 (±0.88)	3.16 (±0.54)	1.65 (±0.23)	4.73 (±0.60)	2.48 (±0.34)	0.94 (±0.09)	5.74 (±0.84)	0.64 (±0.13)	26.5 (±4.05)
	7%	15%	4%	12%	6%	18%	9%	4%	22%	2%	7%
Day 2	1.51 (±0.03)	3.58 (±0.09)	1.13 (±0.81)	2.91 (±0.11)	1.56 (±0.10)	4.28 (±0.18)	2.25 (±0.00)	0.82 (±0.02)	5.36 (±0.21)	0.62 (±0.06)	22.9 (±0.86)
	7%	16%	5%	13%	7%	19%	10%	4%	23%	3%	
Day 9	1.52 (±0.22)	3.73 (±0.10)	1.57 (±0.23)	2.90 (±0.21)	1.52 (±0.06)	4.44 (±0.17)	2.27 (±0.05)	0.91 (±0.04)	5.39 (±0.34)	0.57 (±0.04)	24.8 (±0.56)
	6%	15%	6%	12%	6%	18%	9%	4%	22%	2%	

	PFBA	PFPeA	PFBS	PFHxA	PFHpA	PFHxS	PFOA	PFNA	PFOS	PFDA	Total
Day 19	1.55 (±0.07)	3.71 (±0.07)	1.63 (±0.25)	2.91 (±0.22)	1.54 (±0.07)	4.42 (±0.11)	2.29 (±0.05)	0.94 (±0.04)	5.31 (±0.34)	0.61 (±0.05)	24.9 (±0.62)
	6%	15%	7%	12%	6%	18%	9%	4%	21%	2%	
Final	1.66 (±0.06)	3.78 (±0.07)	1.57 (±0.22)	2.66 (±0.70)	1.51 (±0.04)	4.52 (±0.10)	2.30 (±0.05)	0.96 (±0.04)	5.36 (±0.16)	0.62 (±0.05)	24.9 (±0.74)
	7%	15%	6%	11%	6%	18%	9%	4%	21%	3%	
49.8 mg/L total PFAA batch reactors											
Initial	3.45 (±0.11)	7.48 (±0.13)	3.32 (±0.04)	5.18 (±1.86)	3.06 (±0.11)	8.72 (±0.03)	4.57 (±0.10)	1.77 (±0.07)	11.0 (±0.73)	1.17 (±0.05)	49.8 (±2.26)
	7%	15%	7%	10%	6%	18%	9%	4%	22%	2%	
Day 2	2.88 (±0.16)	7.30 (±0.23)	2.95 (±1.02)	5.62 (±1.34)	3.14 (±0.13)	9.05 (±0.45)	4.60 (±0.12)	1.64 (±0.08)	11.2 (±0.28)	1.16 (±0.16)	49.5 (±2.05)
	6%	15%	6%	11%	6%	18%	9%	3%	23%	2%	
Day 9	3.41 (±0.09)	7.64 (±0.13)	3.41 (±0.04)	5.90 (±0.33)	3.10 (±0.08)	8.95 (±0.61)	4.63 (±0.09)	1.73 (±0.04)	11.5 (±0.37)	1.09 (±0.04)	51.4 (±1.38)
	7%	15%	7%	11%	6%	17%	9%	3%	22%	2%	7%
Day 19	3.34 (±0.15)	7.54 (±0.11)	3.40 (±0.04)	6.11 (±0.36)	3.14 (±0.10)	9.06 (±0.14)	4.59 (±0.04)	1.74 (±0.07)	11.5 (±0.36)	1.12 (±0.10)	51.6 (±0.94)
	6%	15%	7%	12%	6%	18%	9%	3%	22%	2%	
Final	3.71 (±0.10)	7.77 (±0.07)	3.22 (±0.30)	6.10 (±0.08)	3.16 (±0.08)	9.21 (±0.28)	4.67 (±0.07)	1.90 (±0.03)	11.4 (±0.50)	1.14 (±0.09)	52.3 (±0.60)
	7%	15%	6%	12%	6%	18%	9%	4%	22%	2%	
61.7 mg/L total PFAA batch reactors											
Initial	3.90 (±0.13)	8.93 (±0.14)	4.21 (±0.09)	7.43 (±0.25)	3.65 (±0.09)	10.6 (±0.35)	5.53 (±0.07)	2.14 (±0.02)	13.7 (±0.42)	1.45 (±0.06)	61.7 (±1.15)
	6%	14%	7%	12%	6%	17%	9%	3%	22%	2%	
Day 2	3.42 (±0.08)	8.64 (±0.24)	4.19 (±0.13)	7.23 (±0.28)	3.65 (±0.17)	10.6 (±0.41)	5.47 (±0.15)	1.93 (±0.11)	13.8 (±0.65)	1.49 (±0.14)	60.5 (±1.98)
	6%	14%	7%	12%	6%	18%	9%	3%	23%	2%	
Day 9	4.03 (±0.49)	9.14 (±0.18)	4.18 (±0.07)	7.29 (±0.23)	3.72 (±0.11)	10.7 (±0.33)	5.51 (±0.11)	2.13 (±0.08)	13.5 (±0.59)	1.27 (±0.11)	61.5 (±1.11)
	7%	15%	7%	12%	6%	17%	9%	3%	22%	2%	
Day 19	4.3 (±0.11)	9.22 (±0.12)	3.76 (±0.89)	7.33 (±0.21)	3.81 (±0.13)	10.9 (±0.09)	5.57 (±0.06)	2.11 (±0.13)	13.9 (±0.6)	1.42 (±0.15)	62.4 (±1.31)
	7%	15%	6%	12%	6%	18%	9%	3%	22%	2%	

	PFBA	PFPeA	PFBS	PFHxA	PFHpA	PFHxS	PFOA	PFNA	PFOS	PFDA	Total
Final	5.78 (±0.51)	9.99 (±0.28)	4.17 (±0.09)	7.32 (±0.3)	3.85 (±0.18)	11.4 (±0.17)	5.81 (±0.13)	2.95 (±0.18)	13.7 (±0.82)	1.38 (±0.12)	66.5 (±2.13)
	9%	15%	6%	11%	6%	17%	9%	4%	21%	2%	9%
101 mg/L total PFAA batch reactors											
Initial	6.44 (±0.18)	14.4 (±0.16)	7.23 (±0.15)	11.7 (±0.33)	5.93 (±0.19)	17.1 (±0.13)	8.98 (±0.04)	3.29 (±0.1)	23.5 (±1.07)	2.26 (±0.12)	101 (±1.03)
	6%	14%	7%	12%	6%	17%	9%	3%	23%	2%	
Day 2	5.38 (±0.12)	13.9 (±0.08)	7.01 (±0.17)	11.9 (±0.15)	5.93 (±0.12)	17.0 (±0.49)	8.77 (±0.13)	3.05 (±0.07)	24.2 (±0.67)	2.34 (±0.18)	99.7 (±1.58)
	5%	14%	7%	12%	6%	17%	9%	3%	24%	2%	
Day 9	7.3 (±0.17)	15.2 (±0.19)	7.13 (±0.1)	11.9 (±0.24)	6.18 (±0.1)	17.8 (±0.37)	9.14 (±0.13)	3.53 (±0.12)	23.8 (±0.94)	2.08 (±0.17)	104 (±1.64)
	7%	15%	7%	11%	6%	17%	9%	3%	23%	2%	
Day 19	7.33 (±0.16)	15.1 (±0.16)	7.22 (±0.1)	11.0 (±2.2)	6.18 (±0.09)	18.5 (±0.39)	9.25 (±0.06)	3.53 (±0.19)	24.9 (±0.7)	2.29 (±0.14)	105 (±1.61)
	7%	14%	7%	11%	6%	18%	9%	3%	24%	2%	
Final	10.0 (±0.62)	16.5 (±0.21)	7.13 (±0.13)	12.0 (±0.16)	6.23 (±0.15)	17.9 (±0.1)	9.55 (±0.13)	4.91 (±0.26)	23.6 (±0.88)	2.16 (±0.2)	110 (±1.57)
	9%	15%	6%	11%	6%	16%	9%	4%	21%	2%	
61.7 mg/L total PFAA batch reactors											
Initial	3.90 (±0.13)	8.93 (±0.14)	4.21 (±0.09)	7.43 (±0.25)	3.65 (±0.09)	10.6 (±0.35)	5.53 (±0.07)	2.14 (±0.02)	13.7 (±0.42)	1.45 (±0.06)	61.7 (±1.15)
	6%	14%	7%	12%	6%	17%	9%	3%	22%	2%	
Day 2	3.42 (±0.08)	8.64 (±0.24)	4.19 (±0.13)	7.23 (±0.28)	3.65 (±0.17)	10.6 (±0.41)	5.47 (±0.15)	1.93 (±0.11)	13.8 (±0.65)	1.49 (±0.14)	60.5 (±1.98)
	6%	14%	7%	12%	6%	18%	9%	3%	23%	2%	
Day 9	4.03 (±0.49)	9.14 (±0.18)	4.18 (±0.07)	7.29 (±0.23)	3.72 (±0.11)	10.7 (±0.33)	5.51 (±0.11)	2.13 (±0.08)	13.5 (±0.59)	1.27 (±0.11)	61.5 (±1.11)
	7%	15%	7%	12%	6%	17%	9%	3%	22%	2%	
Day 19	4.3 (±0.11)	9.22 (±0.12)	3.76 (±0.89)	7.33 (±0.21)	3.81 (±0.13)	10.9 (±0.09)	5.57 (±0.06)	2.11 (±0.13)	13.9 (±0.6)	1.42 (±0.15)	62.4 (±1.31)
	7%	15%	6%	12%	6%	18%	9%	3%	22%	2%	
Final	5.78 (±0.51)	9.99 (±0.28)	4.17 (±0.09)	7.32 (±0.3)	3.85 (±0.18)	11.4 (±0.17)	5.81 (±0.13)	2.95 (±0.18)	13.7 (±0.82)	1.38 (±0.12)	66.5 (±2.13)
	9%	15%	6%	11%	6%	17%	9%	4%	21%	2%	9%

	PFBA	PFPeA	PFBS	PFHxA	PFHpA	PFHxS	PFOA	PFNA	PFOS	PFDA	Total
101 mg/L total PFAA batch reactors											
Initial	6.44 (±0.18)	14.4 (±0.16)	7.23 (±0.15)	11.7 (±0.33)	5.93 (±0.19)	17.1 (±0.13)	8.98 (±0.04)	3.29 (±0.1)	23.5 (±1.07)	2.26 (±0.12)	101 (±1.03)
	6%	14%	7%	12%	6%	17%	9%	3%	23%	2%	
Day 2	5.38 (±0.12)	13.9 (±0.08)	7.01 (±0.17)	11.9 (±0.15)	5.93 (±0.12)	17.0 (±0.49)	8.77 (±0.13)	3.05 (±0.07)	24.2 (±0.67)	2.34 (±0.18)	99.7 (±1.58)
	5%	14%	7%	12%	6%	17%	9%	3%	24%	2%	
Day 9	7.3 (±0.17)	15.2 (±0.19)	7.13 (±0.1)	11.9 (±0.24)	6.18 (±0.1)	17.8 (±0.37)	9.14 (±0.13)	3.53 (±0.12)	23.8 (±0.94)	2.08 (±0.17)	104 (±1.64)
	7%	15%	7%	11%	6%	17%	9%	3%	23%	2%	
Day 19	7.33 (±0.16)	15.1 (±0.16)	7.22 (±0.1)	11.0 (±2.2)	6.18 (±0.09)	18.5 (±0.39)	9.25 (±0.06)	3.53 (±0.19)	24.9 (±0.7)	2.29 (±0.14)	105 (±1.61)
	7%	14%	7%	11%	6%	18%	9%	3%	24%	2%	
Final	10.0 (±0.62)	16.5 (±0.21)	7.13 (±0.13)	12.0 (±0.16)	6.23 (±0.15)	17.9 (±0.1)	9.55 (±0.13)	4.91 (±0.26)	23.6 (±0.88)	2.16 (±0.2)	110 (±1.57)
	9%	15%	6%	11%	6%	16%	9%	4%	21%	2%	

Table A.3 Initial and final PFAS concentrations (mg/L) in microcosms. For each entry, the average value of 5 microcosm measurements is shown. The standard deviation is provided in parenthesis and the proportion of total PFAAs by mass for each PFAA is shown as a percentage. PFBA=perfluorobutrycic acid, PFPeA=perfluoropentanoic acid, PFBS=perfluorobutane sulfonic acid, PFHxA=perfluorohexanoic acid, PFHpA= perfluoroheptanoic acid, PFHxS=perfluorohexane sulfonic acid, PFOA=perfluorooctanoic acid, PFNA=perfluorononanoic acid, PFOS= perfluorooctane sulfonic acid, and PFDA=perfluorodecanoic acid.

	PFBA	PFPeA	PFBS	PFHxA	PFHpA	PFHxS	PFOA	PFNA	PFOS	PFDA	Total
9.25 mg/L total PFAA (final) microcosms											
Initial	1.35 (±0.18)	2.32 (±0.18)	0.53 (±0.08)	2.36 (±0.17)	0.74 (±0.09)	1.72 (±0.16)	1.05 (±0.08)	0.47 (±0.13)	1.66 (±0.35)	0.13 (±0.01)	12.3 (±1.06)
	11%	19%	4%	19%	6%	14%	9%	4%	13%	1%	
Day 4	1.1 (±0.15)	2.12 (±0.14)	0.59 (±0.05)	2.39 (±0.25)	0.78 (±0.05)	1.83 (±0.21)	1.03 (±0.07)	0.81 (±0.54)	1.78 (±0.42)	0.15 (±0.04)	12.6 (±0.74)
	9%	17%	5%	19%	6%	15%	8%	6%	14%	1%	
Day 12	0.14 (±0.1)	1.27 (±0.18)	0.42 (±0.06)	2.16 (±0.16)	0.62 (±0.07)	1.69 (±0.15)	0.79 (±0.06)	0.35 (±0.05)	1.09 (±0.27)	0.09 (±0.01)	8.63 (±0.89)
	2%	15%	5%	25%	7%	20%	9%	4%	13%	1%	
Day 21	0.04 (±0.05)	1.35 (±0.1)	0.37 (±0.05)	2.07 (±0.32)	0.66 (±0.06)	1.62 (±0.18)	0.9 (±0.05)	0.47 (±0.09)	1.2 (±0.33)	0.1 (±0.02)	8.77 (±0.61)
	0%	15%	4%	24%	8%	18%	10%	5%	14%	1%	
Day 28	1.49 (±0.31)	2.06 (±0.14)	0.41 (±0.03)	1.87 (±0.17)	0.71 (±0.06)	1.78 (±0.16)	0.93 (±0.07)	0.46 (±0.1)	1.43 (±0.2)	0.08 (±0.04)	11.2 (±0.82)
	13%	18%	4%	17%	6%	16%	8%	4%	13%	1%	
Day 37	0.62 (±0.13)	1.56 (±0.17)	0.23 (±0.18)	1.87 (±0.57)	0.75 (±0.07)	1.54 (±0.13)	0.79 (±0.07)	0.63 (±0.1)	0.89 (±0.13)	0.04 (±0.02)	8.92 (±1.14)
	7%	18%	3%	21%	8%	17%	9%	7%	10%	0%	
Day 57	0.71 (±0.14)	1.88 (±0.14)	0.41 (±0.07)	2.18 (±0.18)	0.77 (±0.06)	1.53 (±0.1)	0.87 (±0.06)	0.15 (±0.19)	1.21 (±0.08)	0.09 (±0.01)	9.81 (±0.46)
	7%	19%	4%	22%	8%	16%	9%	2%	12%	1%	
Day 79	0.84 (±0.12)	1.84 (±0.15)	0.52 (±0.03)	2.06 (±0.29)	0.78 (±0.06)	1.76 (±0.2)	0.89 (±0.07)	0.1 (±0.1)	1.21 (±0.13)	0.1 (±0.02)	10.1 (±0.87)
	8%	18%	5%	20%	8%	17%	9%	1%	12%	1%	
Day 100	0.44 (±0.07)	0.92 (±0.06)	0.26 (±0.01)	0.87 (±0.17)	0.28 (±0.03)	0.83 (±0.06)	0.38 (±0.02)	0.09 (±0.07)	0.49 (±0.03)	0.06 (±0.01)	4.61 (±0.32)
	10%	20%	6%	19%	6%	18%	8%	2%	11%	1%	

	PFBA	PFPeA	PFBS	PFHxA	PFHpA	PFHxS	PFOA	PFNA	PFOS	PFDA	Total
Day 124	1.02 (±0.57)	1.28 (±0.55)	0.33 (±0.14)	1.13 (±0.48)	0.41 (±0.16)	0.99 (±0.39)	0.58 (±0.23)	0.24 (±0.1)	0.84 (±0.25)	0.04 (±0.02)	6.86 (±2.84)
	15%	19%	5%	16%	6%	14%	8%	3%	12%	1%	
Final	0.97 (±0.08)	1.79 (±0.11)	0.45 (±0.06)	1.79 (±0.13)	0.62 (±0.04)	1.33 (±0.07)	0.85 (±0.05)	0.3 (±0.05)	1.11 (±0.14)	0.05 (±0.02)	9.25 (±0.64)
	10%	19%	5%	19%	7%	14%	9%	3%	12%	1%	100%
19.4 mg/L total PFAA (final) microcosms											
Initial	2.59 (±0.43)	4.86 (±0.21)	1.12 (±0.14)	4.95 (±0.32)	1.62 (±0.08)	3.51 (±0.15)	2.26 (±0.1)	0.8 (±0.17)	3.95 (±0.61)	0.33 (±0.04)	26 (±1.67)
	10%	19%	4%	19%	6%	14%	9%	3%	15%	1%	
Day 4	2.29 (±0.24)	4.51 (±0.24)	1.18 (±0.09)	4.95 (±0.17)	1.57 (±0.08)	3.79 (±0.29)	2.19 (±0.15)	0.64 (±0.23)	3.49 (±0.37)	0.29 (±0.03)	24.9 (±0.92)
	9%	18%	5%	20%	6%	15%	9%	3%	14%	1%	
Day 12	1.05 (±0.18)	3.13 (±0.17)	1.04 (±0.06)	4.44 (±0.1)	1.49 (±0.03)	3.35 (±0.13)	1.91 (±0.06)	0.43 (±0.02)	3.11 (±0.23)	0.27 (±0.07)	20.2 (±0.87)
	5%	16%	5%	22%	7%	17%	10%	2%	16%	1%	
Day 21	0.76 (±0.12)	3.03 (±0.11)	1 (±0.04)	4.51 (±0.09)	1.4 (±0.05)	3.49 (±0.12)	1.9 (±0.05)	0.67 (±0.12)	2.56 (±0.44)	0.18 (±0.04)	19.5 (±0.72)
	4%	16%	5%	23%	7%	18%	10%	3%	13%	1%	
Day 28	2.04 (±0.27)	4.07 (±0.16)	1.01 (±0.07)	4.15 (±0.33)	1.48 (±0.09)	3.59 (±0.26)	1.93 (±0.04)	0.96 (±0.17)	2.9 (±0.34)	0.21 (±0.02)	22.4 (±0.65)
	9%	18%	5%	19%	7%	16%	9%	4%	13%	1%	
Day 37	1.49 (±0.25)	3.24 (±0.45)	0.98 (±0.13)	3.98 (±0.61)	1.37 (±0.17)	2.96 (±0.42)	1.69 (±0.23)	0.78 (±0.15)	2.12 (±0.55)	0.11 (±0.09)	18.7 (±2.88)
	8%	17%	5%	21%	7%	16%	9%	4%	11%	1%	
19.4 mg/L total PFAA (final) microcosms continued											
Day 57	1.64 (±0.12)	3.72 (±0.06)	0.94 (±0.05)	4.21 (±0.04)	1.47 (±0.09)	3.16 (±0.17)	1.76 (±0.06)	0.76 (±0.16)	2.46 (±0.31)	0.21 (±0.02)	20.3 (±0.61)
	8%	18%	5%	21%	7%	16%	9%	4%	12%	1%	
Day 79	1.82 (±0.21)	3.61 (±0.15)	1.01 (±0.05)	4.37 (±0.11)	1.48 (±0.05)	3.56 (±0.07)	1.88 (±0.05)	0.48 (±0.21)	2.67 (±0.23)	0.18 (±0.02)	21.1 (±0.48)
	9%	17%	5%	21%	7%	17%	9%	2%	13%	1%	
Day 100	1.27 (±0.09)	1.93 (±0.01)	0.51 (±0.02)	1.82 (±0.05)	0.6 (±0.01)	1.56 (±0.03)	0.82 (±0.03)	0.27 (±0.05)	1.12 (±0.14)	0.11 (±0.02)	10 (±0.28)
	13%	19%	5%	18%	6%	16%	8%	3%	11%	1%	
Day 124	2.9 (±0.12)	3.94 (±0.11)	0.97 (±0.05)	3.54 (±0.17)	1.24 (±0.02)	2.89 (±0.14)	1.79 (±0.06)	0.79 (±0.04)	2.35 (±0.13)	0.11 (±0.01)	20.5 (±0.57)

	PFBA	PFPeA	PFBS	PFHxA	PFHpA	PFHxS	PFOA	PFNA	PFOS	PFDA	Total
	14%	19%	5%	17%	6%	14%	9%	4%	11%	1%	
Final	2.14 (±0.09)	3.64 (±0.05)	0.95 (±0.04)	3.63 (±0.12)	1.3 (±0.04)	2.83 (±0.16)	1.75 (±0.04)	0.68 (±0.06)	2.35 (±0.27)	0.13 (±0.04)	19.4 (±0.63)
	11%	19%	5%	19%	7%	15%	9%	4%	12%	1%	
38.7 mg/L total PFAA (final) microcosms											
Initial	5.41 (±0.26)	9.58 (±0.25)	2.45 (±0.12)	10.12 (±0.18)	3.42 (±0.12)	7.66 (±0.34)	4.61 (±0.06)	1.7 (±0.15)	8 (±0.58)	0.67 (±0.03)	53.6 (±0.83)
	10%	18%	5%	19%	6%	14%	9%	3%	15%	1%	
Day 4	4.58 (±0.24)	8.46 (±0.22)	2.43 (±0.09)	9.87 (±0.12)	3.28 (±0.12)	7.9 (±0.66)	4.28 (±0.08)	1.14 (±0.22)	7.47 (±0.19)	0.65 (±0.05)	50.1 (±1.3)
	9%	17%	5%	20%	7%	16%	9%	2%	15%	1%	
Day 12	2.82 (±0.15)	6.6 (±0.14)	2.33 (±0.04)	9.16 (±0.23)	3.01 (±0.05)	7.69 (±0.25)	3.88 (±0.11)	0.79 (±0.19)	6.32 (±0.32)	0.45 (±0.06)	43 (±0.64)
	7%	15%	5%	21%	7%	18%	9%	2%	15%	1%	
Day 21	2.33 (±0.17)	5.75 (±0.14)	2.17 (±0.08)	8.89 (±0.24)	2.85 (±0.1)	7.5 (±0.4)	3.82 (±0.07)	1.01 (±0.12)	6.16 (±0.22)	0.42 (±0.05)	40.9 (±0.8)
	6%	14%	5%	22%	7%	18%	9%	2%	15%	1%	
Day 28	3.8 (±0.13)	7.92 (±0.16)	2.26 (±0.07)	8.54 (±0.3)	3.02 (±0.14)	6.99 (±0.51)	3.98 (±0.03)	1.59 (±0.27)	5.72 (±0.35)	0.46 (±0.06)	44.3 (±1.2)
	9%	18%	5%	19%	7%	16%	9%	4%	13%	1%	
Day 37	3.39 (±0.14)	7.04 (±0.23)	2.1 (±0.05)	8.46 (±0.11)	2.86 (±0.08)	6.31 (±0.11)	3.64 (±0.08)	1.49 (±0.1)	4.93 (±0.53)	0.32 (±0.02)	40.5 (±0.62)
	8%	17%	5%	21%	7%	16%	9%	4%	12%	1%	
Day 57	3.3 (±0.23)	7.39 (±0.19)	2.07 (±0.05)	8.41 (±0.08)	2.93 (±0.08)	6.2 (±0.19)	3.65 (±0.1)	1.22 (±0.22)	4.98 (±0.31)	0.4 (±0.04)	40.5 (±0.56)
	8%	18%	5%	21%	7%	15%	9%	3%	12%	1%	
Day 79	3.63 (±0.36)	7.2 (±0.19)	2.2 (±0.06)	9.07 (±0.31)	2.97 (±0.05)	6.96 (±0.25)	3.85 (±0.08)	1.02 (±0.25)	5.2 (±0.16)	0.42 (±0.04)	42.5 (±0.82)
	9%	17%	5%	21%	7%	16%	9%	2%	12%	1%	
Day 100	3.04 (±0.2)	3.94 (±0.05)	1.01 (±0.04)	3.6 (±0.05)	1.28 (±0.03)	3.07 (±0.1)	1.71 (±0.02)	0.73 (±0.14)	2.11 (±0.13)	0.18 (±0.02)	20.7 (±0.52)
	15%	19%	5%	17%	6%	15%	8%	4%	10%	1%	
Day 124	5.24 (±0.13)	7.74 (±0.11)	2.03 (±0.05)	7.3 (±0.11)	2.48 (±0.06)	5.94 (±0.17)	3.52 (±0.08)	1.61 (±0.06)	4.57 (±0.32)	0.29 (±0.06)	40.7 (±0.57)
	13%	19%	5%	18%	6%	15%	9%	4%	11%	1%	
Final	4.2 (±0.07)	7.32 (±0.04)	1.97 (±0.05)	7.28 (±0.11)	2.55 (±0.04)	5.69 (±0.38)	3.51 (±0.03)	1.36 (±0.05)	4.51 (±0.29)	0.29 (±0.06)	38.7 (±0.6)

	PFBA	PFPeA	PFBS	PFHxA	PFHpA	PFHxS	PFOA	PFNA	PFOS	PFDA	Total
	11%	19%	5%	19%	7%	15%	9%	4%	12%	1%	
91.3 mg/L total PFAA (final) microcosms											
Initial	11.89 (±0.49)	20.31 (±0.41)	5.28 (±0.11)	21.43 (±0.52)	7.13 (±0.17)	16.54 (±0.51)	9.91 (±0.22)	3.81 (±0.25)	21.86 (±0.76)	1.75 (±0.12)	120 (±1.63)
	10%	17%	4%	18%	6%	14%	8%	3%	18%	1%	
Day 4	10.14 (±0.71)	18.11 (±0.35)	5.51 (±0.23)	21.03 (±0.26)	7.14 (±0.19)	17.14 (±0.48)	9.37 (±0.14)	2.38 (±0.3)	20.34 (±0.97)	1.51 (±0.18)	112.7 (±1.69)
	9%	16%	5%	19%	6%	15%	8%	2%	18%	1%	
Day 12	6.87 (±0.37)	14.73 (±0.46)	5.07 (±0.16)	19.23 (±0.22)	6.33 (±0.1)	16.33 (±0.2)	8.35 (±0.21)	2.04 (±0.27)	15.78 (±0.98)	1.12 (±0.08)	95.9 (±1.02)
	7%	15%	5%	20%	7%	17%	9%	2%	16%	1%	
Day 21	5.72 (±0.12)	12.53 (±0.22)	5.02 (±0.19)	19.17 (±0.32)	6.22 (±0.08)	15.42 (±0.34)	8.27 (±0.09)	1.84 (±0.16)	14.29 (±0.68)	1.02 (±0.05)	89.5 (±1.33)
	6%	14%	6%	21%	7%	17%	9%	2%	16%	1%	
Day 28	8.13 (±0.55)	16.77 (±0.26)	4.93 (±0.05)	17.94 (±0.32)	6.25 (±0.15)	14.86 (±0.16)	8.44 (±0.17)	3.37 (±0.32)	14.5 (±0.97)	0.97 (±0.12)	96.2 (±2.12)
	8%	17%	5%	19%	6%	15%	9%	4%	15%	1%	
Day 37	7.34 (±0.34)	15.05 (±0.34)	4.59 (±0.09)	17.98 (±0.27)	5.97 (±0.18)	14.01 (±0.29)	7.89 (±0.21)	2.42 (±0.21)	11.56 (±0.34)	0.73 (±0.07)	87.5 (±1.49)
	8%	17%	5%	21%	7%	16%	9%	3%	13%	1%	
Day 57	7.43 (±0.25)	15.66 (±0.19)	4.58 (±0.11)	18.03 (±0.45)	6.11 (±0.25)	13.76 (±0.27)	7.79 (±0.21)	3.07 (±0.45)	12.09 (±0.86)	0.89 (±0.05)	89.4 (±1.27)
	8%	18%	5%	20%	7%	15%	9%	3%	14%	1%	
Day 79	7.8 (±0.66)	15.22 (±0.44)	4.84 (±0.17)	18.97 (±0.43)	6.11 (±0.08)	14.88 (±0.48)	8.14 (±0.22)	2.38 (±0.16)	13.54 (±0.95)	0.88 (±0.12)	92.8 (±2.25)
	8%	16%	5%	20%	7%	16%	9%	3%	15%	1%	
Day 100	6.7 (±0.19)	8.37 (±0.07)	2.06 (±0.07)	7.6 (±0.11)	2.76 (±0.03)	6.58 (±0.13)	3.72 (±0.07)	1.77 (±0.19)	5.76 (±0.63)	0.39 (±0.05)	45.7 (±1.04)
	15%	18%	5%	17%	6%	14%	8%	4%	13%	1%	
Day 124	11.37 (±0.44)	16.65 (±0.52)	4.43 (±0.2)	15.98 (±0.46)	5.49 (±0.21)	13.21 (±0.36)	7.79 (±0.27)	3.53 (±0.22)	12.15 (±0.62)	0.71 (±0.07)	91.3 (±2.89)
	12%	18%	5%	18%	6%	14%	9%	4%	13%	1%	
Final	1.02 (±0.57)	1.28 (±0.55)	0.33 (±0.14)	1.13 (±0.48)	0.41 (±0.16)	0.99 (±0.39)	0.58 (±0.23)	0.24 (±0.1)	0.84 (±0.25)	0.04 (±0.02)	6.86 (±2.84)
	15%	19%	5%	16%	6%	14%	8%	3%	12%	1%	

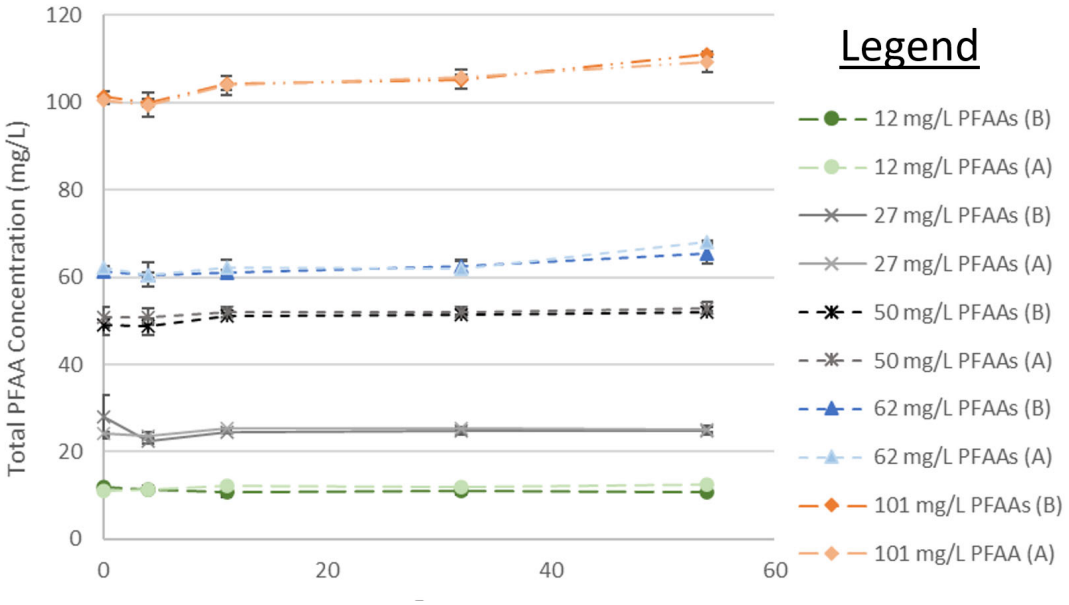


Figure A.1 Total PFAA concentration in batch reactors over time. Batch reactor sets are grouped by color and labeled based on the average total PFAA concentration. For each PFAA concentration set, the average PFAA concentrations are plotted for bioaugmented batch reactors (B) and abiotic, sterilized batch reactors (A). One standard deviation is represented with error bars.

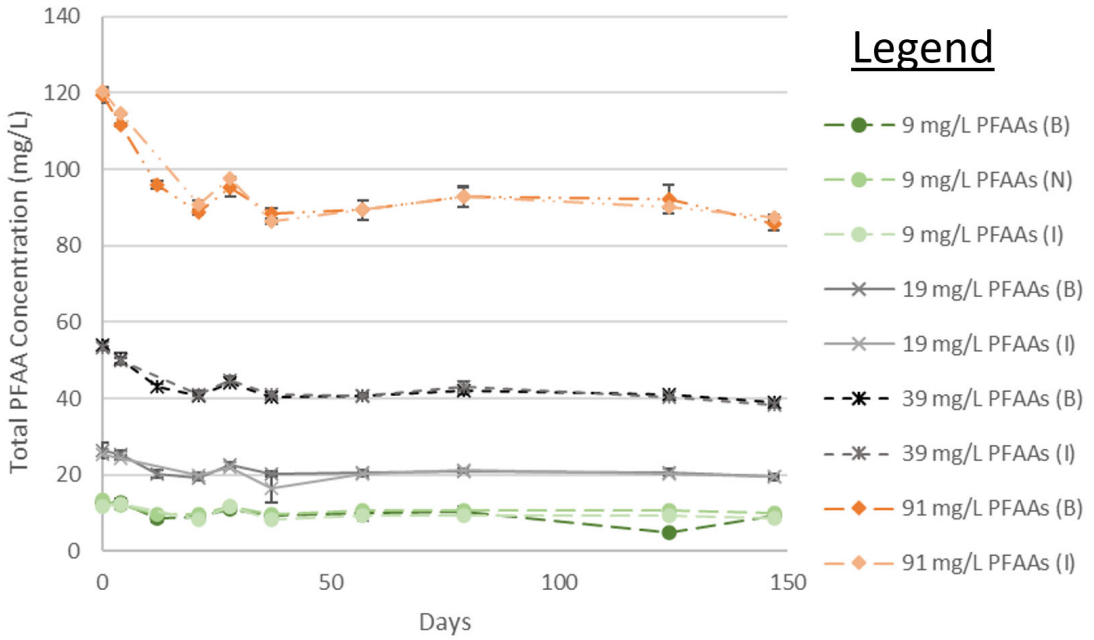


Figure A.2 Total PFAA concentration in microcosms over time. Microcosm sets are grouped by color and labeled based on the average total PFAA concentration at the end of the experiments. For each final PFAA concentration set, the average PFAA concentrations are plotted for bioaugmented microcosms (B), non-bioaugmented microcosms (N), and microcosms inhibited by the addition of sodium azide (I). One standard deviation is represented with error bars.

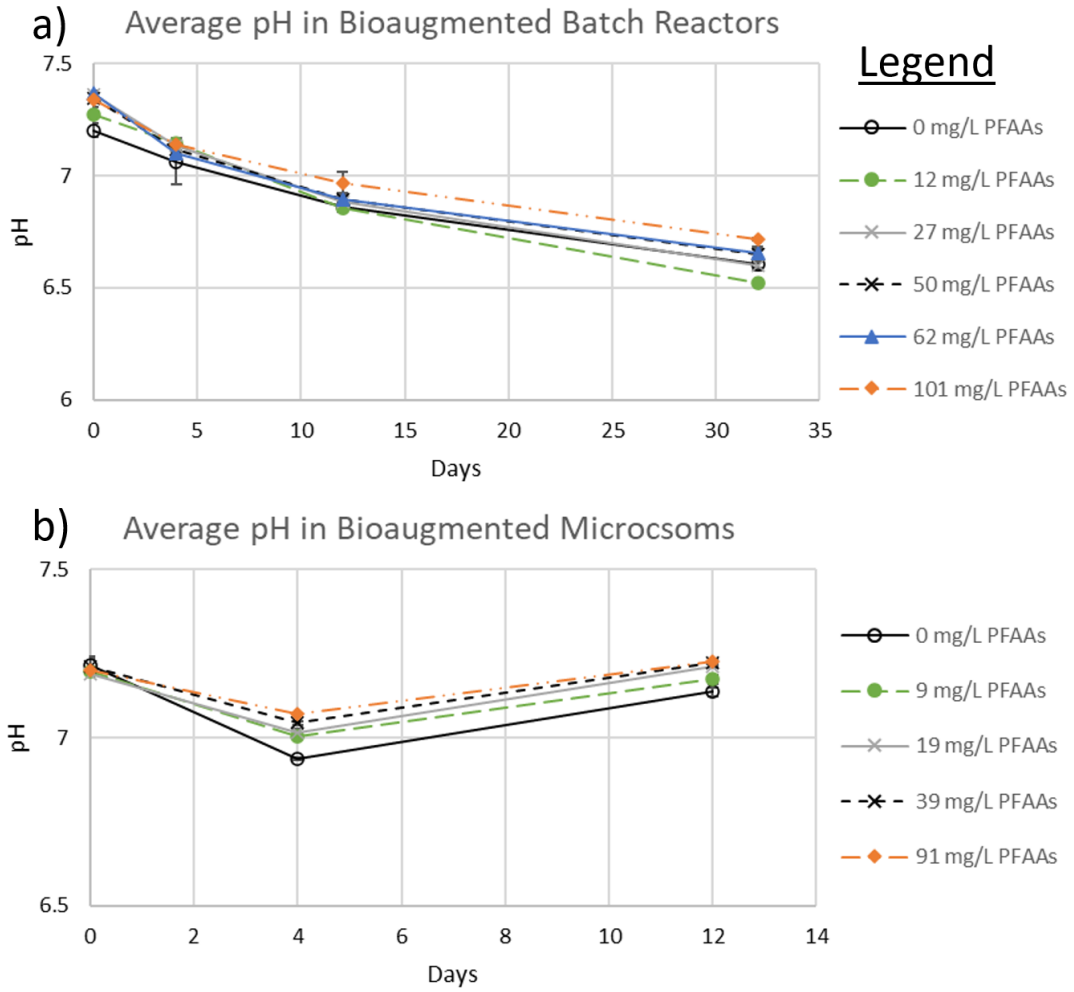


Figure A.3 Average pH in bioaugmented **a)** batch reactor and **b)** microcosm experiments over time. The average of three measurements are plotted and one standard deviation is represented by vertical error bars.

A.3 Mathematical Modeling of Biodegradation

Each overall MRD reaction rate R_i^b in **equation 3.1** is the sum of the individual reductive dechlorination rates that increase or decrease its aqueous concentration. That is, $R_{\text{PCE}}^b = -r_{\text{PCE}}$, $R_{\text{TCE}}^b = r_{\text{PCE}} - r_{\text{TCE}}$, $R_{\text{DCE}}^b = r_{\text{TCE}} - r_{\text{DCE}}$, $R_{\text{VC}}^b = r_{\text{DCE}} - r_{\text{VC}}$, and $R_{\text{ethene}}^b = r_{\text{VC}}$. When electron donor is in excess, as in the experiments modeled, the individual reductive dechlorination rates [M/L^3/T] are determined by the following Monod kinetics expression:

$$r_i = \frac{k_{\max,i} X_j^a C_i^a}{K_{s,i} + C_i^a} \qquad \textbf{(A.1)}$$

where $k_{\max,i}$ is the maximum substrate utilization rate [M/T/cell], X_j^a is the biomass concentration [cell/L^3] of the microbe j that mediates the dechlorination, and $K_{s,i}$ is the half-saturation constant [M/L^3].

Under Monod kinetics the biomass concentration of dechlorinating microbe j changes according to:

$$\frac{d}{dt}\left(X_j^a\right) = \sum_i (Y_i r_i) - k_j^b X_j^a \qquad \textbf{(A.2)}$$

where the summation is over all chlorinated ethenes that microbe j reductively dechlorinates, Y_i is the yield coefficient[cell/M], and k_j^b is the endogenous decay constant [T^{-1}]. Originally adapted from the enzyme literature, Monod kinetics is an empirical model that describes the rate of MRD for a particular chlorinated ethene in an aqueous solution as a function of the concentration of electron donors and/or acceptors [200]. Here the electron donor is assumed in excess and the chlorinated ethene serves as the electron acceptor. The Monod equation reduces to a first order kinetic model at low concentrations and zero-order kinetic model at high concentrations. $k_{max,i}$ represents the maximum rate at which each *Geo* or *Dhc* cell can mediate MRD (i.e., the zero-order rate), and $K_{s,i}$ is the substrate (i.e., chlorinated ethene) concentration at which reaction kinetics transition between first- and zero-order. The model is typically coupled to a microbial growth equation where Y_i represents the associated growth of *Geo* or *Dhc* populations and k_j^b represents biomass decay in the absence of electron acceptors. An accurate estimation of the Monod kinetic parameters is important if (1) laboratory experimental results are to be applied for field scale MRD predictions, (2) the bioremediation capacity of different inoculums are to be compared, or (3) the impact of different environmental conditions on MRD are to be assessed.

The KB-1® inoculum used contains fermenters and other anaerobic bacteria which support MRD. The fermentation processes require a carbon source and electron donor to proceed. In the experiments modeled, lactate was supplied in excess, precluding the need to include fermentation in the model formulation.

Geo can only perform reductive dechlorination of PCE to TCE and TCE to *cis*-DCE [275]. Although some *Dhc* strains in the KB-1® inoculum are capable of dechlorinating TCE and PCE, for this model it is assumed that *Dhc* only transforms *cis*-DCE to VC and VC to ethene. This assumption is supported by previous MRD experiments using TCE and KB-1® that have shown that measurable *Dhc* population growth occurred only during *cis*-DCE and VC degradation, and have estimated that 80% of TCE degradation by the KB-1® consortium is attributable to Geo [254, 275]. Thus, in **equations A.1** and **A.2**, i is PCE and TCE when j is *Geo* and i is *cis*-DCE and VC when j is *Dhc*.

To model interphase mass transfer of each compound i between the gaseous headspace and aqueous phases, equilibrium partitioning is assumed. Applying Henry's law to equation 1 and rearranging yields an ordinary differential equation (ODE) describing changes in C_i^a with respect to time.

$$\frac{d}{dt}(V^a C_i^a) + \frac{d}{dt}\left(\frac{V^g C_i^a}{H_i RT}\right) = V^a R_i^b + R_i^s \quad \textbf{(A.3)}$$

$$\left(V^a + \frac{V^g}{H_i RT}\right)\frac{d}{dt}(C_i^a) = V^a R_i^b + R_i^s \quad \textbf{(A.4)}$$

$$\frac{d}{dt}(C_i^a) = \frac{V^a R_i^b + R_i^s}{V^a + \frac{V^g}{H_i RT}} \quad \textbf{(A.5)}$$

where H_i is the Henry's law coefficient for compound i [M/L^3/P], R is the ideal gas constant [energy / temperature / M], and T is the system temperature.

Determining the concentrations C_i^a and X_j^a for all times $t > 0$ requires numerically integrating a set of seven ODEs: two equations of the form of **equation A.2** for *Geo* and *Dhc* and five equations of the form of **equation A.5** for the chlorinated ethenes and ethene. Completing that numerical integration requires a value for R_i^s, the rate at which compound i is entering or exiting the stopper. As described in **Section 4.1.2**, that rate is approximated with an analytical solution (**equation 4.2**) for planar diffusion.

The amount m_i^r of compound i in the stopper (idealized as a cylinder of cross-sectional area A and length L) is derived by integrating equation 2 from $x = 0$ to $x = L$.

$$m_i^r(t) = \int_0^L A\, C_i^r(x,t)dx \quad \textbf{(A.6)}$$

$$m_i^r(t) = AK_i^{ra}C_i^a\left[L\,\mathrm{erfc}\left(\frac{L}{2\sqrt{D_i t}}\right) + \sqrt{\frac{D_i t}{\pi}}\left(1 - \exp\left[-\frac{L^2}{4D_i t}\right]\right)\right] \quad \textbf{(A.7)}$$

Which for notational simplicity will be represented below as:

$$m_i^r(t) = C_i^a f_i(t) \quad \textbf{(A.8)}$$

The analytical solution given by **equation 4.1** assumes a constant aqueous phase concentration C_i^a, so the expressions above cannot be used directly to model the experimental system. However, a superposition scheme based on these expressions can be implemented to approximate R_i^s, provided that the rubber phase concentration at the outside face of the stopper, $C_i^r(x = L, t)$, remains small. This superposition scheme is as follows:

Divide time into steps $k = 0, 1, 2, 3$ ... of length h. Assume that the rubber phase initially contains zero moles of compound i.

$$m_{i,k=0}^r = 0 \quad \textbf{(A.9)}$$

The model prediction for the total amount of compound i in the rubber phase at time step k will be a sum of k terms functionally similar to **equation A-1.8** except C_i^a will be replaced with an aqueous concentration change $\Delta C_{i,k}^a$. The first concentration change $\Delta C_{i,k=0}^a$ is equal to the initial aqueous phase concentration.

$$\Delta C_{i,k=0}^a = C_{i,k=0}^a \quad \textbf{(A.10)}$$

After the first-time step of length h, the total amount of compound i in the rubber phase is approximately:

$$m_{i,k=1}^{r} = \Delta C_{i,k=0}^{a} f_i(h) \tag{A.11}$$

The aqueous phase concentration at time step $k = 1$ can be approximated by subtracting $m_{i,k=1}^{r}$ from the moles initially present in the batch reactor bottle and accounting for equilibrium partitioning between the aqueous and gaseous phases:

$$C_{i,k=1}^{a} = \frac{C_{i,k=0}^{a}\left(V^{a} + \frac{V^{g}}{H_i RT}\right) - m_{i,k=1}^{r}}{V^{a} + \frac{V^{g}}{H_i RT}} \tag{A.12}$$

where V^a is the aqueous phase volume and V^g is the gaseous headspace volume.

For all following time steps $k > 0$, the aqueous phase concentration change is:

$$\Delta C_{i,k}^{a} = C_{i,k}^{a} - C_{i,k-1}^{a} \tag{A.13}$$

The amount of compound i present in the rubber phase at the end of time step $k > 0$ is approximated with a superposition of k terms:

$$m_{i,k}^{r} = \sum_{n=0}^{k-1} \Delta C_{i,n}^{a} f_i([k-n]h) \tag{A.14}$$

And the corresponding aqueous phase concentration is:

$$C_{i,k}^{a} = \frac{C_{i,k=0}^{a}\left(V_{k=0}^{a} + \frac{V_{k=0}^{g}}{H_i RT}\right) - m_{i,k}^{r} - C_{i,k-1}^{a} V_k^{s}}{(V_{k-1}^{a} - V_k^{s}) + \frac{V_{k-1}^{g} + V_k^{s}}{H_i RT}} \tag{A.15}$$

where V_k^s is the volume of aqueous phase that was removed for sampling during that time step k (if no sample was removed then $V_k^s = 0$).

To confirm that the rubber phase concentration on the outside face of the stopper remains small, the rubber phase concentration profile can be computed using:

$$C_{i,k}^{r}(x) = \sum_{n=0}^{k-1} \Delta C_{i,n}^{a} K_i^{ra} \operatorname{erfc}\left(\frac{x}{2\sqrt{D_i h(k-n)}}\right) \tag{A.16}$$

The values of C_i^a and X_j^a at the end of each time step k are determined by numerically integrating **equations A.2** and **A.5** via an algorithm available from the SciPy Integration and ODEs submodule [197]. It is assumed that $R_i^s = 0$ over the first-time step $k = 1$. For all following time steps R_i^s is approximated with a superposition that lags by one time step. Specifically, for time step $k \geq 2$ the rate of compound i entering or exiting the rubber phase is:

$$R_{i,k}^{s} = \frac{m_{i,k-1}^{r} - m_{i,k-2}^{r}}{h} \tag{A.17}$$

A.3.1 Model Fitting

To obtain stopper sorption/diffusion parameters, the model described in the previous section (with $R_i^b = 0$) was first fit to abiotic batch reactor experiments for PCE and TCE . An objective function $J_{1,i}$ was defined for $i =$ PCE and TCE to measure goodness-of-fit:

$$J_{1,i} = \sum^{g} \sum^{k} \left(C_{ikg}^{a,\text{meas}} - C_{ikg}^{a,\text{sim}} \right)^2 \quad \textbf{(A.18)}$$

where g is an index corresponding to each abiotic batch reactor experiment and k is the sample time step index. Note that, since no correlation between PFAA concentration and mass loss was observed, one set of mass loss parameters was estimated using all abiotic batch reactors.

Unique best-fit values for the PCE and TCE diffusive mass loss parameters could not be determined with aqueous concentration measurements alone since there is a linear correlation between the optimal values of $\log K_{\text{i}}^{ra}$ and $\log D_{\text{i}}$. Thus, independent estimates of these parameters were sought in the literature. Göbel et al. measured D_i and K_i^{ra} for PCE in butyl rubber [246, 247]. Based upon those measurements, similar values of D_{PCE} and K_{PCE}^{ra} were selected that minimized the residuals for the PCE abiotic experiments.

The Göbel et al. measurements were then combined with commonly used correlations to estimate mass loss parameters for TCE, *cis*-DCE, VC, and ethene. To estimate the rubber phase diffusion coefficients a linear regression was fit to the squared Chung diameter versus $\log D_i$ [248, 249]. To estimate the rubber-aqueous linear partitioning coefficients a linear regression was fit to the log octanol-water partitioning coefficient versus $\log K_i^{ra}$ [250, 251]. The resulting D_i and K_i^{ra} estimates for *cis*-DCE, VC, and ethene were used directly. Final D_{TCE} and K_{TCE}^{ra} values for use in the model were selected so that they minimized the squared residuals computed by **equation A.18** and were close to the Göbel et al.-based estimates.

An example model fit with a mass loss formulation in which the rate of mass loss is first-order dependent on the aqueous phase concentration is depicted in **Figure A.4**. Example abiotic batch reactor model fits for the improved mass loss formulation used in this study are presented in **Figure A.5**. Mass loss parameter values used in this study are presented in **Table A.4**.

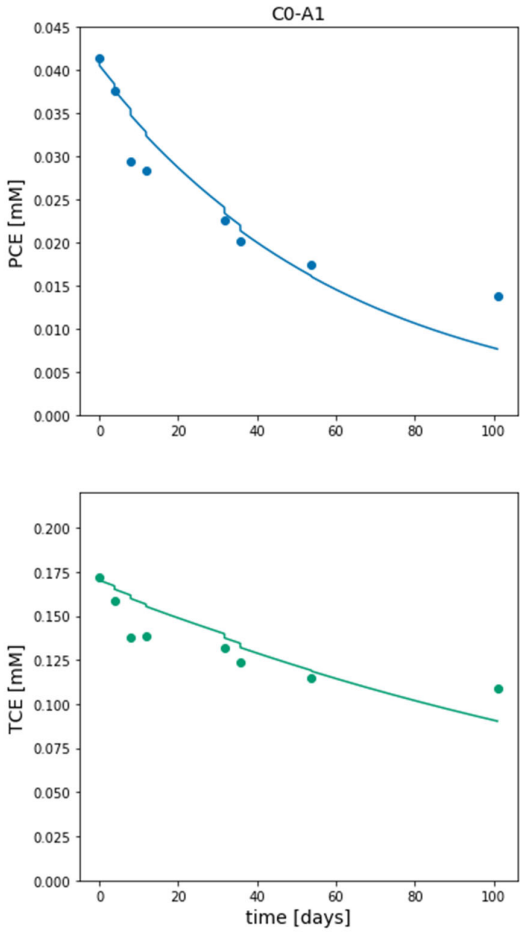


Figure A.4 Example fit of model with original mass loss formulation (curves) to abiotic batch reactor experiment data (points).

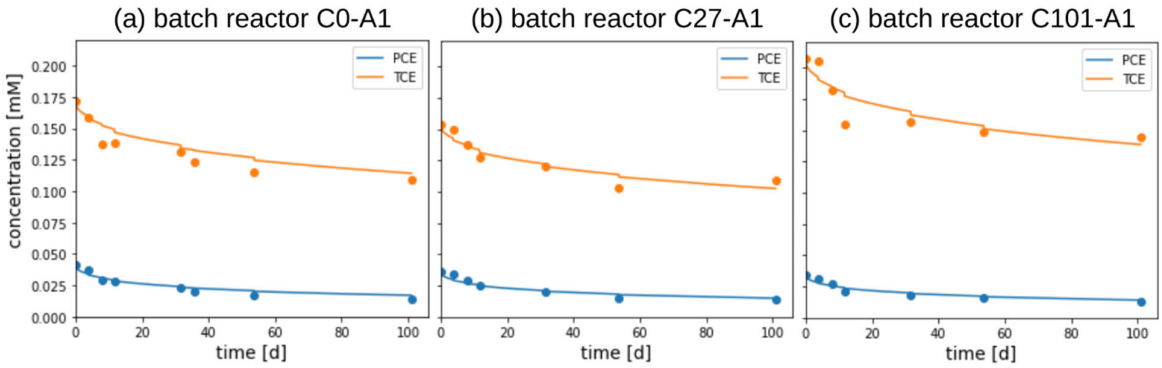


Figure A.5 Example fits of model with improved mass loss formulation (curves) to abiotic batch reactor data (points).

Table A.4 Diffusional mass loss parameters (see **equations 4.1** and **A.7**). Here, PCE and TCE mass loss parameters were fit to abiotic batch reactor data; parameters for *cis*-DCE, vinyl chloride, and ethene were estimated using literature data and correlations, as described in **Appendix A.3**.

Compound	rubber-aqueous linear partitioning coefficient K_i^{ra} [dimensionless]	rubber phase diffusion coefficient D_i [dm^2/d]
PCE	6.6×10^{2}	1.9×10^{-6}
TCE	1.6×10^{2}	3.49×10^{-6}
cis-DCE	8.4	2.39×10^{-6}
VC	3.3	3.09×10^{-6}
ethene	1.6	3.99×10^{-6}

Model fitting for the biotic batch reactors was completed in two phases. The objective of the first phase was to estimate a single and complete set of Monod kinetic parameters for *Geo* and *Dhc* in systems with no PFAAs (see **Table A.5**). Here, the model was fit to chlorinated ethene and qPCR biomass data from three biotic control batch reactors (see **Figure A.6**) [200]. The objective of the second phase was to estimate maximum substrate utilization rates ($k_{\max,i}$) for systems with varying concentrations of PFAAs (see **Figure A.7**). This phase employed chlorinated ethene data from batch reactor experiments with total PFAA concentrations ranging from 11.7 to 101 mg/L. During the second phase of model fitting, all parameters other than the maximum substrate utilization rates were held constant to their estimated or assumed values from the first phase of model fitting. Note that GC measurements of ethene concentration were several times larger than what would be consistent with mass balance considerations, attributed to coelution with methane. Thus, GC ethene measurements were deemed unreliable and not used in model fitting. In addition, the short time required for PCE and TCE dechlorination resulted in too few GC measurements of these compounds for precise estimation of the PCE and TCE yield coefficients; therefore, literature values [276] were selected for these parameters and no Geo qPCR measurements were used in the model fitting objective function (**equation A.19**).

The optimization function used for the first model-fitting phase is:

$$J_2 = \sum_{g}^{}\sum_{i}^{}\sum_{k}^{}\frac{\left(C_{i,k,g}^{a,\text{meas}} - C_{i,k,g}^{a,\text{sim}}\right)^2}{\sigma_i^2} + \sum_{g}^{}\sum_{k}^{}\frac{\left(X_{\text{Dhc},k,g}^{a,\text{meas}} - X_{\text{Dhc},k,g}^{a,\text{sim}}\right)^2}{\sigma_{k,g}^2} \qquad \textbf{(A.19)}$$

where g indexes to one of three triplicate control batch reactor experiments, i indexes to one of four chlorinated ethenes (PCE, TCE, *cis*-DCE, and VC), and k indexes to a sampling event. The quantities σ_i^2 [$(M/L^3)^2$] and $\sigma_{k,g}^2$ [$(cell/L^3)^2$] represent the estimated variances of measurement error for GC and qPCR analysis, respectively.

The optimization function used for the second model-fitting phase is:

$$J_{3,mg} = \sum_{i}^{}\sum_{k}^{}\frac{\left(C_{i,k}^{a,\text{meas}} - C_{i,k}^{a,\text{sim}}\right)^2}{\sigma_i^2} \qquad \textbf{(A.20)}$$

where m indexes over the six total PFAA concentrations tested (0 mg/L, 11.7 mg/L, 26.5 mg/L, 49.8 mg/L, 61.7 mg/L, and 101 mg/L) and g indexes over the three triplicate batch reactor experiments conducted for each total PFAA concentration m.

The GC measurement error standard deviation in **equations A.19** and **A.20** is estimated via:

$$\sigma_i = (\mathrm{CV})_i \bar{C}_i^{a,\mathrm{meas}} \qquad \textbf{(A.21)}$$

where $(\mathrm{CV})_i$ is the measurement error coefficient of variation (estimated by extracting data from published GC calibration curves [277] and fitting a linear regression to the sample standard deviations for each standard solution) and $\bar{C}_i^{a,\mathrm{meas}}$ is the average measured aqueous phase concentration for each chlorinated ethene.

The qPCR measurement error standard deviation in **equation A.19** was estimated with triplicate qPCR measurements of the *Dhc* 16S rRNA, *Geo* 16S rRNA, *tceA*, *vcrA*, and *bvcA* genes. A linear regression in log-log space was fit using the mean of the triplicate measurements as a predictor variable and the sample standard deviation of the triplicate measurements as a response variable. The resulting estimate of $\sigma_{k,g}$ is given by:

$$\sigma_{k,g} = 2.26\left(X_{\mathrm{Dhc},k,g}^{a,\mathrm{meas}}\right)^{0.891} \qquad \textbf{(A-22)}$$

where $X_{\mathrm{Dhc},k,g}^{a,\mathrm{meas}}$ and $\sigma_{k,g}$ have units of genes/mL. Note that *Dhc* contains one 16S rRNA gene copy per genome [278], so standard deviation estimates given by **equation A.22** could be used directly in equation S19 with no unit conversion. The best-fit Monod kinetic parameters obtained by minimizing **equation A.19** are listed in **Table A.5**. As indicated in this table, the optimization range for each calibration parameter are based on literature ranges from studies that used KB-1® inoculum. None of the best-fit values in **Table A.5** are pinned to an optimization boundary, indicating that the minimum of the objective function (**equation A.19**) returned by the differential evolution optimization algorithm does not differ greatly from previously published results for experiments that used the same culture. Parameter ranges for the MRD literature as a whole are at least an order of magnitude larger than the KB-1® literature ranges [200]. The fact that good model fits (see R^2 values in **Section 4.1.2** of the text) were achieved within the subset of parameter values specific to KB-1® inoculum indicates good agreement with the prior work.

A differential evolution algorithm [279], implemented in the SciPy Optimization and Root Finding Module [197], was used to identify a unique set of calibration parameter values for each model fitting that minimizes the respective optimization function (**equation A.19** or **A.20**). The fit k_{max} values are shown in **Table A.6**.

Table A.5 Summary of Monod kinetic parameters (see **equations A.1** and **A2**) fitted to chlorinated ethene and qPCR biomass data from three biotic control batch reactor experiments (**Figure A.6**) by minimizing the objective function **A.19** (Phase 1 optimization). Parameter optimization ranges were derived from literature ranges and are presented in column 3.

times	Value	Note	Optimization Range†
Maximum substrate utilization rates [mmol/cell/d]			
$k_{\text{max,PCE}}$	7.75×10^{-13}	calibration parameter	7.54×10^{-13} to 1.57×10^{-10}
$k_{\text{max,TCE}}$	2.36×10^{-12}	calibration parameter	7.54×10^{-13} to 1.57×10^{-10}
$k_{\text{max,DCE}}$	1.66×10^{-12}	calibration parameter	3.93×10^{-14} to 2.08×10^{-11}
$k_{\text{max,VC}}$	9.64×10^{-13}	calibration parameter	2.36×10^{-13} to 8.40×10^{-12}
Half-saturation constant [mM]			
$K_{s,\text{PCE}}$	4.12×10^{-3}	calibration parameter	4.00×10^{-3} to 1.00×10^{-2}
$K_{s,\text{TCE}}$	4.07×10^{-3}	calibration parameter	4.00×10^{-3} to 1.00×10^{-2}
$K_{s,\text{DCE}}$	1.95×10^{-1}	calibration parameter	1.00×10^{-3} to 1.96×10^{-1}
$K_{s,\text{VC}}$	1.77×10^{-1}	calibration parameter	1.00×10^{-3} to 1.97×10^{-1}
Yield coefficients [cell/mmol]			
Y_{PCE}	9.93×10^{10}	fixed to literature value[SI34]	not applicable
Y_{TCE}	9.93×10^{10}	fixed to literature value[SI34]	not applicable
Y_{DCE}	9.50×10^{10}	calibration parameter	1.02×10^{9} to 5.19×10^{11}
Y_{VC}	2.25×10^{11}	calibration parameter	1.02×10^{10} to 5.19×10^{11}
Endogenous decay constant [d^{-1}]			
k^{b}_{Geo}	1.00×10^{-2}	assumed equal to k^{b}_{Dhc}	not applicable
k^{b}_{Dhc}	1.00×10^{-2}	independently approximated prior to model fitting by observing decay in qPCR measurements made after complete MRD	not applicable
Initial biomass concentration [cells/mL]			
$X^{a}_{\text{Geo},t=0}$	7.10×10^{6}	fixed to estimate based on dilution of KB-1® inoculum	not applicable
$X^{a}_{\text{Dhc},t=0}$	1.07×10^{7}	calibration parameter	2.38×10^{6} to 1.42×10^{7}

† Optimization ranges for maximum substrate utilization rates, half-saturation coefficients, and yield coefficients are based on literature ranges for studies that used KB-1® inoculum [254, 280, 281]. The optimization range for $X^{a}_{\text{Dhc},t=0}$ was a 95% confidence interval calculated using replicate qPCR measurements of KB-1® inoculum.

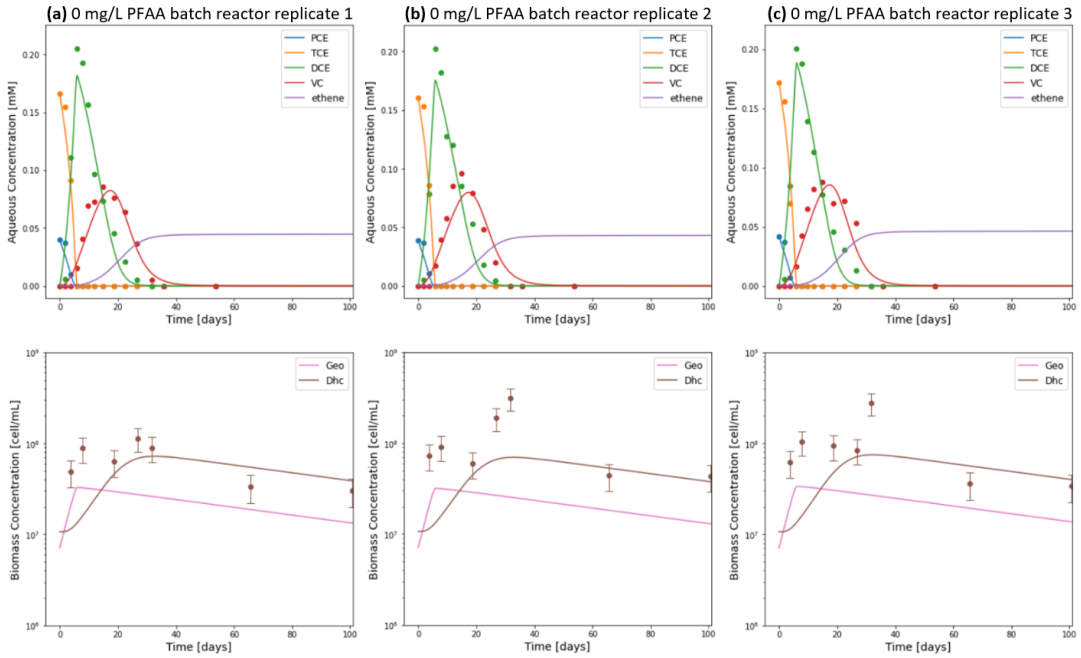


Figure A.6 Model fits to batch reactors with 0 mg/L PFAAs (parameters from **Table A.1**). Curves represent model values, points represent measurements, and error bars around qPCR measurements represent one standard deviation as estimated by **equation A.22**. As noted in **Appendix A.1**, *GeoSZ qPCR* measurements were not used to fit *GeoSZ* biomass values and were omitted from this figure.

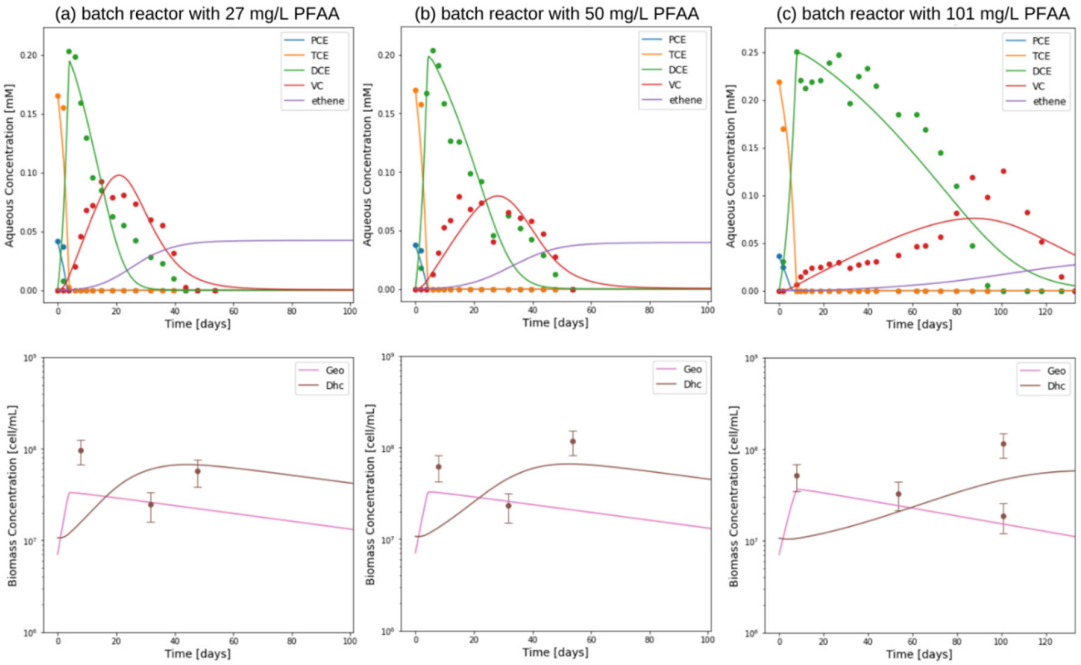


Figure A.7 Example model fits to batch reactors with varying concentrations of PFAAs. Curves represent model values, points represent measurements, and error bars around qPCR measurements represent one standard deviation as estimated by **equation A.22**. As noted in **Appendix A.1**, *GeoSZ qPCR* measurements were not used to fit *GeoSZ* biomass values and were omitted from this figure.

Table A.6 Average maximum substrate utilization rates for each set of batch reactors in units of mmol/day/cell. **Bold** entries are significantly lower than the average for the 0 mg/L reactor set ($p<0.05$). *Italicized* entries are higher than the average for the 0 mg/L reactor set. Calculated p-values are included comparing the average maximum substrate utilization rate for each set of reactors with PFAAs to those of the positive control (0 mg/L PFAA) reactors.

Batch Reactor PFAA concentration	mean $k_{max,PCE}$ (±st. dev)	mean $k_{max,TCE}$ (±st. dev)	mean $k_{max,DCE}$ (±st. dev)	mean $k_{max,VC}$ (±st. dev)
0 mg/L	7.75×10^{-13} ($\pm1.64\times10^{-14}$)	2.37×10^{-12} ($\pm6.13\times10^{-14}$)	1.67×10^{-12} ($\pm9.17\times10^{-15}$)	9.21×10^{-13} ($\pm8.75\times10^{-14}$)
12 mg/L	7.41×10^{-13} ($\pm4.98\times10^{-14}$) p=0.18	*2.59×10^{-12} ($\pm4.78\times10^{-14}$)* p=0.01	**1.30×10^{-12} ($\pm5.06\times10^{-14}$)** p=0.003	**7.79×10^{-13} ($\pm4.06\times10^{-14}$)** p=0.013
27 mg/L	*1.09×10^{-12} ($\pm1.66\times10^{-13}$)* p=0.04	*3.45×10^{-12} ($\pm7.67\times10^{-14}$)* p=0.001	1.55×10^{-12} ($\pm1.70\times10^{-13}$) p=0.17	**6.02×10^{-13} ($\pm2.12\times10^{-14}$)** p=0.0007
50 mg/L	*3.77×10^{-12} ($\pm5.07\times10^{-12}$)* p=0.21	*5.38×10^{-11} ($\pm8.72\times10^{-11}$)* p=0.21	**1.10×10^{-12} ($\pm2.13\times10^{-13}$)** p=0.02	**5.74×10^{-13} ($\pm2.28\times10^{-14}$)** p=0.0007
62 mg/L	7.06×10^{-13} ($\pm4.94\times10^{-13}$) p=0.42	*5.48×10^{-11} ($\pm8.84\times10^{-11}$)* p=0.21	**5.70×10^{-13} ($\pm6.11\times10^{-14}$)** p=0.0005	**5.50×10^{-13} ($\pm1.77\times10^{-13}$)** p=0.034
101 mg/L	*5.65×10^{-12} ($\pm8.57\times10^{-12}$)* p=0.21	2.64×10^{-12} ($\pm9.40\times10^{-13}$) p=0.34	**3.32×10^{-13} ($\pm1.57\times10^{-14}$)** p=0.00002	**2.89×10^{-13} ($\pm1.66\times10^{-14}$)** p=0.0001

The optimization function used to fit the log-logistic dose-response model (**equation 4.2**) is:

$$J_{3,i} = \sum^{m}\sum^{g}\left(k^{\text{est}}_{\text{inh},img} - k^{\text{sim}}_{\text{inh},img}\right)^2 \qquad \textbf{(A.23)}$$

where m indexes over the five non-zero total PFAA concentrations, g indexes over the three triplicate batch reactor experiments conducted for each total PFAA concentration, $k^{\text{est}}_{\text{inh},img}$ are the estimated inhibited maximum substrate utilization rates from the second model-fitting phase, and $k^{\text{sim}}_{\text{inh},img}$ are the inhibited maximum substrate utilization rates predicted by **equation 4.2**. An optimization is performed to minimize **equation A.23** using the Levenberg-Marquardt algorithm [282, 283] implemented the SciPy Optimization and Root Finding Module [197], yielding a best-fit b_i and $C^{a}_{50,i}$ value for each chlorinated ethene.

A.4 Sorption of TCE and PCE

Surface soil collected from Loring Air Force Base (Aroostook County, ME) in October 2017 was analyzed for PCE and TCE sorption. Prior to testing, the soil was air dried, gently ground with a mortar and pestle, and passed through a No. 40 mesh sieve. To create PCE and TCE sorption isotherms, 5 mg samples of Loring Air Force base soil (dried, ground and sieved as described above) were placed in 20 mL crimp cap vials with Teflon-lined rubber caps. After adding soil, each vial was filled with sterile, low salts anaerobic medium containing dissolved PCE or TCE and sealed. Vials were filled to minimize headspace (<8% headspace by volume) with an average headspace volume of 2.0% (±2.4%). Negative control vials were set up with anaerobic medium and PCE or TCE but no soil to account for losses of chlorinated ethenes from the vial over the duration of the experiment. Sets of 6 vials (3 with soil and 3 without) were prepared with initial concentrations of 10, 25, 50, 100, and 200 mg/L TCE and 5, 10, 25, 50, and 100 mg/L PCE. An additional 26 vials (15 with soil and 11 without) were prepared with 100 mg/L TCE to determine if 3 days were sufficient to reach sorption equilibrium. All vials were placed on a shaker tray and incubated at room temperature (21ºC).

Vials were destructively sampled after at least 3 days of mixing. Vials were centrifuged at 400 rpm (65 x g) for 30 minutes in an Eppendorf 5810R centrifuge (Eppendorf, Hauppauge, NY) to separate soil particles. After centrifugation, a 1 mL aqueous sample was removed using a needle and syringe and placed in a crimp-cap headspace vial for chlorinated ethene analysis by GC-FID. The vial was then opened and the remaining aqueous volume was removed and replaced with 10 mL of methanol for extraction of sorbed chlorinated ethenes. Vials containing the soil-methanol mixture were shaken manually, then placed on a shaker tray to equilibrate for 24 to 48 hours at room temperature. The vials were then centrifuged as described above and methanol was sampled using a needle and syringe, placed in a 1.8 mL glass autosampler vial, and analyzed by GC with μECD. After analysis, the methanol was removed and replaced, and the extraction was repeated three times (until chlorinated ethenes were no longer detected in the sample).

Equilibrium soil and aqueous concentrations were used to create sorption isotherms for PCE and TCE as shown in **Figure A.8** and **Figure A.9**. A linear sorption isotherm best fit both sets of data (average R^2=0.97) resulting in K_d values of 1.30×10^{-3} for TCE and 4.70×10^{-3} for PCE. Freundlich sorption isotherms also fit the data well (average R^2=0.96) with K_f values of 7.13×10^{-4} for TCE and 2.69×10^{-3} for PCE and n values of 0.879 and 0.929 for TCE and PCE, respectively.

Based on the measured sorption isotherms and the aqueous-solid ratios used in the microcosm experiments (12.9-15.7% solids by weight), less than 1% of the aqueous mass of PCE and TCE was expected to adsorb to the solid phase. Therefore, sorption of PCE and TCE to solids in the microcosms was considered to be negligible and did not substantially affect the rates of degradation observed. The less chlorinated TCE degradation products (*cis*-DCE and VC) are less likely to sorb to solids based on published organic carbon partitioning coefficient (K_{OC}) values [284] and, therefore, sorption of *cis*-DCE and VC to solids also had a negligible effect on observed degradation.

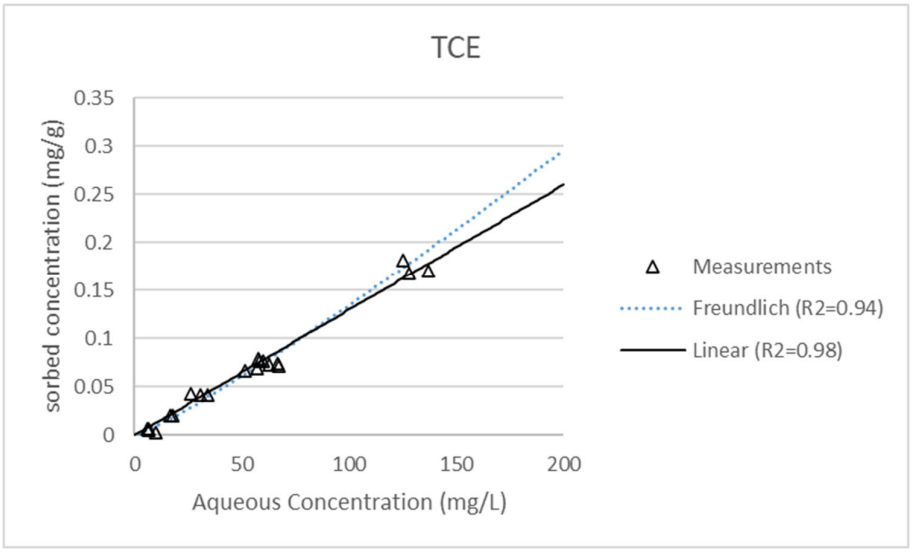


Figure A.8 TCE sorption isotherms and equilibrium measurements

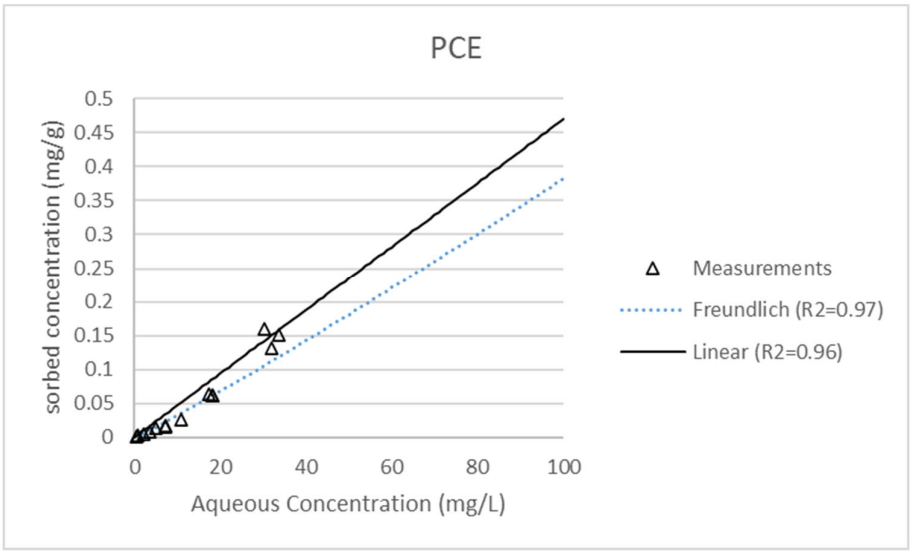
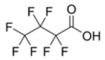
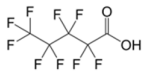
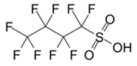
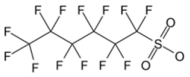
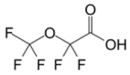
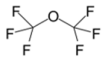
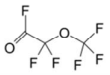
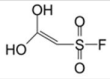
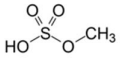
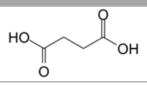
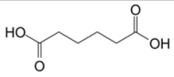
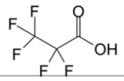
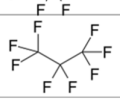
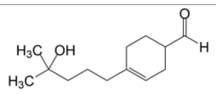
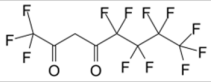
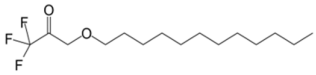


Figure A.9 PCE sorption isotherms and equilibrium measurements

A.5 PFOS Degradation Products

Table A.7 Intermediate by-products derived from PFOS degradation, characterized by their mass-to-charge ratio (m/z)

No	Chemical name	Formula	Chemical structure	BDD	CNTs-NF	Confidence score
1	Perfluorobutanoic acid	$C_4HF_7O_2$		↑	↑	1
2	Perfluoropentanoic acid	$C_5HF_9O_2$		↑	-	1
3	Perfluoro-1-butanesulfonic acid (PFBS)	$C_4HF_9O_3S$		-	↓	1
4	Perfluoro-1-pentanesulfonate (PFHpS)	$C_5HF_{11}O_3S$		↓	↓	1
5	Perfluoro-1-hexanesulfonic acid (PFHxS)	$C_6HF_{13}O_3S$		↓	↑	1
6	Perfluoro-1-octanesulfonic acid (PFOS)	$C_8HF_{17}O_3S$		↓	↓	1
7	Difluoro(perfluoromethoxy) acetic acid	$C_3HF_5O_3$		-	↑	3
8	Unsaturated fluoro diEther hexanoic acid	$C_4HF_5O_4$		-	↑	3
9	Trifluoro(trifluoromethoxy)methane	C_2F_6O		-	↓	3
10	Difluoro(trifluoromethoxy) acetyl fluoride	$C_3F_6O_2$		↓	↓	3
11	Trifluoroacetic acid	$C_2HF_3O_2$		↑	↓	3
12	2,2-Dihydroxyethene sulfonyl fluoride	$C_2H_3FO_4S$		↑	↓	3
13	Methyl bisulfate	CH_4O_4S		-	↓	3

No	Chemical name	Formula	Chemical structure	BDD	CNTs-NF	Confidence score
14	Succinic acid	$C_4H_6O_4$		↓	↑	3
15	Adipic acid	$C_6H_{10}O_4$		-	↑	3
16	Perfluoropropanoic acid	$C_3HF_5O_2$		↑	-	3
17	2H-Perfluoropropane	C_3HF_7		↑	↓	3
18	3-Hydroxy-5,5-bis(trifluoromethyl)furan-2(5H)-one	$C_6H_2F_6O_3$		-	↑	3
19	4-(4-Hydroxy-4-methylpentyl)cyclohex-3-ene-1-carbaldehyde	$C_{13}H_{22}O_2$		-	↑	3
20	1,1,1,5,5,6,6,7,7,8,8,8-dodecafluorooctane-2,4-dione	$C_8H_2F_{12}O_2$		↓	↓	3
21	3-(Dodecylsulfanyl)-1,1,1-trifluoroacetone	$C_{15}H_{27}F_3OS$		↑	↑	3
22	Unsaturated fluoro diEther hexanoic acid	$C_4HF_5O_4$		↓	↑	3
23		CHF_3O_4S		↑	↓	3
24		$C_3H_3F_3O_{10}S_5$		↑	↓	3
25		CHF_3O_4S		↓	↑	3
26		CHF_3S_4		-	↑	4

↑	Increase Concentration Major (more than 1 million)
↑	Increase Concentration Minor(Less than 1 million)
↓	Decrease Concentration Major
↓	Decrease Concentration Minor

* *Major: The value of the slop is more than 1 million*

Minor: The value of the slop is less than 1 million

Appendix B: List of Scientific/Technical Publications

B.1 Peer-Reviewed Papers

Lee, J., C. Kim, C. Liu, M. Wong, N.L. Cápiro, K.D. Pennell, and J.D. Fortner. 2023. Ultra-high capacity, multifunctional nanoscale sorbents for PFOA and PFOS treatment. NPJ *Clean Water,* 6: 62, doi.org/10.1038/s41545-023-00263-9.

Hnatko, J.P., C. Liu, J. Elsey, S. Dong, J.D. Fortner, K.D. Pennell, L.M. Abriola and N.L. Cápiro. 2023. Microbial reductive dechlorination by a commercially available dechlorinating consortium is not inhibited by perfluoroalkyl acids (PFAAs) at field-relevant concentrations. *Environmental Science and Technology,* 57: 8301-8312, doi.org/10.1021/acs.est.2c04815.

Liu, C., J. Chu, N.L. Cápiro, J.D. Fortner, K.D. Pennell. 2022. In-situ sequestration of perfluoroalkyl substances using polymer-stabilized ion exchange resin. *Journal of Hazardous Materials*, 422: 126960, doi.org/10.1016/j.jhazmat.2021.126960.

Liao, S., Arshadi, M., Woodcock, M.J., Saleeba, Z.S., Pinchbeck, D., Liu, C., Cápiro, N.L., Abriola, L.M. and Pennell, K.D., 2022. Influence of residual nonaqueous-phase liquids (NAPLs) on the transport and retention of perfluoroalkyl substances. *Environmental Science & Technology*, 56(12), pp.7976-7985, doi.org/10.1021/acs.est.2c00858

Liao, S., Saleeba, Z., Bryant, J.D., Abriola, L.M. and Pennell, K.D., 2021. Influence of aqueous film forming foams on the solubility and mobilization of non-aqueous phase liquid contaminants in quartz sands. *Water Research*, 195, p.116975, doi.org/10.1016/j.watres.2021.116975

Naidu, R., P. Nadebaum, C. Fang, I. Cousins, K. Pennell, J. Conder, C.J. Newell, D. Longpré, S. Warner, N.D. Crosbie, A. Surapaneni, D. Bekele, R. Spiese, T. Bradshaw, D. Slee, Y. Liu, F. Qi, M. Mallavarapu, L. Duan, L. McLeod, M. Bowman, B. Richmond, P. Srivastava, S. Chadalavada, A. Umeh, B. Biswas, A. Barclay, J. Simon, P. Nathanail. 2020. Per- and poly-fluoroalkyl substances (PFAS): Current status and research needs, *Environmental Technology and Innovation*, 19: 100915, doi.org/10.1016/j.eti.2020.100915.

Lee, J., O. Durak, S.S.S. Lee, S. Maisto, N. Capiro, K.D. Pennell, and J.D. Fortner. Enhanced Photocatalytic Oxidation of PFOA with Functionalized Metal Organic Framework (MOF) Composites. submitted to *ACS Applied Materials and Interfaces*.

Yun, E.T., J. Lee, S. Maisto, L. Watt, N. Capiro, K.D. Pennell, and J.D. Fortner. Rapid, Electrochemical-based Cathodic Oxidation of Perfluorooctane Sulfonate (PFOS) through Enhanced Interfacial Adsorption and Surface-bound Sulfate Radical Production via CNTs-Nickel Foam Electrode. submitted to *Applied Catalysis B: Environmental*.

Dong, S., P.-F. Yan, M.J. Woodcock, J.D. Fortner, K.D. Pennell, and N.L. Cápiro. Microbial Reductive Dechlorination Upgradient of In-Situ Sorptive Materials for Improved Treatment of a Mixed Perfluoroalkyl Acids and Chlorinated Ethenes Plume. submitted to *Water Research.*

B.2 Presentations/Posters:

Pennell, K.D. 2023. Evaluation of Injectable Amendments for *In Situ* Treatment of PFAS-Impacted Groundwater, REMTEC & Emerging Contaminants Summit, October 3-5, 2023, Westminster, CO (invited).

Pennell, K.D. 2023. Experimental and Modeling Studies of PFAS Transport and Remediation in Porous Media. Colorado School of Mines, October 6, 2023, Golden, CO (invited).

Pennell, K.D. 2022. Development and Testing of Injectable Amendments for *In Situ* Treatment of PFAS-Impacted Groundwater. SERDP/ESTCP OE Innovation Symposium, November 29-December 2, 2022. Arlington, VA (invited).

Pennell, K.D. 2022. Environmental Restoration: Research Progress and Remaining Challenges, REMTEC & Emerging Contaminants Summit, October 2-4, 2022, Westminster, CO (invited).

Pennell, K.D. 2022. Development and Testing of Injectable Amendments for *In Situ* Treatment of PFAS-Impacted Groundwater. Session W7A: Advances in PFAS Remediation: Soil and Groundwater. International CleanUp Conference, September 11-14, 2022. Adelaide, Australia (invited keynote).

Cápiro, N.L. J. P. Hnatko, C. Liu, J. Elsey, S. Dong, J. D. Fortner, L. M. Abriola, and K. D. Pennell. 2022. Bioremediation of Chlorinated Ethenes in Contaminant Mixtures Containing Perfluorinated Alkyl Acids. International CleanUp Conference. September 11-14, 2022, Adelaide, Australia (invited keynote).

Pennell, K.D., N.L., Cápiro, N. Akladiss, C. Newell. 2022. Fate, Transport, and Mass Flux of Environmental Contaminants in the Subsurface, Workshop course, International CleanUp Conference, September 15, 2022. Adelaide, Australia.

Lee, J., C. Liu, S. Lee, S. Maisto, S.H. Chae, N.L. Cápiro, K.D. Pennell, J.D. Fortner. 2022. Understanding Oriented Attachment and Sorption Behavior of Perfluoroalkyl Substances (PFASs) on Surface Tailored Iron Oxide Nanocrystals by QCM-D. AEESP Research and Education Conference, June 28-30, 2022. St. Louis, MO.

Hnatko, J.P., C. Liu, J. Lee, S. Dong, H. Torkzadeh, J.D. Fortner, K.D. Pennell, and N.L. Cápiro. 2022. Sequential Biological and Adsorptive Material Treatment of Chlorinated Ethenes and PFAS Co-contaminated Contaminated Groundwater. AEESP Research and Education Conference, June 28-30, 2022. St. Louis, MO.

Manz, K.E. 2022. Utilizing High Resolution Non-Targeted Mass Spectrometry to Investigate Environmental Systems and Health Impacts. AEESP Research and Education Conference, June 28-30, 2022, St. Louis, MO.

Hnatko. J., J. Elsey, C. Liu, L.M. Abriola, K.D. Pennell, J. Fortner, N.L. Cápiro. 2022. Presence of Solid Phase Can Prevent Inhibition of *Dehalococcoides mccartyi* by Terminal PFAS. Battelle Chlorinated Conference, May 22-26, 2022, Palm Springs, CA.

Liao, S., 2021. Interactions of Aqueous Film Forming Foams with Non-aqueous Phase Liquids, RemTec & Emerging Contaminants Summit, March 9-11, 2021 (Remote due to Covid-19).

Pennell, K.D. 2020. Development of Injectable Sorbents for In Situ Sequestration of PFAS, University Consortium Meeting, September 30, 2020 (invited).

Pennell, K.D., J. Costanza, C. Liu, M. Arshadi, L.M. Abriola, N.L. Capiro, J. Fortner. 2019. Transport and Remediation of Per- and Polyfluoroalkyl Substances (PFAS) in the Subsurface, International Cleanup Conference, Sepetember 8-12, 2019, Adelaide, Australia (invited).

Liu, C., K.D. Pennell, B. Marion, N.L. Cápiro, W.A. Arnold, M.F. Simcik, J. Hatton. 2019. In-situ Sequestration of Per and Polyfluoroalkyl Substances (PFAS) using Polymer-Stabilized Powdered Activated Carbon (S-PAC), RemTec Summit, February 26-28, 2019, Denver, CO.

Pennell, K.D., C. Liu, Y. Aly, N.L. Cápiro, J.D. Fortner, J. Hatton, W. Arnold, M.F. Simcik. 2018. Development of Reactive Materials for In Situ Treatment of Per and Polyfluoroalkyl Substances (PFAS). American Chemical Society National Meeting; August 19-23, 2018, Boston, MA (invited).

Pennell, K.D., C. Liu, B.L. Lyon-Marion, N.L. Cápiro, W.A. Arnold, M.F. Simcik, J. Hatton. 2018. In Situ Sequestration of Per and Polyfluorinated Substances (PFAS) from Contaminated Groundwater. Emerging Contaminants Summit, March 6-8, 2018, Westminster, CO (invited).

B.3 Patents and Patent Applications:

Pennell, K.D., C. Liu. 2021. Formulations and Processes for Treating Water from Impacted Sources. Publication No. WO2021207132, International Application No. PCT/US21/025884. International Filing Date: April 6, 2021. U.S. Patent Application No. 17/995,639.

Lee, J., S.S. Lee, C. Kim, J.D. Fortner. 2023. Ultra-high Capacity Multifunctional Nanoscale Adsorbents for PFAS Treatment," Patent Application Pending.

Appendix C: Other Supporting Materials

C.1 Per- and Polyfluoroalkyl Substances (PFAS) Analyte List

Project: ER-2714

PI: Kurt Pennell

Date: November 16, 2018

The following list of PFAS compounds are being quantitated using a Waters Ultra Performance Liquid Chromatograph (UPLC) connected to a Waters Xevo TQ-S tandem quadrupole mass spectrometer (MS/MS) located in the School of Engineering at Brown University.

Compound Name	Abbreviation	CAS	Labelled Surrogate
Perfluorobutanoic acid	PFBA	375-22-4	MPFBA
Perfluoropentanoic acid	PFPeA	2706-90-3	M5PFPeA
Perfluorohexanoic acid	PFHxA	307-24-4	M5PFHxA
Perfluoroheptanoic acid	PFHpA	375-85-9	M4PFHpA
Perfluorooctanoic acid	PFOA	335-67-1	M8PFOA
Perfluorononanoic acid	PFNA	375-95-1	M9PFNA
Perfluorodecanoic acid	PFDA	335-76-2	M6PFDA
Perfluoroundecanoic acid	PFUnA	2058-94-8	M7PFUnDA
Perfluorododecanoic acid	PFDoA	307-55-1	MPFDoA
Perfluorotridecanoic acid	PFTriA	72629-94-8	
Perfluorotetradecanoic acid	PFTreA	376-06-7	M2PFTeDA
Perfluorobutanesulfonic acid	PFBS	375-73-5	M3PFBS
Perfluoropentanesulfonic acid	PFPeS	2706-91-4	
Perfluorohexanesulfonic acid	PFHxS	355-46-4	M3PFHxS
Perfluoroheptanesulfonic acid	PFHpS	375-92-8	
Perfluorooctanesulfonic acid	PFOS	1763-23-1	M8PFOS
Perfluorononanesulfonic acid	PFNS	68259-12-1	
Perfluorodecanesulfonic acid	PFDS	335-77-3	
Perfluorooctanesulfonamide	PFOSA	754-91-6	M8PFOSA
Fluorotelomer sulfonic acid 4:2	FtS 4:2	757124-72-4	M24:2FTS
Fluorotelomer sulfonic acid 6:2	FtS 6:2	27619-97-2	M26:2FTS
Fluorotelomer sulfonic acid 8:2	FtS 8:2	39108-34-4	M88:2 FTS
2-(N-Ethylperfluorooctanesulfonamido) acetic acid	NEtFOSAA	2991-50-6	D3-N-EtFOSAA
2-(N-Methylperfluorooctanesulfonamido) acetic acid	NMeFOSAA	2355-31-9	D3-N-MeFOSSA

C.2 Standard Operating Procedures for PFAS Sample Collection Preparation, and Analysis

1. Sample Collection

Samples will be collected from laboratory-scale batch, column, and aquifer cell systems where technical grade PFAS precursors are introduced and degradation products are produced. Aqueous and solid phase sampled will be analyzed to determine concentrations of PFAS precursors and degradation products.

a. Equipment/Supplies

2 mL polypropylene (PP) centrifuge tubes

15 mL PP centrifuge tubes

3 mL PP syringe with rubber plunger and stainless-steel needle

50 mL and 100 mL high-density polyethylene (HDPE) bottles

Isotopically labelled PFAS from Wellington Laboratories Inc. (Ontario, Canada)

b. Collection Process

Aqueous effluent samples will be collected with a fraction collector during column experiments in 15 mL PP centrifuge tubes. Additional aqueous samples will be collected from batch and aquifer cell systems using a 3 mL PP syringe with stainless steel needle and placed into 2 mL PP centrifuge tubes. Solid (soil) samples will be collected from batch, column, and aquifer cell systems and transferred into HDPE bottles.

c. Decontamination Procedures

Syringes will be used once and discarded, or they will be rinsed with methanol followed by ultrapure water before collecting each sample. The PP centrifuge tubes and HDPE bottles will be used once and discarded.

d. QC Samples

The isotopically-labelled PFAS extraction standards paired with each PFAS introduced (e.g., M8-PFOA when PFOA is present) will be added to each sample as an internal standard to track the extraction process (i.e., extracted internal standard). The instrument response to the labelled PFAS will be used when recoveries are between 50% and 150% of added amounts (Table B-15, DOD/DOE QSM 5.1.1). If recoveries are outside these limits, the sample result will be discarded.

A method blank (MB) will be collected using the procedures described in section 1.b. during each sampling event from either the uncontaminated background solution or solids being utilized in the experiment. A matrix spike (MS) and a matrix spike duplicate (MSD) will be prepared with each batch of samples by adding a low-level PFAS standard to the background solution or solids being used in each experiment. The MS and MSD will be used to show that the % recovery is within

70% to 130%, and the relative percent difference (RPD) is less than 30% (Table B-15, DOD/DOE QSM 5.1.1).

e. Sample Preservation, Shipping, and Hold Times

The PP centrifuge tubes and HDPE bottles will be placed in a 4 °C refrigerator immediately after sample collection. Aqueous samples will be analyzed within 28 days of collection. Solid samples will be extracted within 14 days of collection and extracts will be analyzed within 28 days of extraction.

2. Sample Preparation

Aqueous samples used for PFAS analysis will be prepared by collecting a small volume from each PP centrifuge tube and diluting this in a 2 mL autosampler vial to a final 80:20 water to methanol mix. Solid phase extraction (SPE) of the aqueous sample will not be employed as there will be insufficient volume of aqueous sample available (i.e., much less than 250 mL). Solid samples for PFAS analysis will be extracted three sequential times using methanol with 400 mM ammonium acetate (Munoz et al. 2018).

a. Equipment/Supplies

LC-MS grade Methanol (Honeywell Burdick & Jackson) containing 400 mM of ammonium acetate

Solid Phase Extraction (SPE) Clean Up cartridges (e.g. ENVI-Carb)

HPLC grade water (Honeywell Burdick & Jackson)

2 mL glass autosampler vials

Pipette with PP tips

Centrifuge (type, model? capacity/speed)

b. Preparation Technique

For aqueous samples, each PP centrifuge tube containing an aqueous sample will be centrifuged at 4,000 rpm for 5 min to remove suspended solids. Thereafter, a 100 µL aliquot will be transferred from each PP centrifuge tube by pipette with PP tip and placed into a 2 mL glass autosampler vial. The 100 µL aliquot will be diluted by adding 700 µL of HPLC grade water and 200 µL of LC-MS grade methanol. Each sample will be vortexed for 15 seconds to ensure mixing.

For solid samples, a 4 mL volume of LC-MS grade methanol with 400 nM ammonium acetate will be added to 1 g of solid sample, vortexed for 0.5 min, sonicated in a water bath for 10 min, and centrifuged at 5,000 rpm for 5 min (Munoz et al. 2018). Following sonication, the extract will be passed through a SPE cartridge to remove interfering compounds and then concentrated under a stream of nitrogen to a final volume of 5 mL. A 150 µL of the final extract will be transferred to 2 mL glass autosampler vial for LCMS analysis.

c. Sample QC

Laboratory control spike (LCS) consisting of low-level PFAS added to an uncontaminated 80:20 water to methanol mix will be prepared with each batch of samples.

3. Sample Analysis

Samples consisting of 80:20 water to methanol and methanol with 400 mM ammonium acetate will be analyzed by liquid chromatography with tandem mass spectrometry (LC-MS/MS). In addition, aqueous samples will be analyzed by ion chromatography for fluoride.

a. Equipment/Supplies

Waters Acquity ultra performance liquid chromatograph (UPLC) connected to a Waters Xevo tandem quadrupole (TQ)-S micro mass spectrometer (MS).

Dionex DX500 modular ion chromatography system

Isotopically-labelled PFAS from Wellington Laboratories, Inc

PFAS analytical standards from Sigma-Aldrich

SPEX CertiPrep standards for fluoride

b. Instrument Conditions

Analyte separation will be achieved with a Waters BEH C-18 column (1.7 µm dia., 2.1 × 50 mm) operated at a flow rate of 0.4 mL/min with an eluent gradient consisting of 10 mM ammonium acetate in water. Large volume injection (50 µL) will be employed to improve sensitivity. The Waters TQ-S micro will be operated in the negative electrospray ionization (ESI) mode with desolvation gas (nitrogen) flow at 450 L/hr and temperature of 55°C. Cone gas flow of 30 mL/min and collision gas (argon) flow at 0.2 mL/min. The source temperature will be maintained at 150°C and the electrospray capillary voltage at 0.6 kV. The multiple reaction monitoring (MRM) conditions for select PFAS are given in Table 1. These conditions will be optimized during the mass spectrometer tuning.

c. Analytical Standards and Calibration Procedure

The LC-MS/MS system will be mass calibrated using internal standards (sodium iodide and cesium iodide) and tuned to maximize instrument response using PFAS reference standards obtained from Wellington Laboratories who are accredited to produce reference materials [i.e., American National Standards Institute (ANSI) and American Society for Quality (ASQ) National Accreditation Board (ANAB) accredited reference material producer]. The currently used tune and quantification parameters are given in Tables 1, 2, and 3 at the end of this document.

The initial calibration (ICAL) will be performed using at least 5 concentrations of isotopically labeled PFOA and PFOS from Wellington Laboratories and mass spectra will be acquired at greater than 10 scans across each chromatographic peak. These concentrations will cover the range of expected concentrations. No unknown samples will be analyzed until the initial calibration has achieved the following criteria:

- Signal to noise ratio of 10:1 for all quantification ions
- The %RSD of the response factors for all analytes is less than 20%
- The calibration curve is linear with an $r^2 = 0.99$

The initial calibration will be verified (ICV) using unlabeled PFAS analytical standards obtained from the National Institute of Standards and Technology (NIST). After the initial calibration, the calibration samples will be analyzed prior to and after analyzing unknown samples to serve as a continuing calibration verification (CCV) where concentrations must be within 30% of the calibration standards.

d. Instrument Cleanliness

Two checks will be used to verify instrument cleanliness as well as to flush out the system after analyzing samples with high PFAS concentrations. One check is a zero-volume injection (i.e., instrument blank) to determine if there is carry-over on the UPLC column and the other check is the analysis of a PFAS-free 80:20 water to methanol to evaluate carry-over on the LC injection needle. These two checks will be performed after every 10 to 12 sample are analyzed to determine cleanliness of the instrument.

If the check results after a batch of 10 to 12 samples have significantly elevated PFAS concentrations compared to the other check results ($P > 0.05$) then the batch of samples will be analyzed again with additional blank checks included to determine which sample is causing carry-over.

4. References

Munoz, G., P. Ray, S. Mejia-Avendaño, S. Vo Duy, D. Tien Do, J. Liu, S. Sauvé. 2018. Optimization of extraction methods for comprehensive profiling of perfluoroalkyl and polyfluoroalkyl substances in firefighting foam impacted soils. Analytica Chimica Acta, 1034: 74-74.

Table 1 – Waters TQ-S Multiple Reaction Monitoring Conditions for Carboxylates								
Compound	Internal Standard	Molecular Ion	Cone Voltage (V)	Collision Energy (V)	Quant. Ion (m/z)	Cone Voltage (V)	Collision Energy (V)	Quant. Ion (m/z)
PFBA	[$^{13}C_4$] PFBA	213	10	8	169	--	--	--
PFPeA	[$^{13}C_5$] PFPeA	263	2	5	219	--	--	--
PFHxA	[$^{13}C_5$] PFHxA	313	4	4	269	4	20	119
PFHpA	[$^{13}C_4$] PFHpA	363	20	7	319	20	16	169
PFOA	[$^{13}C_8$] PFOA	413	2	9	369	2	12	169
PFNA	[$^{13}C_9$] PFNA	463	8	10	419	8	14	219
PFDA	[$^{13}C_6$] PFDA	513	11	10	469	6	18	219
PFUnA	[$^{13}C_7$] PFUnA	563	13	12	519	20	18	269
PFDoA	[$^{13}C_2$] PFDoA	613	15	12	569	4	26	169
PFTriA	--	663	15	13	619	--	--	--
PFTreA	[$^{13}C_2$] PFTreA	713	14	13	669	--	--	--
Internal Standards								
[$^{13}C_4$] PFBA		217	10	8	172	--	--	--
[$^{13}C_5$] PFPeA		268	10	8	223	--	--	--
[$^{13}C_5$] PFHxA		318	19	7	273	19	7	120
[$^{13}C_4$] PFHpA		367	20	8	322	20	20	169
[$^{13}C_8$] PFOA		421	7	9	276	7	16	172
[$^{13}C_9$] PFNA		472	10	11	427	10	14	223
[$^{13}C_6$] PFDA		519	11	11	474	11	16	219
[$^{13}C_7$] PFUnA		570	13	12	525	13	16	270
[$^{13}C_2$] PFDoA		615	4	11	570	--	--	--
[$^{13}C_2$] PFTreA		715	20	14	670	--	--	--

Table 2 – Waters TQ-S Multiple Reaction Monitoring Conditions for Sulfonates								
Compound	Internal Standard	Molecular Ion	Cone Voltage (V)	Collision Energy (V)	Quant. Ion (m/z)	Cone Voltage (V)	Collision Energy (V)	Quant. Ion (m/z)
PFBS	[$^{13}C_3$] PFBS	299	2	30	80	2	30	99
PFPeS	--	349	15	32	80	15	32	99
PFHxS	[$^{13}C_3$] PFHxS	399	2	34	80	2	32	99
PFHpS	--	449	14	38	80	14	38	99
PFOS	[$^{13}C_8$] PFOS	499	4	50	80	4	40	99
PFNS	--	549	10	43	80	10	43	99
PFDS	--	599	2	55	80	2	48	99
Internal Standards								
[$^{13}C_3$] PFBS		302	15	25	99	15	25	80
[$^{13}C_3$] PFHxS		402	25	25	99	25	25	80
[$^{13}C_8$] PFOS		506	15	32	78	10	33	80

Table 3 – Waters TQ-S Multiple Reaction Monitoring Conditions for Sulfonamide, Telomer Sulfonates, and Sulfonamidoacetatic Acids								
Compound	Internal Standard	Molecular Ion	Cone Voltage (V)	Collision Energy (V)	Quant. Ion (m/z)	Cone Voltage (V)	Collision Energy (V)	Quant. Ion (m/z)
PFOSA	[$^{13}C_8$] FOSA	498	16	32	78	--	--	--
FtS 4:2	[$^{13}C_2$] FtS 4:2	327	5	17	307	5	25	81
FtS 6:2	[$^{13}C_2$] FtS 6:2	427	5	21	407	5	19	81
FtS 8:2	[$^{13}C_2$] FtS 8:2	527	10	26	507	10	35	81
NMeFOSAA	D3MeFOSA	570	5	18	419	5	20	512
NEtFOSAA	D5EtFOSAA	584	5	18	419	5	17	526
Internal Standards								
[$^{13}C_8$] FOSA		506	15	32	78	--	--	--
[$^{13}C_2$] FtS 4:2		329	5	18	309	5	20	81
[$^{13}C_2$] FtS 6:2		429	5	22	409	5	25	81
[$^{13}C_2$] FtS 8:2		529	10	27	509	10	35	81
D3MeFOSAA		573	10	19	419	5	20	515
D5EtFOSAA		589	10	19	419	10	18	531